RUHR-UNIVERSITÄT BOCHUM

RUB

Analysis and Design of Sheet Metal Structures under the Influence of Polymorphic Uncertainties

Niklas Miska

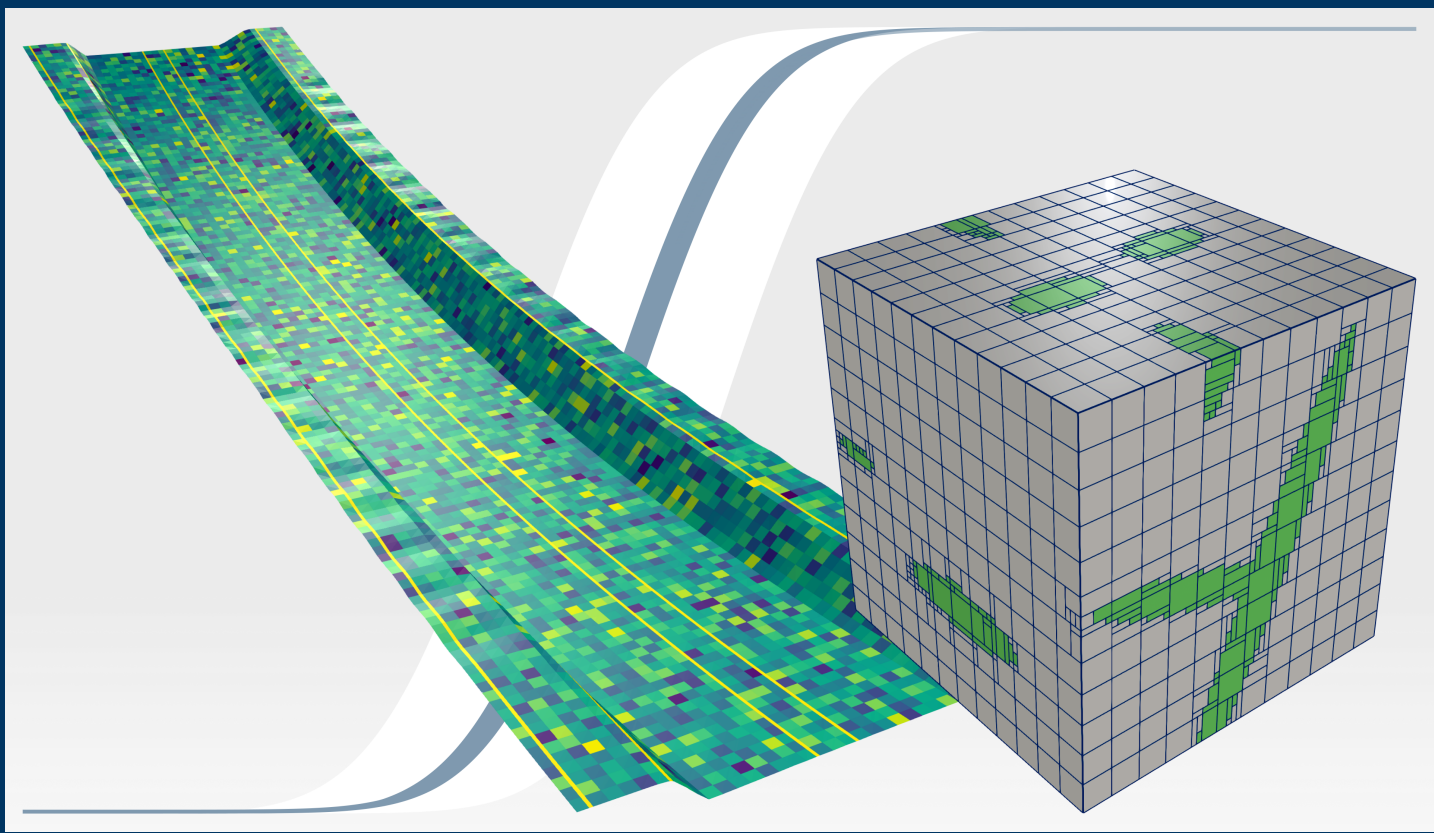

Analysis and Design of Sheet Metal Structures under the Influence of Polymorphic Uncertainties

Zur Erlangung des Grades
Doktor-Ingenieur (Dr.-Ing.)
an der Fakultät Bau- und Umweltingenieurwissenschaften
der Ruhr-Universität Bochum
genehmigte Dissertation

von

Niklas Miska

Bochum 2024

Mitteilungen aus dem Institut für Mechanik
Nr. 191

Publisher:

Institute of Mechanics
Ruhr University Bochum
D-44780 Bochum

Prof. Dr.-Ing. habil. Daniel Balzani
Chair of Continuum Mechanics

Herausgeber:

Institut für Mechanik
Ruhr-Universität Bochum
D-44780 Bochum

Prof. Dr.-Ing. habil. Daniel Balzani
Lehrstuhl für Kontinuumsmechanik

ISBN: 978-3-935892-69-8

Tag der Einreichung (thesis submission):	16.01.2024
Tag der mündlichen Prüfung (thesis defense):	22.04.2024
Erstgutachter (first referee):	Prof. Dr.-Ing. habil. Daniel Balzani
Zweitgutachter (second referee):	Prof. Dr.-Ing. habil. Steffen Freitag
Prüfungsvorsitz (committee chair):	Prof. Dr.-Ing. habil. Torsten Wichtmann

Preface

This thesis is the result of my work as a research assistant at the Chair of Continuum Mechanics at the Ruhr-University Bochum since 2017. All of the research described herein would not have been possible without the input, help and support of many amazing people, to whom I would like to express my deepest gratitude.

First of all, I would like to thank Professor Daniel Balzani, who ignited the spark of interest for numerical simulations and gave me the opportunity to research on the topics covered in this thesis. This work would not have been possible without his encouragement, guidance and academic supervision. I am thankful for giving me the freedom to tackle the arising problems as I thought best, but also for supporting me whenever asked. The created environment at the chair allowed me to learn, research and grow as a person.

Secondly, I would like to thank Professor Steffen Freitag, who not only agreed to provide a review for this thesis, but also accompanied my research. Thanks to fruitful discussions and supportive feedback, I was able to learn a lot in regard to artificial neural networks. The excellent collaborative work lead to the publication of a joint journal paper, which is also reflected in this thesis.

I would like to acknowledge Professor Wolfgang Graf and Professor Michael Kaliske, who initiated the priority program 1886 “Polymorphic uncertainty modelling for the numerical design of structures” of the german research foundation, in the context of which the research project I worked on was situated. Thanks to the priority program, not only I got to know many experts from the field of uncertainty quantification, but it also allowed me to present, discuss and improve my research on international conferences and internal meetings on a regular basis.

Next, I address my gratitude to my coworkers, who made the overall experience of conducting research a lot more entertaining. I am lucky to have had and still have an amazing group of coworkers, who not only support me when asked, but also make the life in the office more enjoyable. Special thanks are addressed to my former office roommate, Erik Tamsen, who created a fun and entertaining atmosphere by always having a positive outlook on life, providing constructive feedback and simply being there to talk or listen. Also, I would like to thank my former colleague Yannick F. Fangye, not only for supervising my diploma thesis at the end of my civil engineering studies in Dresden, but also for the joint research work we conducted on the topic of the Finite Cell Method, which resulted in the publication of a joint journal paper.

I want to thank my parents for their unconditional support throughout my life and especially during the phases of creation of this thesis. I am grateful for my friends distracting me from work if necessary and I thank my girlfriend for her patience, support and advice, in particular during the last stages of this thesis.

Abstract

The objective of the presented thesis is the development and application of a framework for the analysis and design of a car front bumper under the influence of polymorphic uncertainties. The interest on the consideration of uncertainties in engineering applications has increased in the recent years, which leads to the requirement of suitable methods for this purpose. Uncertainties can be caused by various factors such as inherent natural variation, imprecise or incomplete data and measurements and much more, all with their own respective demands in view of an appropriate consideration in the application of interest. The car front bumper of interest is made of an advanced high strength steel, a dual-phase steel. The behavior of such a steel results from its distinct heterogeneous microstructure, however, due to the production process this microstructure is not directly controllable. Thus, the properties of the dual-phase steel becomes uncertain and together with further uncertainties imposed during the production of the car front bumper, the behavior of said front bumper can not be reliable predicted without consideration of uncertainties.

In this thesis a method is developed to quantify the uncertainty in the behavior of the dual-phase steel, which is based on the numerical homogenization of a set of microstructure realizations. These microstructures are constructed, such that their variation of the microscale is similar to the variation of the real material's microstructure, whilst the geometrical complexity of the virtual microstructures is kept as low as possible to ensure numerical efficiency. In order to avoid the required effort to construct individual finite element meshes for each and every considered microstructure, the Finite Cell Method is applied. Since the Finite Cell Method requires the construction of so-called subcells, which is conventionally performed with an Octree split, additional numerical effort is introduced. This effort can be reduced by the application of the Optimal Decomposition approach presented in this thesis, which exploits features of the geometry representation to construct less subcells with a better approximation accuracy.

The obtained information on the variability of the dual-phase steels properties are then used as input uncertainties to an uncertainty analysis of the sheet metal forming process. For this purpose, the existing Optimal Uncertainty Quantification framework was extended to the capability of polymorphic uncertainty quantification and additionally integrated with the idea of discretized fuzzy numbers to allow a structured analysis of different interval combinations. When spatially uncertain quantities should be investigated, often random fields are the tool of choice. Random fields usually introduce significant numerical costs, such that in many cases reliable conclusion can hardly be drawn. Thus, a nested application of the extended Optimal Uncertainty Quantification is presented, which incorporates the often incomplete data random fields of, e.g., spatially distributed material parameters. Eventually, the extended Optimal Uncertainty Quantification framework is combined with reliability-based design optimization. This allows the optimization of the car front bumper in view of the dissipated energy during a crash, whilst a pre-defined threshold of safety is preserved.

Zusammenfassung

Das Ziel der vorliegenden Arbeit ist die Entwicklung und Anwendung eines Frameworks für die Analyse und den Entwurf eines PKW-Frontstoßfängers unter dem Einfluss polymorpher Unschärfen. Die Berücksichtigung von Unschärfen in ingenieurwissenschaftlichen Anwendungen hat in den letzten Jahren an zusätzlicher Bedeutung gewonnen, weshalb geeignete Methoden für die Unschärfequantifizierung verwendet oder gar entwickelt werden müssen. Unschärfen können durch verschiedene Faktoren verursacht werden, wie z.B. inhärente natürliche Schwankungen, ungenaue oder unvollständige Daten und Messungen und vieles mehr, die alle ihre eigenen Anforderungen im Hinblick auf eine angemessene Berücksichtigung haben. Das Stoßelement eines PKWs, welches im Rahmen dieser Arbeit betrachtet wird, besteht aus einem hochfesten Stahl, einem Dualphasenstahl. Das Verhalten eines solchen Stahls ergibt sich aus seinem ausgeprägten heterogenen Gefüge, welches jedoch aufgrund des Herstellungsprozesses nicht direkt kontrollierbar ist. Deshalb sind die Eigenschaften des Dualphasenstahls unscharf, und zusammen mit weiteren Unschärfen, die bei der Herstellung des Stoßfängers auftreten, kann das Verhalten des Stoßfängers ohne Berücksichtigung von Unschärfen nicht zuverlässig vorhergesagt werden.

In dieser Arbeit wird eine Methode zur Quantifizierung unscharfer Eigenschaften des Dualphasenstahls entwickelt, die auf der numerischen Homogenisierung einer Reihe von Mikrostrukturrealisierungen beruht. Diese Mikrostrukturen werden so konstruiert, dass ihre Variation auf der Mikroskala der Variation der Mikrostruktur des realen Materials entspricht, während die geometrische Komplexität der virtuellen Mikrostrukturen so gering wie möglich gehalten wird, um die numerische Effizienz zu steigern. Um zu vermeiden, für jede einzelne betrachtete Mikrostruktur ein eigenes Finite-Elemente-Netz konstruieren zu müssen, wird die Finite-Cell-Methode angewendet. Da die Finite-Cell-Methode die Konstruktion von sogenannten Subcells erfordert, die herkömmlicherweise mittels eines Octree-Splits erzeugt werden, entsteht ein zusätzlicher numerischer Aufwand. Dieser Aufwand kann durch die Anwendung des in dieser Arbeit vorgestellten Ansatzes der Optimal Decomposition reduziert werden, der die Eigenschaften des Geometriedatenformats ausnutzt, um weniger Subcells mit einer besseren Approximationsgenauigkeit zu konstruieren.

Die gewonnenen Informationen über die Variabilität der Eigenschaften des Dualphasenstahls werden dann als Eingangsunschärfen für eine Unschärfeanalyse des Blechumformprozesses verwendet. Zu diesem Zweck wurde das vorhandene Optimal Uncertainty Quantification Framework für die Quantifizierung von polymorpher Unschärfe erweitert und zusätzlich mit der Idee der diskretisierten Fuzzy-Zahlen ergänzt, um eine strukturierte Analyse verschiedener Intervallkombinationen zu ermöglichen. Für die Untersuchung räumlich verteilter unscharfer Größen werden häufig Zufallsfelder verwendet. Wenn räumlich unscharfe Größen untersucht werden sollen, sind häufig Zufallsfelder das Mittel der Wahl. Zufallsfelder verursachen in der Regel erhebliche numerische Kosten, so dass in vielen Fällen nur schwer verlässliche Aussagen getroffen werden können. Daher wird eine verschachtelte Anwendung der erweiterten Optimal Uncertainty Quantification vorgestellt, die die oft unvollständigen Daten resultierend aus Zufallsfeldern von z.B. räumlich verteilten Materialparametern einbezieht. Schließlich wird das erweiterte Optimal Uncertainty Quantification Framework mit der zuverlässigkeitsorientierten Designoptimierung kombiniert. Dies ermöglicht die Optimierung des vorderen Stoßfängers eines Fahrzeugs im Hinblick auf die dissipierte Energie während eines Aufpralls, wobei eine vordefinierte Obergrenze für die Versagenswahrscheinlichkeit eingehalten wird.

Contents

1 Introduction

1.1 Motivation and State of the Art

Albeit the job title engineer, as it is understood today, has emerged only a few centuries ago, one of their core capabilities has been practiced by humankind for a far longer time: the abstraction of real processes in terms of comparatively simpler models to explain and predict rather complex natural phenomena and processes. Whilst in earlier ages, e.g., the recurrences of seasons and weather phenomena were important for survival, nowadays much more complex models are used in research and development to analyze, predict or design more efficient, more precise or otherwise improved buildings, machines and/or processes. All of these models are based on observations of the reality and thus, try to replicate the observed causal connections between an initial and final state of the system of interest. The construction of models is inevitable affiliated with the introduction of uncertainties, since every model is a mathematical idealization of the reality and therefore incomplete by nature. In this regard, the term "model" may not only be understood in reference to the mathematical formalization of e.g., a physical or chemical process, but also pertaining to the incorporation of the uncertainties mentioned before. As a consequence, the engineer or model builder is faced with the challenge of not only building an appropriate physical model, but also employing meaningful models for the appearing uncertainties.

The appropriate choice of such models for the uncertainties depends on various factors and circumstances of the problem at hand. One important aspect is the overall objective of the problem, i.e., should the outcome of an existing setting be investigated due to uncertainties in the input parameters (uncertainty quantification) or are there some adjustable parameters, which can be tuned, such that the result improves in robustness or reliability (optimization under uncertainties). For example, the load-bearing capacity of a bridge depends on, among others, material properties of the building materials and the geometric design of the supporting structure. These quantities are usually affected by uncertainties, stemming from e.g., intrinsic variation of macroscopic concrete material properties due to its random mesostructure or an imprecise fabrication of the supporting structure, and hence, the overall load-bearing capacity of the bridge becomes uncertain as well. These uncertainties are instances of parametric uncertainties, i.e. uncertainties in quantities, which servers either as model input parameters or as ultimate values, which are compared against model output values. The bridge-example potentially comprises another type of uncertainties, which are model uncertainties. Model uncertainties are a result from a discrepancy between the real system and the mathematical reflection, e.g., by negligence of certain variables or approximate (numerical) solutions such as finite element methods. The impact of all of these uncertainties may be overcome by the utilization of large safety factors, but a more economic, efficient and reliable design can be obtained by incorporating a sophisticated uncertainty quantification in the design process.

Another decisive factor is the source of the uncertainties, which can be, for example, inherent natural variation of properties and loads, impreciseness or incompleteness of measurements and data, vague lingual information and many more. Usually, the source of the uncertainty is directly coupled with the amount of knowledge available for the uncertain quantity. Since a single mathematical model, that can deal with all sources of uncertainties and all amount of

available knowledge has not yet been found, uncertainties are commonly divided in two different classes: aleatory and epistemic uncertainties, cf., e.g. Kiureghian and Ditlevsen [73], Beer et al. [10] or Oberkampf et al. [107]. The name aleatory stems from the Latin word *alea* for dice and thus, the class of aleatory uncertainties comprises all those uncertainties, which are caused by the mentioned inherent natural variation, which is fully known. It is well agreed on in the literature, cf. e.g., Oberguggenberger [106], that these kind of uncertainties are suitably characterized by methods from the mathematical field of probability theory, cf. e.g., Billingsley [14]. Since additional data, e.g., in form of additional measurements or additional experiments, can not improve the mathematical description of these uncertainties, they are sometimes also referred to as objective or irreducible uncertainties. The second class of uncertainties is named after the Greek word *episteme* ($\varepsilon\pi\iota\sigma\tau\eta\mu\eta$) for knowledge and incorporates all remaining uncertainties. Typically, these uncertainties are characterized by a lack of knowledge, i.e., even if the uncertain quantity may follow a hidden natural variation, the mathematical rules for that variation are not known, which is manifested in imprecision or incompleteness. Therefore, additional data points can improve the description of the associated uncertainty and reduce the lack of knowledge, which is why these uncertainties can also be referred to as reducible or subjective uncertainties. The potential origins of these type of uncertainties are diverse and includes, among many others, errors in measurements, insufficient data or experiments due to e.g., monetary or practical reasons, vague lingual information and many more. Since this type includes all uncertain quantities, for which the available data ranges from nearly nothing to just shy of a full probability distribution function, several methods for the inclusion of these uncertainties in an uncertainty quantification have been proposed in the literature. The "correct" categorization of an uncertain quantity in one of these two categories is not only a subjective choice of the responsible engineer, but also much discussed in the literature, cf. e.g., the works of [73] or [10]. Usually, an uncertainty quantification problem does not contain only one or the other type of uncertainties, but rather both. For these kind of problems, the term "polymorphic" uncertainty quantification has been coined in the last years. It should be noted in this context, that term polymorph can also refer to a single uncertain quantity, for which mathematical models for both types are coupled to express a single uncertain quantity, which will be discussed later.

The overall objective of this thesis is the design of a car front bumper made out of a dual-phase steel as exemplary illustrated in Fig. 1.1. This car front bumper is subjected to the influence of polymorphic uncertainties due to its base material as well as its production process. Hence, the uncertainties regarding the material properties of the base steel as well as fabrication parameters should be considered during the optimization. Consequently, an uncertainty quantification framework for both aleatory as well as epistemic uncertainties is necessary for the uncertainty quantification during the design optimization. The optimization target is the maximization of the dissipated energy in a crash scenario, whilst a pre-defined threshold on the probability of failure must not be exceeded. Since the outer dimensions of the front bumper are assumed to be fixed, the optimization design variables are laser-hardened traces, which can be positioned on the sheet metal to locally improve the material properties, cf., Wagner et al. [159]. These traces are hardened by a laser, which locally melts the base material. A subsequent controlled cool-down allows a phase-transformation of the steel, leading to locally modified and improved material properties. In this particular application, the positions of such traces can be altered to identify the optimal location of the traces.

The material of the base sheet metal, from which the car front bumper is produced, is a dual-phase steel (DP-steel). A dual-phase steel consists, as the name indicates, of two different steel phases, a ferrite matrix in which island-like portions of martensite are embedded. These martensite portions are created by a phase-transformation from austenite while the steel cools down during the production. The martensite portions within the steel are certainly not in-

Figure 1.1: Highlighted in orange, a normally hidden car front bumper, shown by means of a Toyota Yaris. The overall objective of this thesis is the optimization of the performance of such a front bumper in a crash scenario, considering polymorphic uncertainties.

clusions in a physical sense like aggregates are inclusions in concrete, but due to the typical volume fraction of 15 to 25 %, the geometric character of the martensite portions is reminiscent of such inclusions. Therefore, if the martensite may be referenced to as inclusion for clarity, it is only meant in the geometrical, but not in the physical sense. Since the exact location and shape of these martensite portions can hardly be controlled during the production, their location and shape are random to some extend. In consequence, the microstructure of this type of steel is random as well, which implies an influence on the macroscopic behavior of this steel. Since the macroscopic behavior of the DP-steel is of particular significance for the production as well as the performance of the car front bumper, some information and insight in the uncertain behavior of the DP-steel is necessary. Certainly, the required data could be obtained by a series of experiments, such as e.g., tension tests, on a large set of different specimens of the same material. However, these real experiments are expensive in terms of costs and required labor, such that virtual experiments in terms of numerical simulations using finite elements are a more viable approach. A crucial step for these virtual experiments is the appropriate reconstruction of the material's microstructure morphology. One possible approach is the quantification of the inclusion-like phase, in terms of probability density functions (PDF), which are used to describe and generate the physical shape and spatial distribution of the inclusion, cf., e.g. Hiriyur et al. [66], Savvas et al. [125] with Stefanou et al. [142]. For the specific class of polycrystalline alloys, a method based on reduced-order representations of the texture evolution by means of the Karhunen-Loève expansion is proposed in Kouchmeshky and Zabaras [75], from which stochastic quantities of interest for e.g., the Young's or the bulk modulus, can be derived in reasonable time. In Liu et al. [80] and Deng et al. [23] an attempt to reconstruct the material's microstructure from statistical correlation of binary images of the microstructure with subsequent homogenization and experimental validation has been presented. A first-order perturbation scheme for geometrical deviations and material properties of the microstructure is presented in Wen et al. [160], which includes a stochastic homogenization for the prediction of the stochastic distribution of the macroscopic material properties. Further approaches for random microstructure morphologies are given in Vel and Goupee [156] and Ma et al. [83]. The effective material behavior of concrete due to random distribution and size of the aggregates is of interest in Tal and Fish [149]. Therein, the morphology variation is quantified by scalar statistics and subsequently reconstructed, such that the properties of interest can be computed by numerical homogenization. Many of the discussed approaches are restricted to either a special class of material or scalar statistical analysis. In order to capture the variability of the dual-phase steels microstructure morphology, in Miska and Balzani [93], a general framework was proposed, which utilizes higher order, i.e. non-scalar, statistical descriptors to construct a set of artificial microstructures, which

exhibits the same variability as the real materials microstructure. Therein, the construction of the artificial microstructures is based on the idea of Statistically Similar Representative Volume Elements (SSRVEs), cf., e.g. Balzani et al. [4] and Scheunemann et al. [126]. Numerical homogenization of these microstructures then leads to the distribution of macroscopic material properties of interest.

As discussed before, the two different types of uncertainties are reflected by different mathematical models in the uncertainty analysis. Whilst the aleatory uncertainties are well reflected by probability measures, cf., e.g. Billingsley [14] or Oberguggenberger [106], the model choice for epistemic uncertainties is not as straight forward. This is partially motivated by the wide spectrum of characters an epistemic uncertainty can take. A quantity, for which only bounding values are known, is of epistemic uncertainty type, as well as another quantity, for which the type of an underlying probability density function can be estimated, but the exact parameters are only vague. Thus, many different approaches for epistemic uncertainty quantification can be found in the literature. In the context of Bayesian Probabilities, the parameters of probability density functions are assumed to be distributed according to their own distribution, and hence, known tools for the probability theory can be used, cf., e.g. Rackwitz [120] or Sankararaman and Mahadevan [123]. However, a crucial step therein is the choice of the type of distributions, which can have a potentially large impact on the computed results, see for example Fetz and Oberguggenberger [39], Zhang and Shields [168], or Zhang and Shields [169]. Hence, alternatives have emerged from the field of imprecise probabilities, cf. Beer et al. [10] for an overview. Contrary to Bayesian-based methods, these alternative do not assume probability density functions for all uncertain quantities and allow for the consideration of only intervals or fuzzy numbers for individual uncertain quantities, cf. e.g., Zadeh [165, 166] or Möller et al. [101]. By that, a different interpretation of uncertainties is introduced. Whilst a probability density assigns a certain weighting to values within the range of the uncertain quantity expressing the likelihood of values to occur, an interval or a fuzzy number only expresses the possibility, that any value from within its range can occur, but does explicitely not assume any weighting above that. Thus, a uniform distribution and an interval for the same range do have fundamentally different meanings and interpretations for the uncertainty quantification. Intervals and fuzzy numbers can not only be used to model an uncertain quantity itself, similar to the Bayesian approach, they can also be used to model parameters of a probability density function, see e.g., Möller et al. [102], Götz et al. [57] or Faes et al. [34]. A slightly different or rather extended interpretation of intervals and fuzzy numbers can be found in the context of possibility theory, in which the possibility and necessity of events and probabilities is analyzed, cf. Hose and Hanss [68].

The development and application of methods for the quantification and design of polymorphic uncertainties has gained additional traction in the last couple of years. This may be partially due to the priority program "Polymorphic uncertainty modelling for the numerical design of structures" of the german research foundation (SPP1886). In this priority program, a lot of different problem settings and methods have been investigated and proposed by individual research groups. Examples of covered application examples are uncertainty quantification with experimental verification of wind turbine blades, cf., Drieschner et al. [27], multi-objective design optimizations of wooden structures, cf., Schietzold et al. [129], a reliability-based design optimization of tunnel linings, cf., Neu et al. [104], and the behavior of earth structures, cf., Schmidt et al. [133], among others. Moreover, methodological developments have been made in regards to e.g., multilevel surrogate models based on artificial neural networks, cf., Freitag et al. [45], surrogate models based on proper orthogonal decomposition and hierarchical tensor approximations, cf., Kastian et al. [72], model order reduction, cf., Pivovarov et al. [118] and domain decomposition approaches coupled with polynomial chaos expansion, cf., domain decomposition Schmidt and Lahmer [132]. Further developments were published

for the optimization under polymorphic uncertainties with nested inherence of objectives, cf., Schietzold et al. [130], fuzzy probability random fields, cf., Schietzold et al. [128], data driven uncertainty analysis, cf. Zschocke et al. [170]. The work in the priority program was completed by joint works on benchmark problems, cf., Papaioannou et al. [116], Mäck et al. [84] or Drieschner et al. [28], and joint articles, in which different approaches to polymorphic uncertainty quantification were compared, e.g., for methods concerning uncertainty quantification of multiscale problems in Kremer, Edler, Miska, Leichsenring, Balzani, Freitag, Graf, Kaliske, and Meschke [76].

A method with distinct features from the methods discussed before is the Optimal Uncertainty Quantification (OUQ), cf. Owhadi et al. [110]. The OUQ allows the computation of the mathematically sharpest bounds possible on a probability of interest by considering only bounds for the uncertain quantities itself as well as for stochastic moments of these quantities, whilst a specification of a probability density function is not necessary. This method is based on the optimization of weights and positions of convex combinations of Dirac measures, cf., McKerns et al. [88] for additional details and Balzani et al. [6] for an application of the OUQ to a rupture problem of biological tissues. However, the original OUQ considers all uncertainties as epistemic uncertainties, which makes it in principle unusable for polymorphic uncertainty quantification problems. Therefore, in Miska and Balzani [96] the framework was extended to incorporate aleatory uncertainties as well. Additionally, the idea of fuzzy numbers was integrated, which allows the systematic investigation of different combinations of intervals. This extended Optimal Uncertainty Quantification framework can also be used for the consideration of spatially varying properties, cf., Miska, Freitag, and Balzani [100]. Therein, the spatially variation of certain material properties is modeled by means of random fields, for which details can be found in Vořechovský [158], Ghanem and Spanos [50], Vanmarcke [155] and Schwab and Todor [138]. Since the OUQ framework contains an optimization problem and the problem of interest contains a numerical problem in terms of finite elements, it can be beneficial to substitute the costly finite element simulations by an a-priori trained surrogate model in terms of an artificial neural network (ANN), cf, Haykin [61] or Rojas [122] and Freitag [44] for an overview on the application of ANNs in structural mechanics . Among others, ANNs are a popular choice as surrogate model in terms of uncertainty quantification problems and are widely used in the literature, see for example the works of e.g., Papadrakakis et al. [113], Hurtado [70], Papadrakakis and Lagaros [112], Most and Bucher [103], Freitag et al. [45], Edler et al. [32] or Cao et al. [20]. Alternative approaches for polymorphic random fields can be found in Henning et al. [63], Schietzold et al. [128] or Schmidt et al. [133].

With information on the uncertain material properties and a framework for polymorphic uncertainty quantification at hand, only one part is missing for the overall objective of this thesis. In order to include the uncertain quantities in the search of the optimal design of the car front bumper, a framework for the design optimization under constraints is necessary. For this purpose, methods for the Reliability-Based Design Optimization (RBDO) were developed, for example in Enevoldsen and Sørensen [33], Frangopol and Maute [43], Schuëller and Jensen [137], Beaurepaire et al. [9], Valdebenito and Schuëller [154], Götz [56] or Mäck et al. [84]. RBDO-methods aim to identify the optimal design of the structure, whilst a constraint in regard to the reliability of the resulting structure is satisfied. Usually, this constraint is formulated in terms of an upper limit on the probability of failure. Therefore, the extended OUQ is integrated in an RBDO-context, at which the OUQ is not only used for the computation of the constraint, but also for the computation of the performance of the structure under the influence of polymorphic uncertainties.

Subsequently, the proposed RBDO framework is used to optimize a car front bumper, for which three different production and lifetime scenarios are investigated: the deep-drawing, a

spring-back analysis with prior trimming of the sheet metal and a simplified crash scenario. The degrees of freedom are positions of locally laser-hardened traces, by which the local material properties such as the yield strength of the sheet metal can be significantly improved, cf., e.g., Wagner et al. [159].

1.2 Structure

As briefly mentioned in the motivation, the overall objective of this thesis is the optimization of a car front bumper, such that the dissipated energy due to plastic deformation in a crash is maximized. In order to reach this goal, different methods and intermediate steps are required, which are discussed in individual chapters.

In the next chapter, Chapter 2, the necessary notations and definitions for parametric uncertainty quantification are introduced. Special focus is on the mathematical foundations for probability measures, interval and fuzzy numbers, such that the mathematical models for both aleatory and epistemic uncertainty quantification are available. Additionally, methods such as Monte Carlo simulation and optimization methods are discussed, which are necessary to solve uncertainty quantification problems based on the aforementioned models.

In Chapter 3 a brief overview of continuum mechanics and finite element simulations is presented. The finite elements used for numerical homogenization are based on the finite cell method, which allow the numerical computation of macroscopic material properties in a virtual lab.

Since a numerical homogenization of a set of different microstructures requires an individual mesh for each microstructure, an automatized approach to the mesh generation is inevitable. The selected approach here is the application of the finite cell method, which allows the use of regular grids as finite element mesh and a geometry approximation by subcells. The traditional approach to the construction of subcells is based on an Octree split, which can lead to high numerical costs. Therefore, in Fangye, Miska, and Balzani [37] an enhanced algorithm, the Optimized Decomposition, was proposed, which exploits the cuboid-shaped nature of the geometry representation in terms of voxel data. The Optimized Decomposition is described in detail and compared to the conventional Octree split in Chapter 4.

In Chapter 5, an approach for the quantification of macroscopic material properties related to the hardening behavior of a Dual-Phase steel (DP-steel) resulting from variation of the microstructure morphology is described. The method, originally published in Miska and Balzani [93], is split into three submethods: at first, the variation of the real microstructure morphology is quantified based on a distance functional, which measures the difference of a selected subsection of the microstructure and a representative element in terms of higher order statistical measures. Then, a set of artificial microstructures with a less complex morphology is constructed, such that the variation of this set in terms of the morphology variation is as similar as possible to the previously obtained real variation. Finally, these artificial microstructures are tested in a virtual lab, i.e. by numerical homogenization, such that the macroscopic material behavior is obtained. In order to perform the computational homogenization efficiently, a Multi-Level Monte Carlo approach is introduced.

In Chapter 6, the Optimal Uncertainty Quantification framework, cf. [110], is extended to the capability of polymorphic uncertainty quantification, cf. Miska and Balzani [96]. In its original form, only epistemic uncertainties, i.e. quantities, which are uncertain due to imprecision or incompleteness, could be considered, the extension allows for the incorporation of aleatory uncertainties in form of probability density functions as well. Furthermore, for a structured investigation of different ranges of epistemic input quantities, a combination of

the OUQ framework with fuzzy numbers is shown. The overall efficiency of the framework is improved by the reformulation of the underlying optimization problem in terms of canonical moments, cf. also Dette and Studden [24] and Stenger et al. [143]. A special case is the nested application of the extended Optimal Uncertainty Quantification framework to problems with spatially varying properties, also known as random fields, which is presented in Miska, Freitag, and Balzani [100]. Since numerical simulations based on such random fields are usually complex and therefore, expensive to evaluate, often only limited information on the statistical distribution of the target quantity can be deduced. These limited data are used for an inner OUQ problem, whilst the remaining uncertainties of the problem are incorporated in the outer OUQ problem. By that, assumptions on results from complex random fields can be avoided.

In Chapter 7, the extended OUQ from Chapter 6 is embedded in a reliability-based design optimization context. Thereby, a method is obtained to design a structure under the influence of polymorphic uncertainties, whilst a pre-defined level of safety, which is measured in terms of the probability of failure, is maintained. The framework is demonstrated by means of a numerical example of a car front bumper, for which the production and a simple crash scenario are investigated.

Lastly, this work closes with a brief summary of the presented methods and results in Chapter 8.

2 Uncertainty Quantification for Engineering Applications

As mentioned in the introduction, the abstraction of real world phenomena by means of mathematical and physical models is always associated with the introduction and consideration of uncertainties. Hence, the incorporation of models for the emerging uncertainties in the design and construction phases of appliances and structures is a sensible course of action for many engineering fields. However, the appropriate choice of such models is not always straight forward and may vary depending on the context of the uncertain quantity. In this chapter, first some definitions and terminologies for different uncertainty types are introduced, before subsequently different mathematical models and tools for uncertainty quantification problems are discussed. Only selecting the mathematical models for individual uncertainties is, however, not sufficient for a successful uncertainty quantification. Since the engineer's task is to assess the preformance or safety of a certain structure, the impact of uncertain quantities on the relevant performance measures needs to be computed, which is known as uncertainty quantification. This task, in connection with rather complex physical models is usually not analytically tractable and requires the use of numerical approaches. Therefore, in series to the mathematical models for uncertainty representations, numerical tools are presented to perform the uncertainty propagation. For the case of stochastic quantities the Monte Carlo simulation is introduced and for epistemic uncertainties the challenge of optimization problems is discussed. As both types of uncertainties can be combined and mixed for a realistic uncertainty analysis, the Monte Carlo simulation and optimization may be applied in a nested manner. While both approaches rely on a large number of evaluations of the underlying deterministic model for the physics of the problem, the nested approach leads to an even higher number. Thus, as closing section of this chapter a brief introduction on artificial neural networks (ANNs) is given, because ANNs are a well-suited method to construct surrogate models. They are numerically cheaper to evaluate than a complex physical model, while yielding approximately the same results as the complex model.

2.1 Terminology and Types of Uncertainties

Before different mathematical models are introduced for uncertainties and uncertainty quantification, first the term "uncertainty" itself and the discrimination of different uncertainties in categories is recapitulated. By definition, uncertainty simply refers to the lack of certainty, i.e., based on the available, potentially limited, knowledge or information, it is impossible to exactly describe or predict the actual or future status of a system of interest. Since the latter is a central interest in many engineering applications, the arising uncertainties should be considered in the respective phases and actions to ensure the creation of safe designs. Due to the various sources of uncertainties, it is unlikely, that a single mathematical model can be sufficient to reflect all possible settings incorporating uncertainties. Thus, it is meaningful to categorize uncertainties, for which different, suitable models and approaches can be utilized. A common approach to this challenge is the differentiation of uncertainties by the amount of available data and the causes for the uncertainties, respectively. If an uncertainty is solely caused by inherent natural randomness and sufficient data for its description is available,

these uncertainty is of aleatory type. The mathematical models commonly used for these uncertainties stem from the field of probability theory, i.e., an uncertainty of aleatory type can be modeled by means of a probability measure with its associated probability density. These tools are introduced in Sec. 2.2. Since aleatory uncertainties are caused by natural variation and are perfectly described by an probability measure, additional data samples can not improve the mathematical description, hence, aleatory uncertainties are irreducible and sometimes also referred to as *objective* uncertainties. On the other hand, however, there are also uncertain quantities, for which fixed probability measures may not be the appropriate choice, as e.g., to little data is available, errors in measurements could not be avoided or only vague information is given, e.g., by subjective lingual information. These uncertainties are called *epistemic* uncertainties. It can't be precluded, that these uncertain quantities are distributed according to a probability distribution as well, but since the available data is not sufficient for an unique determination of such a distribution and hence, only the available data should be used as is in the uncertainty analysis. Because additional data in form of e.g., additional measurements, can improve their description, epistemic uncertainties are in principle reducible and sometimes called *subjective* uncertainties. Furthermore, in contrast to the aleatory uncertainties, there is no go-to choice in terms of a mathematical model, since the class of epistemic uncertainties spans from very little knowledge, e.g. in terms of an intervals for bounds on a quantity, to almost full knowledge, for which imprecise or conditional probabilities may be utilized. In Sec. 2.3, intervals and fuzzy numbers are introduced, which are a common choice for epistemic uncertainties. On top of that, such intervals or fuzzy numbers, which in itself can only express bounds on a quantity, may be used to model parameters of probability distributions, leading the mentioned imprecise probabilities. This combination couples models for aleatory and epistemic uncertainties and is therefore also known as *polymorphic* uncertainty quantification.

2.2 Probability Theory

Since tools from the field of probability theory, namely the probability measures and their associated probability density functions (PDFs), are commonly used to model aleatory uncertainties, this section is meant to outline the essential concepts of probability theory. The explanations of this section are based on Billingsley [14], Borovkov [18] and Hable [58], while the notations follow the latter reference.

2.2.1 Probability Measures and Probability Measure Spaces

Before a probability measure can be introduced, the general notation of a measure with its requirements has to be introduced. For that matter, first a *measurable space*

$$(\Omega, \mathcal{A}) \tag{2.1}$$

is defined, which consists of the *sample space* Ω and the associated σ*-algebra* $\mathcal{A}$ on Ω. The sample space Ω, sometimes also referred to as possibility or outcome space, is a set, which contains all possible outcomes or *realizations* ω of an experiment. In the context of probabilities, commonly used examples for such experiments are tossing a coin or rolling a fair dice. Then, the sample space would consist of the possible values the coin or the dice could take, i.e. $\Omega = \{1, 2, 3, 4, 5, 6\}$ for the fair dice. It should be noted, that the dice and also the coin experiment are examples for discrete measures, which is no premise for probability measures and measures in general. An example for a continuous experiment, which is also not related to probabilities, measures the area of arbitrary rectangles in a two-dimensional domain. Thus, the sample space is $\Omega = \mathbb{R}^2$.

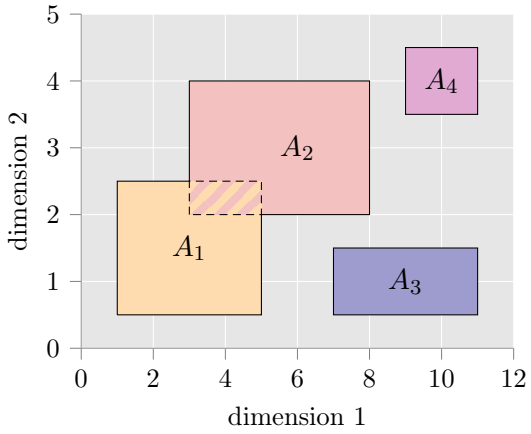

Figure 2.1: Example for a continuous two-dimensional sample set with four events A_1, A_2, A_3 and A_4. The associated measure μ calculates the area of the rectangles.

The σ-algebra associated to the sample space Ω as mentioned in (2.1) is a set of some subsets of Ω, for which the to be defined measure should assign a (non-zero) value, mandatory including the empty set $\emptyset$ and the entire sample space Ω. In fact, the trivial σ-algebra on Ω contains only $\emptyset$ and Ω. In general, the choice of a σ-algebra is not unique and depends on the application case, but in many cases the so-called Borel σ-algebra is used, which is the smallest possible σ-algebra containing all open sets for continuous problems. The elements of $\mathcal{A}$ are called measurable sets, also referred to as "events". For the example of the rolled dice, events of interest, aside the atomic events of a particular value, could be e.g., an odd number, i.e. $\{1, 3, 5\} \in \mathcal{A}$, or a number larger than four, i.e. $\{5, 6\} \in \mathcal{A}$. Since a σ-algebra has to be closed under complement, also the complementary events have to be an element of $\mathcal{A}$, i.e., $\{2, 4, 6\} \in \mathcal{A}$ and $\{1, 2, 3, 4\} \in \mathcal{A}$. These examples make also use of the closure under countable union, i.e. since the atomic events $\{1\}$, $\{2\}$, $\{3\}$, $\{4\}$, $\{5\}$ and $\{6\}$ are elements of $\mathcal{A}$, also all possible unions of these events are part of $\mathcal{A}$.

Based on the measurable space, a function can be defined, which assigns every element of $\mathcal{A}$ a numerical value, which may be interpreted as "mass" or "size" of that particular element:

$$\mu : \mathcal{A} \to [0, \infty]. \tag{2.2}$$

This function μ is called *measure* on the measurable space $(\Omega, \mathcal{A})$, and the triple $(\Omega, \mathcal{A}, \mu)$ is referred to as measure space. The measure in Eq. (2.2) is a finite measure, if $\mu(\Omega) < \infty$ and hence, $\mu(A) < \infty \ \forall A \in \mathcal{A}$. Whilst a measure maps to only non-negative values, a signed measure can map to the entire real line and at most one of $\{\pm\infty\}$, i.e.,

$$\mu : \mathcal{A} \to \mathbb{R} \cup \{\pm\infty\}. \tag{2.3}$$

A measure of special interest for this work is the normalized measure, for which $\mu(\Omega) = 1.0$ and $0 \leq \mu(A) \leq 1$ holds. This measure is also called *probability measure*, since the "mass" assigned to the events of $\mathcal{A}$ can be interpreted as probability, and the triple of $(\Omega, \mathcal{A}, \mu)$ is called probability space. Often, a probability measure μ is alternatively denoted by $\mathbb{P}$. The following text will refer to probability measures explicitly, although many presented rules apply to general measures as well. The terms measure of an event and probability of an event may be used interchangeably.

A probability measure μ exhibits a few properties, which are important for the calculation of probabilities for specific events. Foremost, the empty set $\emptyset$ should have zero probability and

thus, $\mu(\emptyset) = 0$. Also, if $A_1, A_2, \dots A_n \in \mathcal{A}$ are pairwise disjoint elements, i.e., $A_1 \cup A_2 = \emptyset$, the measure of the union is equal to the sum of the measure of the individual sets:

$$\mu(\bigcup A_n) = \sum \mu(A_n). \tag{2.4}$$

This property is referred to as σ-additivity and in the context of probabilities also known as the third axiom of Kolmogorov. If an event A_1 is a subset of an event A_2, the measure of the first event should be less or equal to the measure of the latter set:

$$A_1 \subset A_2 \;\Rightarrow\; \mu(A_1) \leq \mu(A_2). \tag{2.5}$$

As an extension and under the premise, that the probability of event A_1 is finite, the probability of the complement of event A_2 with respect to A_1 is given by

$$A_1 \subset A_2 \;\wedge \mu(A_1) < \infty \;\Rightarrow\; \mu(A_2 \backslash A_1) = \mu(A_2) - \mu(A_1). \tag{2.6}$$

If two events A_1 and A_2 are intersecting each other, the union of both events can by computed by the sum of the measures of the two individual events subtracted by the value of the intersection:

$$\mu(A_1 \cap A_2) < \infty \;\Rightarrow\; \mu(A_1 \cup A_2) = \mu(A_1) + \mu(A_2) - \mu(A_1 \cap A_2). \tag{2.7}$$

This property is also visualized in Fig. 2.1, in which the two areas A_1 and A_2 are intersecting each other. A simple addition of both areas would yield a value too large and thus, the area of the intersection has to be subtracted.

2.2.2 Random Variables

A *random variable* is often used to describe a quantity, which depends an on inherent randomness and should be described by means of probability theory. Purely mathematically spoken, however, a random variable Y is a deterministic function mapping from one probability space, denoted by $(\Omega, \mathcal{A}, \mu)$, to another $(\Omega', \mathcal{A}', \mu')$, i.e.,

$$Y : \Omega \to \Omega', \;\; \omega \mapsto \omega'. \tag{2.8}$$

In many applications the random variable should yield a real value, i.e. $Y : \Omega \to \mathbb{R}^d$, which leads to a real, potentially vector-valued, random variable. The probability measure μ' on $(\Omega', \mathcal{A}')$ is then given as push-forward measure by

$$\mu' : \mathcal{A}' \to [0; 1], \;\; \Omega' \mapsto \mu'(\Omega') = \mu(\{\omega \in \Omega \,|\, Y(\omega) \in \Omega'\}). \tag{2.9}$$

In this context, μ' is called probability distribution of Y (under μ'). In practical applications, however, the underlying probability space $(\Omega, \mathcal{A}, \mu)$ and also the exact function Y are of minor significance, whilst the major interest is on the probability distribution μ' of Y on $\mathbb{R}^d$, since μ' is the probability measure for all realizations of Y.

2.2.3 Discrete and Continuous Probability Measures

Up until now, only the idea of the probability measure was introduced, but no information on how such measures are defined or actually computed. For this purpose, the two types of probability measures, discrete and continuous measures, are differentiated and individually discussed in the next two subsections.

Discrete Measures A probability measure μ defined on $(\Omega, \mathcal{A})$ is a discrete probability measure, if there is a subset $D \subset \Omega$, which has a finite or at most a countable infinite number of elements, for which $\mu(D) = 1.0$ holds, see also Fig. 2.2a). In consequence, for the remainder of the sample space outside of D, every element has a zero probability assigned ($\mu(\Omega \backslash D) = 0$). Additionally, every element has to be contained as set of size one in the σ-algebra: $\{d\} \in \mathcal{A}\ \forall d \in D$. A characterizing function of a discrete probability measure μ is the *probability function* f, which is defined as $f : D \to [0; 1],\ d \mapsto \mu(\{d\})$. A simple example for such a function is plotted in Fig. 2.2a), in which the grid points represent the events d and the values in the boxes characterize the individual probability of the respective grid point. Usually, these probability functions depend on one or more characteristic parameters, which determine the exact distribution and shape of the probability function.

One of the simplest discrete probability measures is the Dirac measure. Consider a measure space $(\Omega, \mathcal{A})$, a set $A \in \mathcal{A}$ and a fixed point $x \in \Omega$, i.e., here $D = x$. Then, the Dirac measure is defined by

$$\delta_x(A) = \begin{cases} 1, & \text{if } x \in A \\ 0, & \text{if } x \notin A, \end{cases} \tag{2.10}$$

which essentially measures if x is contained in a set $A \in \mathcal{A}$. By these evaluations, the function $\delta_x : \mathcal{A} \to [0; \infty], A \mapsto \delta_x(A)$ is a measure on $(\Omega, \mathcal{A})$ and due to $\delta_x(\Omega) = 1$ it is also a probability measure. Further possible choices for discrete probability measures are the Binomial distribution or the Poisson distribution. The latter is visualized for two different parameter choices in Fig. 2.3a).

Although there are many types of discrete probability measures, it is possible to express any of those measures by a convex combination of Dirac measures. For this, the mass of a single event may be defined as $w_d := \mu(\{d\})$ for every $d \in D$, at which $D \in \mathcal{A}$ is again a subset of the σ-algebra of a measurable space $(\Omega, \mathcal{A})$. Then, the probability measure for an event A can be written as

$$\mu(A) = \sum_{d \in D} w_d \cdot \delta_d(A) = \sum_{d \in A \cap D} w_d \cdot \delta_d(A) + \sum_{d \in D \backslash A} w_d \cdot \delta_d(A) = \sum_{d \in A \cap D} w_d. \tag{2.11}$$

This important property will be used in a later chapter as a central part of the Optimal Uncertainty Quantification in Chapter 6.

Continous Measures In contrast to the discrete measures, continuous or sometimes also general measures are defined on continuous domains, usually on $\mathbb{R}$ or subsets therefrom, see also Fig. 2.2b). Here, it is not sufficient or rather not possible to assign probabilities to single events in order to compute probabilities for general sets. Instead, a probability density is defined on the domain of the probability measure. Thus, the evaluation of the probability measures relies on the computation of integrals, i.e. for a measurable space $(\Omega, \mathcal{A})$, the probability measure for an event A reads

$$\mu(A) = \int_A \mathrm{d}\mu = \int_A \widehat{f}(u)\mathrm{d}u, \tag{2.12}$$

wherein $\widehat{f}$ denotes the *probability density function* $\widehat{f} : \mathbb{R} \to [0; \infty]$ of the probability measure μ, short PDF. In order to ensure, that μ represents a valid probability measure, a PDF has to satisfy $\mu(\Omega) = \int_\Omega \widehat{f}(u)\mathrm{d}u = 1.0$. Similar to the probability function, which is characterizing for a discrete probability measure, the probability density is characterizing for a continuous probability measure. Also, the exact shape of a probability density functions is usually dependent on one or more characteristic parameters. The probability density function allows

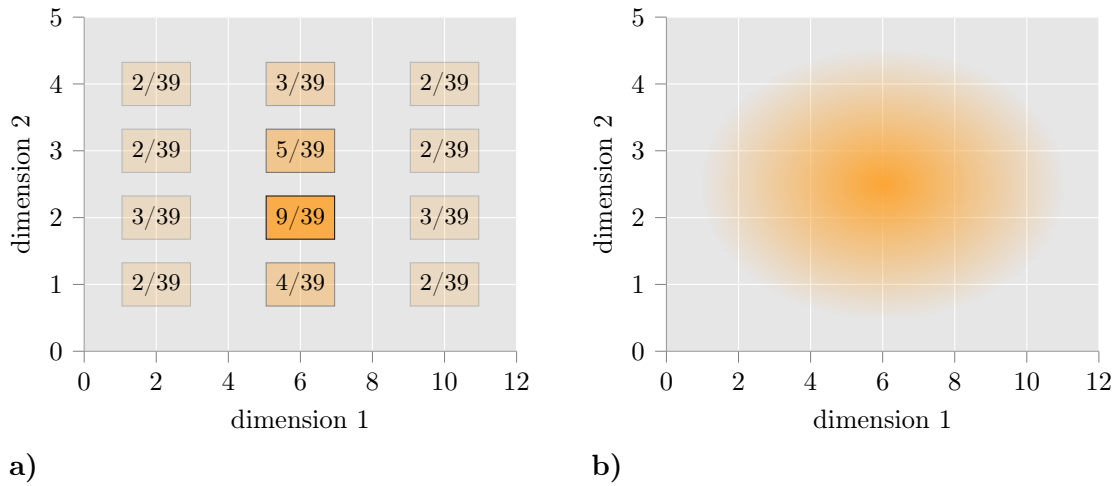

Figure 2.2: Example illustrations of simple probability measures in a two-dimensional space. In subfigure **a)**, a discrete measure is plotted, for which the weights are located only at the grid points, i.e., only at those locations a probability can be computed. Continuous measures on the other hand can only be visualized by means of their probability density function as shown in subfigure **b)**. The highest density is in the center and radially fading out to the borders.

the computation of the *cumulative distribution function* (CDF) as

$$F(t) = \int_{-\infty}^{t} \widehat{f}(u)\mathrm{d}u, \tag{2.13}$$

which in itself is a probability measure for the event, that a realization drawn from the associated random variable is less than the given argument, i.e. $\mu(Y \leq t) = F(t)$. Examples for continuous probability distributions are the normal distribution, uniform distribution, beta and gamma distributions or a gumbel distribution among many others. All of these distributions differ in regards to properties such as non-negativity, symmetry and shape. In Fig. 2.3b) the probability density function of a normal distribution and a gamma distribution are plotted. Both functions share the same mean and variance, which are explained in the next section, but exhibit a completely different shape. It is clearly visible, that especially for the estimation of events in the tails of the PDF, the choice of the type of PDF has a large impact on the computed result.

2.2.4 Stochastic Moments

With the existence of a random variable, characterizing quantities of the distribution or density, the so called *stochastic moments* can be defined. The first moment is the expectation value of the random variable Y with respect to μ:

$$\mathbb{E}_{\mu}[Y] = \int_{\Omega} Y \mathrm{d}\mu. \tag{2.14}$$

Further moments are obtained by raising the power of the random variable, wherein the power is referred to as the order of the computed moment:

$$\mathbb{E}[Y^n] = \int_{\Omega} Y^n \mathrm{d}\mu. \tag{2.15}$$

The aforementioned moments are classic or standard moments, which are computed with respect to the origin of the underlying sample space. Since these values may become very

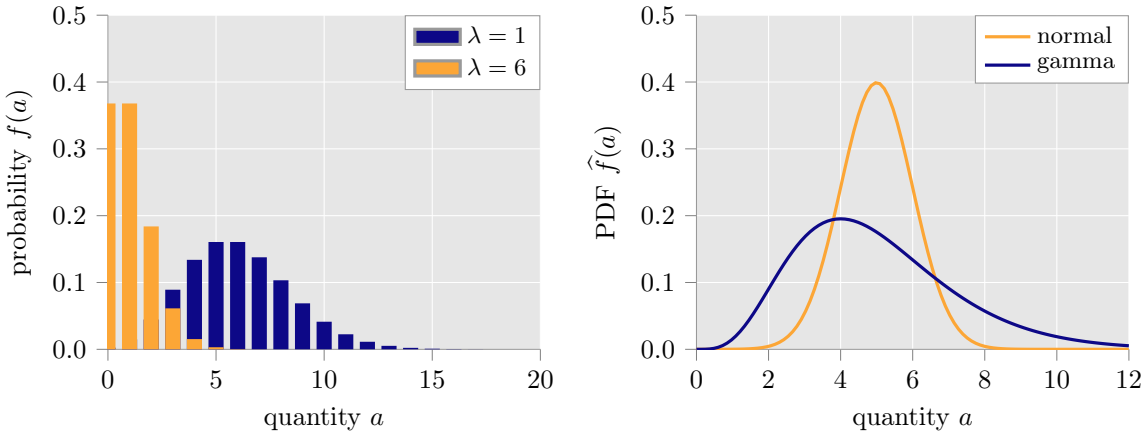

Figure 2.3: a) Comparision of the Poisson distribution for two different choices of the characterizing parameter λ. **b)** Illustration of a normal and a gamma probability density function, which both exhibit a mean of $\mathbb{E}[a] = 5.0$ and a variance of $\mathbb{E}[(a - \mathbb{E}[a])^2] = 1.0$.

large or small, central moments are introduced, which compute the moments with respect to the mean of the distribution, i.e.:

$$\mathbb{E}[(Y - \mathbb{E}_\mu[Y])^n] = \int_\Omega (Y - \mathbb{E}_\mu[Y])^n \mathrm{d}\mu. \tag{2.16}$$

A well known central moment of second order is the variance σ^2, which is obtained by setting the order to $n = 2$. The square-root of the variance is known as standard deviation σ. Sometimes, the skewness ($n = 3$) and the kurtosis ($n = 4$) are used to describe the shape of a probability distribution beyond the variance. These two quantities are central moments, which are normalized with respect to the respective power of the standard deviation. For example, the skewness γ is computed by

$$\gamma = \mathbb{E}[((Y - \mathbb{E}_\mu[Y])/\sigma)^3]. \tag{2.17}$$

The stochastic moments are useful quantities, since they allow the description of the distribution of a random variable to an certain extend. Just based on the moments of up to order four mentioned here, a good understanding on the location, the spread and skewness of a distribution can be gained. Additionally, reliable estimators are available to compute estimators for said moments from given samples, e.g. from measurement data from a series of experiments. However, while a given probability distribution function allows a straight-forward computation of the associated moments, the inverse relationship is a lot more complicated. Usually, just a few moments are not sufficient to uniquely identify a specific distribution. Thus, if a probability density function is assumed based on such moments without further knowledge, a subsequent uncertainty analysis may lead to faulty results.

2.2.5 Product Measures, Covariance and Stochastic Independence

Usually, any uncertainty quantification problem of interest consists of more than one quantity and by that, the dependence of those quantities needs to be considered. A first indicator for the interaction of two or more random variables is the covariance, which is defined by

$$\mathrm{CoV}(Y_1, Y_2) = \mathbb{E}[(Y_1 - \mathbb{E}[Y_1])(Y_2 - \mathbb{E}[Y_2])]. \tag{2.18}$$

If the covariance is equal to zero, i.e., $\mathrm{CoV}(Y_1, Y_2) = 0$, the random variables and their probability distributions are stochastic independent of each other. In these cases, the joint

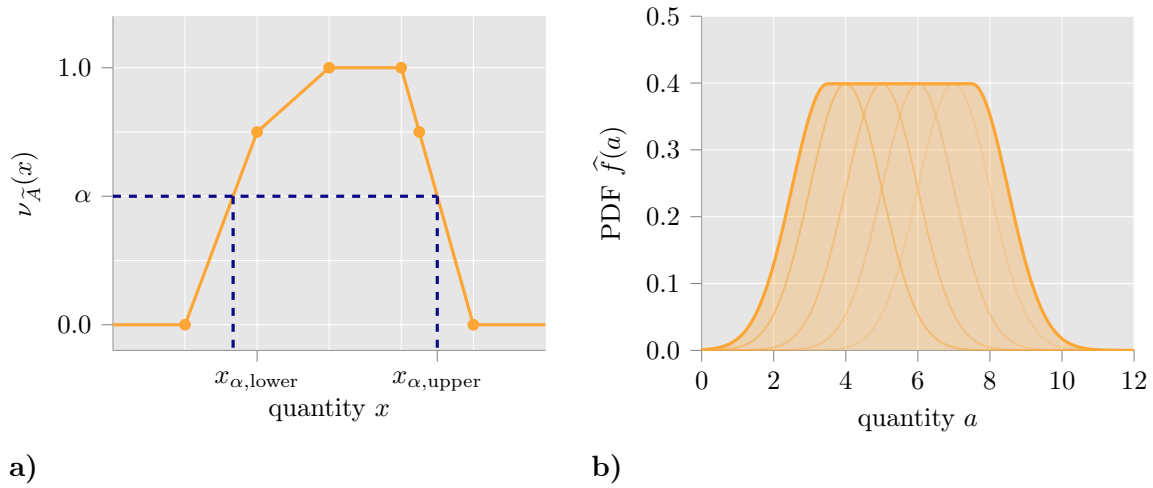

Figure 2.4: a) Schematic deduction of a discrete α-level of a trapeziodal fuzzy number. **b)** An imprecise normal distribution with an interval-valued mean.

probability space with a joint probability measure and a joint probability density function can be computed by means of a product measure. The product measure of n joint random variables is defined as

$$\mu = \mu_1 \otimes \cdots \otimes \mu_n = \bigotimes_{i=1}^{n} \mu_i, \tag{2.19}$$

and can be computed by the solution of the multivariate integral:

$$\mu(A) = \int_A \widehat{f_1}(u_1) \cdot \cdots \cdot \widehat{f_n}(u_n) \mathrm{d}u_1 \cdots \mathrm{d}u_n. \tag{2.20}$$

2.3 Intervals, Fuzzy Numbers and Imprecise Probabilities

Whilst the stochastic tools presented in Sec. 2.2 are well suited to model aleatory uncertainties, different models are necessary for epistemic uncertainties as discussed before in Sec. 2.1. This is due to the lack of knowledge, which is characterizing for epistemic uncertainties, such that no exact probability measure can be specified.

If hardly any data is available, an epistemic quantity x may only be specified to be within certain bounds. Any additional restriction beyond that, such as a certain weighting within these bounds, like a uniform probability distribution would assign, should be avoided. Then, an interval would be a valid choice, which only characterizes the possibility of a range of values for the uncertain quantities. The interval is denoted by

$$x \in [x_{\text{lower}}, x_{\text{upper}}], \tag{2.21}$$

wherein x_{lower} and x_{upper} are the lower and upper bound of the interval, respectively.

In certain situations however, an interval may not be able to reflect the available knowledge on an uncertain quantity well. For example, different experts can have different opinions on the correct range for certain values or the data has been passed along by vague linguistic information. Then, possibly conflicting data can occur and has to be adequately considered. One possible approach for the systematic investigation of such information is given by normalized fuzzy numbers, cf., e.g. [101] or [10], which allows the investigation of different combinations of individual intervals and subsequent analysis of the resulting outcomes. A normalized fuzzy

number $\widetilde{A}$ for the representation of a quantity x can conveniently be constructed by the specification of individual intervals on the respective α-cuts, cf. Fig. 2.4a). The α-cuts or α-levels are the result of a normalized weighting (within the range $[0,1]$) of the different intervals through its so-called membership function $\nu_{\widetilde{A}}$ by

$$\nu_{\widetilde{A}} : \mathbb{R} \mapsto [0,1] \quad \text{with} \quad \exists x \mid \nu_{\widetilde{A}}(x) = 1. \tag{2.22}$$

Usually, the membership functions is denoted in the literature by $\mu_{\widetilde{A}}$, but here the notation $\nu_{\widetilde{A}}$ is chosen to emphasize the difference to probability measures μ. In principle, the membership function can be any arbitrary normalized function, but commonly only convex and piecewise linear functions are used. Then, the membership function is usually not explicitly specified and the fuzzy number is defined in a discretized form by set of α-levels, where each α-level is defined as

$$\widetilde{A}_\alpha = \left\{ x \in \mathbb{R} \mid \nu_{\widetilde{A}}(x) \geq \alpha \right\} \quad \text{with} \quad \alpha \in [0,1]\,. \tag{2.23}$$

This explicit definition of an α-level defines an interval containing all those possible values of the described quantity, for which the membership function yields a value of at least α. In practice, the intervals resulting from an α-cut are getting sharper with increasing α, i.e. the interval for $\alpha = 0.5$ is smaller than for $\alpha = 0.2$. For this purpose, the condition $\tilde{A}_{\alpha_2} \in \tilde{A}_{\alpha_1}$ for $\alpha_2 \geq \alpha_1$ needs to hold. Then, with a convex membership function, every α-level can also be specified through a single interval, i.e. $\widetilde{A}_\alpha = [x_{\alpha,\text{lower}},\ x_{\alpha,\text{upper}}]$, cf. also Fig. 2.4a).

If the available data is sufficiently large, an interval or a fuzzy number are potentially carrying to little information and the result of an uncertainty quantification could be improved by the utilization of the additional data. Then, intervals and fuzzy numbers can be combined with probability functions or probability density functions, such that models for imprecise probabilities will result. The combination is performed by substituting the usually scalar-valued parameters of a PDF by an interval or fuzzy number. By that, a specific type of PDF is chosen, but due to the range of possible values for the parameters, a range of PDFs can systematically be investigated. An example of a normal distribution with an interval-valued mean parameter is drawn in Fig. 2.4b). Clearly visible is the substantially larger area compared to a precise normal distribution, which is covered by this imprecise probability density function.

2.4 Monte Carlo Simulations

The selection of appropriate models for uncertainties is only one part for uncertainty quantification, also methods to quantify the influence of these uncertainty models on the result of the structural problem are required. For the case of stochastic models, the effect of the probability measures on the result $f(Y)$ can be computed by

$$\mathbb{E}[f(Y)] = \int_\Omega f(Y) \mathrm{d}\mu, \tag{2.24}$$

see also Eq. (2.12). There, a similar integral notation was introduced for the computation of moments of random variables and also for the computation of probabilities itself, cf., also the example in Fig. 2.5. Usually, these integrals can't be computed analytically and numerical methods have to be employed. A common approach for this purpose are Monte Carlo methods, cf., e.g. Zhang [167] for an overview.

The Monte Carlo simulation is based on the convergence behavior of random variables. For a sequence of independently and identically distributed (i.i.d.) samples $Y^{(1)}, Y^{(2)}, \ldots$ following

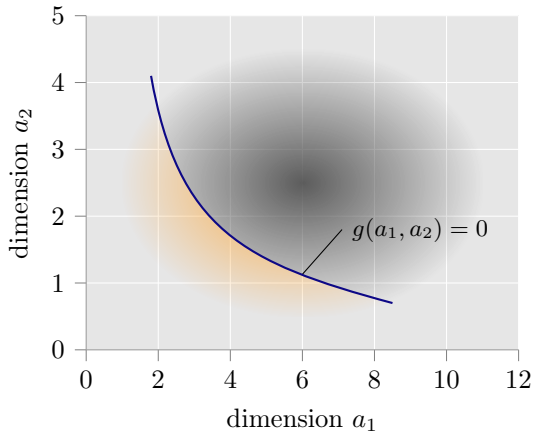

Figure 2.5: Illustration of an examplary integration problem, in which the colored failure region is devided from the safe region by the limit state function g. The integral over the failure region yields the failure probability, which is usually computed by Monte Carlo approaches.

a random variable Y with a finite mean value $\mathbb{E}[Y]$, the sample average can be computed by

$$S_n := \frac{1}{n} \sum_{i=1}^{n} Y^{(i)}. \tag{2.25}$$

The weak law of large number states, that for every possible positive real number ε, a sample size n can be found, such that

$$\mathbb{P}\left[\left|\frac{1}{n} \sum_{i=1}^{n} Y^{(i)} - \mathbb{E}[Y]\right| > \varepsilon\right] = 0 \;\; \forall \varepsilon > 0, \tag{2.26}$$

wherein $\mathbb{P}$ is an alternative way to denote the probability measure. The strong law of large number states, that the probability, that the limit of the aforementioned sample average equals the mean of the random variable, is equal to one and by this, the safe event:

$$\mathbb{P}\left[\lim_{n \to \infty} \frac{1}{n} \sum_{i=1}^{n} Y^{(i)} = \mathbb{E}[Y]\right] = 1. \tag{2.27}$$

These two laws are the foundation for the Monte Carlo simulation, since it allows the approximation of the desired values by a sequence of generated samples $Y^{(i)}$ by

$$\mathbb{E}[f(Y)] \approx S_n(Y) := \frac{1}{n} \sum_{i=1}^{n} f(Y^{(i)}). \tag{2.28}$$

Naturally, an infinite number of samples is numerically intractable and thus, there will be a certain approximation error due to the limited sample size. Due to the central limit theorem, the values of the sample average are normally distributed with an increasing number of samples, which allows the estimation of the approximation error by

$$\mathbb{V}[S_n(f)] = \frac{1}{n^2} \sum_{i=1}^{n} \mathbb{V}[f(X)] = \frac{\mathbb{V}[f(X)]}{n}. \tag{2.29}$$

Therefore, in order to increase the approximation accuracy of the Monte Carlo simulation, the variance of the sample average should be decreased. As it can be seen from Eq. (2.29),

the variance can be reduced by increasing the sample size n. Since an increasing sample size leads to increasing numerical costs, alternative approaches to variance reduction have been developed, such as importance sampling, e.g. Papaioannou et al. [115], advanced line sampling, e.g. de Angelis et al. [22], or multilevel Monte Carlo methods, e.g. Giles [51] or Heinrich [62]. The latter will be discussed in detail and applied in Chapter 6.

2.5 Optimization Problems

While numerical integration in terms of Monte Carlo is the method of choice for the quantification of the impact of aleatory uncertainties, the consideration of epistemic uncertainties in terms of intervals, fuzzy numbers or imprecise probabilities leads to optimization problems to identify the best or worst solution. An optimization problem itself is the mathematical search for the some, not necessarily unique, element x, which leads to the optimal, i.e., either the maximum or minimum value of a function f. This function f is referred to as objective function. The general formulation of such an optimization problem is

$$\begin{aligned} \text{extremize: } & f(x) \\ \text{with respect to: } & x \in \mathcal{X} \\ \text{subject to: } & g_i(x) \leq 0 \text{ for } i = 1, 2, \dots, \end{aligned}$$

wherein $\mathcal{X}$ denotes the search space and g_i are constraints to the optimization. A point x fulfilling the constraints is called feasible, which leads to the definition of the feasible set

$$\{x \in \mathcal{X} \mid g_i(x) \leq 0 \text{ for } i = 1, 2, \dots\}. \tag{2.30}$$

If all constraints are absent, the optimization problem is called unconstrained, although, in many realistic applications at least one constraint is present. Refer e.g. to Sullivan [147] for further discussions on optimizations in context of uncertainties.

If a solution to an optimization problem can be found, depends heavily on the objective function and the formulated constraints. If the objective function is convex, a local optimum is also a global optimum and can be found by approaches such as gradient descend methods using the first derivative of the objective function. On the other hand, if the objective function is non-convex, many local optimums can exist and the global optimum is by magnitudes more difficult to identify. Moreover, for convex optimizations the global optimum can be proven to be found, which is not the case for non-convex problems. Here, global optimization strategies are required. In general, a global optimization of a non-convex function with a potential high number of local extremums is numerically hard, especially if constraints are present and the feasible space is very small. Then, algorithms based on random search can be applied, for which, however, no guarantee of finding the extremum can be given. One of these algorithms, which is applied in this work, is Differential Evolution, cf.[144]. The core idea behind the Differential Evolution is to emulate the behavior of real populations and their evolution. For that matter, a population of solution vectors evolves over generations by preserving fitter population members, i.e. those, who lead to a better value of the objective function, whilst weaker members are discarded. From each generation to the next, offspring vectors are created by adding differences between randomly selected population members to other members. If the offspring performs better than the parent, the parent is discarded from the population and vice versa. The optimization is stopped, if for a certain number of generations no better individual can be found and the best value of the objective remains unchanged. The performance of the method is controlled by hyperparameters, which influence the population size as well as the exact way, how the offspring is generated.

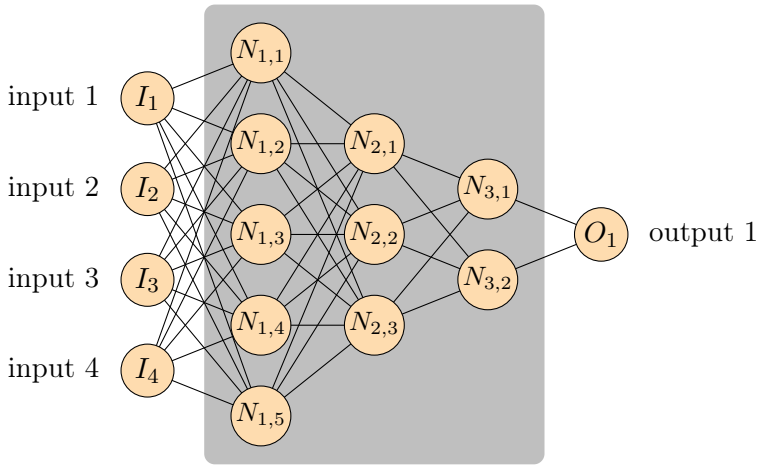

Figure 2.6: Exemplary artificial neural network with four input neurons, one output neuron and three hidden layers.

2.6 Neural Networks as Surrogate Models

The methods described in this chapter, both the precise and imprecise probabilities, usually require a large number of model evaluations in order to correctly measure the events of interest. Especially in the context of rather complex, non-linear finite element simulations, where a single model evaluation can take hours or even days, a full uncertainty quantification becomes computationally infeasible due to the associated numerical costs. Therefore, several different techniques have been developed to replace the costly evaluation of the real model with a numerically cheaper alternative, the so called surrogate models, which maintains a comparatively quality of the response, see e.g. Sudret et al. [146] for an overview. Popular approaches are based on polynomial chaos expansions (PCE), see e.g., Ghanem and Spanos [50], gaussian processes or kriging (Ebden [31]), or artificial neural networks (ANN), e.g. Bishop [15], Goodfellow et al. [55] or Aggarwal [1]. All of these techniques require some sort of training or a learning phase, before a suitable surrogate model is obtained. In this work only artificial neural networks with feed-forward architecture are utilized and explained more detailed in the following. Although artificial neural network per se do not aim to replicate neural networks from the human brain, they inherited the name, since ANNs consists of small units, the artificial neurons, which are connected to each other by links for data exchange. Typically, an ANN with a feed-forward architecture consists of multiple layers, in which the individual neurons are located. Special layers are the input layer I_j and the output layer O_j, which are responsible for the input and output of data to and from the ANNs. In between those two layers, several hidden layers can be placed, the number of those hidden layers depends on the complexity of the actual problem the ANN should substitute. For fully connected feed-forward ANNs, each neuron $N_{p,j}$ on layer p is connected to all neurons in the previous layer $p-1$ and all neurons in the next layer $p+1$, but not to neurons on the same layer. The number of neurons on the input layer is determined by the number of input parameters the ANN should take, similarly the number of neurons on the output layer depends on the number of output quantities. Again, the number of neurons on the several hidden layers depends on the problems complexity and can be freely varied, however, a too little number can lead to a poor approximation quality, whilst a too large number may induce overfitting of the available data. Often, it is impossible to choose the right network architecture from the start and multiple different architecture need to be trained and analyzed. In Fig. 2.6, an exemplary simple artificial neural network is displayed.

A single neuron can take an input value or input signal from each of the links, which are

connected to it from the previous layer. These signals are output values from the neurons on the previous layer, but due to the transport on the links, this output signal is multiplied by weighting factors w_{jh}^{p}. The neuron adds all input signals together, additionally a bias value b_j^p may be added. The resulting value is the input to the neurons activation function a_j, i.e., the function which dictates, how the neuron reacts to incoming signals. The output of this function is then used as output signal $n_{p,j}$, which is transported to the next layer. Since common choices for the activation function are hyperbolic tangent, linear and logistic activation functions, usually the input signals to an ANN are transformed to dimensionless signals in the range of $[-1, 1]$. With that, the output signal $n_{p,j}$ of neuron $N_{p,j}$ in layer p can be computed by

$$n_{p,j} = a_j^p \left(\sum_{h=1}^{H} \left[n_{p-1,h} \cdot w_{jh}^p \right] + b_j^p \right) . \tag{2.31}$$

As mentioned before, any ANN needs to be trained to the available data, before it can substitute the more complex function. The free parameters of the network are the weights and bias values on all links and neurons. In the beginning, these values are randomly initialized and adapted by a backpropagation algorithm, see e.g., Haykin [61], in order to minimize the error between the network output and the desired response of the quantity of interest. The available data is usually split into training, test and validation data to prevent overfitting and to ensure a reasonably well approximation quality. Only the data contained in the training data is used for the training und thus, for the determination of the weights and bias values. Since the training is performed in individual loops, the so called epochs, in which the backpropagation is applied to modify only a few weights and bias values. Thus, a stopping criterion is required, which is often formulated in terms of the validation test set. If the approximation of the data contained therein is sufficiently, the training is stopped. Finally, the performance of the trained ANN is measured by means of the test data set. The data contained within this set is entirely new to the neural network and by that, it is possible to judge if the ANN can predict also new scenarios or if only those scenarios contained in the training data were learned (overfitting). Thus, the entire data set should be sufficiently large and cover the entire input and output space. Such data sets can be prepared by e.g., regular grids, random sampling or Latin hypercube sampling.

As it can be seen from Eq. (2.31), a lot of the computations for the evaluation of an ANN involve addition and multiplication. These operations can be represented by matrix-matrix and matrix-vector operations. Since modern computers have special units, in which such operations can efficiently be computed, an evaluation of a ANN is rather quick and numerically cheap, which is why ANNs are a suitable method for the construction of surrogate models.

3 Continuum Mechanics and Finite Element Simulations

One of the most powerful tools for a mechanical or civil engineers are calculations based on the finite element method. This work is no exception and in later chapters, the finite element method is used in both the development of a new method for the numerical quantification of material properties based on its heterogeneous microstructure as well as in uncertainty quantification problems of sheet metal forming processes. Thus, in this chapter, the necessary fundamentals of continuum mechanics and the finite element method (FEM) are introduced. The notations and definitions in this chapter are based on the works of Bathe and Zimmermann [8], Belytschko et al. [11], Holzapfel [67], Marsden and Hughes [86], Ogden [108] and Wriggers [163].

3.1 Continuum Mechanics

The classic continuum mechanics can be understood as a field theory, which allow the description and analysis of materials by means of quantities such as displacement, velocity, density or stiffness at every spatial point. The name of this theory arises from the fact, that the described body of interest is approximated as continuum and the underlying structure of the matter, i.e., atoms and molecules, are significantly smaller. Instead of considering forces acting on discrete masses (e.g. atoms) at discrete positions, all descriptive fields act as (dis)continuous functions which can be evaluated at all points of the body.

3.1.1 Kinematics

The field of kinematics is used to describe the position and movement of material points in a continuum over time as well as for the definition of associated strain measures. For this purpose, an undeformed body $\mathcal{B}$ is assumed at time $t = t_0$, which is also referred to as reference configuration. Therein, each material point is uniquely described by its position vector $\boldsymbol{X} = X_a \boldsymbol{E}_A$ in reference to a chosen origin. Over time, the considered body is exposed to deformation and rigid body motions and therefore, transforms to its deformed configuration, denoted by $\mathcal{S}$. In this deformed configuration, the material point is characterized by the position vector $\boldsymbol{x} = x_i \boldsymbol{e}_i$, which can also be seen as non-linear map from the undeformed to the deformed configuration, i.e. $\boldsymbol{x} = \varphi(\boldsymbol{X}, t) : \mathcal{B} \rightarrow \mathcal{S}(t)$. With the position vectors of a material point in both configurations, the displacement $\boldsymbol{u}$ of this material point is defined as

$$\boldsymbol{u} = \boldsymbol{x} - \boldsymbol{X}. \tag{3.1}$$

The deformation of an infinitesimal element can be described by the deformation gradient $\boldsymbol{F} = F_{iA} \boldsymbol{e}_i \otimes \boldsymbol{E}_A$, which is defined as

$$\boldsymbol{F} = \mathrm{Grad}[\boldsymbol{x}] = \frac{\partial \boldsymbol{x}}{\partial \boldsymbol{X}} = \boldsymbol{1} + \frac{\partial \boldsymbol{u}}{\partial \boldsymbol{X}}, \tag{3.2}$$

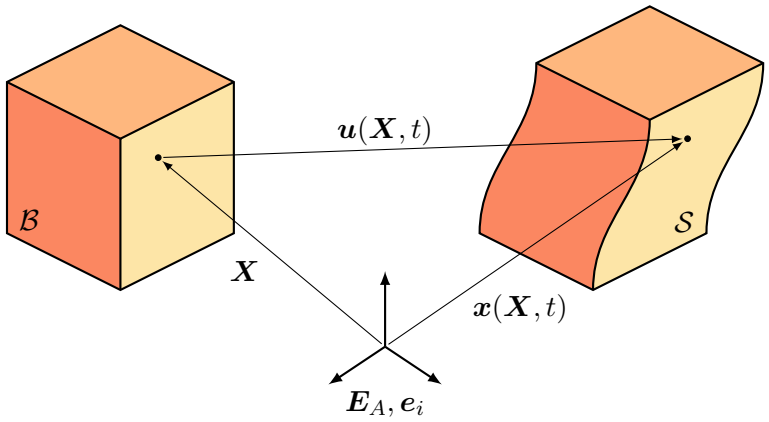

Figure 3.1: Relationship of a point $\boldsymbol{X}$ in the undeformed state $\mathcal{B}$ and its counterpart $\boldsymbol{x}$ in the deformed state $\mathcal{S}$ by deformation $\boldsymbol{u} = \boldsymbol{x} - \boldsymbol{X}$.

wherein $\mathbf{1}$ denotes the second order identity tensor. With the help of the deformation gradient, an infinitesimal line element in the reference configuration $\mathrm{d}\boldsymbol{X}$ can be mapped on its counterpart in the deformed configuration $\boldsymbol{x}$ by

$$\mathrm{d}\boldsymbol{x} = \boldsymbol{F}\mathrm{d}\boldsymbol{X}, \tag{3.3}$$

refer also to the visulisation in Fig. 3.1. From a physical standpoint, the mapping based on $\boldsymbol{F}$ needs to be bijective i.e. each material point in the reference configuration is associated to exactly one point in the deformed configuration in order to preserve the integrity of the continuum. To fulfill this requirement, $\boldsymbol{F}$ must not be singular, which implies, that the Jacobi-determinant of the deformation gradient is strictly positive:

$$J = \det[\boldsymbol{F}] > 0. \tag{3.4}$$

This Jacobi-determinant J is also used to link the volume of an infinitesimal volume element in the reference configuration $\mathrm{d}V$ to its counterpart in the deformed configuration $\mathrm{d}v$ by

$$\mathrm{d}v = J\mathrm{d}V. \tag{3.5}$$

Consequently, a non-positive value of the Jacobi-determinant would describe a negative or a vanishing volume, which is not physical. Similar to the volume elements, infinitesimal area elements can be mapped between the both configurations by Nansons-formula:

$$\mathrm{d}\boldsymbol{a} = \boldsymbol{n}\mathrm{d}a = J\mathrm{d}\boldsymbol{F}^{-\mathrm{T}}\boldsymbol{N}\mathrm{d}A = J\boldsymbol{F}^{-T}\mathrm{d}\boldsymbol{A}. \tag{3.6}$$

Although $\boldsymbol{F}$ measures the deformation of infinitesimal elements, it can also contain portions of rigid-body motions and rotations and is thus, not a suitable deformation measure for the formulation of material models. Therefore, alternative strain measures have been found, which are based on the multiplicative split of the deformation gradient into an ortho-normal rotation tensor $\boldsymbol{R}$ and a stretch tensor by

$$\boldsymbol{F} = \boldsymbol{R}\boldsymbol{U} = \boldsymbol{V}\boldsymbol{R}, \tag{3.7}$$

for which $|\boldsymbol{R}| = 1$ and hence $\boldsymbol{R}^{-1} = \boldsymbol{R}^{\mathrm{T}}$ holds. $\boldsymbol{U}$ and $\boldsymbol{V}$ are referred to as left and right stretch tensors, respectively. Based on this decomposition, which is sometimes also called polar decomposition, the left and right Cauchy-Green-tensors are defined by

$$\boldsymbol{b} = \boldsymbol{F}\boldsymbol{F}^{\mathrm{T}} \quad \text{and} \quad \boldsymbol{C} = \boldsymbol{F}^{\mathrm{T}}\boldsymbol{F} = \boldsymbol{U}^{\mathrm{T}}\boldsymbol{R}^{-1}\boldsymbol{R}\boldsymbol{U} = \boldsymbol{U}^{\mathrm{T}}\boldsymbol{U}. \tag{3.8}$$

As it can be seen, the rotational components cancel itself out and only portions related to the actual deformation of the body are taken into account. Both $\boldsymbol{C}$ and $\boldsymbol{b}$ will yield the identity tensor if no deformation occurs. Therefore, a further strain measure given by the Green-Lagrange-tensor

$$\boldsymbol{E} = \frac{1}{2}\left(\boldsymbol{C} - \boldsymbol{1}\right), \tag{3.9}$$

is introduced, which equals zero for no deformation.

3.1.2 Stress Measures

The exposition of a body to deformations leads to internal loading states, for which characterization stress tensors are used. Depending on the desired configuration, different stress measures may be used. The Cauchy stress tensor $\boldsymbol{\sigma}$ relates a normal vector $\boldsymbol{n}$ of a chosen surface to the effective tension vector $\boldsymbol{t}$, which would act on the corresponding surface by

$$\boldsymbol{t} = \boldsymbol{\sigma}\boldsymbol{n}, \tag{3.10}$$

also known as Cauchy's stress theorem. Since the Cauchy stress is posed in the deformed configuration, it is also referred to as true stress, since it can be interpreted as the actual force acting on the deformed surface. However, the true stress posseses difficulties in terms of experiments and measurements. Often, it is only possible to measure the undeformed area. Thus, another possibility is the representation of the stresses in a mixed configuration, which may be interpreted as actual force acting on the reference surface area. This stress tensor is referred to as first Piola-Kirchhoff stress tensor $\boldsymbol{P}$. Similarly, the stress vector $\boldsymbol{T}$ may be computed therefrom by

$$\boldsymbol{T} = \boldsymbol{P}\boldsymbol{N}, \tag{3.11}$$

at which the traction vector $\boldsymbol{T}$ is parallel to $\boldsymbol{t}$, but related to the undeformed surface area $\mathrm{d}A$, $\boldsymbol{T}\mathrm{d}A = \boldsymbol{t}\mathrm{d}a$. With the use of Nansons formula, cf. (3.6), the first Piola-Kirchhoff stress tensor can be computed from the Cauchy stress by

$$\boldsymbol{P} = J\boldsymbol{\sigma}\boldsymbol{F}^{-\mathrm{T}}. \tag{3.12}$$

In contrast to the Cauchy stress $\boldsymbol{\sigma}$, $\boldsymbol{P}$ is not necessarily symmetric. The second Piola-Kirchhoff stress tensor $\boldsymbol{S}$, which is entirely in the reference configuration, can be computed by

$$\boldsymbol{S} = \boldsymbol{F}^{-1}\boldsymbol{P} = J\boldsymbol{F}^{-1}\boldsymbol{\sigma}\boldsymbol{F}^{-\mathrm{T}}. \tag{3.13}$$

Unlike the previous stress tensors, $\boldsymbol{S}$ does not have a physical interpretation, it is a purely mathematical construct. However, since the formulation of constitutive equations for the material modelling require work-conjugate pairs of stress and strain measures, the second Piola-Kirchhoff stress tensor is required, since it forms such a pair with the Green-Lagrange-strain tensor $\boldsymbol{E}$: $(\boldsymbol{S}, \boldsymbol{E})$. Another work-conjugate pair is given by $(\boldsymbol{P}, \boldsymbol{F})$.

3.1.3 Balance Equations

With the introduction of the kinematic behavior of material points and stress measures, a set of five balance equations can be introduced, which reflect physical observations of the real world. These balances are fundamental for continuum mechanics, however, it should be noted, that the following forms are only valid for closed systems and one phase continua.

Balance of Mass: The first balance equation states, that the mass of the observed system does not change over time, i.e. the total mass of the system stays constant, which can be expressed by

$$m = \int_{\mathcal{B}} \rho_0 \mathrm{d}V = \int_{\mathcal{S}} \rho \mathrm{d}v \Rightarrow \rho_0 = J\rho. \tag{3.14}$$

Balance of Linear Momentum: Similar to the mass balance, the balance of linear momentum states, that the change in linear momentum $\boldsymbol{L}$ over time, i.e. $\dot{\boldsymbol{L}}$, equals the sum of all external forces acting on the system of interest. Usually, these forces are body forces due to gravity and traction vectors on the surface of the body of interest,

$$\dot{\boldsymbol{L}} = \int_{\mathcal{S}} \rho \boldsymbol{g} \mathrm{d}v + \int_{\partial\mathcal{S}} \boldsymbol{t} \mathrm{d}a \quad \text{with} \quad \boldsymbol{L} = \int_{\mathcal{S}} \rho \dot{\boldsymbol{x}} \mathrm{d}v, \tag{3.15}$$

wherein $\boldsymbol{g}$ denotes the acceleration due the gravity of the earth. Reformulated in its local form, the balance of linear momentum for static processes (neglecting effects of inertia), reads

$$\mathrm{Div}[\boldsymbol{P}] + \rho_0 \boldsymbol{g} = \rho_0 \ddot{x} \quad \Rightarrow \mathrm{Div}[\boldsymbol{P}] + \boldsymbol{f}^{\mathrm{b}} = 0, \tag{3.16}$$

wherein $\boldsymbol{f}^{\mathrm{b}}$ is a short-hand notation of the body forces.

Balance of Angular Momentum: Not only the change of the linear, but also of the angular momentum has to be equal to the acting quantities, which are the applied moments for the angular moments. In its local form, the symmetry of the Cauchy stress tensor follows, i.e. $\boldsymbol{\sigma}^{\mathrm{T}} = \boldsymbol{\sigma}$, which also leads to the symmetry of the second Piola-Kirchhoff stress tensor $\boldsymbol{S}$.

Balance of Energy: The balance of energy is also known as the first law of thermodynamics and states, that the change of energy in a closed system equals the sum of applied power of external forces. Since in this work only the mechanical energy is of interest, this balance with contributions from e.g., heat sources, is not explicitly discussed. However, it may be noted, that for sophisticated descriptions of e.g., plastic or damage processes, the dissipation of strain energy in terms of heat can be incorporated.

Entropy Inequality: In contrast to the previous four balances, the fifth balance is an inequality, which states, that the entropy of a system can only increase over time. Its local form leads to the Clausius-Duhem inequality, which can be written as

$$\boldsymbol{S} : \dot{\boldsymbol{E}} - \dot{\psi} \geq 0, \tag{3.17}$$

wherein ψ denotes stored energy due to deformation per unit reference volume, which is related to the free Helmholtz-energy $\tilde{\psi}$ by $\psi = \rho_0 \tilde{\psi}$. An important approach with this inequality is the Coleman Noll [21] procedure, that ensures for each independent possible process a thermodynamic consistent model is obtained. This leads to well known relations such as $\frac{\partial \psi}{\partial \boldsymbol{E}} = \boldsymbol{S}$, which allows the link of the stresses $\boldsymbol{S}$ and strains $\boldsymbol{E}$ by a constitutive equation for the stored energy ψ by means of a so-called material model, cf. Sec. 3.3.

3.2 Numerical Simulation by means of Finite Elements

In the previous section, the local form of linear momentum was introduced, which allows the mathematical description of structural mechanical problems in terms of the displacement of points. Since that form is a partial differential equation, it can only be solved analytically for a few, simple problems. Realistic and thus, more interesting and complex problems, need to be solved numerically. One possible method, which will be used in the remainder of this work, is the finite element method (FEM).

3.2.1 Variational Problem

In Sec. 3.1.3 the strong form of the linear momentum balance was introduced, cf. Eq. (3.16). Until today, no closed, analytical solution has been found for this partial differential equation and thus, the PDE has to be solved numerically. A first step for this purpose is the derivation

of the weak form by means of a variational approach, i.e., the strong form is firstly multiplied with a vectorial test function δu and then a volume integral is computed, which leads to the following weak form

$$G = \int_{\mathcal{B}} \left(\mathrm{Div}[\boldsymbol{P}] + \boldsymbol{f}^{\mathrm{b}}\right) \cdot \delta\boldsymbol{u} \mathrm{d}V = 0, \tag{3.18}$$

wherein G can be interpreted as the scalar value of the virtual work performed by the virtual displacements δu. Since $\mathrm{Div}[\boldsymbol{P}] \cdot \delta\boldsymbol{u} = \mathrm{Div}[\boldsymbol{P}^{\mathrm{T}}\delta\boldsymbol{u}] - \boldsymbol{P} : \mathrm{Grad}[\delta\boldsymbol{u}]$, the Gauss theorem can be applied and the volume integral can be transformed to a surface integral as $\int_{\mathcal{B}} \mathrm{Div}[\boldsymbol{P}^{\mathrm{T}}\delta\boldsymbol{u}]\mathrm{d}V = \int_{\partial\mathcal{B}_t} \delta\boldsymbol{u} \cdot \boldsymbol{t}\mathrm{d}A$. Together with the prescribed boundary conditions of the problem, the weak form can be rewritten as

$$G = G^{\mathrm{int}} - G^{\mathrm{ext}} = 0 = \int_{\mathcal{B}} \boldsymbol{P} : \mathrm{Grad}[\delta\boldsymbol{u}]\mathrm{d}V - \int_{\partial\mathcal{B}_t} \delta\boldsymbol{u} \cdot \boldsymbol{t}\mathrm{d}A + \int_{\mathcal{B}} \delta\boldsymbol{u}\boldsymbol{f}^{\mathrm{b}}\mathrm{d}V. \tag{3.19}$$

3.2.2 Linearization

In general, the system of equations posed by Eq. (3.19) is non-linear in the primary variable, here $\boldsymbol{u}$, and thus, a non-linear system of equations has to be solved. Usually, iterative procedures are used to solve such systems, e.g. the Newton-Raphson method. One particular advantage of this method is the quadratic convergence behavior in the vicinity of the solution. This means, the initial guess for the solution variable has to be sufficiently close to the solution, which can hardly be fulfilled if the initial guesses are randomly chosen. Thus, usually a load-stepping scheme is employed, starting from zero load, which obviously yields the trivial solution of zero displacement, and subsequent increments of the load by means of virtual time steps. That allows the utilization of the solution of the previous time step as initial guess, which should be in the neighborhood of the sought solution. However, in order to be able to apply the Newton method to the problem at hand, the weak form needs to be linearized, formally written as

$$\mathrm{Lin}G = G + \Delta G = 0. \tag{3.20}$$

Herein, G is also referred to as the residual and ΔG denotes the increment or difference of G between two subsequent iteration steps n. Usually, the difference operator Δ denotes the difference between two iteration steps of a quantity $\square$, i.e.,

$$\Delta\square_{n+1} = \square_{n+1} - \square_n, \tag{3.21}$$

however, since G is a function of a primary variable, the increment of a function $\bullet$ dependent on a variable $\square$ can be obtained by

$$\Delta \bullet (\square) = \left.\frac{\partial \bullet}{\partial \square}\right|_{\square_n} \Delta\square. \tag{3.22}$$

Under the assumption of conservative traction forces $\boldsymbol{t}$, i.e. they are displacement independent, and the negligence of the body-forces due to, e.g., gravitation, the increment of the virtual work can be written as

$$\Delta G = \int_{\mathcal{B}} \Delta\boldsymbol{P} : \delta\boldsymbol{F}\mathrm{d}V, \tag{3.23}$$

in which $\Delta\boldsymbol{P} = \frac{\partial \boldsymbol{P}}{\partial \boldsymbol{F}} : \Delta\boldsymbol{F} = \mathbb{A} : \Delta\boldsymbol{F}$. The expression $\frac{\partial \boldsymbol{P}}{\partial \boldsymbol{F}} = \mathbb{A}$ is referred to as the tangent modulus. Note, that the symbol $\mathbb{A}$ refers to the tangent modulus derived with respect to the deformation gradient. Alternatively, the tangent modulus can be derived for the strain measures $\boldsymbol{E}$ or $\boldsymbol{C}$, which are work-conjugated to the stress tensor $\boldsymbol{S}$, which results in $\mathbb{C} := \frac{\partial \boldsymbol{S}}{\partial \boldsymbol{E}} = 2\frac{\partial \boldsymbol{S}}{\partial \boldsymbol{C}}$. Using the aforementioned tangent modulus $\mathbb{A}$, the linearized form of G can be written as

$$\mathrm{Lin}G = \int_{\mathcal{B}} \delta\boldsymbol{F} : \boldsymbol{P}\mathrm{d}V - \int_{\partial\mathcal{B}_t} \delta\boldsymbol{u} \cdot \boldsymbol{t}\mathrm{d}A + \int_{\mathcal{B}} \delta\boldsymbol{u}\boldsymbol{f}^{\mathrm{b}}\mathrm{d}V + \int_{\mathcal{B}} \delta\boldsymbol{F} : \mathbb{A} : \Delta\boldsymbol{F}\mathrm{d}V. \tag{3.24}$$

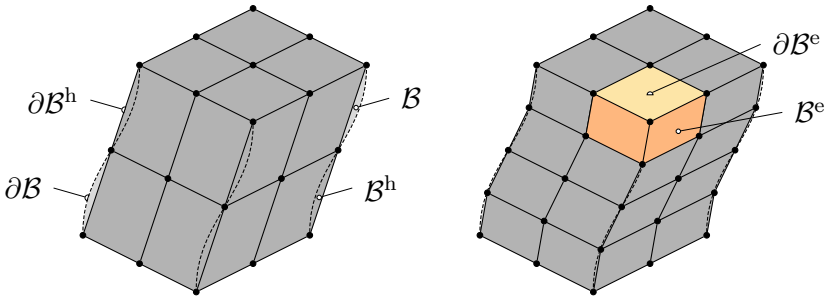

Figure 3.2: Exemplary finite element approximation $\mathcal{B}^{\mathrm{h}}$ of the real body $\mathcal{B}$ with a coarse mesh on the left and a finer mesh on the right side.

3.2.3 Discretization

An important part of the application of the finite element method is the so called discretization of the physical body of interest $\mathcal{B}$ into a finite set of elements and nodes. By that, the domain of this body is subdivided into a set of smaller domains of simpler geometrical shape, which are referred to as finite elements. A single element may be referred to as $\mathcal{B}^{\mathrm{e}}$ from here. Every element consists of a certain number of nodes n_{e}, which are the discrete points within the domain, at which the governing equations are actually solved. In this context the displacements, and all quantities derived therefrom, are interpolated at every point within the finite element based on the nodal values. Together, the nodes and the elements form the finite element mesh, cf. Fig. 3.2 for an illustration of two different meshes for the same geometry. The union of all finite elements serves as approximation $\mathcal{B}^{\mathrm{h}}$ of the domain of interest $\mathcal{B}$, i.e. $\mathcal{B} \approx \mathcal{B}^h = \bigcup_{e=1}^{n_{\mathrm{e}}} \mathcal{B}^{\mathrm{e}}$. Similarly, the surface $\partial\mathcal{B}$ is approximated by the surface of the finite element mesh $\partial\mathcal{B}^{\mathrm{h}}$, which consists of outward-facing element surfaces $\partial\mathcal{B}^{\mathrm{e}}$. These approximations, as the name already indicates, do not perfectly reflect the reality, especially in highly-non-linear regions of the geometry. This is due to the interpolation concept within the finite element. For this purpose, shape functions are used:

$$\boldsymbol{X}(\xi,\eta,\zeta) = \sum_{I=1}^{n_n} N_I(\xi,\eta,\zeta)\boldsymbol{X}_I \quad \text{and} \quad \boldsymbol{x}(\xi,\eta,\zeta) = \sum_{I=1}^{n_n} N_I(\xi,\eta,\zeta)\boldsymbol{x}_I, \tag{3.25}$$

as well as

$$\boldsymbol{u}(\xi,\eta,\zeta) = \sum_{I=1}^{n_n} N_I(\xi,\eta,\zeta)\boldsymbol{d}_I. \tag{3.26}$$

If the shape functions are used to interpolate both the geometry and the primary variables, the isoparametric concept is applied. Therein, any element of the same type, either in reference or actual configuration, is mapped onto a reference element of fixed size. In Fig. 3.3, the reference element with domain $\mathcal{B}_{\mathrm{iso}}$ and its counterparts in reference ($\mathcal{B}$) and actual configuration ($\mathcal{S}$) are depicted together with the required transformation maps. It should be noted, that only the map between the reference and actual configuration reflects an actual deformation, the maps referencing the isoparametric element may be interpreted as fictitious deformation. As it can be seen in the figure, the isoparametric element is defined in the coordinate system of $\boldsymbol{\xi}$. To transform any vector to the physical space, the necessary Jacobi matrices are defined as

$$\boldsymbol{J} = \frac{\partial \boldsymbol{X}}{\partial \boldsymbol{\xi}}. \tag{3.27}$$

With these tools at hand, the approximated form of the gradient of the displacements, Grad[$\boldsymbol{u}$], which is required to approximate the deformation gradient $\boldsymbol{F}$, can be obtained

as

$$\mathrm{Grad}[\boldsymbol{u}] = \mathrm{Grad}\left[\sum_{I=1}^{n_n} N_I \boldsymbol{d}_I\right] = \sum_{I=1}^{n_n} \mathrm{Grad}[N_I]\boldsymbol{d}_I, \tag{3.28}$$

wherein $\mathrm{Grad}[N_I]$ may be rewritten as

$$\mathrm{Grad}[N_I] = \frac{\partial N_I}{\partial \boldsymbol{X}} = \frac{\partial N_I}{\partial \boldsymbol{\xi}} \frac{\partial \boldsymbol{\xi}}{\partial \boldsymbol{X}} = \boldsymbol{J}^{-\mathrm{T}} \frac{\partial N_I}{\partial \boldsymbol{\xi}}. \tag{3.29}$$

A commonly used shorthand for the formulation of this gradient is the B-matrix, which contains the derivatives of all the shape functions, cf. e.g., [163] for concrete examples. The B-matrix allows the short notation of Eq. (3.28) as

$$\mathrm{Grad}[\boldsymbol{u}] = \sum_{I=1}^{n_n} \boldsymbol{B}_I \boldsymbol{d}_I, \tag{3.30}$$

wherein $\boldsymbol{B}_I$ is the B-matrix associated to node I. With an appropriate assembly of the element displacement vector $\boldsymbol{d}^e$, the element shape function matrix $\boldsymbol{N}^e$ and element B-matrix $\boldsymbol{B}^e$, the displacement and deformation gradient at every point $\boldsymbol{\xi}$ within element e can be computed by the matrix-vector multiplications

$$\boldsymbol{u} = \boldsymbol{N}^e(\boldsymbol{\xi})\boldsymbol{d}^e \quad \text{and} \quad \boldsymbol{F} = \boldsymbol{1} + \boldsymbol{B}^e(\boldsymbol{\xi})\boldsymbol{d}^e. \tag{3.31}$$

Inserting these approximations in the linearized form of the virtual work, cf. Eq. (3.24), the components of the virtual work for a single finite element can by computed by

$$G^e = \delta \boldsymbol{d}^{e\mathrm{T}} \left[\int_{\mathcal{B}^e} \boldsymbol{B}^{e\mathrm{T}} \boldsymbol{P} \mathrm{d}V - \int_{\partial\mathcal{B}^e} \boldsymbol{N}^{e\mathrm{T}} \boldsymbol{t} \mathrm{d}A - \int_{\mathcal{B}^e} \boldsymbol{N}^{e\mathrm{T}} \boldsymbol{f} \mathrm{d}V\right] \tag{3.32}$$

and

$$\Delta G^e = \delta \boldsymbol{d}^{e\mathrm{T}} \left[\int_{\mathcal{B}^e} \boldsymbol{B}^{e\mathrm{T}} \mathbb{A} \boldsymbol{B}^e \mathrm{d}V \Delta \boldsymbol{d}^e\right]. \tag{3.33}$$

Note, that these approximated formulations allow to factor out the test functions $\delta \boldsymbol{d}^{e\mathrm{T}}$, which is important for the solution of the finite element problem.

3.2.4 Gaussian Quadrature

The discretized form of the linearized weak form still requires the computation of integrals over the domain of interest. Besides other numerical schemes such as the trapezoidal or Simpson's

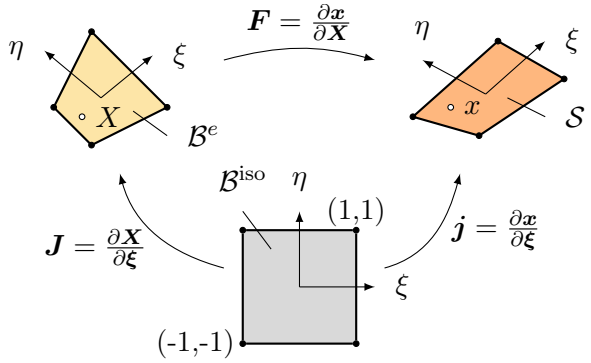

Figure 3.3: Isoparametric mapping for a two-dimensional quadrilateral element of four nodes.

Table 3.1: Points and Weights for the one-dimensional Gauss integration up to order three.

n_{GP}	l	ξ_l	w_l
1	1	0.0	2
2	1	$-1/\sqrt{3}$	1
	2	$+1/\sqrt{3}$	1
3	1	$-\sqrt{3/5}$	5/9
	2	0.0	8/9
	3	$+\sqrt{3/5}$	5/9

method or even Monte Carlo integration approaches, usually the Gauss quadrature is applied to finite element problems. In contrast to the other methods, the Gauss quadrature allows to integrate polynomials up to a chosen order exactly. As the shape functions in the scope of this work are Lagrangian polynomials, the appearing integrals can be computed exactly based on the Gauss quadrature. Since the isoparametric concept is used, the integral over the physical domain of the body of interest can be transformed to an integral over the domain of the isoparametric element, i.e.,

$$\int_{\mathcal{B}^e} \square(\boldsymbol{X}) \mathrm{d}V^e = \int_{\mathcal{B}^{\mathrm{iso}}} \square(\boldsymbol{X}(\boldsymbol{\xi})) \det[\boldsymbol{J}(\boldsymbol{\xi})] \mathrm{d}V^{\mathrm{iso}}. \tag{3.34}$$

Since the isoparametric element is the same for every finite element, the Gauss quadrature needs to be defined only once for the isoparametric element. Following the Gauss quadrature, the integral expression is substituted by a weighted sum of the integrand evaluated at specific integration points:

$$\int_{\mathcal{B}^{\mathrm{iso}}} \square(\boldsymbol{X}(\boldsymbol{\xi})) \det[\boldsymbol{J}(\boldsymbol{\xi})] \mathrm{d}V^{\mathrm{iso}} \approx \sum_{l=1}^{n_{\mathrm{GP}}} \square(\boldsymbol{X}(\boldsymbol{\xi}_l)) \det[\boldsymbol{J}(\boldsymbol{\xi}_l)] w_l. \tag{3.35}$$

The weighting factors w_l and integration points $\boldsymbol{\xi}_l$ are chosen, such that a polynomial of order p can be exactly integrated by $n_{\mathrm{GP}} > (p+1)/2$ integration points. For one-dimensional polynomials up to order three, the weighting factors and integration points are given in Tab. 3.1. Points and weights for higher dimensions for cuboid-shaped elements can be generated therefrom as a product for each coordinate direction.

3.2.5 Global Assembly

Until this point, the approximation of the weak form of the linear momentum was only considered for a single finite element. In order to compute the solution field for the displacement for the entire body of interest $\mathcal{B}$, the contributions of all elements need to be assembled into global counterparts. These global counterparts form a system of linear equations, which can be solved by available algorithms. Thus, the elemental residual vector

$$\boldsymbol{r}^e = \int_{\mathcal{B}^e} \boldsymbol{B}^{e\mathrm{T}} \boldsymbol{P} \mathrm{d}V \approx \sum_{l=1}^{n_{GP}} \boldsymbol{B}_l^{\mathrm{T}} \boldsymbol{P}_l \det[\boldsymbol{J}(\boldsymbol{\xi}_l)] w_l, \tag{3.36}$$

and the elemental stiffness matrix

$$\boldsymbol{k}^e = \int_{\mathcal{B}^e} \boldsymbol{B}^{e\mathrm{T}} \mathbb{A} \boldsymbol{B}^e \mathrm{d}V \approx \sum_{l=1}^{n_{GP}} \boldsymbol{B}_l^{\mathrm{T}} \mathbb{A}_l \boldsymbol{B}_l \det[\boldsymbol{J}(\boldsymbol{\xi}_l)] w_l, \tag{3.37}$$

are required to assemble the global stiffness matrix $\boldsymbol{K}$ and the global residual vector $\boldsymbol{R}$ using the assembly operator A

$$\boldsymbol{K} = \mathop{\mathsf{A}}_{e=1}^{n_{\mathrm{el}}} \boldsymbol{k}^{\mathrm{e}} \quad \text{and} \quad \boldsymbol{R} = \mathop{\mathsf{A}}_{e=1}^{n_{\mathrm{el}}} \boldsymbol{r}^{\mathrm{e}}. \tag{3.38}$$

The global displacement vector, the test function and the increment of the global displacement vector are obtained by unification of the element displacements $\boldsymbol{d}^e$ by

$$\boldsymbol{D} = \bigcup_{e=1}^{n_{\mathrm{el}}} \boldsymbol{d}^{\mathrm{e}}, \quad \delta\boldsymbol{D} = \bigcup_{e=1}^{n_{\mathrm{el}}} \delta\boldsymbol{d}^{\mathrm{e}} \quad \text{and} \quad \Delta\boldsymbol{D} = \bigcup_{e=1}^{n_{\mathrm{el}}} \Delta\boldsymbol{d}^{\mathrm{e}}. \tag{3.39}$$

With these global matrices and vectors at hand, the system of equations can be written as

$$\mathrm{Lin}G = \delta\boldsymbol{D}^{\mathrm{T}}[\boldsymbol{K}\Delta\boldsymbol{D} + \boldsymbol{R}] \stackrel{!}{=} 0 \quad \Rightarrow \quad \boldsymbol{K}\Delta\boldsymbol{D} = -\boldsymbol{R}. \tag{3.40}$$

Since Eq. (3.40) has to be fulfilled for every possible choice of test functions $\delta\boldsymbol{D}$, the second term in the brackets has to be equal to zero, which leads to the actual system of linear equations, which is solved. As previously described, the actual unknown variable of the to be solved equations are the increments of the displacement $\Delta\boldsymbol{D}$. Since the underlying problem is linearized, the computed increments are used to update the displacements $\boldsymbol{D}$, which leads to a change in the residual $\boldsymbol{R}$. Thus, the Newton iterations need to be repeated, until a convergence criteria is met and the converged displacement vector $\boldsymbol{D}$ for a certain load is obtained. Usually applied convergence criteria are for example based on the local energy norm or euclidean norms of increment of the displacements $|\Delta\boldsymbol{D}|$ or the norm of the residual $|\boldsymbol{R}|$, which need to become smaller than an a-priori defined threshold.

3.3 Constitutive Material Modeling

As mentioned in Sec. 3.1.3, the Clausius-Duhem inequality allows the formulation of constitutive material laws based on the stored energy ψ. Since the Clausius-Duhem inequality must not be violated, by means of the standard argument of the rational continuum mechanics the relation of strains $\boldsymbol{F}$ and stresses $\boldsymbol{P}$ is derived from the Clausius-Duhem inequality to

$$\boldsymbol{P} = \frac{\partial\psi}{\partial\boldsymbol{F}}. \tag{3.41}$$

Given the variety of materials in the world, a wide variety of functions may be chosen for ψ. However, certain demands, which are beyond the scope of this work, in regards to thermodynamics and mathematical convexity must not be violated, cf. e.g. Balzani et al. [7] or Neumeier et al. [105]. Usually, ψ is formulated in terms of $\boldsymbol{C}$ (or $\boldsymbol{F}$) and is thus, referred to as strain energy function. One class of materials are compressible neo-Hookean formulations, where characteristcally the incompressible neo-Hookean formulation $\mu/2(\mathrm{tr}[\boldsymbol{C}] - 3)$ is complemented with volume penalties in terms of J. Here, it is important to formulate convex penalties w.r.t. the dependence onto J by e.g.,

$$\psi(\boldsymbol{C}) = \frac{\mu}{2}\left(\mathrm{tr}[\boldsymbol{C}] - 3 - 2\ln[J]\right) + \frac{\lambda}{2}\left(J-1\right)^2. \tag{3.42}$$

Therein, λ and μ are the characterizing parameters of this particular material model, the Lame-constants. These parameters are determined by a fit, i.e. an optimization process, in which the parameters are adjusted such that available experimental data is optimally reflected by its virtual counterparts in terms of finite element computations. Often, material models are constructed, such that at least some of its parameters represent material properties, such as e.g., the Young's modulus, Poisson's ratio or the yield stress. However, for more complex

material behaviors, it is certainly possible, that a set of parameters is used and fitted, for which no physical interpretation can be found.

Considering Eq. (3.42), the neo-Hookean material law describes only elastic material behavior, i.e., all deformations are fully reversible. More complex materials, for example for plasticity or damage phenomena, require additional arguments in the strain energy density in order to take the loading history and therefore the formation of microstructures of the particular material into account. This loading history is an important quantity to correctly model permanent strains due to plastic behavior or an increasing internal damage. The additional variables are referred to as internal or history variables, here generally denoted by $\boldsymbol{\alpha}$. In these cases, a common approach is the additive split of the strain energy into an elastic part ψ^{el} and an inelastic part ψ^{inel},

$$\psi(\boldsymbol{C}, \boldsymbol{\alpha}) = \psi^{\mathrm{el}}(\boldsymbol{C}) + \psi^{\mathrm{inel}}(\boldsymbol{\alpha}), \tag{3.43}$$

wherein the elastic parts depends on the strain $\boldsymbol{C}$, whilst the inelastic contributions are a result of the internal variables $\boldsymbol{\alpha}$.

The presented approach to material modeling is a viable way for many classes of materials, especially if the material's microstructure is homogeneous. However, for many materials exhibiting a heterogeneous microstructure with two or more phases, where the individual phases show different constitutive behavior e.g. kinematic hardening in phase 1 whereas phase 2 behaves elastically, the phenomenological material modeling becomes difficult due to factors such as the complex interactions of the phases on a microstructural level. Then, the approach of computational homogenization as described in the following section may be applied.

3.4 Computational Homogenization

Albeit many engineering materials can be sufficiently described by a purely phenomenological material model, sometimes the direct incorporation of microstructural phenomena is desired. Then, concepts from the field of numerical homogenization can be applied, which allow the computation of effective, macroscopic material properties from boundary value problems based on the material's microstructure, cf. e.g., the works of Smit et al. [140], Feyel [40], Feyel and Chaboche [41], Miehe et al. [89], Miehe et al. [90], Schröder [135], Geers et al. [46], Geers et al. [47], Geers et al. [48], Geers et al. [49], Tamsen and Balzani [151] and Tamsen [150], among many others. These approaches are particularly important for materials exhibiting a distinct microstructure, such as e.g., concrete or multi-phase steels. Thus, at least two different scales are investigated, which differ in magnitudes, i.e. $\overline{L}_{\mathrm{macro}} \gg L_{\mathrm{micro}}$, wherein L_{micro} refers to the characteristic length of mechanical fields on the smaller scale, the so-called microscale, and $\overline{L}_{\mathrm{macro}}$ to their counterparts on the larger scale, the macroscale. It is important to note, that in this work the names of the different scales should not be understood in material science interpretation, where macro and micro, as well as meso and nano refer to rather specific dimensions. Instead, micro always refer to the smaller scale, on which details and features of the material's lower scale behavior are resolved, whilst macro is referring to the scale of the structural problem. In the context of this description of computational homogenization, quantities denoted by an overline, i.e. $\overline{\boldsymbol{F}}$, are associated with the macroscale, whilst quantities without overline are related to the microscale, i.e. $\boldsymbol{F}$.

Given at least two different length scales of interest, a naive approach to the consideration of features from the microscale would be a finite element discretization with elements, that are small enough to approximate the microstructure sufficiently, but over the entire domain of interest on the macroscale, sometimes referred to as direct numerical solution (DNS). The result would be a finite element mesh with a huge number of finite elements and thus, a large

number of degrees of freedom. The associated numerical costs not only for solving, but also assembling such a system of equations would be tremendously high, which is why this rather naive approach is usually not followed.

Instead, the conceptual idea of computational homogenization and FE^2 is the separation of scales, in which individual boundary value problems are posed on sections of the material's microstructure of limited size. These microstructural BVPs are connected to the structural problem on the macroscale by suitable kinematic links, by which the deformation of macroscopic points is used to impose boundary conditions on the microscale. The points on the macroscale are the quadrature points of the macroscopic elements, and by that, the microscale BVPs are used to replace the material model evaluation on the macroscale. Since a conventional material model returns the stresses and stiffness, upscaling relations are used to deduce the macroscopic stresses and stiffness from the microscale BVPs. In consequence, there are as many microscopic boundary value problems as there are quadrature points in the macroscopic problem. Whilst this approach to computational homogenization is certainly cheaper than the aforementioned DNS approach, it is still linked with large numerical costs, since a full solution of all microscale BVPs is necessary to compute one Newton iteration on the macroscale. However, since the microstructural BVPs are independent of each other, the FE^2-methods is perfectly suitable for trivial parallelization on modern computers with minimal inter-process communications.

A special, but very useful application of the FE^2-method is virtual material testing, wherein simple deformations such as homogeneous tension or shear are prescribed on the macroscale and the material response in terms of homogenized stresses is computed by the microscale BVPs. Due to the simple nature of the macroscopic problems, usually a single finite element with just a single quadrature point is sufficient, such that only one microscale BVP has to be solved. This allows an efficient virtual lab, in which many different microstructures with different materials and morphologies can be tested without being physically produced. In Sec. 5, this method for virtual material tests is applied in order to quantify the variation of selected macroscopic material properties.

3.4.1 Representative Volume Element

A crucial part for the computational homogenization is the choice of the microstructure geometry for the boundary value problem on the microscale. This geometry is referred to as representative volume element (RVE) and should be chosen, as the name already indicates, such that it holds all information on the materials microstructure in a representative way. Unfortunately, the term "representative" is neither objective nor unique and thus, the appropriate choice of an RVE is a well discussed topic in the literature. One approach following Hill [64] is to demand the RVE to represent the average of the materials microstructure resp. to contain a typical amount of all phases of the microstructure. Thus, the RVE has to be large enough to do so, but still much smaller than the structure of the macroscopic problem, cf., Hashin [60]. Alternatively, according to Drugan and Willis [29],the RVE should represent the smallest subsection of the material, which is sufficient to represent the mechanical response of the material. Following Ostoja-Starzewski [109], a clear definition for an RVE is only possible for perfect periodic materials, whose microstructure consists of aligned unit cells, and for materials, in whose microstructure such a large number of inclusion is embedded, such that statistical homogeneity can safely be assumed. An in depth overview on the various definitions can be found in Gitman et al. [52]. Many of these RVE definitions are joint in a sense, that a trade-off between the size of RVE and with that, the accuracy of the computations, and the efficiency is sought. One approach is to utilize simpler geometries, which are similar to the real material's microstructure in terms of statistical measures and mechanical

response. These artificial microstructures are called statistically similar representative volume elements (SSRVEs), cf. e.g., Balzani et al. [3], Balzani et al. [4], Scheunemann et al. [127] or Sasagawa et al. [124]. In Sec. 5, the idea of these SSRVEs is further discussed and extended to create a set of artificial microstructures with the same variability in the morphology as the real material. Usually, a cube or cuboid is used as shape for an RVE, however, in Glüge et al. [54], different shapes such as spheres are discussed. For the scope of the present work, only cuboid-shaped RVEs are considered.

3.4.2 Homogenization of Deformation Gradient and Stresses

Given the conceptual idea of computational homogenization and an appropriate RVE as domain for the microscale BVP, the different scales still needs to be linked in terms of the mechanical quantities of interest. This link is usually motivated by the assumption from classical continuum mechanics, that the deformation gradient as well as the stresses are distributed uniformly, i.e., constant, over an infinitesimal volume element. Since the microstructure is such an infinitesimal volume element from the perspective of the macroscale, a reasonable approach is to assume, that the macroscopic deformation gradient $\overline{\boldsymbol{F}}$ and the macroscopic stresses $\overline{\boldsymbol{P}}$ are uniform over the domain of the RVE and are equal to the volume average of the corresponding quantities of the microscale. In this context, the volume average for an arbitrary quantity $\square$ is defined by

$$\langle \square \rangle = \frac{1}{V} \int_{\mathcal{B}} \square \mathrm{d}V, \tag{3.44}$$

wherein $\mathcal{B}$ is the domain and V the volume of the RVE. Since the macroscopic deformation gradient $\overline{\boldsymbol{F}}$ is distributed uniformly over the domain of the microstructure, it imposes an homogeneous portion of the microscopic deformation $\boldsymbol{x}$. Therefore, under the assumption of a centered coordinate system in the center of the RVE, an additive split of the microscopic deformation as follows is assumed:

$$\boldsymbol{x} = \overline{\boldsymbol{F}}\boldsymbol{X} + \widetilde{\boldsymbol{u}}, \tag{3.45}$$

wherein $\overline{\boldsymbol{F}}\boldsymbol{X}$ represents the mentioned homogeneous part and $\widetilde{\boldsymbol{u}}$ a fluctuation part. Since the macroscopic deformation gradient $\overline{\boldsymbol{F}}$ is a known quantity at the level of the microscale BVPs, the deformation fluctuation $\widetilde{\boldsymbol{u}}$ is the remaining unknown and thus, the primary variable for the solution of the microscale BVP. Similarly, the microscopic displacements $\boldsymbol{u} = \overline{\boldsymbol{H}}\boldsymbol{X} + \widetilde{\boldsymbol{u}}$, microscopic deformation gradient $\boldsymbol{F} = \overline{\boldsymbol{F}} + \widetilde{\boldsymbol{F}}$ and the microscopic stresses $\boldsymbol{P} = \overline{\boldsymbol{P}} + \widetilde{\boldsymbol{P}}$ can be split into an macroscopic and a fluctuating part.

The definition of the microstructural deformation $\boldsymbol{x}$ according to Eq. (3.45) is not sufficient for a meaningful computation. Without any additional constraint, the energetically most favorable state of no deformation can be obtained, if the fluctuations $\widetilde{\boldsymbol{u}}$ simply oppose the deformation induced by the macroscopic deformation gradient, i.e., $\widetilde{\boldsymbol{u}} = -\overline{\boldsymbol{F}}\boldsymbol{X}$. Therefore, additional boundary constraints to the microscale BVP are required. Before these boundary constraints can be discussed, first the macro-homogeneity condition has to be introduced.

3.4.3 Macro-Homogeneity Condition

A fundamental principle for the connection of multiple scales in terms of finite elements is the macro-homogeneity condition, cf., Hill [65] and Mandel [85], which states, that the macroscopic power is equal to the volume average of the microscopic power:

$$\overline{\boldsymbol{P}} \cdot \dot{\overline{\boldsymbol{F}}} = \langle \boldsymbol{P} \cdot \dot{\boldsymbol{F}} \rangle = \frac{1}{V} \int_{\mathcal{B}} \boldsymbol{P} \cdot \dot{\boldsymbol{F}} \mathrm{d}V. \tag{3.46}$$

This principle, sometimes also referred to as Hill-Mandel condition, ensures, that the mathematical concept of the homogenization neither consumes nor produces any energy and the scale transitions can be computed at no energetic costs. An alternative form of Eq. (3.46) is given by

$$\overline{\boldsymbol{P}} \cdot \dot{\overline{\boldsymbol{F}}} = \frac{1}{V} \int_{\partial \mathcal{B}} \boldsymbol{t} \cdot \dot{\boldsymbol{x}} \, \mathrm{d}A. \tag{3.47}$$

Considering the additive split of the microscopic stresses and deformation gradient, it can be shown, that the volume average of the fluctuation parts vanishes, i.e.,

$$\begin{aligned} \langle \widetilde{\boldsymbol{P}} \rangle &= \langle \boldsymbol{P} - \overline{\boldsymbol{P}} \rangle = \langle \boldsymbol{P} \rangle - \overline{\boldsymbol{P}} = 0, \\ \langle \widetilde{\boldsymbol{F}} \rangle &= \langle \boldsymbol{F} - \overline{\boldsymbol{F}} \rangle = \langle \boldsymbol{F} \rangle - \overline{\boldsymbol{F}} = 0. \end{aligned} \tag{3.48}$$

With this information, the additive split can be inserted in the Hill-Mandel-condition (3.46) by

$$\begin{aligned} \langle \widetilde{\boldsymbol{P}} \cdot \dot{\overline{\boldsymbol{F}}} \rangle &= \langle (\overline{\boldsymbol{P}} + \widetilde{\boldsymbol{P}}) \cdot (\dot{\overline{\boldsymbol{F}}} + \dot{\widetilde{\boldsymbol{F}}}) \rangle, \\ &= \overline{\boldsymbol{P}} \cdot \dot{\overline{\boldsymbol{F}}} + \langle \widetilde{\boldsymbol{P}} \cdot \dot{\widetilde{\boldsymbol{F}}} \rangle. \end{aligned} \tag{3.49}$$

Comparing this result with the initial Hill-Mandel-condition (3.46), it can be seen, that the volume average of the power contributions of the fluctuation components has to vanish, i.e.,

$$\langle \widetilde{\boldsymbol{P}} \cdot \dot{\widetilde{\boldsymbol{F}}} \rangle = 0. \tag{3.50}$$

3.4.4 Permissible Boundary Conditions

With the Hill-Mandel-condition (3.46) at hand, it is now possible to formulate boundary conditions for the microscopic BVP, which fulfill this condition. For this purpose, the averaging equations $\overline{\boldsymbol{F}} = \langle \boldsymbol{F} \rangle$ and $\overline{\boldsymbol{P}} = \langle \boldsymbol{P} \rangle$ are rewritten as follows. Under the assumption of no displacement jumps due to e.g., cracks and cavities, the gradient theorem

$$\int_{\mathcal{B}} \mathrm{Grad} \boldsymbol{X} \mathrm{d}V = \int_{\partial \mathcal{B}} \boldsymbol{X} \otimes \boldsymbol{N} \mathrm{d}A = \boldsymbol{1} V, \tag{3.51}$$

can be used to transform the equality $\overline{\boldsymbol{F}} = \langle \boldsymbol{F} \rangle$ to constraints in terms of surface displacements only. For this purpose, the macroscopic deformation gradient $\overline{\boldsymbol{F}}$ is expanded to

$$\overline{\boldsymbol{F}} = \overline{\boldsymbol{F}} \, \boldsymbol{1} \, \frac{V}{V} = \frac{\overline{\boldsymbol{F}}}{V} \int_{\mathcal{B}} \mathrm{Grad} \boldsymbol{X} \mathrm{d}V = \frac{1}{V} \int_{\partial \mathcal{B}} (\overline{\boldsymbol{F}} \boldsymbol{X}) \otimes \boldsymbol{N} \mathrm{d}A = \frac{1}{V} \int_{\partial \mathcal{B}} \boldsymbol{x} \otimes \boldsymbol{N} \mathrm{d}A, \tag{3.52}$$

wherein the relation $\boldsymbol{x} = \overline{\boldsymbol{F}} \boldsymbol{X}$ is used. A reverse application of the gradient theorem proves, that the equality $\overline{\boldsymbol{F}} = \langle \boldsymbol{F} \rangle$ is maintained:

$$\overline{\boldsymbol{F}} = \frac{1}{V} \int_{\partial \mathcal{B}} \boldsymbol{x} \otimes \boldsymbol{N} \mathrm{d}A = \frac{1}{V} \int_{\mathcal{B}} \mathrm{Grad} \boldsymbol{x} \mathrm{d}V = \frac{1}{V} \int_{\mathcal{B}} \boldsymbol{F} \mathrm{d}V = \langle \boldsymbol{F} \rangle. \tag{3.53}$$

Similarly, a formulation for the macroscopic first Piola-Kirchhoff stress tensor in terms of only surface traction vectors $\boldsymbol{t} = \overline{\boldsymbol{P}} \boldsymbol{N}$ can be derived as

$$\overline{P} = \frac{1}{V} \int_{\partial \mathcal{B}} \boldsymbol{t} \otimes \boldsymbol{X} \mathrm{d}A. \tag{3.54}$$

Considering the balance of linear momentum $\mathrm{Div} \boldsymbol{P} = 0$ for quasi-static problems and the divergence theorem, the macroscopic first Piola-Kirchhoff stress tensor can be computed as volume average

$$\overline{P} = \frac{1}{V} \int_{\mathcal{B}} \boldsymbol{P} \mathrm{d}V = \langle \boldsymbol{P} \rangle. \tag{3.55}$$

Uniform Traction Boundary Conditions: By inserting Eq. (3.52) into the alternative form of the Hill-Mandel-condition (3.47), one obtains

$$0 = \frac{1}{V}\int_{\partial\mathcal{B}} \dot{\boldsymbol{x}} \cdot (\overline{\boldsymbol{P}}\boldsymbol{N} - \boldsymbol{t})\mathrm{d}A, \tag{3.56}$$

which can be fulfilled by the boundary conditions

$$\boldsymbol{t} = \overline{\boldsymbol{P}}\boldsymbol{N} \text{ on } \partial\mathcal{B}. \tag{3.57}$$

Linear Displacement Boundary Conditions: Similar to the uniform traction boundary conditions, the insertion of Eq. (3.54) in Eq. (3.47) leads to

$$0 = \frac{1}{V}\int_{\partial\mathcal{B}} \boldsymbol{t} \cdot (\dot{\overline{\boldsymbol{F}}}\boldsymbol{X} - \dot{\boldsymbol{x}})\mathrm{d}A, \tag{3.58}$$

which can be satisfied by the linear displacement boundary conditions

$$\boldsymbol{u} = (\boldsymbol{F} - \boldsymbol{1})\boldsymbol{X} \quad \text{and} \quad \widetilde{\boldsymbol{u}}(\boldsymbol{X}) = \boldsymbol{0}, \ \forall \boldsymbol{X} \in \partial\mathcal{B}. \tag{3.59}$$

Similar to standard finite elements, displacement and traction boundaries can be mixed, which leads to the mixed boundary conditions. For this purpose, the boundary $\partial\mathcal{B}$ is split in two distinct parts $\partial\mathcal{B}_u$ and $\partial\mathcal{B}_t$, on which the individual boundary conditions are prescribed. While the implementation of these boundary conditions is rather straight forward, although requiring an implicit solution scheme, it has been found, that the homogenized stiffness is often overestimated and an overall stiffer macroscopic material response is obtained.

Periodic Boundary Conditions: Thus, another type of boundary conditions is preferred for RVEs, the periodic boundary conditions (PBC). Although PBCs are designed and well suited for periodic RVEs, sufficient results can also be obtained for non-periodic structures. Considering Eq. (3.58), the term in the parenthesis represents the time derivative of the deformation fluctuations, cf., Eq. (3.45). Thus, Eq. (3.58) can alternatively written as

$$0 = \frac{1}{V}\int_{\partial\mathcal{B}} \boldsymbol{t} \cdot \dot{\widetilde{\boldsymbol{u}}}\,\mathrm{d}A. \tag{3.60}$$

For the application of PBCs, the boundary of the RVE ∂B is split in two opposing sets of surfaces B^+ and B^- with $B^+ \cup B^- = \partial\mathcal{B}$ and $B^+ \cap B^- = \emptyset$. By this split of the boundary, the Hill-Mandel-condition can be further expanded to

$$0 = \frac{1}{V}\int_{\partial\mathcal{B}} \boldsymbol{t}(\boldsymbol{X}^+) \cdot \dot{\widetilde{\boldsymbol{u}}}(\boldsymbol{X}^+)\,\mathrm{d}A + \frac{1}{V}\int_{\partial\mathcal{B}} \boldsymbol{t}(\boldsymbol{X}^-) \cdot \dot{\widetilde{\boldsymbol{u}}}(\boldsymbol{X}^-)\,\mathrm{d}A. \tag{3.61}$$

Given pairs of of parallel surfaces of equal size on opposite sides of the RVE, $B_i^+ \in B^+$ and $B_i^- \in B^-$, the modified form of the Hill-Mandel-condition can be fulfilled, if

$$\widetilde{\boldsymbol{u}}(\boldsymbol{X}^+) = \widetilde{\boldsymbol{u}}(\boldsymbol{X}^-),\ \boldsymbol{t}(\boldsymbol{X}^+) = -\boldsymbol{t}(\boldsymbol{X}^-) \quad \forall \boldsymbol{X}^+ \in B_i^+ \text{ and } \boldsymbol{X}^- \in B_i^-. \tag{3.62}$$

This introduces special requirements in view of the finite element mesh of the microstructure, since every node needs an counterpart on the other side of the RVE. Especially for unstructured and non-periodic structures additional effort is necessary to construct a periodic mesh.

3.4.5 Consistent Tangent Moduli

Since the overall idea of the FE^2-method is the substitution of a phenomenological material model by BVPs on the microscale, these microscale BVPs have to return not only the homogenized stresses, but also a tangent moduli. However, unlike the stresses, a simple volume average of the tangent moduli, i.e.,

$$\overline{\mathbb{A}} = \langle \mathbb{A} \rangle \tag{3.63}$$

is mechanically only correct, if the strain field on the microscale is uniform. Otherwise, the volume average leads to a stiffer tangent moduli, which is why a softening term has to be considered, cf., e.g [136]. This softening term is the volume average of the sensitivity of the tangent moduli with respect to the fluctuation of the deformation gradient, i.e. a consistent tangent moduli is computed by

$$\overline{\mathbb{A}} = \frac{1}{V} \int_{\mathcal{B}} \mathbb{A} \mathrm{d}V + \frac{1}{V} \int_{\mathcal{B}} \mathbb{A} : \partial_{\overline{\boldsymbol{F}}} \widetilde{\boldsymbol{F}} \mathrm{d}V. \tag{3.64}$$

3.5 Finite Cell Method

The systematic investigation of many different microstructures by means of numerical homogenization as introduced in the previous section poses an additional challenge: the construction of suitable finite element meshes. If only a few, e.g., ten or twenty different microstructures or rather RVEs should be investigated, a manual mesh construction may be feasible. With a further increasing number of different microstructure realizations, that should be investigated, the manual approach becomes quite cumbersome and more time will be spent on mesh construction than on actual finite element computations. Therefore, the construction of meshes should be automatized in favor of a larger number of RVEs, that can be considered. However, while there are algorithms and frameworks for the automatized construction of conforming finite elements, cf., e.g. Schneider et al. [134], arbitrary microstructures with e.g., intersecting ellipsoids in the case of SSRVEs, are still challenging for these algorithms and thus, potential unusable finite element meshes may be generated. In this context, unusable covers for example unnecessarily small elements, or elements, which intersect itself, or elements with degenerated shapes.

An alternative to the manual or potentially faulty automatized generation of conforming finite element meshes is the application of the finite cell method (FCM), cf., e.g. Parvizian et al. [117] or Düster et al. [30]. The core idea of the FCM is the combination of fictitious domains with higher order shape functions. The fictitious domain approach embeds the domain of interest of arbitrarily shape in an outer domain of simpler size such as cubes, cf., e.g. the works of Bishop [16], Ramière et al. [121] or Glowinski and Kuznetsov [53]. These outer domains, the fictitious domains, are then meshed by means of regular grids, such that cube or cuboid-shaped elements originate. By that approach, the meshing effort is reduced to a minimum, as regular cartesian grids are rather simple to generate. Obviously, the resulting meshes are no longer conforming in the sense, that the material interfaces are reflected by element boundaries. In consequence, the approximation of the morphology of the domain of interest is split from the approximation of the displacement field.

Originally, the FCM has been introduced to ease the mesh generation for domains with unregular, arbitrary shape, potentially also including holes. Then, the added fictitious domain around the actual domain of interest was assigned a stiffness of close to zero, such that the mechanical fields are not disturbed. Additional special treatment is required for the application of boundary conditions, since these can only be applied to the fictitious domain, but not to the domain of interest, cf. [30] for more in-depth discussion on the boundary condition

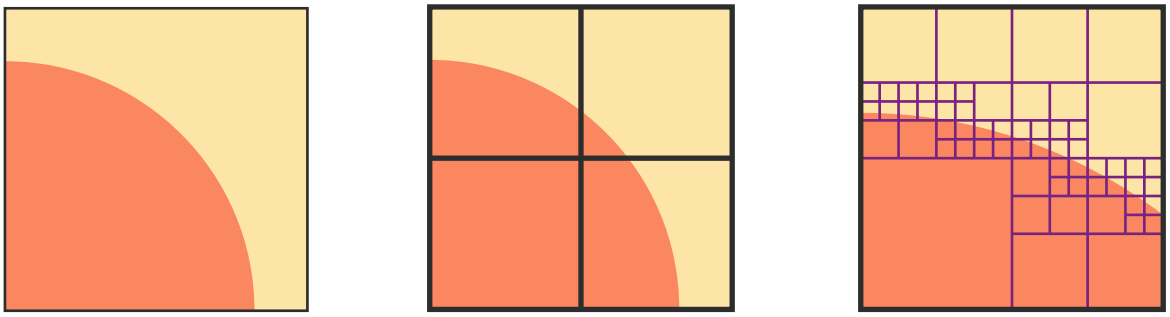

Figure 3.4: Illustration of **a)** the considered geometry of a circular inclusion in a matrix, **b)** example of a structured grid used as finite element mesh for this domain and **c)** decomposition of the top left finite cell from subfigure b) based on the application of the quadtree algorithm with a recursion-depth of 4. Adapted from Fangye, Miska, and Balzani [37].

treatment. For the intended application of the FCM to the microstructure of virtual experiments in the FE^2-sense, the special treatment of boundary conditions can be avoided. The domain of interest and the fictitious domain may be interpreted as two different phases with different material properties, similar to different material phases in a material's microstructure. Additionally, the RVEs as introduced in Sec. 3.4.1 are cuboid-shaped, such that no fictitious domain is necessary and the domain of interest can easily be meshed by regular grids. Since a regular grid is also periodic, the utilization of periodic boundary conditions for the homogenization is straight-forward.

However, since the resulting meshes are non-conforming, two different material phases may appear within a single finite element. This leads to a discontinuity of the integrand in the computation of the element stiffness matrix, cf. Eq. (3.37), and hence, the Gauss integration scheme can not be applied directly. Thus, as central idea of the FCM, the integrand is decomposed into multiple parts, such that each part for itself is continuous with respect to the material phases. Exemplary, for a microstructure with two different phases, related to domains $\mathcal{B}_1$ and $\mathcal{B}_2$ respectively, such that $\mathcal{B}_1 \cup \mathcal{B}_2 = \mathcal{B}$ and $\mathcal{B}_1 \cap \mathcal{B}_2 = \emptyset$ holds, cf. also the illustration in Fig. 3.4a) and Fig. 3.4b). There, the computation of the element stiffness matrix can be decomposed in two separate integrations over the individual material phases by

$$\boldsymbol{k}^{\mathrm{e}} = \int_{\mathcal{B}_1^e} \boldsymbol{B}^{\mathrm{eT}} \mathbb{A}_1 \boldsymbol{B}^{\mathrm{e}} \mathrm{d}V_1 + \int_{\mathcal{B}_2^e} \boldsymbol{B}^{\mathrm{eT}} \mathbb{A}_2 \boldsymbol{B}^{\mathrm{e}} \mathrm{d}V_2. \tag{3.65}$$

Since the individual integrands are continuous with respect to the material phases, the Gauss integration can be used for each integral. The difficult part therein is the determination of the domains $\mathcal{B}_1^e$ and $\mathcal{B}_2^e$. The idea within the FCM is to subdivide the finite element in smaller subsections, the so-called subcells. Unlike the finite element, a subcell consists of only one material phase and thus, the morphology within the finite element is approximated by the subcells. Therefore, the computation of the element matrix may be more generally written for an arbitrary number of subcells per element n_{sc} and using the Gauss integration by

$$\boldsymbol{k}^{\mathrm{e}} = \sum_{sc=1}^{n_{sc}} \sum_{l=1}^{n_{GP}} \left(\boldsymbol{B}_l^{\mathrm{T}} \mathbb{A}_l \boldsymbol{B}_l \right) \det[\boldsymbol{J}(\boldsymbol{\xi}_l)] w_l. \tag{3.66}$$

An open question is the decomposition of the finite element with its contained microstructure morphology into the subcells. In the original proposal, an Octree algorithm was used, cf. [30] or Schillinger and Ruess [131]. The two-dimensional equivalent is shown in Fig. 3.4c). One disadvantage therein is a high number of subcells, which leads to a higher required numerical effort during the assembly stage, which may partially be overcome with smart Octrees,

cf., Kudela et al. [77]. Alternatives are moment fitting approaches, resulting in individual integration rules for every element, cf., Joulaian et al. [71] or Hubrich et al. [69]. In many applications, the geometry data is given in form of pixels or voxels. Since this data is already cube or cuboid-shaped like the subcells or finite elements, it can be beneficial to exploit this property in order to create the smallest number of subcells. An algorithm for this purpose, called "Optimal Decomposition", has been proposed in Fangye et al. [37] and will be discussed in more detail in Sec. 4.

4 Optimal Decomposition of Voxel-Based Geometries for the Finite Cell Method

Within the context of the classic Finite Cell Method (FCM) as described in Sec. 3.5, the decomposition into subcells is mostly performed by means of the Octree algorithm. This offers advantages, e.g., for curved surfaces or domains with arbitrary holes in it, since the Octree algorithm will recursively create more and thus, finer subcells in regions of high geometry discontinuity and less subcells in geometrically constant areas. However, if the geometry representation is already given in a format, in which the smallest base unit is a cuboid, i.e., in terms of pixels or voxels, it may be beneficial to take advantage of their properties and directly aggregate these smaller units to larger cuboids. By that, less subcells may be generated than from the Octree approach for the same geometry, which is favorable in view of the efficiency of the assembly of the underlying finite element problem, since less integration point evaluations are required. In Fig. 4.1, a simple two-dimensional example for the two different subcell decompostion methods is shown: in Fig. 4.1a), the base domain of five by five pixels and two different materials is depicted. If this geometry is decomposed into subcells by means of the Octree, a decompostion as depicted in Fig. 4.1b) will result, in this case, the Octree is refined four times. It should be noted, that the two-dimensional variant of an Octree is called Quadtree, but in order of generalization in this thesis the algorithm is termed Octree even for this two-dimensional example. Although rather small subcells are created, the created subcells cannot match the material boundaries exactly, as since still a few subcells with in theory two materials are shown. Since subcells with two materials are not permissible in the FCM context, either the Octree has to be refined even more or the existing subcells are assigned a single material by e.g., assigning the subcell the material with the larger volume fraction, which would effectively shift the material boundary and modify the boundary value problem at hand. Motivated by these shortcomings, the optimal decomposition as shown in Fig. 4.1c) is proposed, cf. Fangye, Miska, and Balzani [37], which clusters the pixels in an optimal way, such that the least number of subcells is created. By that, the material boundaries are captured exactly and the required numerical effort for the assembly of the

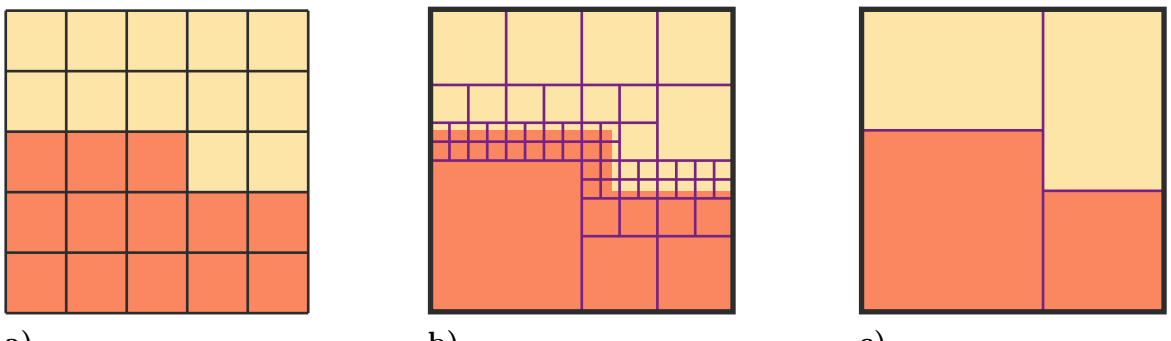

Figure 4.1: Subcell decomposition of a finite cell, **a)** base representation of the geometry with 5 by 5 pixels, **b)** subcell decomposition by means of quadtree until level 4 with intersected subcells and **c)** optimal subcell decomposition. Adapted from Fangye, Miska, and Balzani [37].

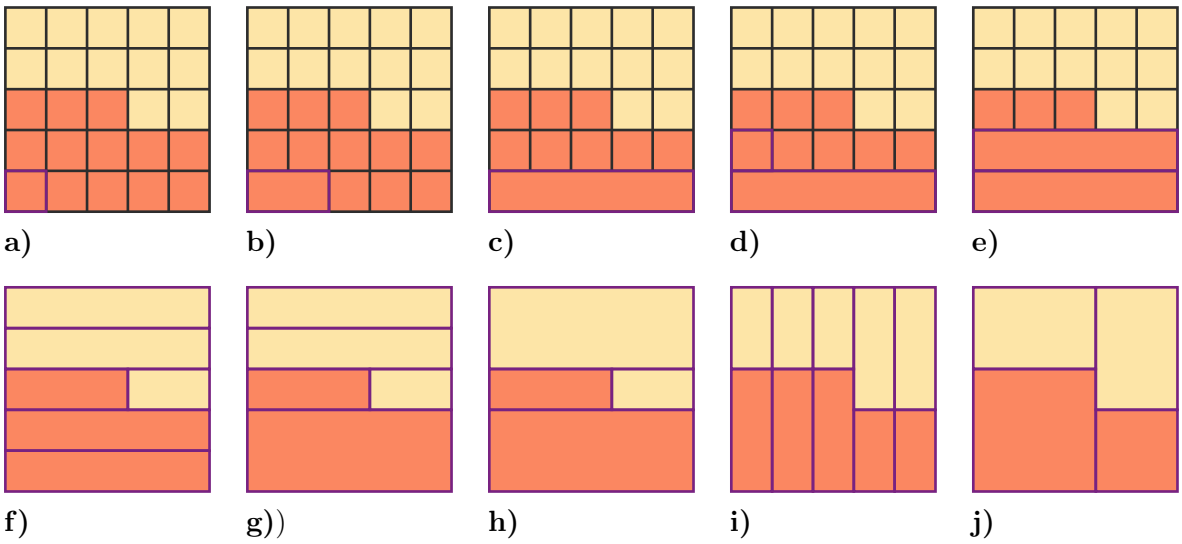

Figure 4.2: Principle algorithm of the Optimal Decomposition (OD) for one single finite cell containing 5 by 5 pixels; **a)** a prototype subcell, **b)** extension in first search direction, **c)** an entire joined row, **d)** and **e)** iterations on the next row, **f)** the result of the extension in the first direction, **g)** merge operation in second direction and **h)** final decomposition result. In **i)** and **j)** the decomposition result for a permutation of the search direction is shown. Adapted from Fangye, Miska, and Balzani [37].

finite element problem is kept as low as possible. Hence, the following chapter presenting the method itself and a numerical comparison against the Octree method, is a reflection of the contents of the mentioned journal paper. In addition, the developed methods have been presented in Fangye, Miska, and Balzani [35] and Fangye, Miska, and Balzani [36].

4.1 Enhanced Subcell Decomposition Approaches for the Finite Cell Method

4.1.1 Optimal Decomposition

The introduction example in Fig. 4.1 is rather easy so solve visually, which is however no practical approach for arbitrary geometries and domains. Therefore, an algorithmic procedure has been developed, which is described in the following. In order to keep this description easy to understand, it will mainly focus on two-dimensional cases, which are also simpler to visualize. However, this is no restriction of the method itself, which can also deal with three-dimensional applications. If the method requires additional or modified steps for the three-dimensional case, this will be explicitly annotated. The algorithm is explained on the basis of the same geometry, which was used in the introductory example, cf., also Fig. 4.2a). It represents a two-dimensional element, in which the geometry is resolved by five by five pixel. From thereon, the following algorithm starts:

1. A start pixel or voxel is identified in a corner of the finite element, in this example the pixel in the lower left corner, outlined by a dark purple box in Fig. 4.2a). This pixel or voxel is considered as prototype subcell with the size of one pixel and will be extended next.

2. Starting from the prototype subcell, a dimension is chosen as search directory, in this example to the right, and the next neighboring pixel is checked for compatibility. In this regard, compatibility checks a), that both the prototype and the neighbor have the

same material, since otherwise an aggregation is not sensible and b), that the size of the prototype and the neighbor are the same in the remaining directions, which are not the search direction. Only then, a merge of both will result in a larger cuboid. If both criteria are fulfilled, the prototype can be extended by the size of the neighboring pixel as shown in Fig. 4.2b). If at least one criterion is not fulfilled, a new prototype subcell is started.

3. The previous step is repeated, until the end of the finite element is reached, cf. Fig. 4.2c). A subcell, which is larger than the enclosing finite element is not permissible. In the example, the entire bottom row of pixel has been joined to one subcell.

4. Once the end of the finite element is reached in the first dimension, the algorithm shifts by one row in the second dimension, see Fig. 4.2d). From there, the two previous steps are repeated again, so that the result as shown in Fig. 4.2e) is obtained.

5. Steps 2 to 4 are repeated, until the end of the finite element in the second dimension is reached as well. The resulting decomposition in Fig. 4.2f) shows, that the material discontinuity in the middle row was captured and a new subcell was started exactly at the material interface. For the two-dimensional example now the next step would be performed, for a three-dimensional problem the aforementioned steps are now also repeated in the third direction, until also there the end of the finite element is reached, cf., also the pseudo-code in lines 3 to 12 of Alg. 1.

6. The result of the previous steps is a set of tube-shaped subcells, since the pixel and subcells were only joined in one dimension. Thus, the next step is to try to merge these tube-shaped subcells in a second direction, if possible. Again and similar to before, the subcells, which should be joined, need to be checked for compatibility, i.e. both subcells have to have the same material and the same size in the non-search directions. The first step of this iteration is shown in Fig. 4.2g), wherein the two subcells at the bottom of the finite element were joined. However, the row above that can not be joined, since for both subcells in the middle row at least the size check will fail. The end result of the merging operation in the second search direction is depicted in Fig. 4.2h). For the two-dimensional case, at this point the end of the algorithm is reached, since all dimensions were searched and subcells joined, if possible. This refers also to lines 14 to 20 in Alg. 1. For a three-dimensional problem, one more search direction remains, since until now a lot of layers with plate-shaped subcells were created. Here, an additional iteration along the third dimension has to be performed to join these subcells into larger cuboids, if compatibility is given. This search along the third dimension is reflected in lines 22 to 28 of Alg. 1.

One crucial part in the presented algorithm is the choice of the starting point. It can not be guaranteed, that the optimal decomposition can be found, if the starting point is always in the lower corner and the dimensions are searched in ascending order. Hence, the proposed algorithm is repeated for all possible permutations of directions, which leads to two runs for two-dimensional and six runs of the algorithm for three dimensions. The impact of different permutations of search directions is visualized in Fig. 4.2i) and Fig. 4.2j) for the chosen example. The tube-shaped subcells are now created in the vertical direction and also the final result looks different. However, the number of generated subcells is the same, at least in this example, such that the numerical cost of assembly is assumed to be the same. In the general case, it can not be proven, that any particular order of search directions is preferable over another, since a less number of subcells is created, or that all permutations perform the same. Thus, in practical applications, all permutations have to be tested to obtain the smallest number of subcells from the Optimal Decompostion. Since the smallest number of

Algorithm 1: Optimal Decomposition (OD)

```
def OptimalDecomposition(finite_cells, voxel_data):
    for fc in finite_cells:                                  # loop over all finite cells
        subcells = []
        for vz in z-direction:                               # iteration to aggregate
            for vy in y-direction:                           # voxels in first direction
                for vx in x-direction:
                    vox = voxel_data[vx,vy,vz]               # get actual voxel
                    last_sc = subcells.Last()                # get current subcell
                    if CheckCompatibility(vox, last_sc, 1):
                        last_sc.ExtendBy(vox)                # extend subcell by voxel
                    else:
                        subcells.Append(vox)                 # start new subcell with voxel

        subcells.Sort()                                      # sort subcells for merge in 2nd direction
        for i in subcells.length:                            # loop over all prototypal subcells
            sc1 = subcells[i]                                # extract neighboring subcells
            sc2 = subcells[i-1]
            if CheckCompatibility(sc1, sc2, 2):
                sc2.ExtendBy(sc1)                            # merge neighboring subcells if possible
                sc1.Remove()

        subcells.Sort()                                      # sort subcells for merge in 3rd direction
        for i in subcells.length:                            # loop over all prototypal subcells
            sc1 = subcells[i]                                # extract neighboring subcells
            sc2 = subcells[i-1]
            if CheckCompatibility(sc1, sc2, 3):
                sc2.ExtendBy(sc1)                            # merge neighboring subcells if possible
                sc1.Remove()
    return subcells
```

subcells per finite element is considered optimal in view of the required numerical costs, the algorithm is named Optimal Decomposition.

In the example, the bounds of the finite element correspond with the interfaces of the pixels (or voxel), which is not necessarily true for all applications. The proposed method is able to also consider pixel or voxel, which are only partially part of the finite element by considered only the portion of the pixel, which is inside the finite element, for the construction of prototype subcells. This is the main reason why the dimensions of the corresponding subcells are carefully checked before a merge operation, to ensure that only cuboid-shaped subcells are obtained. A potential drawback of the Optimal Decomposition is the potential construction of narrow subcells. In the example, all tube-shaped subcells could be joined to larger subcells, however, in real applications very long, but thin subcells may be created, which may lead to problems concerning the numerical quadrature. In order to investigate this effect, a measure called irregularity of the subcells is defined as the ratio of the longest and shortest size of a subcell by

$$\mathrm{irr}[sc] = \frac{\max\{l^{sc}, w^{sc}, h^{sc}\}}{\min\{l^{sc}, w^{sc}, h^{sc}\}}, \tag{4.1}$$

wherein l^{sc}, w^{sc} and h^{sc} denote the length, width and height of the subcell sc, respectively.

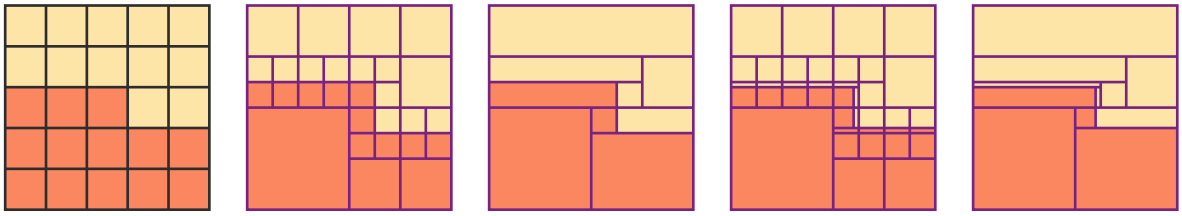

Figure 4.3: Combinations of the Octree with the Optimal Decomposition; **a)** base geometry, **b)** Octree level 3, **c)** the T-M , **d)** the T-OD and **e)** the T-OD-M algorithms. Adapted from Fangye, Miska, and Balzani [37].

4.1.2 Modifications of the Octree Algorithm

Considering the Optimal Decomposition (OD) method introduced in the previous section with its potential drawbacks due to irregular subcells, it can be beneficial to explore the combination of the Octree algorithm with the newly suggested OD. For this purpose, three distinct combinations of both methods are suggested and outlined below.

Octree with Subsequent Global Subcell Merge The OcTree-Merging algorithm (T-M) is obtained by integrating the Octree algorithm with the merge of subcells as suggested in the Optimal Decomposition. To do this, the Octree is initially performed up to specified thresholds, such as level three as illustrated in Fig. 4.3b). Next, the subcells are merged to decrease the overall quantity of subcells, by systematically evaluating all potential combinations of directions. Fig. 4.3c) demonstrates an instance of the outcome, revealing a notable reduction in subcells compared to the pure Octree depicted in Fig. 4.3b). Although the updated approach retains the fundamental principles of the Octree algorithm, it may still fail to precisely capture material boundaries. This is because the subcells generated by the Octree algorithm may not align perfectly with the material boundaries. In the given example, the initial volume fraction of the orange inclusion is calculated to be 52% (13/25) as shown in Fig. 4.3a). However, upon using the Octree algorithm up to level three, the volume fraction is determined to be 53.125% (34/64). The Octree has altered the volume percentage, potentially compromising the accuracy of the integration outcome.

Octree with Subsequent Local Optimal Decomposition in Finest Level The approach at the finest level of the Octree is altered by combining it with the OD in a different way, resulting in a method named OcTree Optimal Decomposition (T-OD). Rather than making a simplistic assignment of the material with the highest volume percentage to each subcell, a more efficient decomposition is carried out within each subcell at the finest level of the octree structure. The fundamental algorithm of OD remains same, with the exception that the boundaries of the matching subcell produced from the Octree are utilized instead of the limits of the finite element. By utilizing an Octree to divide the domain and applying the OD at the finest level, the regular division of the domain prevents the occurrence of excessively small subcells, while a precise approximation of material boundaries is maintained. Utilizing this adapted technique on the current example yields a subcell decomposition, as depicted in Fig. 4.3d). In comparison to the implementation of the initial Octree shown in Fig. 4.3b), the new method appropriately represents the material boundaries but requires a greater number of subcells. Furthermore, a small number of thin subcells are created at the interfaces of the materials. Hence, selecting the optimal finest level for a T-OD application necessitates a trade-off between the preferred quantity of subcells and the irregularity of the generated subcells.

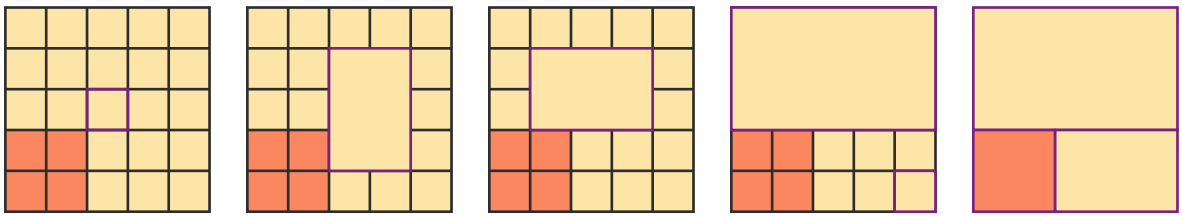

Figure 4.4: Illustration of the Optimized Clustering algorithm (OC), **a)** randomly chosen start pixel, **b)** and **c)** two possible restricted growth modes, **d)** fully grown subcell and **e)** resulting subcell decomposition. Adapted from Fangye, Miska, and Balzani [37].

Octree with Subsequent Local Optimal Decomposition and Global Subcell Merge The OcTree-Optimal Decomposition-Merging (T-OD-M) algorithm is the result of combining the two previous separate modifications of the Octree algorithm. The Octree algorithm is executed until a specified depth of recursion is achieved. Then, the Optimal Decomposition is carried out locally on the subcells at the finest level that still have two materials. Finally, all subcells are globally merged if they are compatible. Executing the T-OD-M on the above case yields the outcome depicted in Fig. 4.3e). It is evident that the quantity of subcells is decreased, however, this also results in the formation of thin subcells. In this scenario, the subcells generated by the Octree algorithm are perfectly aligned with the material boundaries, making it challenging to prevent the formation of small subcells at interfaces. The consequences of this observed behavior are investigated by means of numerical examples in Sec. 4.2.

4.1.3 Optimized Clustering

Given that the proposed changes to the Octree algorithm result in a greater quantity of subcells, they do not offer a direct advantage over the Optimal Decomposition algorithm when narrow subcells are deemed acceptable. Nevertheless, the degree to which the OD algorithm effectively results in the smallest quantity of subcells remains uncertain. In order to examine this issue, a new approach is presented that constructs the subcell decomposition by resolving an optimization problem. To achieve this objective, a random voxel is selected from within a finite element as the initial point, see the two-dimensional example problem shown in Fig. 4.4a). Subsequently, the algorithm tries to group adjacent voxels together in order to expand the initial voxel into a larger cuboid. Initially, it attempts to expand uniformly in every direction, leading to the formation of a larger cubic shape. If it is no longer feasible, such as when a voxel of a different material would be incorporated or the bounds of the finite element are reached, the growth mode is altered. Then, the algorithm restricts the expansion. Initially, one specific direction is restricted to expand only in positive or negative direction, while the other two directions remain unrestricted. This case is depicted in Fig. 4.4b) and Fig. 4.4c), showcasing two potential options for the restricted growth, since volumetric growth is not possible due to the inclusion in the lower left corner. When a growth mode becomes unsuccessful, the algorithm limits another level of flexibility to grow until there are no remaining directions to restrict growth in. By that, the largest possible subcell for the specified starting voxel is identified. Subsequently, the method proceeds by randomly choosing another voxel that has not yet been included in a subcell to initiate the clustering algorithm once more. This can be observed in Fig. 4.4d), where the largest feasible subcell was identified and a new starting voxel was selected at the lower right corner, as shown in Fig. 4.4e). The process is iterated until there are no remaining unoccupied voxels within a limited cell, as shown in Fig. 4.4e). It is evident that specific limitations on the directions of growth offer numerous possibilities for the subcell to expand. As illustrated in Fig. 4.4b) and Fig. 4.4c), the

Algorithm 2: Optimized Clustering (OC)

```
def OptimizedClustering(finite_cells, voxel_data):
    for fc in finite_cells:                                  # loop over all finite cells
        subcells = []
        for idx in monte_carlo_runs:                         # Monte Carlo optimization
            subcells_tmp = []
            while unassigned_voxels in fc:                   # loop free voxels
                start_vox = PickRandomlyFrom(unassigned_voxels)
                subcells_tmp += GrowSubcells(start_vox, subcells_tmp, voxel_data, 1)
            if subcells_tmp.size < subcells.size:            # update list if new minimum found
                subcells = subcells_tmp
    return subcells

def GrowSubcells(startcell, subcell_list, voxel_data, growth_mode):
    switch growth_mode do                                    # recursive call decides growth mode
        case 1:do
            trial_area = grow_cube(startcell)
        case 2:do
            trial_area = grow_cuboidal(startcell)
        case x:do                                            # last growth mode is simply the startvoxel
            trial_area = startcell

    if !CheckElementBounds():                                # next mode if element bounds are intersected
        return GrowSubcells(startcell, subcell_list, voxel_data, growth_mode+1)
    if !CheckOverlap():                                      # next mode if overlap with existing subcell
        return GrowSubcells(startcell, subcell_list, voxel_data, growth_mode+1)
    if !CheckMaterialInterface():                            # next mode if material interface is cut
        return GrowSubcells(startcell, subcell_list, voxel_data, growth_mode+1)

    unassigned_voxel.RemoveVoxelInside(trial_area)
    return trial_area
```

subcell has the potential to expand either horizontally or vertically within the finite element. Due to the difficulty of determining the optimal path in advance, the algorithm employs a heuristic approach and randomly selects a specific growth direction. However, this heuristic approach, together with the random selection of a starting voxel, leads to a realization, that a certain subcell decomposition obtained from this approach may not be the ideal choice in the sense of the least number of subcells. Hence, the Monte Carlo optimization technique is utilized to repeat the method for a specific number of times for each finite element in order to identify the subcell decomposition with the minimum number of subcells. Similar to the Optimal Decomposition, the algorithm of the Optimal Clustering (OC) is concisely outlined as pseudo-code in Alg. 2.

It is important to note, that Alg. 2 is primarily introduced in order to present an estimator for the optimal subcell decomposition, demonstrating that Alg. 1 results in a subcell decomposition that is nearly optimal. The numerical complexity of Alg. 2 is evidently much greater than that of Alg. 1, which has a complexity of around v^3, where v represents the number of voxels per spatial direction. The computational time for Alg. 1, which solely influence the preprocessing time, is significantly smaller than the computational time needed to solve the nonlinear mechanical problem. Therefore, the efficiency of the preprocessing algorithms

itself is not of great significance. Nevertheless, substantial reductions can be achieved in the amount of computer time needed to solve the mechanical problem.

4.2 Numerical Examples

This section analyzes the accuracy and effectiveness of the methods for subcell decompositions proposed in 4.1 in view of their applicability for computational homogenization. Therein, the homogenized mechanical response of various microstructures under macroscopic uniaxial stress conditions is computed by using the Finite Cell Method and the FE^2-method as described in Sec. 3.4. In this context, a uniform problem involving uniaxial tension at the macroscale is investigated. By that, the macroscopic finite element problem is only used to ensure, that the stresses in the directions transversal to the direction of tension vanish. Hence, a single finite element with only one quadrature point is sufficient on the macroscale and the major computational effort has to be performed on the microstructure. The microstructures of the considered examples should represent RVEs of a DP-steel, which consists of martensitic inclusions in a matrix of ferrite. For these two phases, the finite J_2 elasto-plasticity formulation with isotropic hardening according to Klinkel [74] and Simo [139] is used. The material parameters for both phases are taken from Brands et al. [19] and are listed in Tab. 4.1. First, a simple microstructure consisting of a cube-shaped inclusion in a cube and utilizing only one finite element is used to analyze the performance of the proposed algorithms for subcell decomposition. Then, a more realistic microstructure, the SSRVE obtained from Balzani et al. [4], is used to evaluate the performance of the algorithms in a more realistic application. In order to perform the computations, the Finite Cell Method was implemented in a customized version of the FE-software FEAP8.2.

4.2.1 Simple Microstructure with one Finite Element

This initial example serves as an academic demonstration of the precision and effectiveness of the suggested OD technique in comparison to the traditional Octree algorithm. For this purpose, two different, but very similar simple artificial microstructures based on voxels are created. Both microstructures are discretized using a single 27-node hexahedral element, which includes thus both the martensitic and the ferritic phase. The initial microstructure is depicted in Fig. 4.5a) and is characterized by a volume consisting of 16^3 voxels, in which the martensitic phase is situated in a single corner of the microstructure and is characterized by the presence of seven voxels in each spatial direction. The subcells obtained for the Octree of level four and OD approaches are depicted in Fig. 4.5b) and Fig. 4.5c) respectively. The voxel model has been designed in such a way that the material boundaries align precisely with the subcells following four subdivisions of the Octree method. Hence, additional subdivisions do not alter the subcell decomposition. Whilst the total number of subcells needed for the Octree is 323, the OD method achieves an accurate description of the microstructure with just four subcells. The mechanical response due to each subcell decomposition method is illustrated in Fig. 4.5d). As anticipated, the various subcell decompositions, which are caused by different octree levels, yield distinct outcomes. The material response becomes more rigid when the

Table 4.1: Material parameters used for the ferritic and martensitic phases.

	E (MPa)	ν (-)	y_0 (MPa)	y_∞ (MPa)	α (-)	h (-)
Ferrite	206,000.0	0.3	260.0	580.0	9.0	70.0
Martensite	206,000.0	0.3	1000.0	2750.0	35.0	10.0

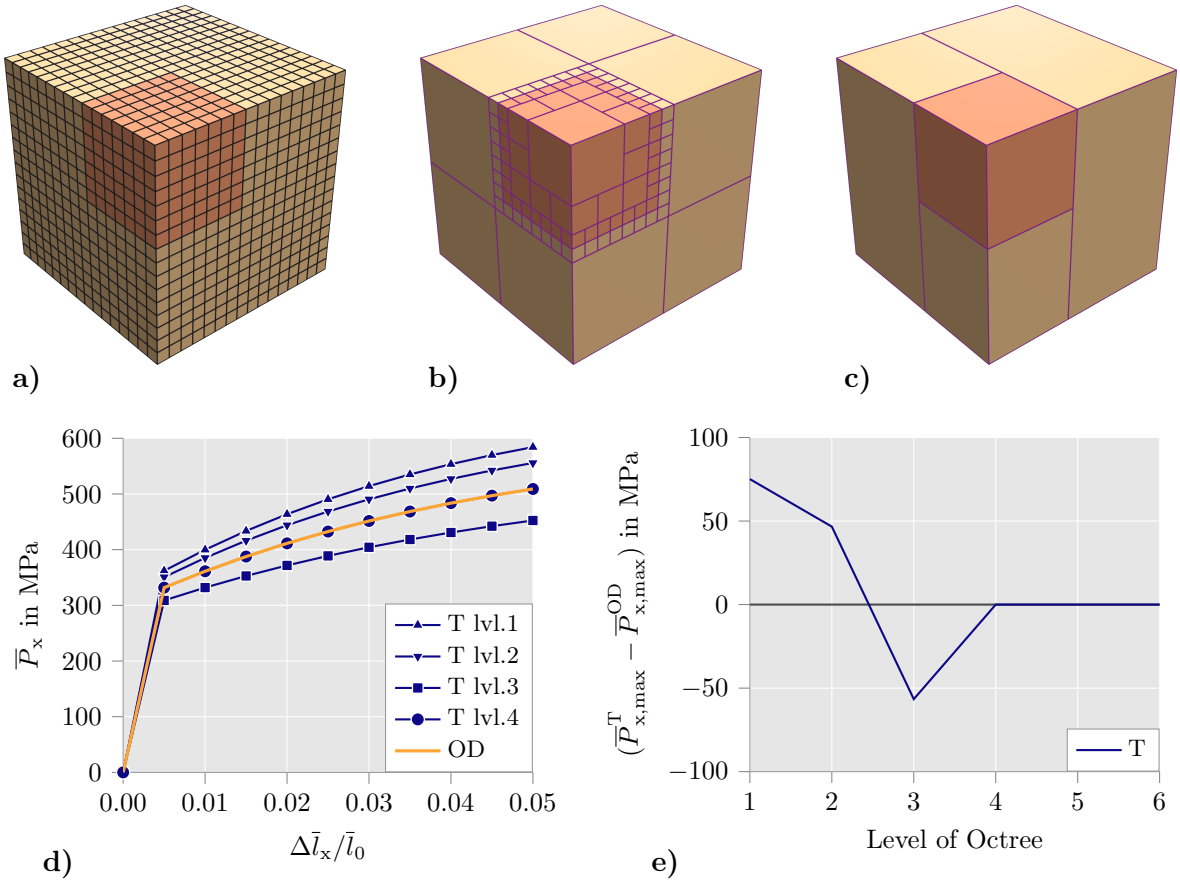

Figure 4.5: **a)** A 16^3 voxels model with a ferritic (light brown color) and a martensitic (orange color) phase, **b)** subcells for the Octree of level 4 (323 subcells), **c)** subcells for the OD approach (4 subcells), **d)** macroscopic stress vs. relative elongation, **e)** difference of maximal macroscopic stresses vs. level of Octree. Taken from Fangye, Miska, and Balzani [37].

martensitic percentage increases due to the fluctuation in volume fraction of this phase at different Octree levels. As an illustration, the integration mesh of the first level of the Octree method, consisting of eight subcells of identical size, exhibits the most rigid material behavior due to its highest percentage of martensite phase. The finest Octree solution is identical to the solution obtained from the Optimal Decomposition. The comparison between the maximum stress values of the Octree solution $\overline{P}^{\mathrm{OD}}_{\mathrm{x,max}}$ and the Optimal Decomposition $\overline{P}^{\mathrm{T}}_{\mathrm{x,max}}$ at an elongation of five percent, is illustrated in Fig. 4.5e). The convergence of the Octree solutions to the solution obtained from the Optimal Decomposition is clearly visible. Starting from level four, both methods yield identical results, thanks to the design of the microstructure that allows the Octree of level four to accurately represent the microstructures morphology.

Concerning the Octree decomposition, it is well possible that even after a certain number of subdivisions, the boundaries of the material may not align with the boundaries of the subcells. As an example, this applies to the model with 24^3 voxel as depicted in Fig. 4.6a). Therein, the martensitic phase has a size of 11^3 voxel, and hence, the total number of voxel for the geometry is no longer a multiple of the martensitic phase size. In Fig. 4.6b) and Fig. 4.6c), the respective subcells for both the Octree with six subdivisions and the OD are displayed. Like the previous example, the OD method needs only four subcells to precisely depict the microstructure. However, the Octree method falls short in reliably capturing the material boundaries, even with up to six subdivisions resulting in a total of 5923 subcells. In Fig. 4.6d), stress-strain curves are shown for simulations with different subcell decompositions.

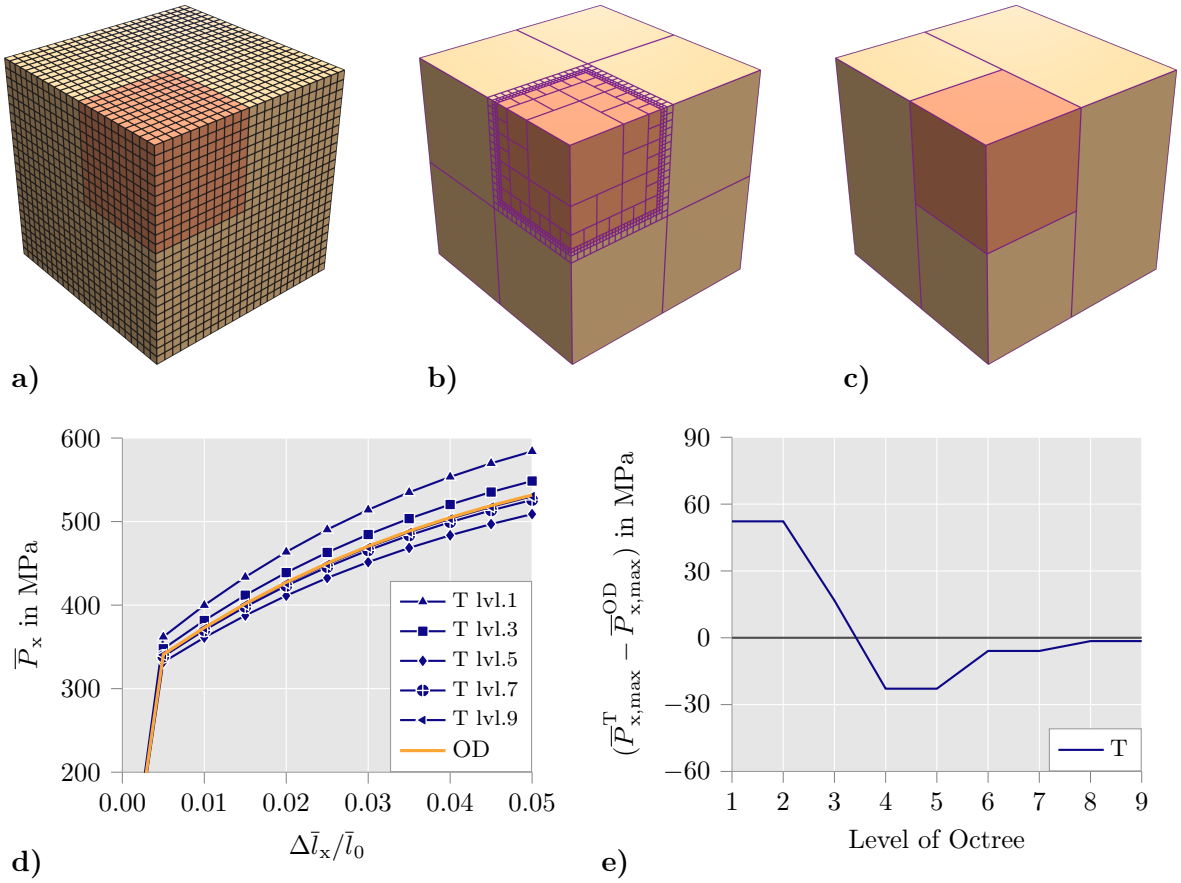

Figure 4.6: **a)** A 24^3 voxels model, **b)** subcells for the Octree of level 6 (5923 subcells), **c)** subcells for the OD approach (4 subcells), **d)** stress vs. relative elongation, **e)** difference of maximal stresses vs. level of Octree. Taken from Fangye, Miska, and Balzani [37].

The Octree splits of level one and two, four and five, six and seven, and eight and nine, result in the same subcell decomposition, respectively, and hence, only one of each pairs is plotted. Fig. 4.6e) illustrates the observed behavior, with the indicated levels connected by a horizontal line. The simulation results are influenced by the level of Octree subdivision, much like in the prior model. It is evident that as the number of subcells increases, the findings of the Octree method approach converge to those of the OD technique. However, even with a recursion depth of nine, the microstructure is not precisely captured.

Both simple microstructures demonstrate that selecting the correct Octree level is not a simple task, as the convergence towards the exact solution does not always follow a consistent pattern. Additionally, it is not recommended to select a high Octree level from the beginning, since it can lead to overly many subcells. Octree levels eight and nine already produce 96,069 subcells, resulting in significant computational inefficiency for this problem. These two examples, comprising basic microstructures and a single finite element, illustrate that the suggested Optimal Decomposition method can precisely and effectively represent the geometry with much less subcells than the traditional Octree decomposition. It is important to consider, that in this rather easy application, a sophisticated Octree would have yielded a significantly reduced quantity of subcells compared to the conventional Octree as well. However, this is solely attributed to the unique characteristics of the problem, which involves a exeactly cuboid-shaped inclusion within a cube. Certainly, the finite element discretization employed in the above examples cannot provide an exact solution to the boundary value problem. However, for the purpose of this analysis, which specifically examines the distinctions among

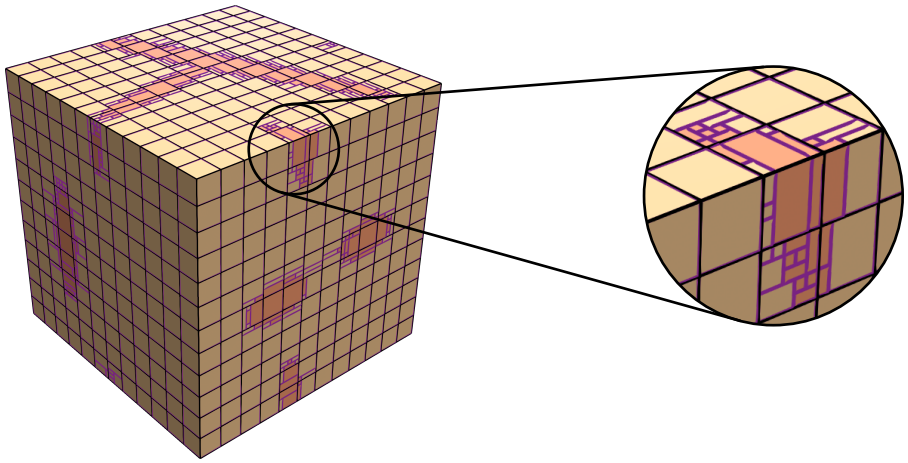

Figure 4.7: Subcells for the optimal decomposition approach for a SSRVE with a martensitic phase (orange color) and a ferritic phase (light brown color). Adapted from Fangye, Miska, and Balzani [37].

different subcell decomposition methods in relation to finite cells, the most precise solution to the boundary value problem, given a fixed discretization, is a subcell decomposition that precisely aligns with the material interface. Such a subcell decomposition is in this examples always obtained from the Optimal Decomposition approach.

4.2.2 Complex Microstructure in Form of a SSRVE

In order to validate the findings of the preceding examples with a more complex microstructure, a SSRVE following the approach of Balzani et al. [4] is employed for a more in-depth analysis. Also, the different combinations of the Optimal Decomposition and the Octree method as proposed in Sec. 4.1 are analyzed. Generally, SSRVEs exhibit a reduced complexity compared to the actual microstructure morphology, however they yield a comparable mechanical behavior. Thus, they require a lower computing power compared to classical RVEs. However, in contrast to the simple Representative Volume Element (RVE) used in the previous examples, the microstructure of a SSRVE is considerably more intricate as it is designed to reflect a real material. In this analysis, the SSRVE for DP steel as identified in Brands et al. [19] is used. The geometry is represented using a resolution of 60^3 voxel. The finite element mesh consists of 12^3 hexahedral finite elements with cubic shape functions. In Fig. 4.7 the integration mesh of the SSRVE for the OD method is displayed as an illustrative example. The effective macroscopic material response in terms of maximum stress is shown against the results from various levels of the Octree algorithm in Fig. 4.8a). The acronym "T" is used to represent the classic OcTree method in the graphs. Additionally, "T-M" is used to refer to the OcTree-Merging technique, "T-OD" is used for the OcTree-Optimal Decomposition, and "T-OD-M" is used for OcTree-Optimal Decomposition-Merging, herein all approaches are described before in Sec. 4.1.2.

Unsurprisingly, the T and T-M approaches yield identical outcomes due to their shared material boundaries. While the simulation for T with level four needs a substantial amount of computational power due to the extensive number of subcells, the effort required for the T-M technique is considerably reduced, as depicted in Fig. 4.8c). Due to the significant memory demands of the pure Octree method, higher Octree levels are only investigated for approaches that use the "merging" phase "M", specifically T-M and T-OD-M. The OD, T-OD, and T-OD-M methods provide identical material responses, as they all precisely represent the

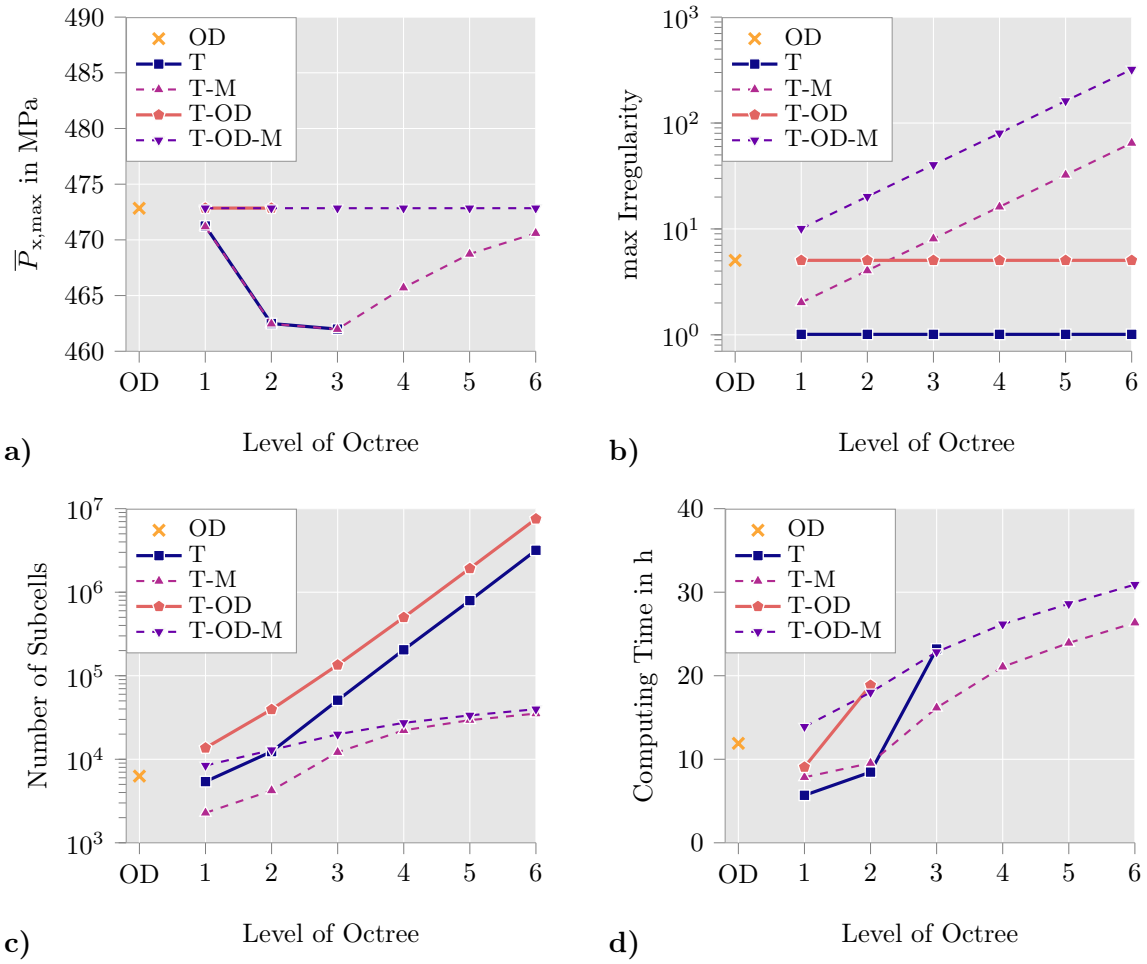

Figure 4.8: Comparison of different approaches **a)** maximal stresses, **b)** irregularity, **c)** number of subcells and **d)** computing time for different level of Octree. Taken from Fangye, Miska, and Balzani [37].

material boundaries. The relationship between T-OD and T-OD-M exhibits a resemblance to the relationship between T and T-M, namely in terms of the reduction in the number of subcells. Similar to the preceding example, it can be noted that the outcomes of the T and T-M methods exhibit a tendency to converge to the findings of OD, T-OD, and T-OD-M as the amount of subcells increases. The irregularity of the subcells as presented in Sec. 4.1 is shown in Fig. 4.8b). The OD, T, and T-OD approaches exhibit a constant and low level of irregularity, but the "M" methods result in a progressively higher level of irregularity as the Octree level increases. Nevertheless, the irregularity does not appear to impact the precision of the integration in this specific case, as the decisive factor is the maintenance of the precise phase fraction of the different microscopic material phases. However, the computing time as depicted in Fig. 4.8d) is influenced by the irregularity of the subcells. While the "M" approaches have a low number of subcells for Octree levels one and two, their calculation time is higher compared to the equivalent T and T-OD approaches. This is because the "M" approaches have a worse convergence behavior in the Newton iterations. Currently, the OD technique offers the most optimal balance in terms of precision, computational efficiency, and irregularity.

The Optimized Clustering as described in Sec. 4.1.3 is also used for the SSRVE example. Therein, the same element discretization as in the previous cases is used. Given that the previous examples have shown that material-preserving procedures produce accurate results,

Table 4.2: Resulting number of subcells, computing time and subcell irregularity for different Monte Carlo sample sizes for the Optimized Clustering approach using 12^3 Elements.

Repetitions	500	1,000	5,000	10,000	50,000	100,000	500,000	1,000,000
Time in s	66	118	543	1,057	4,967	9,422	45,222	87,101
Subcells	7,853	6,839	6,573	6,490	6,385	6,355	6,296	6,285
Irregularity	5	5	5	5	5	5	5	5

the Optimal Clustering method will be analyzed in terms of the generated number of subcells and its overall efficiency. Hence, only the preprocessing phase is investigated, specifically the creation of subcell decompositions, without executing a complex finite element simulation. The used microstructure yields 6,287 subcells and an irregularity value of 5 using the Optimal Decomposition approach. The essential information on the subcell decompositions obtained from the Optimized Clustering technique for various numbers of Monte Carlo runs can be found in Tab. 4.2. Both approaches, i.e. the OD and OC, are similar in terms of the irregularity of the subcells, regardless of the number of Monte Carlo iterations used in Optimal Clustering. Upon examining the quantity of elements and voxels on a single edge, the observed irregularity value of 5 is to be expected, as it is the consequence of dividing the number of voxels by the number of elements. Both strategies resulted in the formation of at least one subcell that extends to the size of only one voxel in two directions, with the third direction being equivalent in length to an element. The total number of subcells varies as the number of Monte Carlo iterations increases. The Optimal Clustering technique requires roughly 24 hours of running time to obtain a minimum of $6,285$ subcells after $1,000,000$ iterations. Therefore, despite the fact that the Optimal Clustering method discovered a subcell decomposition with two subcells less than the Optimal Decomposition, the Optimal Decomposition is considered to be more efficient than the Optimal Clustering. This is because the subcell decomposition was created with the Optimal Decomposition approach in around one second, whilst the OC technique took substantially longer.

5 Quantification of Uncertain Macroscopic Material Properties Resulting From Microstructure Morphology Variation

Quite often, materials with a heterogeneous microstructure are also known to exhibit notable variations in the morphology of their microstructure, and thus, the morphology of the material's microstructure will vary depending on the position inside the material. Due to the influence of the microstructure on the macroscopic response of the particular material, non-deterministic variations in the material properties across different macroscopic positions are to be expected. In principle, the uncertainties related to this variation can be measured experimentally by conducting the same experiments on various samples from different locations of the material. Since this approach is very costly in terms of labor and material, a substitution of physical tests with virtual ones in the context of computational homogenization shows great potential. The virtual experiments are boundary value problems using the FE^2-method, cf. Sec. 3.4, which allows the computation of effective macroscopic material properties based on the chosen microstructure. Hence, if one obtains a large set of different microstructure realizations, which reflect the real material's variation in the microstructure morphology, the variation of the macroscopic material properties may be quantified and used for further analysis. For this purpose, each of the virtual volume elements is virtually tested to obtain the properties for this specific specimen. The obtained data is then gathered in a histogram, which allows insight in the sought variation. Given enough samples, even a probability density function may be fitted to the obtained data. The selection of volume elements for this technique must be made in order to accurately depict the variable microstructure morphology of the material. While numerical simulations offer conceptual advantages over conducting actual tests, they present two primary obstacles, particularly when dealing with specific portions of real microstructure data as volume elements. Firstly, for a proper reflection of the materials microstructure, a significant portion of the real material has to be measured, which is not only costly, but also potentially infeasible in three dimensions. Secondly, with available microstructure morphology data, numerical simulations in terms of finite elements are numerically expensive, since usually rather complex morphologies are investigated. These complex geometries require a fine resolution of the finite element mesh, impeding the practical feasibility of those computations. Hence, substituting the set of actual microstructure reconstructions with a collection of artificial microstructures that accurately represent the variable morphology of the real material is a favorable strategy. For rather specific microstructure morphologies, in the works of Hiriyur et al. [66], Savvas et al. [125], and Tal and Fish [149] approaches for the construction of such artificial microstructures can be found. However, for general complex microstructures, whose morphology can hardly be quantified in terms of parameters of simpler geometries, a more general approach is required. A method to do so, has been published in Miska and Balzani [93], in which a method to quantify the variation of a real microstructure's morphology based on artificial microstructures, which are constructed based on higher order statistics of the microstructures morphology, is proposed. The principle approach to derive statistics on selected macroscopic material parameter from a set of artificial microstructures is outlined in the flowchart in Fig. 5.1. This chapter is meant to introduce this method and discuss the results obtained for the example of a dual-phase steel

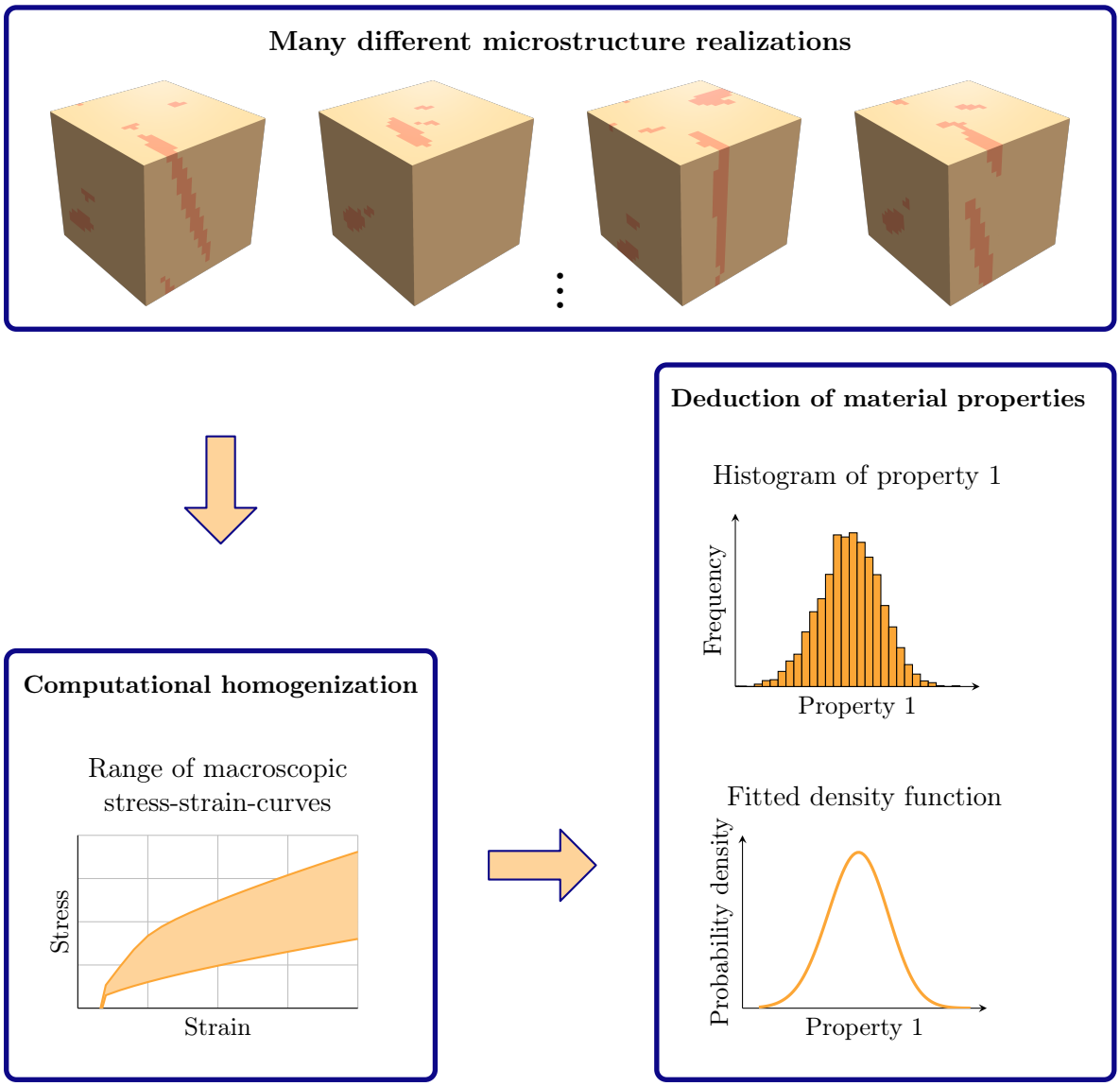

Figure 5.1: Principial scheme to quantify macroscopic material properties based on a set of artificial microstructures, whose morphologies vary in the same way the real material's microstructure does.

and thus, the contents of the aforementioned journal paper are reflected in this chapter. In addition to the journal paper, the methods and parts of the result are presented in Balzani et al. [5], Miska et al. [99] and Miska and Balzani [91].

5.1 Quantification of the Variation of Macroscopic Material Properties

Since the method should be applicable to a broad range of materials, a general approach to the quantification of the material's microstructure variation is required, since specialized methods, which quantify e.g. the variation of radii of sphere characterizing the materials inclusion, have to be discarded. The data obtained from this new approach is then used to construct a set of artificial microstructures, which exhibit the same variation in their morphology. It is nearby to utilize similar methods for the quantification of the real material's microstructure morphology and the artificial microstructure morphology. In this work, the idea of statistically

similar representative volume elements (SSRVEs), cf. Balzani et al. [4], is extended to create a set of artificial volume elements, which allow an increased numerical efficiency by reducing the geometrical complexity, whilst mechanical compatibility is maintained. The resulting set of artificial volume elements is referred to as statistically similar volume elements (SSVEs). For the following descriptions only inclusion-matrix microstructures with two phases are considered to keep the explanations rather simple. This is, however, not a restriction and in principle, also materials with more phases can be analyzed.

5.1.1 Definition of a Functional for Morphology Differences

To measure the differences between two arbitrary volume elements VE_1 and VE_2, a distance functional is established as

$$\mathcal{L} = \sum_{L=1}^{N_\mathrm{L}} \omega_{(L)} \overset{\star}{\mathcal{L}}_{(L)} \quad \text{with} \quad \overset{\star}{\mathcal{L}}_{(L)} = \left(\mathcal{P}_{(L)}^{\mathrm{VE}_1} - \mathcal{P}_{(L)}^{\mathrm{VE}_2} \right)^2 . \tag{5.1}$$

Therein, $\mathcal{P}$ represents suitable statistical descriptors to characterize the microstructure morphology. Such descriptors are thoroughly introduced in the work of Torquato [153], the specific descriptors used for the DP-steel are also explained in Sec. 5.1.2. A collection of N_L distinct statistical descriptors $\mathcal{P}$ is necessary to accurately describe the morphology of the material. In addition, it is necessary to use not just scalar measures, but also higher order descriptors in order to accurately capture all aspects of the morphology. Usually, the microstructure data of actual materials is given as discrete voxel data sets in three dimensions or pixel data sets in two dimensions. Consequently, the statistical measures will also be discrete. The brackets in Eq. (5.1) denote a suitable calculation of the differences between discrete representations of the generalized notion of $\mathcal{P}$, which can be of scalar and higher order. The two volume elements, VE_1 and VE_2, may have varying voxel/pixel resolutions and absolute physical sizes. To achieve this objective, one can either use relative scalar descriptors like the phase volume fraction, or in the case of higher order descriptors such as the spectral density, $\mathcal{P}^{\mathrm{VE}_1}$ and $\mathcal{P}^{\mathrm{VE}_2}$ can be scaled to the same resolution before assessing the difference. The weighting factors $\omega_{(L)}$ are responsible for determining the influence of each individual descriptor, hence playing a crucial role in the selection of the statistical description. Both the selection of statistical descriptors and the determination of weighting factors must be done in a manner that allows for an accurate depiction of the material's morphology.

5.1.2 Statistical Descriptors for Microstructure Morphology

In the definition of the distance functional in Eq. (5.1), higher order statistical descriptors are used. This section will discuss selected descriptors, which are suitable for the characterization of a DP-steel, whilst other materials may require different descriptors, such as in the work of Sasagawa et al. [124], where fiber composites are investigated. The n-point probability function is a useful measure for describing random microstructures. It quantifies the likelihood that n points, with specific relative orientation and distance from each other, belong to the same phase of the microstructure. The first-order function denotes the likelihood that a specific location belongs to a particular phase, such as the inclusion phase. It is equivalent to the proportion of the volume occupied by that phase. The two-point probability function quantifies the likelihood that two points, separated by a specific distance and with a particular relative orientation, belong to the same phase. In the case of a discrete set, where the microstructure is represented in terms of voxel data, a finite number of evaluations of the two-point probability has to be computed, each of which is linked to a distinct relative distance and orientation. This results in four times the amount of voxel computations of the

two-point probability function, cf. also Balzani et al. [3]. As the order of the n-point probability function grows, the number of required evaluations also increases, resulting in a rapid increase in computational demand. Therefore, in practice only a limited number of statistical descriptors can be evaluated, even if a better description could be achieved by utilizing higher order functions. A close relative of the two-point probability function is the spectral density. Alternatively, the lineal-path function may be used, which calculates the likelihood that a full line segment, with a specific relative orientation and distance, is contained entirely within a specific phase. In Balzani et al. [4] the combination of spectral density, volume fraction and lineal-path function was found as accurate statistical characterization of dual-phase steels. Therefore, in this work these three statistical descriptors are investigated.

The volume fraction $\mathcal{P}_{(1)} = V^P/V$ is the ratio of the volume V^P of the martensite inclusion phases P with respect to the total volume V. The spectral density is given for voxel-based representations by

$$\mathcal{P}_{(2)}(u,v,w) := \frac{1}{2\pi\, N} \left|\mathcal{F}(u,v,w)\right|^2 , \tag{5.2}$$

in which the number of voxels is denoted by N, the operator $|(\bullet)|$ represents the conjugate complex of $(\bullet)$ and $\mathcal{F}$ the Fourier-transform. The latter can be computed by

$$\mathcal{F}(u,v,w) = \sum_{p=0}^{N_x-1} \sum_{q=0}^{N_y-1} \sum_{r=0}^{N_z-1} \exp\left(\frac{2\,i\,\pi\,u\,p}{N_x}\right) \exp\left(\frac{2\,i\,\pi\,v\,q}{N_y}\right) \exp\left(\frac{2\,i\,\pi\,w\,r}{N_z}\right) \chi_{(\mathrm{SD})}(p,q,r)\,, \tag{5.3}$$

wherein N_x, N_y, and N_z denote the spatial number of voxels, respectively. The integers u, v, and w denote the positions of the voxels, such that each number in u, v, and w corresponds to a physical position $\boldsymbol{x}(u,v,w)$ at the center of the voxel. The indicator function in (5.3) is defined as

$$\chi_{(\mathrm{SD})}(p,q,r) = \begin{cases} 1, & \text{if } \boldsymbol{x}(p,q,r) \in \mathcal{D}, \\ 0, & \text{otherwise}\,, \end{cases} \tag{5.4}$$

with $\mathcal{D}$ denoting the domain of the inclusion phase P. The spectral density may be preferred over the computation of the two-point-probability function, since there is a number of efficient frameworks to compute the Fourier transform efficiently. The lineal-path function requires the definition of complete line segments $\overrightarrow{\boldsymbol{z}} := \overrightarrow{\boldsymbol{x}_1\boldsymbol{x}_2}$ between two points $\boldsymbol{x}_1$ and $\boldsymbol{x}_2$. Based on these line segments, an indicator function is defined as

$$\chi_{(\mathrm{LP})}(p,q,r,u,v,w) = \begin{cases} 1, & \text{if } \overrightarrow{\boldsymbol{z}}(p,q,r,u,v,w) \in \mathcal{D}, \\ 0, & \text{otherwise}\,, \end{cases} \tag{5.5}$$

where the points of the line segment are connected to the voxels by $\boldsymbol{x}_1(p,q,r)$ and $\boldsymbol{x}_2 = \boldsymbol{x}_1 + \boldsymbol{y}(u,v,w)$. The integers $p = 0...N_x - 1$, $q = 0...N_y - 1$ and $r = 0...N_z - 1$ represent indices of individual voxels. The integers u, v, and w are associated with the relative position vector $\boldsymbol{y}$, which captures the relative orientation and distance between the two points defining the line segment. Based on these definitions, the lineal-path function can be computed by

$$\mathcal{P}_{(3)}(u,v,w) = \frac{1}{N_x N_y N_z} \sum_{p=0}^{N_x-1} \sum_{q=0}^{N_y-1} \sum_{r=0}^{N_z-1} \chi_{(\mathrm{LP})}(p,q,r,u,v,w)\,. \tag{5.6}$$

With the definition of these three statistical descriptors, the difference between two microstructure volume elements can be computed by

$$\mathcal{L}_{(\mathcal{S})} = \omega_{(1)}\mathcal{L}_{(1)} + \omega_{(2)}\mathcal{L}_{(2)} + \omega_{(3)}\mathcal{L}_{(3)}. \tag{5.7}$$

The weighting factors are chosen according to Balzani et al. [4], wherein also further important steps such as an appropriate rebinning of the voxel data in the space of statistical measures is discussed to compare microstructures of different sizes.

5.1.3 Reference Microstructure Data

In order to quantify the variation of microstructure morphology variation by means of the functional introduced in Eq. (5.1), two things are missing. First, measurements of the microstructure morphology need to be obtained, which are large enough to contain sufficient amount of information on the inherent inner variability of the microstructure. This data will be referenced to as reference microstructure data including morphology variation (RMDV), and can be compromised of N_{S} many different, continuous sets of microstructure measurements, which were taken in different locations of the material specimen. The second missing piece for the distance functional is a reference microstructure, against which further sections of the microstructure are compared. In this sense, the reference microstructure should represent the "average" morphology of the microstructure, such that the distance functional quantifies the deviation of the chosen second microstructure from the "average". Therefore, the RVE is a meaningful choice for such a dataset. Although there is extensive discussion on the literature on the definition and selection of an RVE, see also Sec. 3.4.1, it is commonly emphasized that the selection of the representative volume element should be done in a way that any changes in size or position do not have a substantial impact on the statistical characteristics of its microstructure morphology. Now, to ensure all these requirements, an RVE of substantial size has to be chosen, which implies, that the available microstructure measurements to identify the RVE from have to be dimensions larger, which is often simply not possible. Therefore, the requirements on the RVE in context of this work are slightly weakened. For this purpose, the RVE is identified as subsection from the RMDV be utilizing the functional in Eq. (5.1). If the RMDV is utilized as fixed VE_1 and a smaller subsection therefrom as VE_2, the RVE can be identified from the RMDV by means of minimization of the functional, i.e. by reducing the difference in terms of the chosen statistical descriptors. The required dimensions of the RVE are established in such a way, that no larger RVE exists that would result in a noteworthy enhancement in statistical resemblance to the RMDV. This approach may conflict with conventional definitions of an RVE, since here the position of the RVE within the larger microstructure measurement becomes crucial. And indeed, potentially the microstructure identified as RVE may not represent an RVE in all demands, but the location of the selected subsection is chosen such that the highest possible level of statistical similarity is achieved. The choice may not be unique, which is however not important in this situation, as long as the RVE exhibits "average" morphological characteristics. An RVE generated in this manner serves as an appropriate reference microstructure for assessing statistical variations in other microstructure subsections of equal dimensions. It is important to note that, in practical applications, the analysis of different sizes and forms of a material's microstructure is limited due to measuring constraints. Hence, the RMDV is of utmost importance and should be selected to be as extensive as feasible.

5.1.4 Quantification of Microstructure Morphology Variation

Given a suitable Representative Volume Element as a reference microstructure, the statistical difference between an arbitrary volume element $\mathrm{VE}_2(\overline{\boldsymbol{X}})$ at a macroscopic position $\overline{\boldsymbol{X}}$ and the RVE can be computed, i.e., the evaluation of $\mathcal{L}(\overline{\boldsymbol{X}})$ quantifies the extent to which the microstructure morphology at $\overline{\boldsymbol{X}}$ deviates from the average. The frequency distribution $\mathbb{D}[\mathcal{L}]$ of $\mathcal{L}$ is computed by varying the locations $\overline{\boldsymbol{X}}$ of the volume element $\mathrm{VE}_2(\overline{\boldsymbol{X}})$ across all feasible positions. The frequency distribution represents the variation of the microstructure morphology of the material in relation to the deviation from the "mean", which is represented by the RVE. Therefore, the description of the microstructure variation is simplified to a single scalar value. Typically, only two-dimensional measurements are used to measure the RMDV, as three-dimensional measurements are too costly and therefore, the microstructure variation is mostly assessed by two dimensional data only. For practical reasons, the RVE may also

be defined to be the RMDV, and the individual volume elements ($\mathrm{VE}_2(\overline{\boldsymbol{X}})$) as subsections of the RMDV. This avoids the necessity of constructing a suitable RVE, and the computation of microstructure variation relies on purely two-dimensional computations. The definition of the least squares distance functional for the volume element at location $\overline{\boldsymbol{X}}$ is then given by

$$\mathcal{L}^{\mathrm{real}}(\overline{\boldsymbol{X}}) = \sum_{L=1}^{N_{\mathrm{L}}} \omega_{(L)} \overset{\star}{\mathcal{L}}_{(L)} \quad \text{with} \quad \overset{\star}{\mathcal{L}}_{(L)} = \left(\mathcal{P}_{(L)}^{\mathrm{RVE}} - \mathcal{P}_{(L)}^{\mathrm{VE}}(\overline{\boldsymbol{X}}) \right)^2 . \tag{5.8}$$

By varying the positions $\overline{\boldsymbol{X}}$ of the volume element over all $N_{\overline{\mathrm{x}}}$ possible positions $\overline{\boldsymbol{X}}_j$, $j = 1...N_{\overline{\mathrm{x}}}$, the spatial frequency distribution of $\mathcal{L}^{\mathrm{real}}$ of the RMDV $\mathcal{D}^{\mathrm{real}} := \mathbb{D}[\mathcal{L}^{\mathrm{real}}(\mathrm{VE}(\overline{\boldsymbol{X}}_j))]$ is computed. By means of this frequency distribution the variation in the real microstructure morphology can be accurately described. Certainly, the size of the RVE as comparative microstructure does influence the result of the frequency distribution. However, as this size is specifically determined due to the procedure described in Sec. 5.1.3, an unbiased procedure is obtained.

5.1.5 Construction of Artificial Microstructures Reflecting the Variation in Morphology

The variation of the microstructure variation quantified in Sec. 5.1.4 is then used to construct a set of artificial volume elements, the SSVEs. These SSVEs are designed to have a statistical distribution of $\mathcal{L}$ that matches the distribution of the real microstructure. Unlike subsections of the real microstructure, the SSVEs have the potential to enable a more effective numerical simulation, provided that their complexity in terms of microstructure morphology is as simple as possible. On the other hand, it is crucial that their complexity is sufficient to guarantee statistical resemblance to the actual microstructure.

Distance Functional for SSVEs A single SSVE requires an suitable parameterization to be constructed. This parameterization should a priori enable the construction of morphologies with reduced complexity to facilitate efficient numerical discretization. The morphology of a single SSVE i can be parameterized using a generalized column matrix $\boldsymbol{\gamma}_i$, which includes all the parameters for this particular SSVE. Using this general parameterization, the distance function of Eq. (5.1) can be modified to evaluate the deviation of a single SSVE to the reference RVE by substituting VE_1 by an RVE and VE_2 by the SSVE, such that

$$\mathcal{L}^{\mathrm{SSVE}}(\boldsymbol{\gamma}) = \sum_{L=1}^{N_{\mathrm{L}}} \omega_{(L)} \overset{\star}{\mathcal{L}}_{(L)} \quad \text{with} \quad \overset{\star}{\mathcal{L}}_{(L)}(\boldsymbol{\gamma}) = \left(\mathcal{P}_{(L)}^{\mathrm{RVE}} - \mathcal{P}_{(L)}^{\mathrm{SSVE}}(\boldsymbol{\gamma}) \right)^2 . \tag{5.9}$$

It is important to understand that the RVE utilized in this context does not need to be identical to the one mentioned in Eq. (5.8) due to the property of representativeness. In fact, since in Eq. (5.9) there is no requirement for information regarding the variation of the actual material, it is beneficial to use a three-dimensional microstructure of smaller size as the representative volume element. This allows for a direct comparison with three-dimensional SSVEs. In the majority of situations, a discrete voxel dataset may be created using the SSVE parameterization. As a result, the statistical descriptors derived from this dataset will also be discrete.

Construction of a Set of SSVEs An entire set of SSVEs can be defined by summarizing all parameters for the N^{SSVE} SSVEs in a single matrix by $\boldsymbol{\Gamma} = [\boldsymbol{\gamma}_1, \boldsymbol{\gamma}_2, ...\boldsymbol{\gamma}_{N^{\mathrm{SSVE}}}]$. By calculating $\mathcal{L}^{\mathrm{SSVE}}$ for this set $\boldsymbol{\Gamma}$ of different SSVEs, the resulting frequency distribution can be computed by $\mathcal{D}^{\mathrm{SSVE}}(\boldsymbol{\Gamma}) := \mathbb{D}[\mathcal{L}^{\mathrm{SSVE}}(\boldsymbol{\gamma}_i)]$ with $\boldsymbol{\gamma}_i \in \boldsymbol{\Gamma}$. This frequency distribution represents

the variation of the microstructure morphology of the set of SSVEs based on their deviation from the RVE. In order to find the specific set $\mathbf{\Gamma}^{\text{opt}}$ of SSVEs that closely resembles the microstructure variation $\mathcal{D}^{\text{real}}$ of the real material (calculated using the method described in Sec. 5.1.4), an objective functional $\mathcal{E}$ is minimized. This functional measures the differences between the two distributions and is defined by

$$\mathbf{\Gamma}^{\text{opt}} = \text{argmin}\left[\mathcal{E}(\mathbf{\Gamma})\right] \quad \text{with} \quad \mathcal{E}(\mathbf{\Gamma}) := \left(\mathcal{D}^{\text{real}} - \mathcal{D}^{\text{SSVE}}(\mathbf{\Gamma})\right)^2 . \tag{5.10}$$

The use of parenthesis is a shorthand for an appropriate calculation of the differences between the discrete representations of the distributions $\mathcal{L}$. Due to the high cost of minimization, it is more efficient to acquire an accurate estimate of $\mathbf{\Gamma}^{\text{opt}}$ by initially calculating a set of SSVEs and subsequently choosing a suitable subset therefrom using the Metropolis-Hastings algorithm. It should be noted, that the definition of the distance functional $\mathcal{L}$ is similar by to the one described in Balzani et al. [4]. Therein, a statistically similar representative volume element (SSRVE) is obtained by minimizing the value of $\mathcal{L}$. In contrast to the SSVEs, which are constructed following the real materials morphology in certain bounds, the SSRVE is the artificial microstructure, which minimizes the statistical difference to the real material and is therefore representative of the material. In fact, a large collection of SSVEs can be obtained from the optimization of the SSRVE by saving all realizations $\boldsymbol{\gamma}_i$ during the optimization. Then, only the realizations that together provide the required distribution need to be selected.

5.1.6 Multilevel Monte Carlo Method

Using the SSVEs derived by means of the method described in Sec. 5.1.5, a full Monte Carlo simulation to calculate the effective macroscopic quantity of interest may be to costly in terms of computer resources. An effective approach to decrease the computing costs is the implementation of the multilevel Monte Carlo (MLMC) method, as proposed by Heinrich [62] and Giles [51]. Multilevel Monte Carlo approaches utilize multiple levels, denoted by l, which differ by the approximation accuracy of the problem. The coarser levels, which employ simpler discretizations and/or integration techniques, are utilized to estimate the statistical distribution of the quantity of interest. The imprecise statistical distributions that arise from the low quality of approximation are subsequently improved at the finer levels, for which decreasingly smaller number of samples are evaluated. Because it is challenging to acquire various geometric representations of a sample, the utilization of MLMC methods to measure the uncertainty of macroscopic material properties related to microstructure via computational homogenization is difficult. However, since the process of constructing SSVEs based on Sec. 5.1.5 is applicable to voxel resolutions of any kind, various geometric approximations in terms of the finite cell method can be incorporated. Therefore, rather than examining various levels of discretization, as commonly suggested in the literature, the attention is directed towards different levels of integration accuracy in order to establish the specific levels of the MLMC. To achieve a large reduction in processing time, it is important to maintain a somewhat accurate yet efficient discretization at all levels. It is important to observe that a SSVE i is the same on all levels, i.e. the parameterization of the microstructure morphology is the same and the sole variation lies in the resolution of the generated voxel data.

When the specific levels are selected, it is crucial to choose approximations that have distinct differences in their accuracy. Otherwise, these levels will not contribute to an efficient correction. Hence, a numerical measure for the discrepancy in precision between a coarser level and a more refined level can be expressed as

$$\varepsilon_l = ||P_{l-1} - P_l||^2 \quad \text{with} \quad l = 1...L, \tag{5.11}$$

where l represents the level index ranging from 1 to L and P denotes to the mechanical variable of interest, here a macroscopic quantity. Subsequently, the levels are selected in a manner that ensures ε_l is greater than a predefined difference. The highest level of accuracy, denoted as L, can be achieved by a classical finite element convergence analysis. For this analysis, it is practical to simply analyze one microstructure, for which, to achieve maximum representativeness, the Statistically Similar Representative Volume Element can be employed.

The primary objective in the MLMC approach is to determine the most optimal number of SSVE evaluations for each level. In this context, "optimal" refers to a balanced compromise between the least amount of computational time and the highest level of accuracy in the calculated distribution of P. To ensure that sufficient accuracy is achieved, this problem may be formulated as a linear optimization problem. The optimization problem is defined as the minimization of the computational effort, i.e. the cost function

$$e(N_0, N_1, ...N_L) = \sum_{l=0}^{L} N_l \left(\hat{d}_l/\hat{d}_0\right)^3, \tag{5.12}$$

where $\hat{d}_l$ and $\hat{d}_0$ denote the characteristic approximation effort per physical dimension for each level; N_l denotes the number of SSVEs considered at level l. In this context, the various levels are categorized based on their levels of integration accuracy, specifically the quantity of subcells. As the subcells are created using voxel data, this implies that each level considers a different voxel size, resulting in varying accuracy in approximating the microstructure morphology. Thus, $\hat{d}$ represents the actual length of a voxel. Additionally, a constraint is necessary for the optimization problem to ensure that the statistical distribution of P achieves a certain level of precision. Since the multilevel Monte Carlo method is still a Monte Carlo method, the approximation accuracy can be assessed by means of the variation of the estimated mean as explained in Sec. 2.4. Due to the central limit theorem, the estimated mean of P of all SSVEs on level l, i.e. $\mathbb{E}[P] = \frac{1}{N_l}\sum_{i=1}^{N_l} P_i$, is normally distributed for a varying number of samples N_l. Hence, a suitable accuracy of P can be assumed, if the variance of the estimated mean is smaller than a previously defined threshold, leading to a constraint formulation of

$$\mathbb{V}^{\mathrm{N}_l}[\mathbb{E}[P]]\frac{1}{N_l}\mathbb{V}[P] < tol, \tag{5.13}$$

wherein $\mathbb{V}[P] = \frac{1}{N_l}\sum_{i=1}^{N_l}(P_i - \mathbb{E}[P])^2$ represents the variance of P. Since multiple levels are employed in the MLMC, the variance is computed by a so-called telescopic sum, in which the variance computed for the coarsest level is refined by corrections contributed from finer levels by $\mathbb{V}^{\mathrm{ML}}[P] = \mathbb{V}[P_0] + \sum_{l=1}^{L}\mathbb{V}\left[P_l - P_{l-1}\right]$, wherein the last term indicates the corrections. Then, the variance of the expectation in Eq. (5.13) is obtained by

$$\mathbb{V}^{\mathrm{N}_l}\left[\mathbb{E}[P]\right] = \frac{1}{N_0}\mathbb{V}[P_0] + \sum_{l=1}^{L}\frac{1}{N_l}\mathbb{V}\left[P_l - P_{l-1}\right] \tag{5.14}$$

for the multilevel Monte Carlo approach. In consquence, the entire optimization problem can be summarized by

$$e := \sum_{l=0}^{L} N_l \left(\hat{d}_l/\hat{d}_0\right)^3 \rightarrow \min_{(N_0,N_1,...N_L)} \quad \text{with} \quad \frac{1}{N_0}\mathbb{V}[P_0] + \sum_{l=1}^{L}\frac{1}{N_l}\mathbb{V}\left[P_l - P_{l-1}\right] < tol. \tag{5.15}$$

The solution of this optimization problem is the optimal decomposition for the MLMC approach, allowing for an efficient computation of the distribution of P.

Given that the cost function is directly proportional to the number of samples N_l, the optimal solution meeting the constraint may be found simultaneously with the SSVE simulations. For

this purpose, the quantity of samples at the least detailed level is gradually increased by performing the matching SSVE simulations until the adjustment in relation to $\mathbb{V}^{\mathrm{N}_l}[\mathbb{E}[P]]$ become smaller than a given threshold. Then, SSVEs are iteratively simulated at increasingly finer levels until the adjustment exceeds the specified tolerance again. This suggests that conducting more computations at a less detailed level may result in more adjustments, thus requiring additional SSVE simulations at that level until the desired degree of accuracy is achieved once again. This process is repeated until no additional adjustment can be achieved based on these two levels. Subsequently, the procedure is expanded to the subsequent, more detailed level. If more improvements cannot be achieved by raising the sample size at the highest level and the requirement remains unsatisfied, then either the tolerance for the constraint is too narrow or the highest level lacks accuracy. To circumvent the need for implementing this approach, one can incorporate the constraint as a weighted term in the cost function. Specifically, $e \Leftarrow e + \omega(\mathbb{V}^{\mathrm{N}_l}[\mathbb{E}[P]] - tol)$, and employ a black-box optimizer. In this scenario, the variances $\mathbb{V}[(\bullet)]$ in Eq. (5.14) might be set to specific values based on SSVE simulations that were conducted before. The optimizer yields values $(N_0, N_1, ...N_L)$ which can be used as an estimator for determining the optimal distribution of additional SSVE runs for each level. This work utilizes the latter scheme.

5.2 Numerical Example: Application to a Dual-Phase Steel Microstructure

The proposed technique is illustrated in conjunction with the modified approach for the subcell decomposition on a DP steel microstructure. The study focuses solely on the variation of the microstructure morphology, whereas the material properties of the individual phases are considered fixed values at the microscale. Therefore, the distributions derived may not accurately reflect the variability of the actual material behavior, as additional uncertainties, such as those in the parameters of the constitutive material laws of the phases, are not taken into account. Moreover, obtaining additional authentic microstructure data may be necessary to accurately represent the change in microstructure. Furthermore, it would be necessary to conduct experimental validation using a range of mechanical tests in order to ascertain the extent of variance in the properties of the actual material. Hence, this section should be seen as demonstrative example of how the microstructure variation strategy can be quantified.

Initially, it is necessary to choose suitable statistical measurements to accurately depict the shape and structure of the steel. As already mentioned, in Balzani et al. [4] a SSRVE was identified for the same material. Therein, the statistical description provided in Sec. 5.1.2, including the volume fraction, spectral density, and lineal-path function, along with the respective weighting factors of 1.0 for the spectral density and volume fraction, and 1000.0 for the linear-path function, was found to be suitable. The SSRVEs were acquired by executing the complete construction sequence using several sets of descriptors and weighting factors.

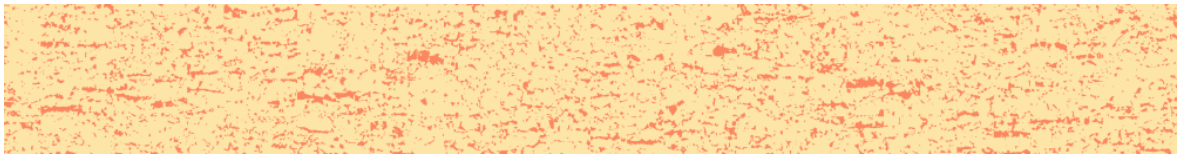

Figure 5.2: Visualization of the large two-dimensional microstructure scan of DP-steel from [19] with a size of 16 mm by 2 mm with ferrite matrix colored in light brown and the martensite inclusions in orange. Taken from Miska and Balzani [93], originally obtained from [19].

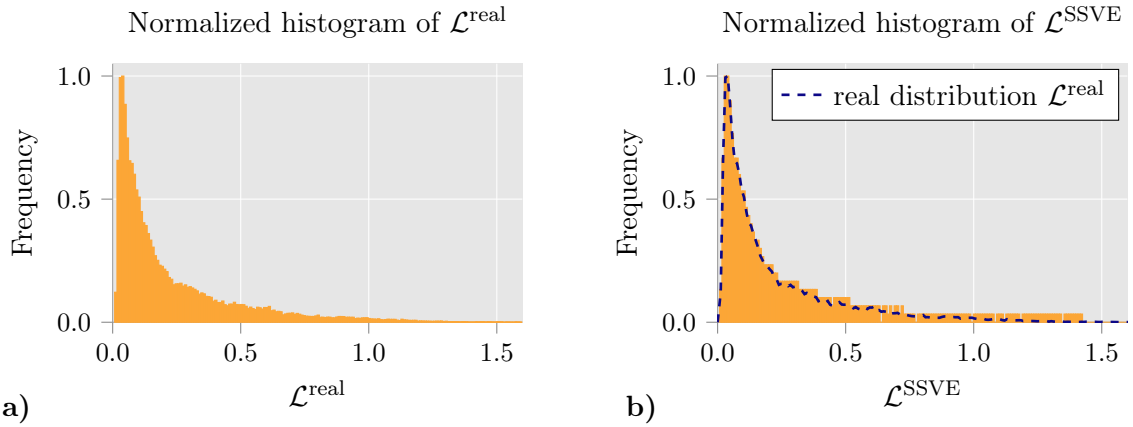

Figure 5.3: Distribution of **a)** $\mathcal{L}^{\text{real}}$ obtained from the larger two-dimensional microstructure scan of DP-steel and **b)** $\mathcal{L}^{\text{SSVE}}$ of the microstructure samples selected for the full Monte Carlo simulation. Taken from Miska and Balzani [93].

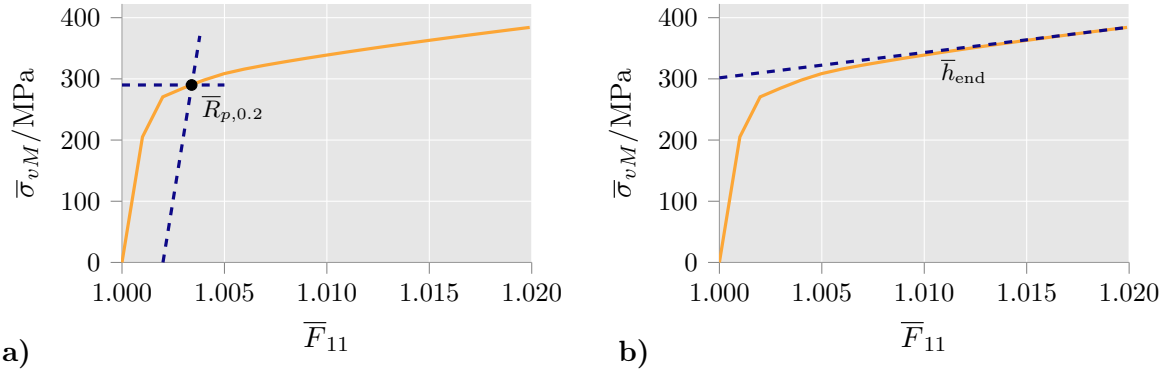

Figure 5.4: Analyzed macroscopic quantities: **a)** effective yield stress $\overline{R}_{p,0.2}$ and **b)** hardening modulus at the end of the prescribed load $\overline{h}_{\text{end}}$. Taken from Miska and Balzani [93].

The SSRVE that exhibited the highest level of mechanical compatibility is assumed to indicate an optimal selection of the statistical description. This selection was a component of the external optimization issue outlined in [4] and thus, the aforementioned selection of descriptors and weighting variables is used here as well. The microstructure data, which includes comprehensive information regarding the variance in morphology known as the RMDV, originates from [19] and was acquired by electron backscatter diffraction (BSD), cf. Fig. 5.2 for an illustration of the microstructure.

The dimensions of each volume element (VE) in Eq. (5.8) are defined as 15.9 µm by 16 µm. This size was determined to be appropriate for a representative volume element of the specific steel studied in Brands et al. [19]. The distribution $\mathcal{D}^{\text{real}}$ for the DP steel, which is illustrated in Fig. 5.3a), is obtained by evaluating the distance functional for all feasible volume elements within the RMDV. It is evident that the majority of the subdomains bear a strong resemblance to the overall dataset, while they are not entirely identical. Therefore, the maximum frequency is not anticipated to occur at $\mathcal{L} = 0$, but is instead observed in close proximity to zero. As $\mathcal{L}$ increases, the frequency declines, indicating that subdomains with greater deviation from the overall data are less probable.

Artificial three-dimensional microstructures are created in order to obtain the set $\mathbf{\Gamma}^{\text{opt}}$ of SSVEs. Previous studies by [4] and [126] have identified a SSRVE with three ellipsoidal inclusions as an appropriate artificial microstructure for DP steel. Thus, in this study also three ellipsoids are used as a parametrization for the inclusion phase. An ellipsoid is defined

Table 5.1: Material parameters used for the ferritic and martensitic phases.

	E (MPa)	ν (-)	y_0 (MPa)	y_∞ (MPa)	α (-)	h (-)
Ferrite	206,000.0	0.3	260.0	580.0	9.0	70.0
Martensite	206,000.0	0.3	1000.0	2750.0	35.0	10.0

by its semi-axes in the directions $\boldsymbol{v}_j$, $j = 1, 2, 3$, the related radii in the directions of the semi-axes r_j, and the center of the ellipsoid $\boldsymbol{x}_c$. Therefore, any point $\boldsymbol{x}$ that lies within the ellipsoid must satisfy

$$\sum_{j=1}^{3} \left(\frac{|\boldsymbol{v}_j \cdot (\boldsymbol{x} - \boldsymbol{x}_c)|}{r_j} \right)^2 \leq 1. \tag{5.16}$$

The orientation vectors $\boldsymbol{v}_j$ can be defined to align with a local orthogonal coordinate system that is rotated from the origin by the angles ϑ, φ and θ. The vector $\boldsymbol{\gamma}_i^k$ for an ellipsoid (k) of SSVE i is thus,

$$\boldsymbol{\gamma}_i^{(k)} = \left[x_c^{(k)}, y_c^{(k)}, z_c^{(k)}, \vartheta^{(k)}, \varphi^{(k)}, \theta^{(k)}, r_1^{(k)}, r_2^{(k)}, r_3^{(k)} \right]_i^{\mathrm{T}}, \tag{5.17}$$

resulting in the parameter vector $\boldsymbol{\gamma}_i = \left[\boldsymbol{\gamma}_i^{(1)\mathrm{T}}, \boldsymbol{\gamma}_i^{(2)\mathrm{T}}, \boldsymbol{\gamma}_i^{(3)\mathrm{T}} \right]^{\mathrm{T}}$ of the SSVE i. Given the periodic nature of the SSVEs, one ellipsoid can be fixed at the center of the SSVE. As a result, the center coordinates of this ellipsoid are not included in $\boldsymbol{\gamma}_i$, and the degrees of freedom are decreased by three. This guarantees that a direct translation of the inclusion phase is not regarded as a novel SSVE.

In order to generate the set of SSVEs that best correspond to the actual variation in microstructure, it is necessary to identify an RVE. In this context, a three-dimensional EBSD-measurement from [4], which has been determined to be an appropriate (RVE)for dual-phase steel, is used here. In order to acquire a highly accurate estimation of the optimal set $\boldsymbol{\Gamma}^{\mathrm{opt}}$ as defined by Eq. (5.10), the following steps are necessary:

1. The optimally representative SSRVE is determined by minimizing a distance function, as described in Balzani et al. [4]. This distance function is defined in Eq. (5.1), where VE_1 is substituted with the RVE and VE_2 is substituted with the SSRVE. For the optimization, the differential evolution algorithm of Storn and Price [144] implemented in the form of the mystic framework (cf. McKerns et al. [88]) with a population size of 1000, a mutation factor of 0.8 and a crossover constant of 0.9 is used. The ellipsoidal inclusion parameters are utilized to create a voxel representation of the microstructure by evaluating whether each voxel satisfies Eq. (5.16). The voxel representation is necessary to compute the deviation between the SSRVE and the RVE in terms of the discrete statistical measures. Since the construction of the microstructure is based on the results of [4], a voxel set measuring 45x42x43 voxels with a total size of 4.5µm x 4.2µm x 4.3µm is employed.

2. During the optimization process, numerous microstructures are evaluated. As a result, the parameterizations of those microstructures that produce a value of $\mathcal{L}^{\mathrm{SSVE}}$ within the statistical similarity bounds as identified from the RMDV are stored.

3. The Metropolis-Hastings algorithm is used to pick the specific set of SSVEs $\boldsymbol{\Gamma}^{\mathrm{opt}}$ from these volume elements. This algorithm produces a distribution of statistical similarity that is similar to the real material, as shown in Fig. 5.3b).

The resulting set now serves as the initial reference for the mechanical analysis. Every SSVE undergoes a macroscopic uniaxial tensile test, which is computed according to the method outlined in Sec. 3.4 using the aforementioned user implementation in FEAP8.2. The analyzed macroscopic quantities are the effective macroscopic yield stress $\overline{R}_{p,0.2}$ (see Fig. 5.4a)) and the macroscopic hardening modulus at the end of the prescribed loading $\overline{h}_{\text{end}}$ (see Fig. 5.4b)). The material model used to describe the ferrite and martensite phases of DP steel is a J_2 elasto-plasticity formulation for finite strains with isotropic exponential hardening, as outlined by Simo [139]. The implementation was carried out by Klinkel [75], and the parameters used were obtained from Balzani et al. [4], see Tab. 5.1. It should be noted that these parameters are constant and not included in the uncertainty analysis. The primary emphasis lies on the variation of the microstructure's morphology, excluding any consideration of the microstructural material properties.

5.2.1 Full Monte Carlo Approach

Initially, a full Monte Carlo simulation is investigated. All 468 microstructure samples that were chosen for the SSVE set $\mathbf{\Gamma}^{\text{opt}}$, as previously explained, are being considered. Each microstructure being studied is approximated using 50 voxels along each edge to generate subcells. The mean and variance values for the initial yield stress and strain hardening modulus distributions resulting from the 468 computed SSVEs are as follows: $\mu[\overline{R}_{p,0.2}] = 289.4$ MPa, $\sigma^2[\overline{R}_{p,0.2}] = 26.0$ MPa^2, $\mu[\overline{h}_{\text{end}}] = 4126.4$ MPa, and $\sigma^2[\overline{h}_{\text{end}}] = 107709.0$ MPa^2. Due to the limited quantity of SSVEs for a complete Monte Carlo computation, the obtained data may not be sufficient to reliably fit a precise PDF to the data. However, the findings may serve as an approximation of the bounds of the macroscopic material properties in question, e.g. expressed in terms of an interval or a fuzzy number. Nevertheless, if the material properties derived from this study were to be expressed in probabilistic terms, a larger number of samples would be necessary to provide a stable solution and a more smooth histogram that can be matched with a suitable probability density function.

5.2.2 Application of the Multilevel Monte Carlo Method

Due to the high cost of simulating a large number of SSVEs, the multilevel Monte Carlo method described in Sec. 5.1.6 is applied to reduce the required numerical effort. Prior to determining the levels, it is necessary to evaluate Eq. (5.11). The variable of interest is the mean value of the homogenized stress at the highest level of strain, calculated from 10 simulations, denoted as P_{11}. Three levels are evaluated, with the coarsest approximation of the microstructure morphology consisting of 10 voxels along one edge. This is followed by 25 and 50 voxels per edge for the subsequent levels. To verify that there is no substantial difference and to confirm that 50 voxels is a reasonable finest level, the situation with 50 voxels was compared to the same setting with 100 voxels. At each level, the number of voxels increases or decreases by a factor of around 2. This aligns with recommendations in the literature, where this factor is advised for adjusting the level of discretization effort, as discussed by Giles [51]. A different choice of levels would be possible, but will also lead to

Table 5.2: Resulting approximation error ε.

level l	$\lvert\overline{P}_{11,l-1} - \overline{P}_{11,l}\rvert$	ε_l
1 (25 voxels/edge)	2.47511 MPa	6.1261 MPa^2
2 (50 voxels/edge)	0.82994 MPa	0.6888 MPa^2
3 (100 voxels/edge)	0.29141 MPa	0.0850 MPa^2

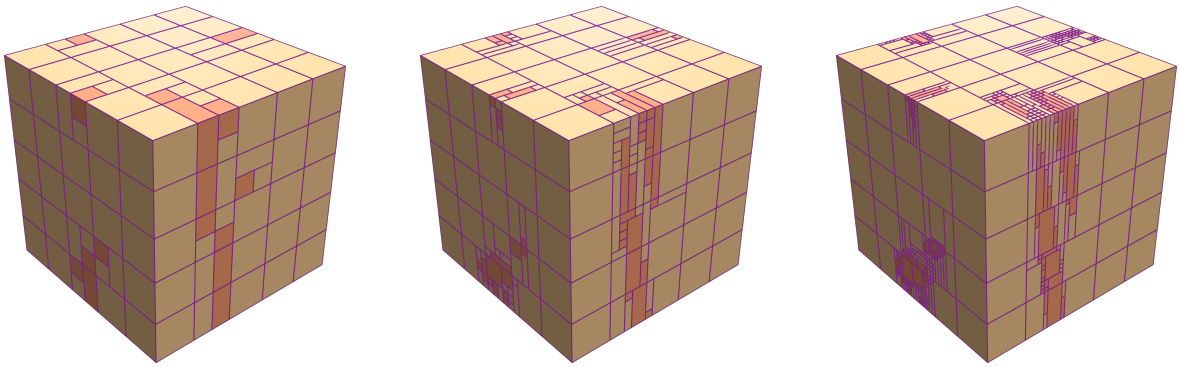

a) 213 subcells **b)** 694 subcells **c)** 2193 subcells

Figure 5.5: Comparison of the different geometry approximations using subcells on the levels with **a)** 10 voxels, **b)** 25 voxels and **c)** 50 voxels along one edge of the sample. Taken from Miska and Balzani [93].

higher computational costs for the same approximation quality. In regard to the definition of the levels here, a higher number of voxel lead to a better integration in terms of the finite cell method, see 4.1.

In Tab. 5.2 the approximation errors obtained according to Eq. (5.11) between two consecutive levels are displayed. Given the sufficiently significant improvement observed between the levels, it is appropriate to use 10, 25, and 50 voxels for the morphology approximation. The increase in the degree of accuracy in the approximation between the levels with 50 and 100 voxels along one edge of the SSVEs is quite insignificant, which confirms the selection of 50 voxels along one edge as the finest level. The three levels being discussed are illustrated for a randomly chosen microstructure in Fig. 5.5, with the least detailed representation shown on the left in subfigure a, and the most detailed representation shown on the right in subfigure c. The improvement in the approximation quality of the inclusion shapes is evident. As stated in Sec. 5.1.6, the optimization problem in the multilevel Monte Carlo approach (refer to Eq. (5.15)) can be resolved using a black-box optimizer. This will yield an estimate for the number of SSVEs on each level, assuming fixed variances. In this case, the differential evolution optimizer from the mystic-framework [88] is employed. The population size was set to 100, while the mutation factor and crossover constant were maintained at 0.8 and 0.9, respectively. A starting set of SSVEs is computed at the chosen levels. The samples are chosen using the Metropolis algorithm, which ensures that the morphological variance of the samples matches the actual variation. Subsequently, these SSVEs undergo evaluation in the simulated macroscopic tension test to acquire the desired macroscopic material properties. Based on the obtained data, Eq. (5.14) is computed, allowing for the solution of the minimization problem stated in Eq. (5.15), using the aforementioned method. The outcome of the minimization process is the "optimal" quantity of samples based on the specified variance of the calculated samples. Since the computed variance of the estimator may not be optimal due to the selected samples, the expected ideal number may differ in size from the actual number of samples at hand. Therefore, due to its computational efficiency, the whole number of samples arising from the minimization of Eq. (5.15) is not entirely computed. Instead, the number of samples on each level is increased by a proportionate amount that is connected to the computing cost on that level. In other words, the less expensive levels have a larger rise in samples compared to the more expensive levels, which have a smaller increase in samples. Afterwards, the variance of the expectation estimator is reevaluated and Eq. (5.15) is solved once more. This procedure is iterated until the variance of the estimator falls below a suitable threshold and the number of samples obtained from minimizing the objective function reaches a stable value. In the present example, this procedure results in a total of 1250 SSVEs on the lowest

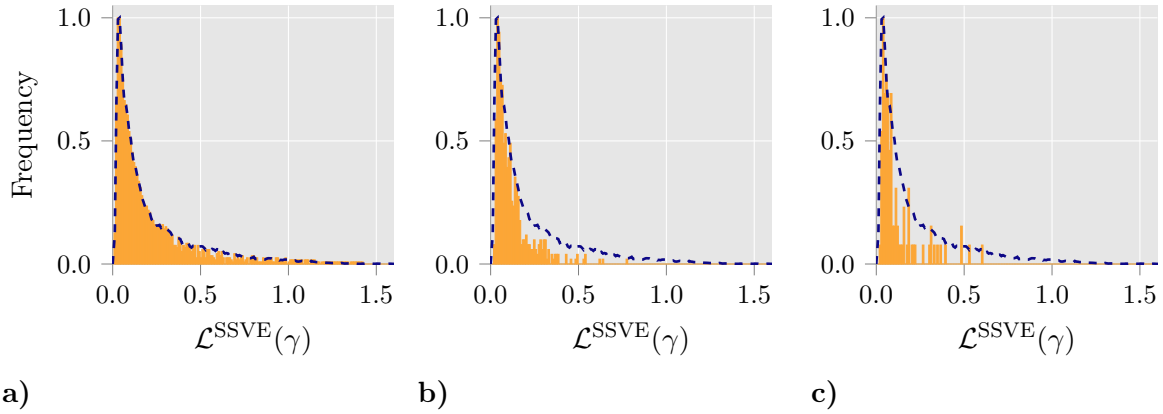

Figure 5.6: Distribution of the microstructure morphology variance measure $\mathcal{L}^{\mathrm{SSVE}}(\gamma)$ for the levels with **a)** 10 voxels, **b)** 25 voxels and **c)** 50 voxels per edge of an SSVE used in the multilevel Monte Carlo simulation. Taken from Miska and Balzani [93].

level, with a morphology discretization of 10 voxels per edge. Among these, 420 samples are also calculated on the intermediate level, with a geometry resolution of 25 voxels. From these 420 SSVEs, 85 are additionally calculated at the highest level with 50 voxels per edge, enabling the calculation of the correction between two consecutive levels using these samples.

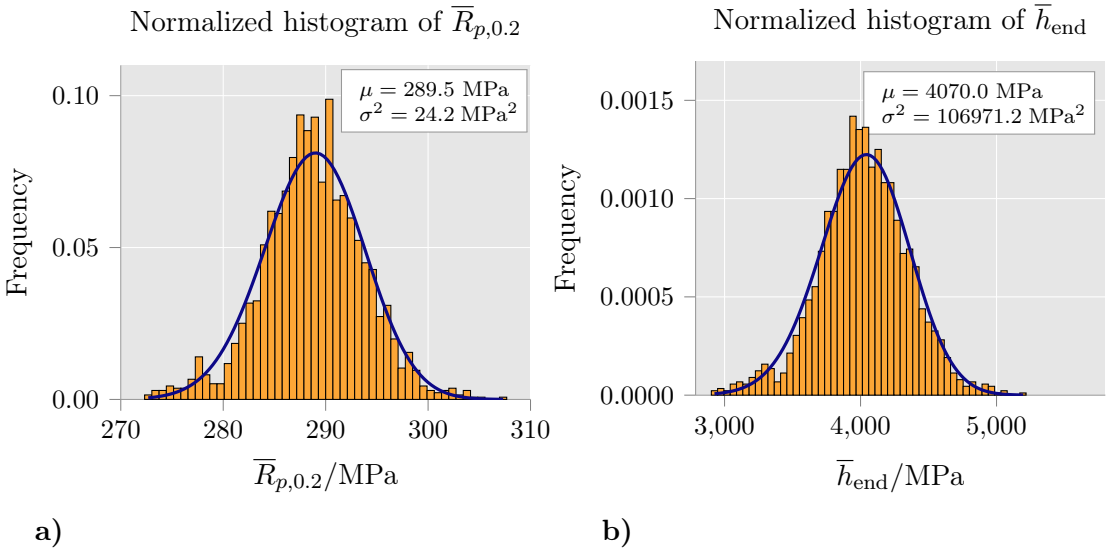

Figure 5.7: Histograms of **a)** effective yield stress $\overline{R}_{p,0.2}$ and **b)** hardening modulus at the end of the prescribed load $\overline{h}_{\mathrm{end}}$ resulting from the multilevel Monte Carlo approach, which are normalized in the sense that the area of the histogram is equal to one. Additionally, a fitted beta-distribution function is plotted. Taken from Miska and Balzani [93].

The histograms in Fig. 5.6 illustrate the variations in microstructure morphology as measured by $\mathcal{L}^{\mathrm{real}}(\gamma)$. It can been noted that the coarsest level, which has the most number of samples, closely fits the given distribution. In contrast, the finer levels have a diminished capacity to resemble this distribution. This outcome is anticipated, as the less detailed levels are employed to align with the statistical characteristics of the quantities of interest, which may be achieved with the given sample size. On the other hand, the more precise levels are utilized to enhance the accuracy of the approximation, requiring progressively less samples. Fig. 5.7a) and Fig. 5.7b) display the histograms of the macroscopic initial yield stress $\overline{R}_{p,0.2}$ and the hardening modulus, respectively. The histograms are generated by extracting the values

from the least detailed level and adjusting the individual SSVEs using their more precisely calculated values on the subsequent levels. This is similar to the computation of higher-order moments in the multilevel Monte Carlo approach. In addition, the histograms of the material parameters are fitted with a beta-distribution function that has shape parameters p and q. The parameters for the beta-distribution are as follows: $p = 6.0171$ and $q = 6.3610$ for the effective yield stress $\overline{R}_{p,0.2}$, with the interval ranging from $a = 272.0$ MPa to $b = 308.0$ MPa. For the hardening modulus, the parameters are $p = 5.1123$ and $q = 4.6798$, with the interval ranging from $a = 2947.0$ MPa to $b = 5098.0$ MPa. When comparing the full Monte Carlo and multilevel Monte Carlo approaches, a strong agreement is found. The mean value of the yield stress $\overline{R}_{p,0.2}$ is $\mathbb{E}[\overline{R}_{p,0.2}] = 289.5$ MPa, resulting in a variation of only 0.04% from the result obtained from the full Monte Carlo simulation. The average value of the hardening modulus shows a deviation of 1.4%, with a value of $\mathbb{E}[\overline{h}_{\text{end}}] = 4070.0$ MPa.

6 Extension of the Optimal Uncertainty Quantification for Polymorphic Uncertainties

The aim of uncertainty quantification is to identify the influence of uncertainties in the input space of a physical model to the respective output space, in order to gain insight in the behavior and to improve the prediction capabilities of said physical model. In Chapter 2, mathematical models for the characterization of uncertainties and basic tools for the uncertainty quantification are introduced. In this chapter, the focus is on a more sophisticated framework for uncertainty quantification, the Optimal Uncertainty Quantification (OUQ) [110]. The application of the OUQ allows the computation of the mathematically sharpest bounds possible on the probability of interest, wherein only available data without uncertified assumptions on potentially underlying distribution functions is incorporated. Therein, uncertain quantities can be characterized by bounds on the quantity itself, moreover, also precise values or bounds for stochastic moments can be considered. However, in its original published form, the OUQ assumes all uncertain quantities to be of epistemic nature, such that aleatory uncertainties, for which the precise probability density function is known, can not be considered. In Miska and Balzani [96] an extension of the OUQ is presented, which allows the incorporation of aleatory uncertainties by two different approaches. Additionally, the idea of the α-level discretization of fuzzy numbers is integrated in the concept of the OUQ framework, which allows the systematic analysis of different combinations of input intervals in the uncertainty analysis. The extended framework is then used in Miska, Freitag, and Balzani [100] to incorporate spatially varying data in terms of random fields and potentially limited data derived therefrom. The following sections are based on the two mentioned journal papers and reflect the proposed developments to the OUQ as well as the computed numerical examples. In addition to that, the extended OUQ is presented in Miska and Balzani [92], Miska and Balzani [94] and Miska and Balzani [95] .

6.1 Optimal Polymorphic Uncertainty Quantification

Since the occurrence of design failure in an engineering structure is a common concern, a probability of special interest is the probability of failure (PoF). Therefore, the Optimal Uncertainty Quantification framework can be used to calculate the optimal bounds on the PoF in order to reliably assess the safety of a design or structure. Since failure is a term that can have several meanings and subjective interpretations, the general event of failure may be denoted by a limit-state function $g : \mathcal{Y} \mapsto \mathbb{R}$, which maps from the product sample space $\mathcal{Y} = \prod_{m=1}^{q} \mathcal{Y}^{(m)}$ spanned by a number of q uncertain quantities to the real line. A value of less then zero from function g denotes failure and hence, a positive value is related to a safe design. As it may be derived from this abstract notation, also all other events may be considered in the OUQ context to compute bounds on the probability for. In the product sample space $\mathcal{Y}$, each individual sample space $\mathcal{Y}^{(m)}$ is related to one uncertain quantity, which can be e.g., input parameters for an underlying physical model or ultimate values for failure modes. The input values $y^{(m)} \in \mathcal{Y}^{(m)}$ for the limit-state function g are realizations of the

associated random variable $Y^{(m)}$, which is distributed according to their individual probability space $(\mathcal{Y}^{(m)}, \Sigma^{(m)}, \mathbb{P}^{(m)})$. If a specific outcome or sample $\boldsymbol{y} = \left[y^{(1)}, \ldots, y^{(q)}\right]^{\mathrm{T}}$ leads to failure, the limit-state function will yield a value below zero, which allows the definition of the PoF as

$$\mathrm{PoF} := \mathbb{P}\left[g(\boldsymbol{Y}) \leq 0\right], \tag{6.1}$$

wherein $\mathbb{P}$ denotes the joint probability measure on $\mathcal{Y}$ and $\boldsymbol{Y} = \left[Y^{(1)}, \ldots, Y^{(q)}\right]^{\mathrm{T}}$ is the vector of all considered random variables. Under the premise, that every single individual probability measure $\mathbb{P}^{(m)}$ is known precisely, the problem would be only influenced by aleatory uncertainties and the PoF could be computed to a precise value by Monte Carlo approaches. As already discussed, this scenario is rather unlikely and in most cases, the available data on a few uncertain quantities will be limited, such that the associated probability measures $\mathbb{P}^{(m)}$ can not be specified exactly. Here, approaches for epistemic uncertainties come into play, and in this case, the Optimal Uncertainty Quantification. As mentioned in Sec. 2.2.4, if the available data is not sufficient to deduce a precise probability measure, it may be sufficient to estimate stochastic moments of limited order by statistical methods. The Optimal Uncertainty Quantification framework allows to incorporate such data without requiring the specification of a probability distribution, which is potentially parameterized in those moments. Thus, a moment of order z can be considered either as exact moment $\mathbb{E}[(Y^{(m)})^z] = c_m^{(z)}$ or more realistically as an interval, i.e. $\mathbb{E}[(Y^{(m)})^z] \in [c_{m,\mathrm{lower}}^{(z)}, c_{m,\mathrm{upper}}^{(z)}]$. The smallest amount of data, which has to be available for a single uncertain quantity, are the bounding values, i.e., $\mathcal{Y}^{(m)}$, e.g. $y^{(m)} \in [y_{\mathrm{lower}}^{(m)}, y_{\mathrm{upper}}^{(m)}]$. Theoretically, this allows an entire range of probability measures μ on $\mathcal{Y}$ to agree with the available data, such that the PoF can be at most computed to lie within a certain interval. The optimal, i.e., the mathematically sharpest, bounds on the PoF are then computed by means of the OUQ.

6.1.1 Extended Optimal Uncertainty Quantification

Before the aleatory extensions can be discussed, to begin with the original version of the OUQ as proposed in [110] is illustrated. Since the primary objective of the OUQ is to calculate the optimal bounds on the potential probability of failure, two optimization problems are posed to compute the optimal lower bound $\mathcal{L}$ and the optimal upper bound $\mathcal{U}$ by

$$\begin{aligned} \mathcal{L} &:= \inf_{(h,\mu)\in\mathcal{A}} \mu\left[g \leq 0\right], \\ \mathcal{U} &:= \sup_{(h,\mu)\in\mathcal{A}} \mu\left[g \leq 0\right], \end{aligned} \tag{6.2}$$

wherein (h, μ) refers to a potential combination of a measurable performance function h, such as a function that calculates the maximum deformation of a structure when subjected to uncertain inputs, and a joint probability measure μ from the set of all admissible scenarios $\mathcal{A}$, which consists of all the data and information relevant to the problem. Thus, every potential combination (h, μ) contained in $\mathcal{A}$ has to comply with the available data and information, which can be represented by the generalized expression $\mathbf{G}(h, \mu) \leq 0$. Then, the set of all admissible scenarios $\mathcal{A}$ can be defined by

$$\mathcal{A} := \left\{(h, \mu) \in \mathcal{G} \times \mathcal{M}^q(\mathcal{Y}) \mid \mathbf{G}(h, \mu) \leq 0\right\}, \tag{6.3}$$

wherein $\mathcal{G}$ denotes the set of admissible measurable performance functions h on $\mathcal{Y}$ and $\mathcal{M}^{(q)}(\mathcal{Y}) := \bigotimes_{m=1}^{q} \mathcal{M}(\mathcal{Y}^{(m)})$ represents the set of products of probability measures on $\mathcal{Y}^{(m)}$. Since the joint probability measure is constructed as a product measure, stochastic independence of all uncertain quantities is induced, see also Sec. 2.2.5. The perfect, but due to the

limited data unknown, solution, i.e., the pair of the precise probability measure $\mathbb{P}$ and performance function H, is also a member of the set $\mathcal{A}$. Due to the lack of knowledge however, this pair is neither identifiable nor can be preferred over another pair also contained in $\mathcal{A}$. All pairs in $\mathcal{A}$ are equally possible and therefore, the most favorable and unfavorable pair in regards to the PoF are sought for, since only these two pairs are of practical meaning for the assessment of the underlying physical problem. The optimization problems in Eq. (6.2) are of infinite dimension, since an endless number of probability measures μ and possible performance functions h can be found, which satisfies the constraints of $\mathcal{A}$. Consequently, solving these problems in practice is deemed to be practically impossible.

At this stage, the reduction theorem as key component of the OUQ [110] is introduced. It builds upon the findings of Winkler [162] and states that the sought after probability measures are situated at the extreme points, i.e. on convex mixture distributions of Dirac masses. Therefore, the joint probability measure $\mu = \mu_1 \otimes \ldots \otimes \mu_m \otimes \ldots \otimes \mu_q$ is composed of convex combinations of Dirac masses, which are given by

$$\mu_m = \sum_{k=0}^{n^m} w_k^{(m)} \cdot \delta(y^{(m)} - y_k^{(m)}), \tag{6.4}$$

with $y_k^{(m)}$ denoting the support points of the k-th Dirac mass of the m-th measure with the associated weight $w_k^{(m)}$, cf. also Sec. 2.2.3 and Eq. (2.11) in particular. This means, regardless if the modeled uncertain quantity is continuous or discrete, here it is approximated by a discrete measure. As it will be seen later, the choice of a discrete measure allows the concentration of mass, which is in this context equal to probability, in regions of interest, leading to the optimal bounds of interest. The number of individual Dirac masses $n^m + 1$ is determined based on the amount of available knowledge for the respective uncertain quantity $Y^{(m)}$. Since the available data is given in terms of bounds on the quantity and potentially also in terms of moment information, the constructed probability measure should exhibit exactly those moments in the specified bounds. Thus, the number n^m has to be set to the number of known moments on the uncertain quantity to ensure, that the constructed probability measures has sufficient flexibility to adapt to the moments. Since Eq. (6.4) is supposed to be a linear convex mixture, the weights have to be normalized, i.e.

$$\sum_{k=0}^{n^m} w_k^{(m)} = 1.0, \;\; m = 1, \ldots, q. \tag{6.5}$$

Example: Let a dimensionless variable x be distributed according to a normal distribution with mean $\mathbb{E}[x] = 5.0$ and the variance $\sigma^2 = 0.5$. Under the assumption, that the specific distribution type is not known and only the two mentioned moments are available, three Dirac masses are required for the convex combination, leading to three support points and three corresponding weights. One possible realization, while not the only one, consists of support points positioned at $x = \{3.6730, 4.8526, 6.0321\}$ and their corresponding weights $w = \{0.125, 0.625, 0.25\}$. This configuration results in a cumulative distribution function as shown in Fig. 6.1a). The support points of the Dirac masses correspond to the locations of the distinct visible steps, whereas the magnitude of each step is determined by the weight of the corresponding Dirac mass.

With the individual probability measures μ_m being reduced to a finite number of support points and weights, the performance function h should be discussed. Usually, the performance is assessed by means of a physical model, which involves sophisticated numerical solution schemes. While this introduces the problem of model uncertainties, which are beyond the

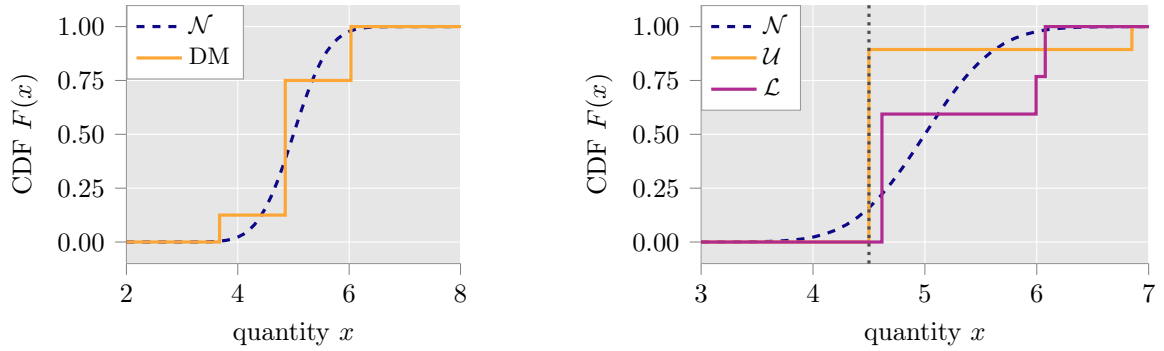

Figure 6.1: a) Comparison of the cumulative density functions (CDF) of a normal distribution $\mathcal{N}$ with mean $\mathbb{E}[x] = 5.0$ and variance $\sigma^2 = 0.5$, and of a convex mixture distribution DM composed of three Dirac masses exhibiting the same two moments. **b)** Optimal upper and lower bound $\mathcal{U}$ and $\mathcal{L}$ on the probability of failure, if failure is defined by $x < 4.5$. Taken from Miska and Balzani [96].

scope of this thesis, the performance function is a precisely known deterministic function and can thus, be omitted from the further uncertainty analysis. Then, the set of admissible scenarios reduces to

$$\mathcal{A}_{\text{red}} = \left\{ \mu \in \bigotimes_{m=1}^{q} \sum_{k=0}^{n^m} w_k^{(m)} \cdot \delta(y^{(m)} - y_k^{(m)}) \mid \mathbf{G}(\mu) \leq 0 \right\}, \tag{6.6}$$

which reduces the optimization problems of Eq. (6.2) to a finite dimension, allowing for a numerical solution of these problems. The objective function for these optimization problems is obtained by inserting the Dirac mass representation of Eq. (6.4) for each μ_m, which leads to the following discrete formula for the probability of failure:

$$\mu\left[g(\boldsymbol{Y}) \leq 0\right] = \sum_{i=0}^{n^{(1)}} \dots \sum_{k=0}^{n^m} \dots \sum_{l=0}^{n^{(q)}} w_i^{(1)} \dots \; w_k^{(m)} \dots \; w_l^{(q)} \chi\left(\boldsymbol{y}_{i\dots k\dots l}\right), \tag{6.7}$$

wherein $\boldsymbol{y}_{i\dots k\dots l} = \left[y_i^{(1)}, \dots, y_k^{(m)}, \dots, y_l^{(q)}\right]^{\mathrm{T}}$ is a vector of the Dirac support points for the combination of terms $i \dots k \dots l$. In Eq. (6.7), function χ with arguments $\boldsymbol{y}_{i\dots k\dots l}$ is introduced. This function computes, wether the specific vector $\boldsymbol{y}_{i\dots k\dots l}$ leads to a failure of the underlying problem, which may be interpreted of the specific probability of failure for a given $\boldsymbol{y}_{i\dots k\dots l}$. Since $\boldsymbol{y}_{i\dots k\dots l}$ is a deterministic vector, the event of failure is also a deterministic quantity and the the PoF can only take the values 0% or 100%. Thus, the function χ is the indicator function defined as

$$\chi\left(\boldsymbol{y}_{i\dots k\dots l}\right) = \begin{cases} 1 \text{ if } g(\boldsymbol{y}_{i\dots k\dots l}) \leq 0, \\ 0 \text{ else.} \end{cases} \tag{6.8}$$

The actual computation of the optimal bounds of the PoF, as described in equations Eq. (6.2), is performed by solving optimization problems with equations Eq. (6.7) as the cost function. This process is also outlined in Alg. 3. The discrete degrees of freedom are of the weights $w_k^{(m)}$ and the support points $y_k^{(m)}$ of the Dirac masses. If a number of n^m moments is known for an uncertain quantity, $2(n^m + 1)$ degrees of freedom are required in the optimization to construct the associate combination of Dirac masses, if the constraint (6.5) is not incorporated a priori. However, in order to parameterize the objective function in this manner, it is necessary to impose constraints on the optimization process. This is because if the degrees of freedom are

randomly generated without any restrictions, it may result in measures that are not included in the set of permissible scenarios $\mathcal{A}_{\text{red}}$, or that are not probability measures at all. The latter problem is resolved by imposing the constraint of normalizing the weights of each measure, as described in equation (6.5). In addition to that, the created probability measures need to by constrained by the available knowledge contained in $\mathcal{A}_{\text{red}}$. In order to do so, the classical or central moment of order z are computed for an individual probability measure by

$$\begin{aligned} \mathbb{E}_{\mu_m}\left[(Y^{(m)})^z\right] &= \textstyle\sum_{k=1}^{n^m} w_k^{(m)} (y_k^{(m)})^z \quad \text{and} \\ \mathbb{E}_{\mu_m}\left[(Y^{(m)} - \mathbb{E}_{\mu_m}\left[Y^{(m)}\right])^z\right] &= \textstyle\sum_{k=1}^{n^m} w_k^{(m)} (y_k^{(m)} - \mathbb{E}_{\mu_m}\left[Y^{(m)}\right])^z. \end{aligned} \tag{6.9}$$

As previously stated, the constraints formulated on the moments, calculated using equation (6.9), may not necessarily be equality constraints, since also bounds on moments can be specified as available knowledge, leading to inequality constraints. Not only is this approach more realistic in various situations, as it might be challenging to precisely estimate moments from sample data, but it also eases the numerical optimization problem by relaxing the strictness of equality constraints with interval constraints. Both cases, however, necessitate an equal amount of degrees of freedom (DoF), which is only controlled by the number of, but not the type of given moment information.

Example: Using the same normal distribution and information provided in the previous example, the event of failure occurs when the quantity x is less than 4.5, i.e. $g(x) = x - 4.5$. This is represented by the dotted vertical line in Fig. 6.1b). Two optimization runs yield the optimal upper and lower bounds on the desired Probability of Failure (PoF). In the upper limit, a Dirac mass is positioned very near the failure threshold to maximize its weight, while the other two masses almost merge into a single mass. Therefore, the upper bound is equivalent to the sum of the Dirac masses in the region of failure, which is $\mathcal{U} = 89.36\%$. Conversely, the lower bound $\mathcal{L}$ is zero since it is possible to position all three Dirac masses within the feasible zone, as depicted in the image. On the other hand, the actual value derived from the underlying normal distribution is $\mathbb{P}[x \leq 4.5] = 15.87\%$. The value is certainly within the calculated bounds, but it is noticeably smaller than the calculated upper bound. The significant disparity arises because the calculations for the bounds only included a restricted amount of information, specifically the first and second order moments. Hence, this straightforward example highlights the significant influence of taking into account either the entire distribution function or a restricted range of moments for an uncertain quantity. It should be noted that the measures created are just the highest and lowest values for the desired probability of failure, but they do not provide the best possible bounds for the cumulative distribution function across its whole range.

Algorithm 3: Evaluation of cost function Eq. (6.7)

Data: All support points $y_k^{(m)}$ and weights $w_k^{(m)}$ with $m = 1, \ldots, q$ and $k = 0, \ldots, n^m$
Result: PoF

```
PoF ← 0
for y_{i...k...l} in {set of possible combinations of support points}:
    if g(y_{i...k...l}) ≤ 0:
        PoF ← PoF + w_i^(1) ... w_k^(m) ... w_l^(q)
return PoF
```

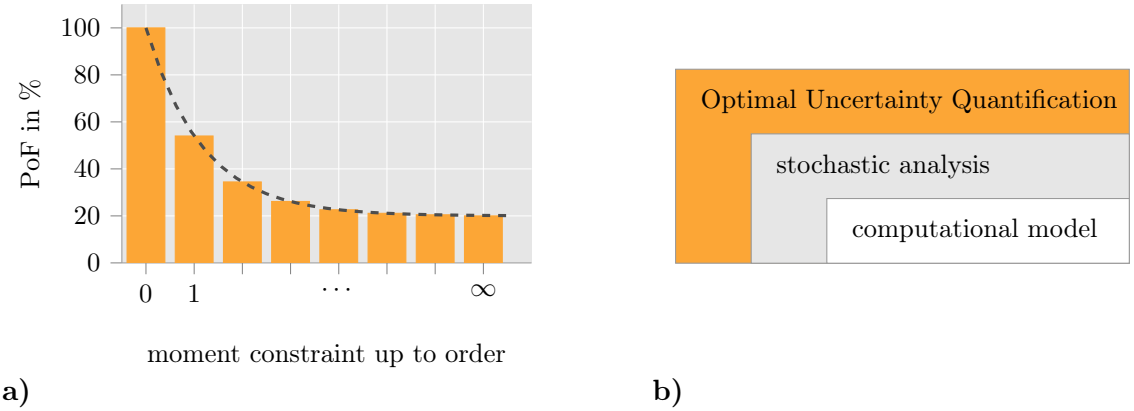

a) **b)**

Figure 6.2: a) Approach 1: convergence of the computed upper bound on the PoF with an increasing number of moment constraints and **b)** Approach 2: nested stochastic analysis within the evaluation of the objective function. Taken from Miska and Balzani [96]

Given that the optimization problems in OUQ are typically non-convex, it is essential to use an effective global optimization algorithm like Differential Evolution, cf. Storn and Price [144]. A reference implementation using Differential Evolution for the original OUQ framework can be found in the *mystic*-framework, cf. McKerns et al. [87].

The original form of the OUQ framework, as described until here, considers all uncertain quantities as epistemic, since only limited data in terms of bounds on the quantity and bounds on the moments can be incorporate. Therefore, in the following two approaches are discussed to also integrate aleatory uncertainties, which then enable a polymorphic uncertainty quantification.

Approach 1: The first approach is a straightforward approach and is based on the assumption, that an aleatory uncertainty can also be described by the complete sequence of its stochastic moments. Since the precise probability density function is usually known for aleatory uncertainties, in principle any moment up to infinite order, if existent, can be computed. Then, these moments may be used to constrain an uncertain quantity in the context of the OUQ as described above. As the number of moment constraints increases, the description of the underlying probability measure becomes more accurate, and the calculated bounds on the PoF should converge as shown in Fig. 6.2a). Nevertheless, due to the inherent uncertainty in determining the necessary number of moments to adequately describe a quantity, it is necessary to conduct multiple optimization runs with increasing numbers of moment constraints in order to evaluate the convergence behavior. Once convergence is obtained, it can be assumed that the number of moments used for a particular quantity is sufficient. However, the inclusion of additional moment constraints requires additional terms in the Dirac representation of the specific measure. As a consequence, the optimization problems become more complex, not only in terms of constraints but also in terms of the degrees of freedom. In addition, the cost of evaluating a single objective function grows as the number of terms in the cost function (6.7) increases. An increasing number of terms therein leads to an increasing number of model evaluations for the limit-state function g, which is usually a drastic performance drawback.

Approach 2: Alternatively, the second approach relies on leveraging the the properties of aleatory uncertainties. Given that the probability density function is usually known for aleatory uncertainties, there is no requirement to estimate the associated probability of failure by a combination of Dirac masses in the first place. Instead, the probability of interest can be determined by directly integrating the joint probability density function of all aleatory uncertainties within the region of failure. By doing so, the overall shape of the cost function

as displayed in Eq. (6.10) remains the same, but in this case χ is not defined as an indicator function, but rather as the integral of the product of the PDFs of the aleatory uncertainties over the failure region, i.e. where the function $g(\boldsymbol{Y})$ is less than or equal to zero, by

$$\chi = \int_{g(\boldsymbol{Y})\leq 0} \prod_{s=1}^{r} \widehat{f}_s(\widehat{Y}^{(s)}) \mathrm{d}\widehat{\boldsymbol{Y}}. \tag{6.10}$$

Herein, the vector $\widehat{\boldsymbol{Y}}$ represents the r aleatory uncertainties, for which the respective probability density functions (PDFs) are known, and $\widehat{f}_s$ represents the PDF of parameter $\widehat{Y}^s$. Given that this integration strategy accounts for r uncertainties, only the $q-r$ remaining epistemic uncertainties of the problem are expressed as convex combinations of Dirac masses. Accordingly, the vector $\boldsymbol{Y}$ is reduced in size and $\boldsymbol{Z} = [\boldsymbol{Y}, \widehat{\boldsymbol{Y}}]$ is introduced as vector containing both aleatory and epistemic uncertain quantities. The outcome is a nested structure, as shown in Fig. 6.2b) and described in Alg. 4. This is because each evaluation of the objective function necessitates the computation of the stochastic problems as presented in Eq. (6.10), which, in turn, rely on evaluations of the fundamental computational model of the problem. As a result, the optimization problem has a reduced number of degrees of freedom and constraints compared to the first approach, facilitating the solution of the optimization problem. However, in order to evaluate each χ, a numerical integration in probability space must be carried out. This can be accomplished using a Monte Carlo technique, cf. e.g., Padmanabhan et al. [111]. Therefore, this method is only practical for either an inexpensive computational model or surrogate models, which are created using a specific number of pre-existing evaluations of a costly computational model.

The second method with its nested approach also accommodates for polymorphic uncertainties, where the probability density function may be specified with interval-valued parameters. This is analogous to interval-probability methods, as in both cases characterizing parameters of a chosen distribution type uncertain quantities in itself. For the specific scenario that all uncertainties are represented solely by bounds on the quantities themselves, the solution methods of both techniques are even the same. Then, all sums in Eq. (6.7) collapse to just one term, so that the evaluation of Eq. (6.10) is performed for one combination of epistemic quantities only. Yet, the Optimal Uncertainty Quantification allows to not only use intervals for those characterizing parameters, it is also possible to specify moment constraints for moments of those parameters, such as e.g. a prescribed mean. Thus, the second approach to integrate aleatory uncertainties in the OUQ allows the choice of intervals on one end to conditional probability-like models on the other end for uncertain quantities. The latter is achieved by progressively specifying more moment constraints on the characterizing parameters of a PDF. An inconvenience of this approach is the quantity of Monte Carlo integrations required to assess the cost function Eq. (6.7) when moment constraints are included. Then however,

Algorithm 4: Evaluation of the modified cost function Eq. (6.10) for Approach 2

Data: All support points $y_k^{(m)}$ and weights $w_k^{(m)}$ with $m = 1, \ldots, q-r$ and $k = 0, \ldots, n^m$ and probability density functions $\widehat{f}_s$ with $s = 1, \ldots, r$

Result: PoF

$PoF \leftarrow 0$

for $\boldsymbol{y}_{i\ldots k\ldots l}$ **in** *{set of possible combinations of support points}*:

$$PoF \leftarrow PoF + \int_{g(\boldsymbol{Y})\leq 0} \prod_{s=1}^{r} \widehat{f}_s(\widehat{Y}^{(s)}) \mathrm{d}\widehat{\boldsymbol{Y}}$$

return PoF

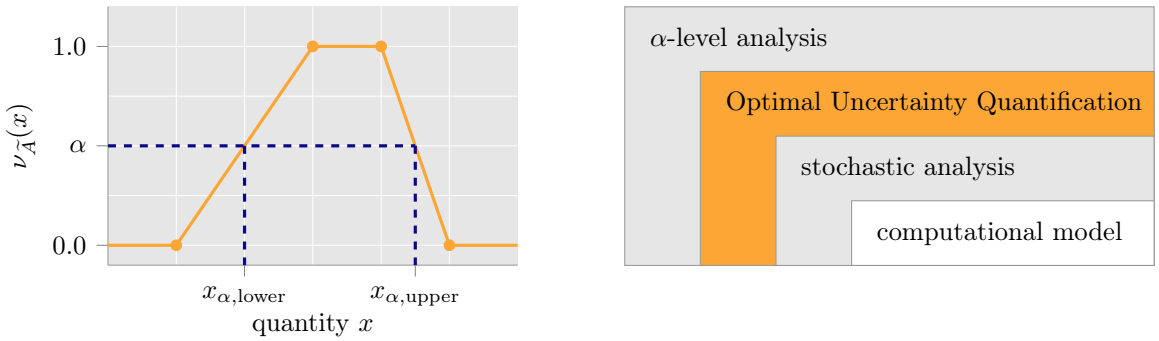

a) **b)**

Figure 6.3: a) Schematic deduction of a discrete α-level of a trapeziodal fuzzy number and **b)** nested solution scheme of a combined OUQ-fuzzy-analysis. Taken from Miska and Balzani [96]

employing more effective Monte Carlo integration methods, such as sequential importance sampling [115], advanced line sampling [22], or subset sampling [2], might yield advantageous results. An additional use of a surrogate model that directly yields the numerical integration result as its output value may be beneficial.

6.1.2 Combination with Fuzzy Numbers

Sometimes, a single interval is not the right choice for either the bounds of an uncertain quantity or for the bounds on a moment, because conflicting information with varying degrees of plausibility should by systematically investigated. Then, fuzzy numbers as introduced in Sec. 2.3 may be a better approach, cf. also [101] or [10], and thus, a combination of the OUQ framework with fuzzy numbers is meaningful. Since fuzzy numbers can be defined in a discretized form, which is essentially a set of weighted intervals, the integration of fuzzy numbers in the OUQ analysis is rather straightforward. For this objective, the subsequent steps have to be taken into account (refer also to Alg. 5 and and Fig. 6.3b)):

- Iterate through all desired α-levels and compute the corresponding α-cut for each α-level according to Fig. 6.3a).
- Construct and solve an OUQ-problem on each α-level with the computed α-cut as input intervals. The OUQ-problem may include a stochastic analysis, as stated in Sec. 6.1.1.
- The output fuzzy number is constructed by means of discrete α-levels, which uses the optimal upper and lower bound on the PoF from the OUQ analysis as interval bounds.

This approach to incorporate fuzzy numbers resembles the algorithmic methodology for fuzzy-probabilities, which also involves a nested stochastic analysis within an outer fuzzy-analysis, as described in [102]. The primary distinction lies only in the optimization performed at each α-level, which is, however, in itself a significant distinction. Unlike interval optimization in the fuzzy-probability technique, the OUQ optimization encompasses all the properties discussed in the previous two sections. This implies that the method is not restricted to fuzzy numbers representing a quantity or parameters of a specific probability density function. It also permits the use of fuzzy numbers to impose bounds on moments. It is feasible to represent an uncertain quantity with limited knowledge, which falls within a specific range and has two different expert opinions for its mean value. The mean can thus be depicted as a fuzzy number. No more assumptions, such as a guess on the type of an underlying probability density function, are required. Therefore, the integration of the OUQ with fuzzy numbers can be regarded as an extension of fuzzy probabilities. However, this generalization has a

Algorithm 5: Solution scheme for the incorporation of fuzzy numbers in the OUQ

Data: Fuzzy numbers describing quantities and/or moments of quantities
Result: Fuzzy number of the PoF
$PoF \leftarrow$ empty fuzzy number
for α **in** *{α-levels to investigate}*:
  derive bounds as α-levels from fuzzy numbers, cf. Fig. 6.3a)
  construct and solve OUQ-problems with these bounds as input, cf. Eq. (6.2)
  add interval to PoF on level α with $\mathcal{L}$ and $\mathcal{U}$ as bounding values
return PoF

drawback. The general OUQ optimization is computationally more expensive compared to interval optimization, because the OUQ optimization involves additional moment constraints on certain quantities, which leads to more degrees of freedom in the optimization problems. While the rise in degrees of freedom is linear, the computational effort required for solving the resulting optimization issues is exponentially growing.

6.1.3 Improving the Efficiency of OUQ with Canonical Moments

As stated earlier, a significant amount of moment constraints, such as those found in Approach 1 for incorporating aleatory uncertainties discussed in Sec. 6.1.1, results in optimization problems with a large number of constraints. Given that optimization in the context of OUQ typically involves non-convex objective functions in the form of Eq. (6.7), a global optimization approaches such as evolutionary algorithms are necessary. Although these algorithms are effective for problems without constraints, where only limits on the degrees of freedom are specified, they face challenges in performing efficiently for constrained problems, where functions on the degrees of freedom are also restricted, cf. e.g., Lampinen [78] or Yong Wang et al. [164]. Given their inherent characteristics, these optimization methods are prone to producing a significant quantity of potential solutions that do not meet the specified constraints. Therefore, in terms of effectiveness, it is more desirable to convert the optimization problem into an unconstrained problem, where all candidates are considered acceptable. An effective strategy in the context of OUQ involves reformulating the objective function by expressing it in terms of the moments of unknown quantities, which are already known within specific intervals. Thus, the limitations on the functions of the Degrees of Freedom (DoFs), specifically in relation to the moment constraints, are directly converted into restrictions on the DoFs themselves, greatly simplifying the solution of the optimization problems.

When a probability measure within the framework of the OUQ should be constructed based on a series of moments, a way has to be found to determine the corresponding weighting factors and the support points of the Dirac masses from said moment sequence. For that matter, the weighting factors can be determined by solving the linear system of equations that arise from the specified moment constraints as

$$\begin{aligned} w_0 &+ \cdots + w_{n^m} &&= 1.0 \\ w_0(y_0)^1 &+ \cdots + w_{n^m}(y_{n^m})^1 &&= c^{(1)} \\ \vdots & \quad\quad \vdots &&= \vdots \\ w_0(y_0)^k &+ \cdots + w_{n^m}(y_{n^m})^k &&= c^{(k)}, \end{aligned} \tag{6.11}$$

wherein $c^{(k)}$ denotes a classic stochastic moment of order k. The support points y_i have to be known beforehand to solve this system of equations. They can be derived as the roots of

specifically constructed polynomials P. These polynomials have to fulfill the orthogonality condition $\int_{-\infty}^{\infty} P_i(y)P_k(y)\mathrm{d}\mu_m(y) = 0$ for $i \neq k$ to ensure, that the zeros are real-valued, distinct and within the support of measure μ_m and thus, can be used as support points.

The issue therein is, that the measure μ_m is a priori not known and therefore, the construction of an appropriate polynomial is not trivial. In [79], a potential way out is proposed by constructing orthogonal polynomials based on determinants of Hankel matrices of the moments without any further knowledge on μ_m. In order to construct a Hankel matrix of adequate size, it is necessary to include all moments from the known orders of 1 to n^m, as well as the moments up to the order of $2n^m + 1$. This ensures that the final polynomial has a total of $n^m + 1$ zeros. As there is no information about those higher order moments, they can be considered as independent degrees of freedom in the context of the OUQ optimization. By exploring this extended moment space, one can obtain all conceivable probability measures, denoted as μ_m. Consequently, the most extreme measures in the context of OUQ can be identified. Unfortunately, the method relying on Hankel matrices is hindered by two numerical limitations that make it challenging to include it into the OUQ. If a greater number of moment constraints are to be included, as demonstrated in Approach 1 in Sec. 6.1.1, the Hankel matrices become ill-conditioned due to the disparities in the magnitudes of the moments. This results in the occurrence of round-off errors and imprecise outcomes. Furthermore, while the higher order moments are not explicitly specified and instead serve as degrees of freedom, they must nonetheless satisfy specific constraints that pertain to the overall interaction between moments of varying orders. Thus, they are still required to stay within bounds which depend on the values of the other moments. Since these values - in case of higher order moments - are the DoFs of the optimization problem, this will lead to dynamic changes of the bounds on the higher order moments. This poses algorithmic inconvenience within the optimizer.

Therefore, a more effective method in form of canonical moments, as described in Dette and Studden [24], are utilized. This approach has been demonstrated to be valuable in the context of the original OUQ framework, as shown by Stenger et al. [143]. Canonical moments may be interpreted as positions of classical moments relative to their admissible moment spaces, cf. [24], page vii. Canonical moments are defined on the interval $[0, 1]$ and similar to the relation of classic and central stochastic moments, a finite series of moments $\hat{\boldsymbol{c}}(\mu_m)$ may be converted to either representation. For example, the first three classical moments $\hat{\boldsymbol{c}}_m^{(3)}(\mu_m) = \{c_m^{(1)}, c_m^{(2)}, c_m^{(3)}\}$ with $c_m^{(z)} = \mathbb{E}_{\mu_m}[(Y^{(m)})^z]$ can be converted into a series of canonical moments. The set $\hat{\boldsymbol{p}}_m^{(3)}(\mu_m)$ consists of three elements, namely $p_m^{(1)}$, $p_m^{(2)}$, and $p_m^{(3)}$, where each $p_m^{(z)}$ is a real number between 0 and 1. Given that classical moments may be converted into central moments and vice versa, a sequence of such moments accurately captures the information that can be obtained for an uncertain quantity in the setting of OUQ. The recursive procedure for calculating the canonical moments from a series of classical moments is described in [24], page 25 (referred to as the "Q-D Algorithm"). With an appropriate sequence of canonical moments at hand, the sought after orthogonal polynomial $P_n(y)$ can be constructed with the recursive three-term formula

$$\begin{aligned} P_{k+1}(y) =& (y - y_{\text{lower}} - (y_{\text{upper}} - y_{\text{lower}})(\zeta_{2k} + \zeta_{2k+1})) \\ & \cdot P_k(y) - (y_{\text{upper}} - y_{\text{lower}})^2 \zeta_{2k-1}\zeta_{2k} P_{k-1}(y), \end{aligned} \tag{6.12}$$

with starting values $P_{-1} = 0$ and $P_0 = 1$. The values y_{lower} and y_{upper} represent the minimum and maximum bound of the support of the measure μ, which correspond to the lower and upper bound of the associated uncertain quantity. The numbers ζ_j are defined as $(1 - p_j)p_{j-1}$ for the purpose of using a shorter notation. The polynomial $P_{n^m+1}(y)$ is orthogonal to the measure μ_m, implying that the n^m+1 zeros of the polynomial correspond to the support points $y_i^{(m)}$ of the individual Dirac masses used in constructing the measure μ_m. The polynomial

Algorithm 6: PoF (strict canonical moments)

Data: sequence of higher order moments $p_{n^m+1}^{(m)} \dots p_{2n^m+1}^{(m)}$ for $m = 1, \dots, q$
Result: *PoF*
for m **in** $1, \dots, q$**:**
  construct orthogonal polynomial P_{n^m+1} based on $p_1^{(m)} \dots p_{n^m}^{(m)}$ and $p_{n^m+1}^{(m)} \dots p_{2n^m+1}^{(m)}$
  compute $y_0^{(m)}, \dots, y_{n^m}^{(m)}$ from P_{n^m+1} by solving $P_{n^m+1}(y) = 0$
  compute $w_0^{(m)}, \dots, w_{n^m}^{(m)}$ by solving the system of linear equations in Eq. (6.11)
compute *PoF* following Eq. (6.10), cf. also Algorithm 3
return *PoF*

$P_{n^m+1}(y)$ of order n^m+1 necessitates canonical moments up to order $2n^m+1$. These include the n^m known moments, as well as n^m+1 extra moments of higher order. The moments of higher order are again free parameters and are degrees of freedom for the optimization. By exploring all possible higher order moments $\{p^{(n^m+1)}, \dots, p^{(2n^m+1)}\}$, all probability measures that exhibit the known lower order moments $\{p^{(1)}, \dots, p^{(n^m)}\}$ can be discovered, cf. [143]. In contrast to the approach based on Hankel matrices, the bounds for the canonical moments do not depend on values of lower order moments and are specified within the interval $[0, 1]$. This allows an easy specification of the bounds for these moments during the optimization. It is important to mention that this approach decreases the number of degrees of freedom. Only n^m+1 higher canonical moments are considered as free parameters, as opposed to the original approach where n^m+1 Dirac support points and n^m+1 associated weights leading to a total of $2(n^m+1)$ degrees of freedom are used for a single uncertain quantity with n^m known moments. As a result, this method improves the optimization process by converting it into a problem that is only limited by constraints on the bounds of the DoFs, and also by significantly lowering the number of variables. However, in Alg. 6, three extra steps must be taken for each considered uncertain quantity during the evaluation of the objective functions. As a result, the computational effort required for a single evaluation of the objective function is greater than in the original framework. Nevertheless, when the number of degrees of freedom increases, the optimization process becomes significantly more complex. Consequently, the linear increase in processing cost for evaluating the objective function becomes rather insignificant.

The presented algorithm only considers precise moments, as opposed to the original OUQ technique, which also permits moment constraints within certain bounds. However, the method employing canonical moments can be somewhat altered by incorporating extra degrees of freedom to provide the same functionality. The additional degrees of freedom refer to the n^m moments of lower order, which are given as available knowledge in certain bounds. Unlike the unrestricted higher-order moments, the known moments are degrees of freedom in the space of classical moments. This is necessary because the calculation of the canonical moments depends on the values of the previous moments of lower order, i.e., the degrees of freedom in the canonical space are not independent. Therefore, the conversion from classical to canonical moments occurs when evaluating the objective function. Therein, the sequence of known lower order moments is known and fixed, refer to Alg. 7 for further details. This adapted approach enables the same analysis of uncertainty as the original Optimal Uncertainty Quantification approach, but it allows for an optimization with only bound constraints on the degrees of freedom. Consequently, it is anticipated to provide enhanced performance. Although the adapted method, which incorporates bounds on the moments, was briefly mentioned in the publication [143], no particular algorithmic implementation or numerical analysis has been provided therein. In the following numerical examples, both presented approaches, along with the original OUQ method are tested in conjunction with the proposed expansions of the OUQ

Algorithm 7: PoF (relaxed canonical moments)

Data: sequence of classical lower and canonical higher order moments $c_m^{(1)}, \dots, c_m^{(n^m)}$ and $p_m^{(n^m+1)}, \dots, p_m^{(2n^m+1)}$ for $m = 1, \dots, q$
Result: *PoF*
for m **in** $1, \dots, q$**:**
  transform $c_m^{(1)}, \dots, c_m^{(n^m)}$ to $p_m^{(1)} \dots p_m^{(n^m)}$
  construct orthogonal polynomial P_{n^m+1} based on $p_m^{(1)} \dots p_m^{(n^m)}$ and $p_m^{(n^m+1)}, \dots, p_m^{(2n^m+1)}$
  compute $y_0^{(m)}, \dots, y_{n^m}^{(m)}$ from P_{n^m+1} by solving $P_{n^m+1}(y) = 0$
  compute $w_0^{(m)}, \dots, w_{n^m}^{(m)}$ by solving the system of linear equations in Eq. (6.11)
compute *PoF* following Eq. (6.10), cf. also Algorithm 3
return *PoF*

to polymorphic uncertainties.

6.1.4 Random Fields for Spatially Varying Properties

For now, the uncertain quantities considered within the OUQ analysis were only parameters for an underlying model and thus, spatially constant. Certain applications, however, require spatially distributed parameters such as, e.g. a varying material parameter. This spatial variation may be reflected in terms of a random field, cf. e.g., Vanmarcke [155] or Sudret [145], which leads to substantial computational costs. Since such costs may lead to less computed samples, the gained data from random fields can become uncertain. In the following, after a short introduction of random fields, a method is described, which nests the evaluation of random fields in the OUQ.

Random Fields A random field, denoted as $\mathcal{R}(\boldsymbol{x}, \omega)$, is a collection of random variables defined on a standard probability spaces $(\Omega, \Sigma, \mathbb{P})$ on the spatial domain $T \subseteq \mathbb{R}^n$. The random variables are indexed by the spatial position $\boldsymbol{x}$, and ω represents a possible outcome from the sample space Ω. Each point $\boldsymbol{x}_0 \in T$ corresponds to a random variable $\mathcal{R}(\boldsymbol{x}_0, \omega) : \Omega \to \mathbb{R}$. While this description assumes a random field that is scalar and has real-valued elements, it is also feasible to have random fields that are based on random vectors. For a specific outcome denoted as $\omega_0 \in \Omega$, the realization of the random field $\mathcal{R}(\boldsymbol{x}, \omega_0)$ is a deterministic function $\mathcal{R}(\boldsymbol{x}, \omega_0) : T \to \mathbb{R}$ for all $\boldsymbol{x} \in T$. Typically, second-order random fields are applied, which are defined by a mean function $\mathbb{E}[\mathcal{R}(\boldsymbol{x}, \omega)]$ and a covariance function $C(\boldsymbol{x}_1, \boldsymbol{x}_2) = \mathrm{Cov}(\mathcal{R}(\boldsymbol{x}_1, \omega), \mathcal{R}(\boldsymbol{x}_2, \omega))$ for $\boldsymbol{x}, \boldsymbol{x}_1, \boldsymbol{x}_2 \in T$. In engineering applications, predominantly stationary random fields are utilized, which results in a constant mean function $\mathbb{E}[\mathcal{R}(\boldsymbol{x})]$ on T and the covariance is only determined by the distance between the two points $\boldsymbol{x}_1 - \boldsymbol{x}_2$, without regard to their specific positions. For isotropic random fields, the covariance is only determined by the magnitude of the distance $||\boldsymbol{x}_1 - \boldsymbol{x}_2||$. The covariance function can be decomposed into two components: the variance, which remains constant for stationary fields, and the correlation function. The correlation function is employed to regulate the correlation between the two points $\boldsymbol{x}_1$ and $\boldsymbol{x}_2$, often aiming for a gradual decrease as the distance between them increases. To adjust the intensity of the correlation decay, a parameter known as the "correlation length" l_c is employed. A greater correlation length results in a more uniform field, whereas a smaller value leads to a more chaotic field. When the correlation length approaches infinity, the random field will have the same value at every point. In the opposite scenario, when l_c tends towards zero, all random variables in the field

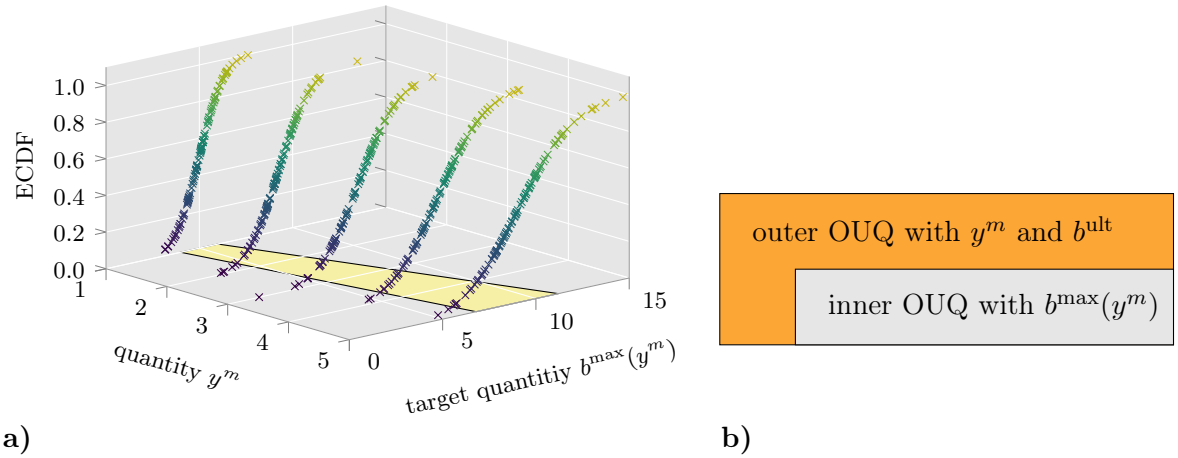

a) **b)**

Figure 6.4: a) Distributions of quantity $b^{\max}$ as result of Monte Carlo simulations of a random field for different fixed values of quantity $y^{(m)}$. The yellow area denotes exemplarily chosen bounds on the mean of the distributions. **b)** Visualization of the nested OUQ approach, in the outer problem the quantities $y^{(m)}$ and b^{ult} are incorporated, the inner problem is based on the statistics on $b^{\max}(y^{(m)})$. Taken from Miska et al. [100].

become uncorrelated and have independent values. As a result, a completely noisy random field will be generated. Provided a random field realization $\mathcal{R}(\boldsymbol{x}, \omega_0)$, it can serve as the input for the underlying model, often relying on a numerical simulation using finite elements. Subsequently, the desired target quantities, such as the maximum value of a general quantity b, can be obtained from the numerical solution of the finite element model. However, in order to understand the statistical behavior of these target quantities, such as the mean value $\mathbb{E}[b^{\max}]$ or the complete distribution function, it is evident that a single model evaluation with only one realization of the random field is inadequate. Multiple realizations of the random field need to be generated and simulated using a Monte Carlo approach. It may be noted, that alternatives to this Monte Carlo simulation approach are available, cf. e.g., Stefanou [141] for an overview, but these approaches are intrusive and require an adaption of the finite element code. The Monte Carlo method, on the other hand, enables the use of finite element codes as a "black-box" but requires more computational effort. This can be partially mitigated by employing multi-fidelity techniques, such as those described by Biehler et al. [13]. To obtain information about the distribution of the target quantity, one can analyze a large number of simulated random fields, similar to traditional Monte Carlo simulations.

However, if the problem at hand is not only influenced by uncertain quantities represented by random fields, but also by spatially constant uncertainties, such as epistemic uncertainties, as seen in the extended OUQ framework for a polymorphic uncertainty analysis, the Monte Carlo simulation of the random fields necessitates additional computational resources. In order to obtain meaningful data on the distribution of the target quantity $b^{\max}$, it is necessary to perform the Monte Carlo simulation multiple times for every possible combination $\boldsymbol{y}_{i\ldots k\ldots l}$ of the spatially constant uncertainties $\boldsymbol{Y}$. This is because the resulting information depends on the value of these uncertainties, and it is important to cover the entire domain of these quantities. Undoubtedly, this approach is not practical due to the significant computational resources and time required. Therefore, Monte Carlo simulations can only be conducted for a limited number of combinations of the constant uncertainties. The resulting distribution of the target quantities can then be interpolated between these selected combinations. For instance, imagine a typical situation that relies on a random field and only one epistemic quantity, denoted as $y^{(m)}$, which remains constant across space. The quantity of interest, denoted as $b^{\max}$, represents the highest value of quantity b that is derived from the numerical solution of the problem. Given that the variable $y^{(m)}$ has an impact on the problem, every variation in

its value will result in a modification of the statistics related to $b^{\max}$. Thus, a limited number of values for $y^{(m)}$ is selected, and separate Monte Carlo simulations are conducted for each value. These simulations are based on the random field and aim to derive statistical data on $b^{\max}$. To view an illustration, refer to Fig. 6.4a), which displays the estimated cumulative distribution functions (ECDF) of $b^{\max}$ for five distinct values of $y^{(m)}$. To determine the appropriate quantifier for the distribution of $b^{\max}$, one must consider the specific needs for the future use of this data. This quantifier should be able to interpolate between the selected values of $y^{(m)}$. In this example, the yellow region represents the estimated upper limit of the mean value, denoted as $b^{\max}$, obtained using interpolation.

Surrogate Model for Random Field Results A surrogate model, such as one based on artificial neural networks (ANNs), can be created to take the random field and additional spatially constant epistemic uncertainty as input and produce the target variables as output. Nevertheless, considering that each finite element, together with its associated parameter from the random field, is considered as an individual input, the input dimension, as well as the model dimension, would become significantly vast. In addition, a large data set would be required for training, testing and validation, such that this approach is not followed here. Instead, Monte Carlo simulations of random field realizations using finite elements for specific combinations of epistemic quantities are conducted as previously described. The target quantities obtained therefrom are then rearranged in ascending order. This allows the construction of the estimated cumulative distribution function for each combination of examined epistemic uncertainties, cf. Fig. 6.4a). Based on the ECDF, percentage of random field realizations that have a target value below a specified threshold based on a certain combination of epistemic variables, can be estimated. In the given case, the empirical cumulative distribution function can be employed to calculate the probability of failure, as $\mathbb{P}[b^{\max} > b^{\text{ult}}] = 1.0 - \text{ECDF}(b^{\text{ult}})$. Hence, the ECDF data is utilized to build the surrogate model. Here, the epistemic quantities, specifically the quantity $y^{(m)}$ and the threshold $b^{\max}$, are considered as input parameters. The output, on the other hand, is represented by $\text{ECDF}(b^{\max})$. As a result, the surrogate model can be substantially downsized, but this comes at the expense of the necessary simple Monte Carlo runs to generate the training data. The quality of the ECDF is directly influenced by the number of random field simulations conducted, which may be restricted.

Nested OUQ-Scheme for Incorporating Limited Random Field Data Considering the motivation provided earlier, it may be more advantageous to focus on specific statistics of the random field results, such as the upper and lower limits or an approximation

Algorithm 8: Computation of Eq. (6.7) for the incorporation of imprecise statistics from random field simulations

Data: Bound and/or moment information on $y^{(m)}, b^{\text{ult}}$ and (limited) random field statistics

Result: Upper bound on the PoF $\mathcal{U}$

$PoF \leftarrow 0$

for $y_i^{(m)}, b_k^{ult}$ **in** *{set of possible combinations of support points}*:

  evaluate random field statistics of $b^{\max}$ based on $y_i^{(m)}$

  construct inner OUQ problem for $b^{\max}$ with $g(y^{(m)}, b^{\text{ult}}, b^{\max})$ following Eq. (6.14)

  solve inner OUQ problem for $\mathcal{U}^{\text{inner}}(y_i^{(m)}, b_k^{\text{ult}})$

  $PoF \leftarrow PoF + w_i^m \cdot \; w_k^{\text{ult}} \cdot \mathcal{U}^{\text{inner}}(y_i^{(m)}, b_k^{\text{ult}})$

return PoF

of the mean within limits as depicted by the yellow region in Fig. 6.4a). Note that this information corresponds precisely to the data that is utilized as input for the extended Optimal Uncertainty Quantification. Unfortunately, it is not feasible to directly include the statistics into an OUQ problem due to the fact that the statistics can vary depending on the spatially constant unknown quantities $\boldsymbol{Y}$. Therefore, in order to obtain the results of the random field computations, a nested scheme of OUQ computations is required for the general case, cf. Alg. 8 for more details. The outer problem is formulated as described in Sec. 6.1, where the variable $y^{(m)}$ and a potentially uncertain ultimate value b^{ult} are included, and compared to $b^{\max}$. The computation of the function χ, as described in Eq. (6.10) for the traditional OUQ, on the other has to be modified. In the context of the uncertain quantities $y^{(m)}$ and b^{ult}, the function may be defined as

$$\chi(y^{(m)}, b^{\mathrm{ult}}) := \mathcal{U}^{\mathrm{inner}}(y^{(m)}, b^{\mathrm{ult}}) \quad \text{with} \quad \mathcal{U}^{\mathrm{inner}} := \sup_{\mu \in \mathcal{A}^{\mathrm{inner}}} \mu[g(y^{(m)}, b^{\mathrm{ult}}, b^{\max}) \leq 0], \quad (6.13)$$

wherein the set of all available information on $b^{\max}$ is denoted by $\mathcal{A}^{\mathrm{inner}}$ and the limit state function is given as

$$g(y^{(m)}, b^{\mathrm{ult}}, b^{\max}) = b^{\mathrm{ult}} - b^{\max}(y^{(m)}). \quad (6.14)$$

Here, $\mathcal{U}^{\mathrm{inner}}$ represents the sharpest upper bound on the probability of failure of the inner OUQ problem. This specific inner OUQ problem focuses solely on a single unknown quantity, namely the target quantity of the random field simulations $b^{\max}$. The data obtained from the random fields, as previously explained, is utilized to establish the essential bound and moment constraints for the maximum value of b (denoted as $b^{\max}$). The quantities $y^{(m)}$ and $b^{\max}$ are inputs from the outer OUQ problem and remain constant during the computation of the inner problem. At every combination of (outer) support points, the statistics on $b^{\max}$ are fixed, which usually requires some sort of interpolation, if the support points do not meet the exact points, for which the random field was evaluated. Only a linear interpolation is used in this study, but the potential impact of more advanced approaches may be explored in future investigations. Using statistics such as bounding values and bounds on the mean of $b^{\max}$, the inner OUQ problem is formulated to determine the optimal bound on $\mathbb{P}[b^{\max} > b^{\mathrm{ult}}]$ (either upper or lower, depending on the objective of the outer optimization). For this reason, only $b^{\max}$ is approximated using Dirac masses, every other quantity is fixated. This is because the other quantities are either constant or they are part of the outer OUQ problem. After solving the inner optimization, the resulting bound is then given back to the outer OUQ problem. By that, a method is available to incorporate only limited statistics on target quantities resulting from random fields under the influence of polymorphic uncertainties.

6.2 Numerical Examples

This section showcases the implementation of the extended Optimal Uncertainty Quantification framework as discussed in the previous sections. For this objective, two examples from classical structural engineering and one instance employing finite elements are examined. The first analysis focuses on the failure event of a two-span beam to compare the results of the two distinct methods for incorporating aleatory uncertainty, as discussed in Sec. 6.1.1. Additionally, this study examines the accuracy and efficiency of the two possible parameterizations of the objective function: one using weights and positions of Dirac masses, and the other using canonical moments. The benchmark problem for polymorphic uncertainty quantification frameworks of Papaioannou et al. [116], is computed and assessed based on the results obtained from the first example. Eventually, the influence of uncertain parameters on the sheet metal forming process of an S-Rail is investigated. Therein, the influence of the spatial distribution of material parameters is investigated and the two presented approaches for the

incorporation of random fields in the context of the OUQ method are studied. Since this example involves numerical simulations in terms of finite elements, surrogate models in form of ANNs are utilized, in which the actual construction of the ANNs was backed by Prof. Dr.-Ing. Steffen Freitag. To enhance the computational efficiency of all examples, the *LSHADE44* extension following Polakova [119] has been implemented in the optimization framework *mystic*, cf. McKerns et al. [87]. This addition not only enables the automated adjustment of the hyperparameters of the underlying Differential Evolution algorithm [144], but it also employs various competing evolution methods to enhance the reliable global optimization of constrained problems.

6.2.1 Two-Span Beam

Description of the problem The problem of concern is a two-span beam, subjected to a continuous load q and two point loads F positioned at the midpoint of each span, as depicted in Fig. 6.5. The beam's geometric properties are assumed to be precisely known. This includes the span-width, which is $l = 5\,\mathrm{m}$, as well as the characteristic properties of a HEA450 cross-section. These properties include the cross-section area, which is $A = 178\,\mathrm{cm}^2$, the moment of resistance, which is $W_{pl,y} = 3216\,\mathrm{cm}^3$, and the area moment of inertia, which is $I_y = 63720\,\mathrm{cm}^4$. These values can be referenced in DIN EN 10034 [25]. The uncertain quantities influencing the failure analysis of the beam are :

- **yield strength y_0:** The distribution of the yield strength y_0 follows a beta distribution with shape parameters $p = 6$ and $q = 6$, and it is limited to the range $y_0 \in \left[200\,\mathrm{N/mm}^2,\ 400\,\mathrm{N/mm}^2\right]$, cf. Fig. 6.6a). Therefore, the uncertainty associated with the yield strength is inherently random, and the two suggested approaches for incorporating aleatory uncertainties in OUQ will be utilized and compared. For the first approach, the first ten central moments are calculated from the beta-distribution as documented in Tab. 6.1. While the distribution is symmetrical, the central moments of odd order are not precisely zero due to limitations in computer accuracy. However, due to their significantly reduced size compared to the nearest even moments, these values are considered sufficiently tiny and are therefore used as given in the table.
- **continuous load q:** The uncertainty associated with the continuous load is assumed to be epistemic. The information regarding q is constrained to its range, which is $q \in [100,\ 150]\ \mathrm{kN/m}$. Additionally, the bounds of the first two moments of q, namely $\mathbb{E}[q] \in [118.75,\ 131.25]\,\mathrm{kN/m}$ and $\mathbb{E}[(q - \mathbb{E}[q])^2] \in [95.0,\ 105.0]$, are known.
- **point load F:** There are two different expert perspectives about the range of the point load F, as well as the limits on its average value. Thus, F is reflected by a Dirac mass representation. However, both the interval on F and the interval on its mean are represented by trapezoidal fuzzy numbers to accurately represent the expert judgments.

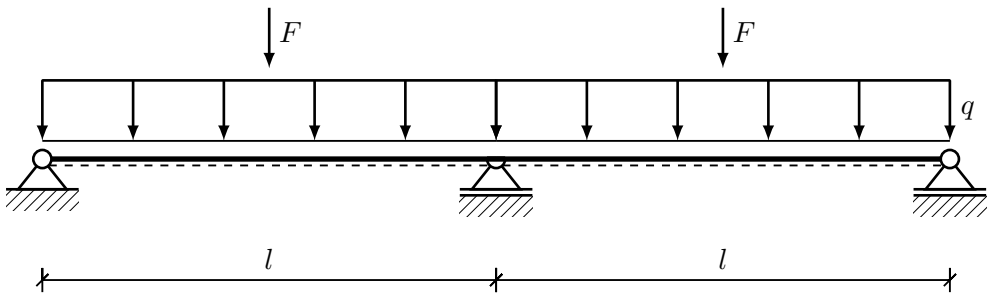

Figure 6.5: Schematic illustration of the two-span beam problem under polymorphic uncertainties. Taken from Miska and Balzani [96].

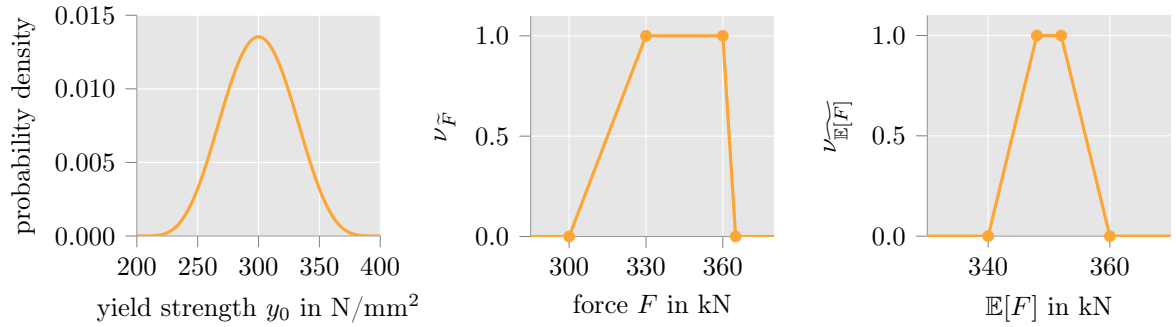

a) **b)** **c)**

Figure 6.6: Uncertain loads of the two-span beam: **a)** beta probability density function of the yield strength y_0, **b)** membership function $\nu_{\widetilde{F}}$ of force $\widetilde{F}$ and **c)** membership function $\nu_{\widetilde{\mathbb{E}}[\widetilde{F}]}$ of the mean of force $\widetilde{F}$. Taken from Miska and Balzani [96].

Table 6.1: Central moments of the distribution of y_0 up to order 10

k	$\mathbb{E}[(q-\mathbb{E}[q])^k]$	k	$\mathbb{E}[(q-\mathbb{E}[q])^k]$
1	0.0	6	$4.524886878 \cdot 10^{09}$
2	$7.692307692 \cdot 10^{02}$	7	$1.371250000 \cdot 10^{02}$
3	$0.000000000 \cdot 10^{00}$	8	$1.667063590 \cdot 10^{13}$
4	$1.538461538 \cdot 10^{06}$	9	$1.702297600 \cdot 10^{07}$
5	$-5.970001221 \cdot 10^{-04}$	10	$7.144555063 \cdot 10^{16}$

Consequently, F is determined indirectly by the two α-levels $\widetilde{F}_{0.0} = [300.0, 365.0]\,\mathrm{kN}$ and $\widetilde{F}_{1.0} = [330.0, 360.0]\,\mathrm{kN}$, cf. Fig. 6.6b) for a plot of the membership function. The fuzzy number of the mean is defined as $\widetilde{\mathbb{E}}[\widetilde{F}]_{0.0} = [340.0, 360.0]\,\mathrm{kN}$ and $\widetilde{\mathbb{E}}[\widetilde{F}]_{1.0} = [348.0, 352.0]\,\mathrm{kN}$, cf. Fig. 6.6c).

The failure of the two-span beam is determined by comparing the maximum bending moment M_E to a permissible value M_R, given that all relevant quantities are available. The maximum bending moments of the beam under the specified loads can be calculated using the formulas provided in standard mechanics textbooks:

$$M_E = -0.125ql^2 - 0.188Fl, \tag{6.15}$$

where all necessary quantities are mentioned above. The Eurocode 3, section 1-1 [26], provides a formula to calculate the allowable amount of the bending moment when the plastic reserves are fully utilized, given by

$$M_R = W_{pl,y} \cdot y_0, \tag{6.16}$$

which leads to the limit-state function being the difference between the resistance moment M_R and the external moment M_E, denoted as $g := M_\mathrm{R} - M_\mathrm{E}$. The lack of all safety factors prescribed by the Eurocode is evident in this example.

Comparison of proposed approaches for aleatory uncertainties The primary aim of the initial analysis of this example is to contrast the two suggested methods for incorporating aleatory uncertainties inside the OUQ framework. To begin, the change of the resulting bounds on the probability of failure (PoF) is examined as the number of prescribed moment constraints on the yield strength y_0 is increased. For that matter, the moments as

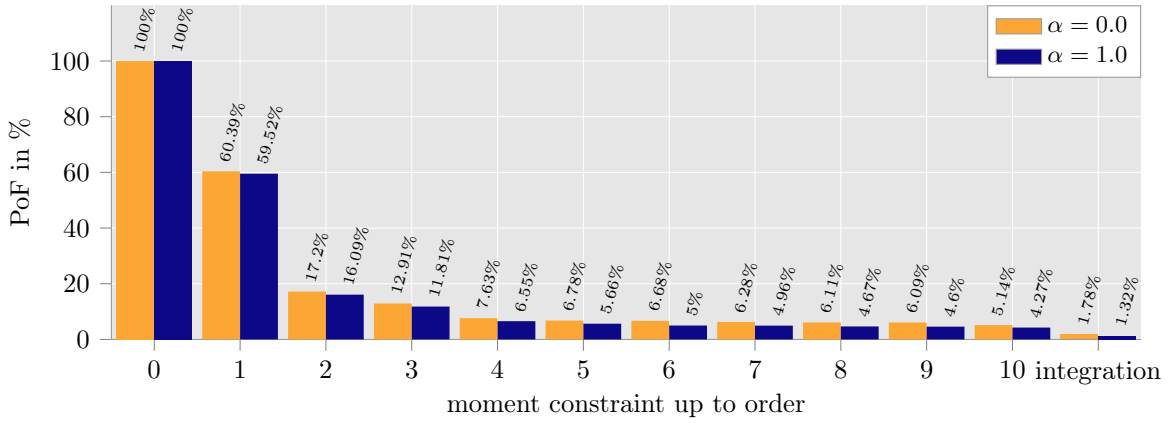

Figure 6.7: Convergence of the computed upper bound on the PoF with an increasing number of prescribed moment constraints on the yield strength (Approach 1), compared to the computed values using the integration approach (Approach 2). Adapted from Miska and Balzani [96].

listed in Tab. 6.1 are used for Approach 1. Afterwards, these results are compared to the outcomes obtained using the integration approach (Approach 2). Initially, the investigation is performed using the conventional approach without utilizing canonical moments, i.e. the degrees of freedom are the support points and weights for the Dirac masses. However, it quickly turned out, that for precise moment constraints, such a parameterization of the objective function is problematic. When incorporating constraints on the moments only up to order 2, the optimizer had already difficulties to construct admissible candidate solutions. This issue become even worse when the number of exact moment constraints was increased even further. Thus, the convergence analysis addressed here focused solely on the parameterization in terms of canonical moments, incorporating exact moment constraints as outlined in section Sec. 6.1.3. Due to the uncertainties in the load q and the forces F, it is not meaningful to impose exact moment constraints on those quantities, and hence, these variables are represented by Dirac masses. Therefore, the optimization problem without any constraints on the yield stress has twelve degrees of freedom, which then increases linearly to 21 DoFs when 10 moment constraints are added to the issue. Similarly, the population size employed in the differential evolution optimizer gradually increases from 200 at the start to 800 at the end, in order to guarantee a sufficient exploration of the search space. Undoubtedly, a population size that grows exponentially would enhance the solution of the optimization problems even further, but a detailed analysis of this matter is postponed to the paragraph comparing Approach 1 and 2. The obtained maximum bounds on the PoF are graphically represented in Fig. 6.7 for both the lower, denoted by $\alpha = 0.0$, and the upper, denoted by $\alpha = 1.0$, α-level of the used fuzzy number. The lower bounds on the PoF are not visually represented as they were all calculated to be 0 percent. The upper limit decreases for both examined α-levels as the number of moment constraints increases, as anticipated due to the enhanced description of the stochastic distribution function for the aleatory uncertainty of the yield strength. However, even when considering ten moment constraints, the upper bounds do not completely converge: there are still little but significant changes in the calculated values. Conversely, imposing restrictions on lower order moments results in significant disparities in the calculated bounds. This discrepancy can be seen as evidence of the significance of including information on low-order moments, if they are available. When comparing the results of both α-levels, the higher level consistently produces a significantly lower upper bound on the PoF. This might be expected, as higher α-levels on uncertain input quantities are supposed to represent sharper constraints on the input and thus, to sharper bounds of the resulting output, i.e. the

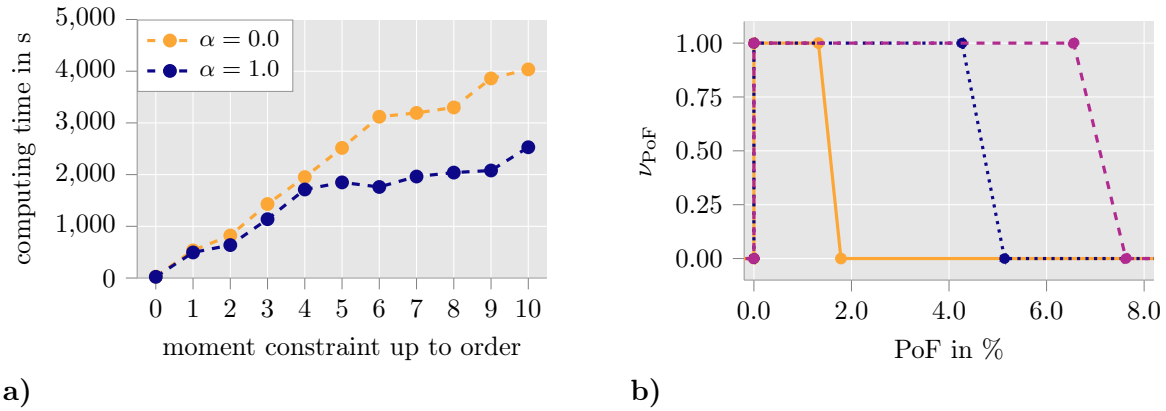

Figure 6.8: a) Required computing time to calculate the upper bound on the PoF with increasing number of moment constraints. **b)** Resulting fuzzy number for the PoF for the integration approach (solid line), ten prescribed moments (dotted line) and four prescribed moments (dashed line). Taken from Miska and Balzani [96].

PoF, but sharper bounds do not necessarily mean smaller bounds overall. Here, these results stem from the fuzzy numbers for the force F, which are specified to limit the range of F and the mean of F for a greater value of α. Reduced ranges result in lower mass of the Dirac masses in the failure region, leading to a decreased PoF. The Fig. 6.8a) displays the average computing times of ten separate optimization runs for the upper bound. As anticipated, the time required increases as the number of prescribed moment constraints rises, owing to the greater number of degrees of freedom and population sizes. The impact of population size on computing time is highly sensitive, making the relative trend of the curves more important than the absolute values of the needed times. Given that only a population size growing linearly with an increasing number of moment restrictions was considered, it follows that the computing times also increase linearly. Remarkably, in all instances, the calculations for the higher α-level necessitated less time compared to the lower level. Given that all settings, such as the number of degrees of freedom and population size, remain the same except for narrower ranges on F, the sole plausible explanation lies in the reduced search space for the optimizer.

The last two bars on the right in Fig. 6.7 display the outcomes of Approach 2, the alternate method to incorporate aleatory uncertainty. In this case, the probability density function of y_0 is integrated using a vanilla Monte Carlo technique with 10^7 samples. The number of samples has been verified using an independent convergence investigation to confirm that increasing the sample size to 10^8 does not affect the outcome of Approach 2. As previously stated, employing advanced techniques like sequential importance sampling would be advantageous in minimizing the influence of internal probability integration on overall efficiency. In this specific scenario, the Monte Carlo integration was unnecessary because the cumulative distribution function could be directly used to calculate the failure probability in this one-dimensional case. However, as a demonstration of the concept, the Monte Carlo approach was still employed. The results indicate that the upper bounds obtained are approximately three times less than the bounds obtained from the optimization runs with 10 constrained moments. Therefore, it seems that 10 moment constraints are not adequate to fully describe the corresponding probability distribution, despite the fact that the variations become relatively small as the number of moment constraints increases. The Monte Carlo integration method necessitates significantly more processing time compared to the first approach, which involves ten restricted moments on the yield stress. Specifically, it requires an average of 10,666 seconds for α-level 0 and 8,459 seconds for α-level 1. It is important to note that significantly more precise, or sharper, estimates of the Probability of Failure (PoF) were achieved. Implementing

an exponential growth model for the population size, as described earlier for Approach 1, will undoubtedly enhance the outcomes of Approach 1 by accommodating the exponential expansion of the search space. Nevertheless, as the upper bound is determined by a maximization problem, any enhancement would correspond to a higher upper bound, resulting in a greater disparity between the outcomes of Approach 1 and Approach 2. Thus, the current findings, which only include population sizes that increase linearly, strongly suggest that Approach 2 is more favorable for incorporating aleatory uncertainties in the uncertainty analysis.

Fig. 6.8b) displays three fuzzy numbers representing the computed probability of failure. The solid line shows the outcome of the integration method, while the dotted line corresponds to the calculation that takes into account moment constraints on the yield strength y_0 up to the 10th order, and the dashed line up to the 4th order. A notable feature of the image is the ratio between the disparities in the solutions of (i) four and ten moment constraints, and (ii) ten moment constraints and the integration approach. Given that the discrepancy (i), resulting from six extra moment constraints on the yield strength, is smaller than the discrepancy (ii), it can be inferred that a significant number of additional moment constraints would be required for the first approach to achieve a similarly precise upper bounds on the PoF as the integration approach. Both approaches necessitate a fairly iterative process of determining either the number of moment constraints to be included for Approach 1, or the effort invested for the probability integration for Approach 2. Converging bounds on the PoF with increased effort need to be identified for both approaches before the obtained bounds may be considered as final result. Thus, due to the considerable number of moment constraints needed for Approach 1 to achieve bounds as precise as Approach 2, the latter might be deemed more efficient. It is important to note that just a basic Monte Carlo integration method was used for the computation in this particular situation, and there are more advanced methods that might be used instead. Furthermore, it is more straightforward to conclude converging bounds for Approach 2 due to the availability of well-established convergence properties on several Monte Carlo approaches.

Convergence analysis using bounds on moments Following the investigation of the problem with strict moment constraints, now a similar study utilizing moment constraints within specified bounds is investigated. These bounds are derived from the values of y_0 stated in Tab. 6.1, which are permitted to fluctuate within a range of $\pm 5\%$ from the given value. It is not anticipated that the calculated upper bound on the PoF will approach the value of the Monte Carlo integration, since the added variability due to the bounded moments should allow for additional failure scenarios. Moment constraints within bounds relaxe the optimization problem numerically and thus, more admissible candidate solutions are expected to be created by the optimizer. For that matter, the optimization problems relax the more, the broader the bounds on the moments are chosen. Therefore, the parameterization of the objective function can be compared between Dirac masses and canonical moments, in contrast to the first study. When the moments are within the acceptable range, the method that utilizes canonical moments necessitates almost double the number of degrees of freedom compared to precise moment limits. However, the resulting number of DoFs is approximately the same number needed for the Dirac mass representation. The population size utilized in this work is exponentially raised, starting with 400 population members for a single moment constraint on the yield strength, and reaching 2800 members for six moment constraints, in order to accommodate the expanding search space.

The upper bounds for both α-levels, obtained by imposing one to six moment constraints, are depicted in Fig. 6.9a) for the method employing canonical moments and in Fig. 6.9b) for the method utilizing Dirac masses. Initially, when employing canonical moments, the observed behavior closely resembles that of exact moment constraints. Specifically, the upper bound

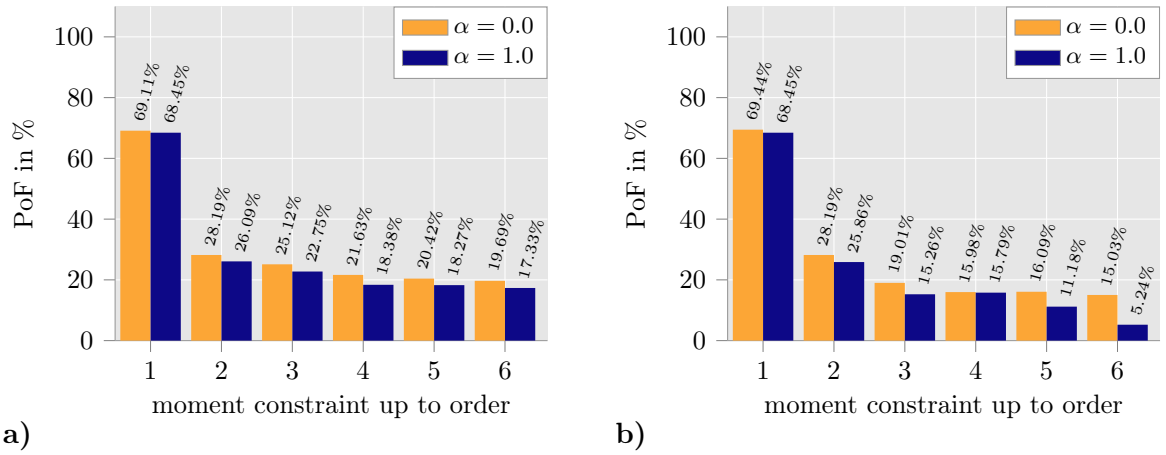

Figure 6.9: Convergence of the computed upper bounds on the PoF with moments in bounds using **a)** canonical moments and **b)** Dirac masses as parameterization of the objective function. Taken from Miska and Balzani [96].

on the PoF decreases as more moment constraints are incorporated. Moreover, the upper limits for the higher α-level are consistently marginally less than those for the lower level. As anticipated, the magnitudes of the computed bounds exceed the values obtained from precise moments. This implies that the variability in the moments enables the probability measure to take more extreme positions in relation to the selected failure criterion. And indeed, if the found extreme measures are investigated regarding the moments, which were constrained in bounds, one finds that these moments are all at the limits of their individual intervals. Exemplary, since a low yield strength is preferable in view of failure of the beam, the mean of the extreme measures is always optimized to the lower bound of the associated interval, whereas e.g. the mean of the continuous load is maximized, which allows for more mass in failure region.

Examining the outcomes of the Dirac mass representation, on the other hand, reveals various and varied discoveries. Initially, the problems with three or more moment constraints result in maximum bounds on the PoF, which are lower than those obtained by the canonical moments approach. Furthermore, the upper bound on level $\alpha = 1.0$ when utilizing three moment constraints is lower than the subsequent bound, suggesting an incorrect response. Similarly, the same problem can be seen in the upper bound when employing four moment constraints at level $\alpha = 0.0$. Both findings indicate that the optimizer encounters challenges in solving the optimization problems without using the canonical moments. Specifically, admissible candidate solutions are obtained by decreasing the extent to which constraints are violated. However, because of the evolutionary nature of the process and the limited search space, the variety of the population diminishes rapidly, causing the candidate solutions to converge. Consequently, the optimizer is susceptible to becoming trapped in an area that is not optimal but still acceptable. This can only be resolved by significantly increasing the population sizes, which hinders the efficiency of the algorithm. However, the outcomes obtained by imposing only one or two moment constraints are similar to those achieved by the canonical moment approach, as a result of the reduced number of constraints in the problems.

Comparing the required computing times plotted in Fig. 6.10a), an advantage for the canonical moments approach is observed while dealing with one or two moment constraints. While the method described in Sec. 6.1.3 necessitates extra processing steps to assess the PoF, it offers a faster solution to the optimization problem. This is because every candidate is considered a valid solution, allowing for quicker exploration of the search space. The computation time for problems with additional moment constraints is not displayed for the Dirac mass

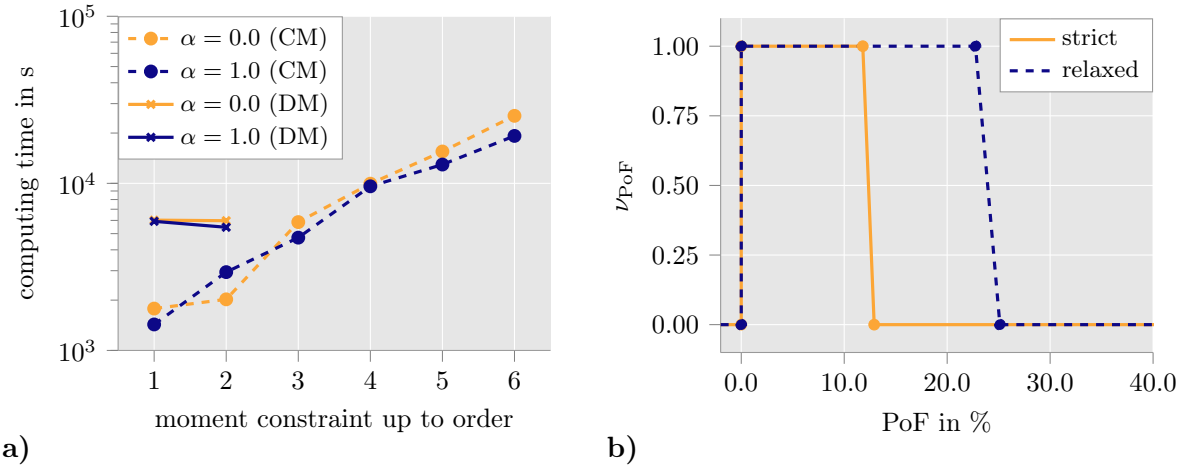

Figure 6.10: a) Comparision of the averaged computing times for relaxed moment constraints using canonical moments (CM) and Dirac mass (DM) parameterizations of the objective function. **b)** Fuzzy numbers of the resulting PoF for strict and relaxed moment constraints with the first three moments constrained. Taken from Miska and Balzani [96].

discretizations, as they produced suboptimal outcomes and a comparison of the computation time would not be meaningful. As previously stated, throughout these computations, the optimizer is prone to becoming trapped in suboptimal areas where no superior solutions are discovered. Once a specific number of iterations has been reached without any improvement in the optimal solution, which in this case is 500 iterations, the optimizer terminates the computation. This process occurs very quickly in these particular areas. Further iterations have shown to be unproductive, as the current population lacks the ability to generate exit vectors. This would necessitate either unreasonably huge population sizes or adjustments to the optimizer in order to generate new population vectors adaptively. The approaches using canonical moments outlined the anticipated pattern of computation time, where the necessary solution time increases in conjunction with the complexity of the optimization problems. The computations involving variable moments are more costly compared to those with fixed moment constraints, which is to be expected given the greater number of degrees of freedom. Fig. 6.10b) illustrates a comparison between the fuzzy number obtained from exact moment constraints and the fuzzy number obtained from flexible moment constraints in the instance with three moment constraints. The substantial variance in the upper bounds is evident, and it is only caused by the diversity in the moment constraints being examined.

6.2.2 Benchmark of DFG Priority Program 1886

In Papaioannou et al. [116], a benchmark problem is posed for polymorphic uncertainty quantification frameworks. Based on the findings of the previous example, i.e. using the integration approach for the inclusion of aleatory uncertainties and canonical moments as parameterization of the objective function, the first challenge of this benchmark problem is addressed in this study using the extended OUQ framework. Furthermore, the obtained results are compared to the fuzzy-probability approach presented in the benchmark publication.

Problem description The benchmark problem involves a steel column with a wide-flange cross-section, as shown in Fig. 6.11. The column is subjected to a compressive load, denoted by P, which can be split into a permanent part P_{p} and an environmental part P_{e}. The steel column will predominantly fail by buckling around the y-axis due to the load. Additionally, the column's initial deflection follows a parabolic shape with a maximum value of δ_0 in the middle. The geometric dimensions of the column are known precisely, the height of the column

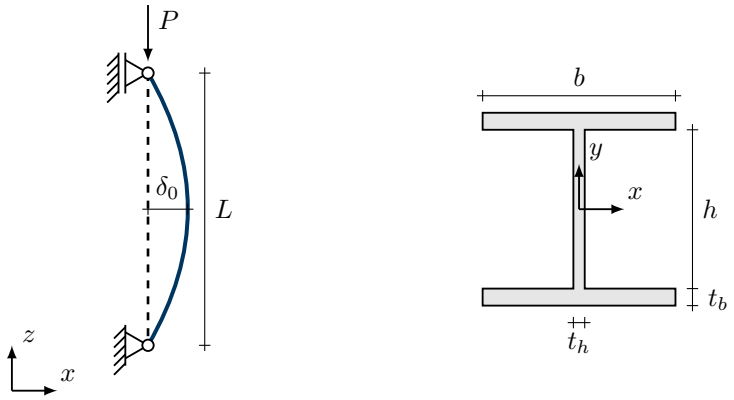

Figure 6.11: Illustration of the benchmark buckling problem as proposed in [116]. Taken from Miska and Balzani [96].

is $L = 7.5$ m, the area is $A = 120$ cm^2, the section modulus is $W_\mathrm{y} = 450.17$ cm^3, and the moment of inertia is $I_\mathrm{y} = 6752.5$ cm^4. Furthermore, the problem is influenced by the subsequent independent uncertainties:

- **permanent load $P_\mathbf{p}$:** There is a limited amount of information accessible regarding the permanent load. Specifically, there are just three expert opinions provided in the form of intervals: $P_\mathrm{p}^{(1)} \in [100\ \mathrm{kN}, 150\ \mathrm{kN}]$, $P_\mathrm{p}^{(2)} \in [150\ \mathrm{kN}, 200\ \mathrm{kN}]$ and $P_\mathrm{p}^{(3)} \in [100\ \mathrm{kN}, 200\ \mathrm{kN}]$. Therefore, the permanent load is considered to be an interval quantity $P_\mathrm{p} \in [100\ \mathrm{kN}, 200\ \mathrm{kN}]$, representing the hull of all expert opinions.

- **environmental load $P_\mathbf{e}$**: The environmental load represents the maximum snow load that the roof, supported by the examined column, experience annually. There is a dataset available of a measurement series over a span of twenty years of P_e, which is represented by the histogram shown in Fig. 6.12c). This data exhibits some indications of potentially following a Gumbel distribution, while the precise distribution function remains unknown. This study examines two distinct approaches to include P_e, which are detailed in Sec. 6.2.2.

- **initial deflection δ_0**: The initial deflection is considered to be the consequence of construction defects. As per the benchmark suggestion, the highest acceptable value is 6 cm, which is closely monitored during the construction process and serves as an upper limit. Hence, the deflection is represented by the interval quantity $\delta_0 \in [0\,\mathrm{cm}, 6\,\mathrm{cm}]$, as negative deflections provide equivalent outcomes, albeit with buckling occurring in the other direction.

- **yield strength y_0**: Considering the material parameters, a large amount of available data is assumed, such that a precise probability distribution can be assumed. Here, the yield strength is represented by a log-normal probability density function with a mean of 400 MPa and a standard deviation of 32 MPa, as seen in Fig. 6.12a).

- **Young's modulus E**: Similar to the yield stress, it is assumed that the distribution of Young's modulus follows a log-normal probability density function. The mean value is $210,000$ MPa with a standard deviation of $8,400$ MPa, as shown in Fig. 6.12b).

Given that the column is supported by hinges on both ends, the buckling mode is Euler mode 2. The critical load may be calculated using the formula $P_\mathrm{b} = \pi^2 E I_y / L^2$. The limit-state

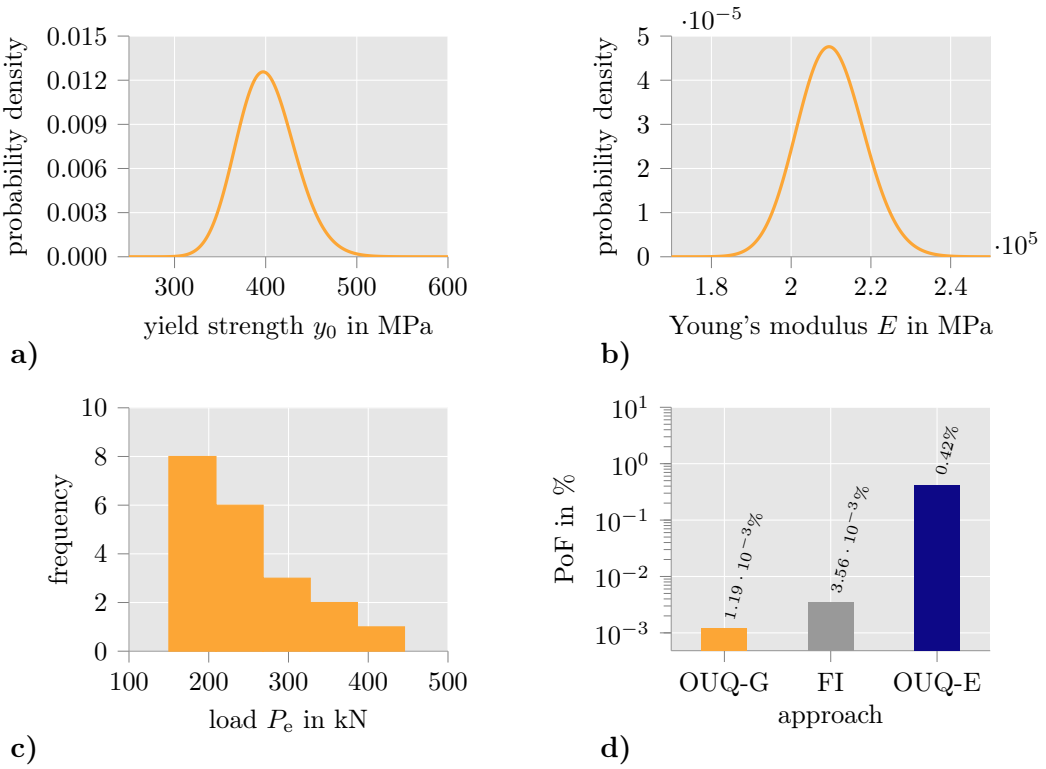

Figure 6.12: Log-normal probability density function of: **a)** yield strength y_0 and **b)** Young's modulus E as well as a histogram of observed values of the environmental load P_e in **c)**. In subfigure **d)**, the computed upper bounds on the PoF are plotted for the two investigated approaches based on the OUQ and the fuzzy-interval approach (FI) from [116]. Therein, OUQ-G represents the approach utilizing the Gumbel distribution function and OUQ-E characterizes the incorporation of the environmental load as epistemic uncertainty. Taken from Miska and Balzani [96].

function g is then defined by

$$g\left(P_\mathrm{p}, P_\mathrm{e}, \delta_0, y_0, E\right) = 1 - \left(\frac{P_\mathrm{p} + P_\mathrm{e}}{y_0 A} + \frac{(P_\mathrm{p} + P_\mathrm{e})\delta_0}{y_0 W_\mathrm{y}} \cdot \frac{P_\mathrm{b}(E)}{P_\mathrm{b}(E) - P_\mathrm{p} - P_\mathrm{e}} \right). \tag{6.17}$$

If the limit-state function produces a value less than zero, the column fails. The benchmark problem aims to obtain certification for the proposed structure based on current standards, which mandate a failure probability of less than $1.3 \cdot 10^{-6}$. Therefore, it is satisfactory to calculate only the maximum bound on the PoF and compare it to the provided threshold. It should be noted that the subsequent computations were repeated 10 times to verify the presence of global optimizers. Identical outcomes were achieved for all 10 computations, up to the level of accuracy specified by the given values.

Estimating the parameters of a Gumbel distribution (OUQ-G) As stated in the above list of uncertain parameters, two distinct approaches are being examined to incorporate the environmental load P_e. The first method involves estimating the parameters a_e and b_e of a Gumbel distribution by fitting it to the given data. This fitting process is carried out using the software-package *scipy* [157]. However, the 20 sample points that are currently available are inadequate for accurately estimating these parameters. As a result, the parameters a_e and b_e of the Gumbel distribution are being examined within a 95% confidence interval. Furthermore, the parameter values of the best fit to the available data are regarded as a mean constraint within a ±5% range. This leads to the following bounds on the parameters of the Gumbel distribution: $a_\mathrm{e} \in [188.0, 236.0]$ kN with $\mathbb{E}[a_\mathrm{e}] \in [201.4, 222.6]$ kN and $b_\mathrm{e} \in$

$[37.0, 74.0]$ kN with $\mathbb{E}[b_e] \in [49.685, 54.915]$ kN. As there are no fuzzy numbers involved in this case, the upper limit on the PoF is a scalar value. Based on the specified data limitations, the calculation of the maximum limits results in $\mathcal{U} = 1.19 \cdot 10^{-5} > 1.3 \cdot 10^{-6}$. This means that the problem cannot be certified.

This lack of certification of the problem aligns with the findings of [116] and particularly with the fuzzy-interval approach described in Section 3.2 of [116]. The chosen data representation and solution scheme in this study are comparable to the approach used in the aforementioned source. The fuzzy-interval approach provides an upper bound on the PoF of $\mathcal{U} = 3.555 \cdot 10^{-5}$. This value is almost three times larger than the result obtained by the OUQ method, cf. also the comparison in Fig. 6.12d). The discrepancy arises from different assumptions made about the data, specifically regarding the Gumbel parameters. In this case, additional information in the form of a mean constraint was taken into account, which leads to the smaller upper bound on the PoF. While the benchmark proposal does not contain information on the required computing time, but based on the same sample size for the Monte Carlo integration (10^8 samples) and a population size of 100 population members, the average computation time over the ten calculations was approximately 64,600 seconds.

Moment constraints on the environmental loads (OUQ-E) The second examined variant does not presuppose a Gumbel distribution for the environmental load. Instead, it relies just on bounds for the first three moments. Despite the data's insufficient amount, the inclusion of a third order moment is justified to accommodate for the data's skewness. To enable a comparison to the preceding approach, the bounds on the moments are chosen, such that the first three moments of all possible realizations of Gumbel distributions are within the specified bounds, which also includes the sample moments of the given data. Moreover, it is crucial to select an appropriate range for the environmental load, taking into consideration that a narrow interval, such as $P_e \in [100.0, 500.0]$ kN would result in a failure region where the probability of failure can only be computed as 0% due to numerical precision limitations. With that, the constraints on the environmental load are $P_e \in [0.0, 1000.0]$ kN with $\mathbb{E}[P_e] \in [209.4, 279.0]$ kN, $\mathbb{E}[(P_e - \mathbb{E}[P_e])^2] \in [2251.91, 9007.66]$ kN^2 and $\mathbb{E}[(P_e - \mathbb{E}[P_e])^3] \in [121775, 974204]$ kN^3. Under these specific data assumptions, the degree of freedoms for the optimization problems in the OUQ are increased by 1 compared to the previous variant. This increase is due to the removal of two uncertain quantities, namely the two parameters of the Gumbel distribution, each having 3 degrees of freedom, whilst the uncertain quantity related to the environmental load necessitates exactly 7 degrees of freedom. However, in this case, no uncertain assumption about the type of distribution function is taken into account, which makes the results more reliable. The adjusted data restrictions result in a maximum upper bound on the PoF of $4.2 \cdot 10^{-3}$. This value is more than 100 times higher than using the Gumbel distribution with imprecise parameters, cf. also the comparison in Fig. 6.12d). By using the Gumbel distribution as a model for limited and uncertain data, one might derive significantly contrasting conclusions about the safety of a structure. This example illustrates the substantial influence of various assumptions on the data that is available. These assumptions must be set with great caution, but they can also provide vital understanding of how the problem behaves under different input choices. Clearly, the problem can not be positively certified with this result either. The average calculating time for the 10 repeated calculations is about $39,300$ seconds, which is much lower than in the previous example. Therefore, altering the underlying assumptions regarding the data not only affects the outcome, but also alters the behavior of the solution process.

6.2.3 S-Rail Sheet Metal Forming Process

The S-Rail forming process is a well-known problem used as a benchmark for sheet metal forming simulations. It was introduced in the Numisheet conference in 1996, cf. Ferreita Duarte and Barata da Rocha [38] and Fig. 6.13 for an illustration. The problem involves pushing an S-shaped die into a flat sheet metal that is securely held in a holder, which results in the desired shape of the sheet. To mitigate significant in-plane normal stresses, lubricants are typically applied to the contact surface between the die and the holder to minimize friction. In this case, the numerical simulation is conducted using the FE-software LS-Dyna R8.1.0 [82].

Definition of the Considered Uncertain Quantities Four different quantities, which are either input parameters for the model or ultimate values for the determination of failure, are regarded to be uncertain. The first two uncertain variables are associated with the hardening behavior of the steel in the sheet metal. In Miska and Balzani [93], the uncertainties in the macroscopic material parameters of a DP600-steel were quantified, which is also discussed in Chapter 5 of this thesis. For the application in this example, the obtained stress-strain curves are fitted for the Swift hardening law incorporated within LS-Dyna, cf. Swift [148], which takes the form $\boldsymbol{\sigma}_y = k\,(\boldsymbol{\varepsilon} + \boldsymbol{\varepsilon}_p)^N$. Therein, $\boldsymbol{\sigma}_y$ denotes the yield stresses, $\boldsymbol{\varepsilon}$ refers to the elastic logarithmic strains, and $\boldsymbol{\varepsilon}_p$ represents the effective logarithmic plastic strains. The yield curve's shape is influenced by the strength coefficient k and the exponential hardening coefficient N, such that these two parameters are considered to be uncertain. The probability distributions of both parameters are derived through a fitting procedure, in which stress-strain curves based on the Swift hardening law are adjusted to stress-strain curves obtained from virtual experiments conducted through computational homogenization of statistically similar volume elements as described in Chapter 5. The fitting was accomplished through the process of least-square minimization utilizing the LS-Opt 5.2 [81] optimizer. The obtained stress-strain curves with respective realizations of k and N are used to generate the corresponding histograms in Fig. 6.14a) and Fig. 6.14b). Since the material parameters k and N are strongly correlated, it is advantageous to consider only the strength coefficient k as uncertain quantity in order to enhance the efficiency of the uncertainty quantification. The exponential hardening coefficient N is thus computed from the parameter k using a third order polynomial fit:

$$\begin{aligned} N(k) = \;& 1.661789 \cdot 10^{-10}\,\widehat{k}^3 - 5.0435951923582 \cdot 10^{-7}\,\widehat{k}^2 \\ & + 6.5798512505658687 \cdot 10^{-4}\,\widehat{k} - 0.11730087709283931741, \end{aligned} \tag{6.18}$$

wherein $\widehat{k} = k\frac{1}{\mathrm{MPa}}$ denotes the unitless nominal value of the strength coefficient k. The correlation polynomial is also depicted in the correlation plot Fig. 6.14c). The histograms indicate that the uncertainty of the material parameter k can be represented by a beta distribution.

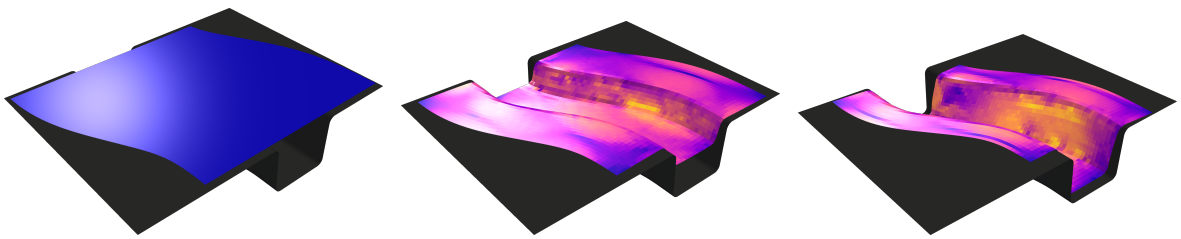

a) **b)** **c)**

Figure 6.13: Illustration of the considered S-Rail forming process with **a)** the originally flat sheet metal, **b)** an intermediate step and **c)** the final deformed state of the sheet metal. The contour depicts the stress magnitude, the punch and the binder are omitted for illustration purposes. Taken from Miska et al. [100].

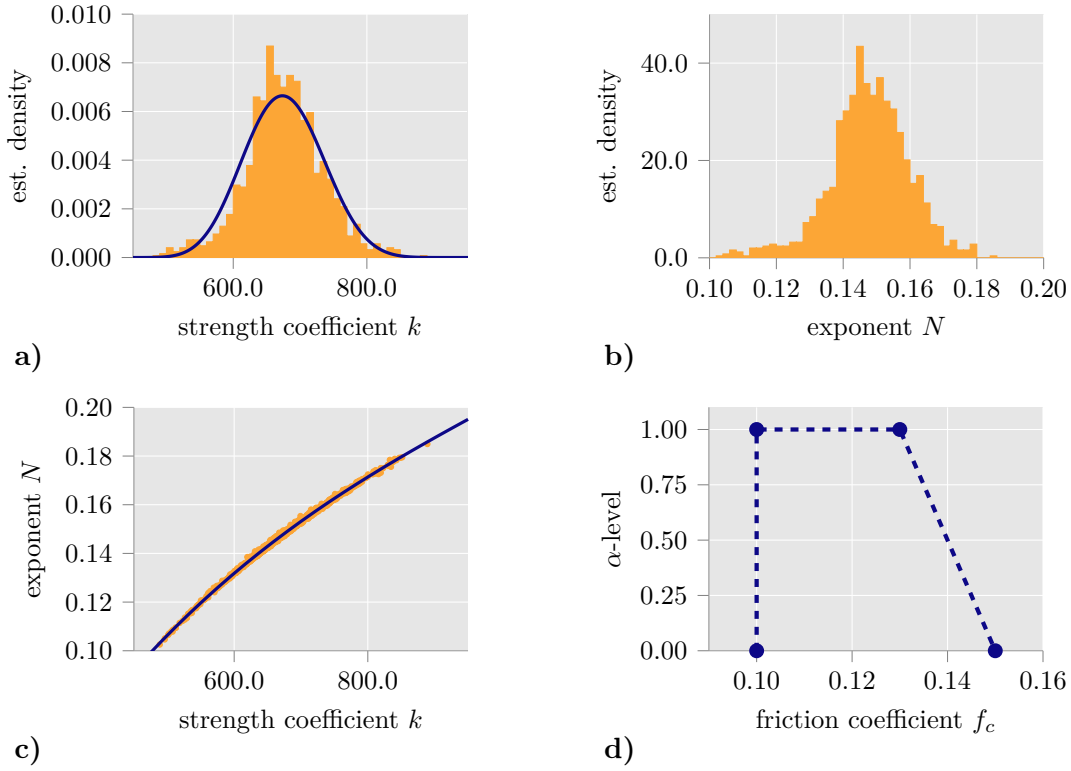

Figure 6.14: Histograms of **a)** the strength coefficient k and **b)** the exponential hardening coefficient N for the used hardening law. Additionally, the beta probability density function for parameter k is plotted in a). **c)** Correlation of parameter k and N with fitted third-order polynomial, cf. Eq. (6.18). **d)** Fuzzy number of the friction coefficient f_c. Taken from Miska et al. [100].

This distribution is defined on the interval $k \in [400.0, 1000.0]$ MPa and has shape parameters $q_1 = 11.6161$ and $q_2 = 13.6657$.
The third uncertain parameter is the friction coefficient, denoted by f_c, which characterizes the friction between the sheet metal and the forming tools in terms of the Coloumb friction law. Due to the difficulty in measuring this quantity, there are only a limited number of data points available, cf. Figueiredo et al. [42]. The data is used to evaluate two distinct intervals for the friction coefficient. Consequently, the uncertainty of the friction coefficient is represented by a trapezoidal fuzzy number, cf. Fig. 6.14d). The interval for the friction coefficient at level $\alpha = 0.0$ is defined as $\widetilde{f}_c^{\alpha=0.0} \in [0.1, 0.15]$. This interval includes all the measured values. Similarly, the interval for the friction coefficient at level $\alpha = 1.0$ is defined as $\widetilde{f}_c^{\alpha=1.0} \in [0.1, 0.13]$. This interval covers the measured values after the tools have been used a few times. Additionally, a mean constraint $\mathbb{E}[\widetilde{f}_c] \in [0.105, 0.115]$ is assumed to be a rectangular fuzzy number. This means that the interval remains the same at every α-level.
The final uncertain variable is linked to the failure of the forming process. In this case, failure is determined using the Cockroft-Latham criterion, cf. Björklund et al. [17] or Tarigopula et al. [152], which is defined by $W_C = \int_0^{\bar{\varepsilon}} \max(\sigma_1, 0) \mathrm{d}\bar{\varepsilon} \geq W_C^{\mathrm{ult}}$ with $\bar{\varepsilon}$ being the equivalent plastic strain, σ_1 the first principial stress and W_C^{ult} the ultimate admissible value. Here, the value of W_C is calculated for each finite element of the sheet metal, such that in the maximum value over the entire sheet metal $\max[W_C(k, f_c)]$ can be determined and then compared to W_C^{ult}. With all parameters being defined, the limit-state function g of this example follows as

$$g(k, f_c, W_C^{\mathrm{ult}}) := W_C^{\mathrm{ult}} - \max[W_C(k, f_c)], \tag{6.19}$$

in which $\max[W_C(k, f_c)]$ refers to the maximum value of the Cockroft-Latham value obtained from a finite element simulation and W_C^{ult} is the uncertain ultimate value for this criterion. Due to the limited data availability for W_C^{ult} for different materials, the measured value for DP-800 steel from [152] is adjusted to account for DP-600 steel. This adjustment results in a range of $W_C^{ult} \in [450.0, 550.0]\,\mathrm{MPa}$.

Case 1: Analysis of Uniformly Distributed Material Parameters First, the sheet metal forming problem is examined under the assumption, that the material properties, namely the strength coefficient k and the exponential hardening coefficient N, remain constant across the sheet metal domain. Since the solution of the forming process involves a numerical simulation in terms of finite elements, an Artificial Neural Network (ANN) is used to approximate the FE simulation. The ANN was constructed in collaboration with Prof. Dr.-Ing. Steffen Freitag and has three inputs (friction coefficient f_c, strength coefficient k, and exponential hardening coefficient N) and one output ($\max[W_C(k, f_c)]$). The network architecture is 3–5–5–1, with two hidden layers and five hidden neurons in each layer. 375 FE simulation results were used, and a regression coefficient of R = 0.99978 was achieved.

OUQ Analysis Using the previously described ANN, the probability of failure for the forming problem is computed by using the extended Optimal Uncertainty Quantification. Again, the optimization problems are addressed using the LSHADE44-optimizer [119], in conjunction with the mystic optimization package [88, 87], which automatically adjusts the hyperparameters of the Differential Evolution method. Due to the presence of both aleatory and epistemic uncertainties, a numerical integration according to Eq.(6.10) has to be performed in order to evaluate the function χ. Furthermore, the first method presented in Sec. 6.1.1 for the incorporation of aleatory uncertainties is studied. This involves calculating the first ten moments of the beta-distribution of parameter k and gradually imposing them as constraints. The convergence behavior of the bounds on the PoF is examined, ultimately converging towards the integration result. To accommodate the expanding search space, the population size is exponentially expanded, ranging from 150 to 5700, as the number of moment constraints increases. The Monte Carlo integration strategy utilizes a population size of 50. For the Monte Carlo integration itself, the Combination Line Sampling method proposed in [114] is employed.

The upper bounds on the PoF are displayed in Fig. 6.15a) for the level $\alpha = 0.0$ of the considered fuzzy numbers. The lower bound on the PoF is always zero in all scenarios. As evident, the upper bound diminishes as the number of moment constraints increases, aligning with the anticipated outcome derived from the findings in Sec. 6.2.1. In addition, the inclusion of lower order moments results in a significant decrease in the upper bound, while the introduction of higher order moments of order five or greater leads to only a slight decrease. In contrast to the previous moments, the incorporation of order ten resulted in a significant decrease in the calculated upper bound. However, when compared to the maximum bound obtained from numerically integrating the probability density function for the material parameter, all calculated upper bounds using the moment constraint approach are larger. Hence, the findings align with Sec. 6.2.1, which demonstrated that integrating the probability density functions over the failure region is essential for accurately accounting for aleatory uncertainties within the framework of the OUQ. When comparing the computing times of both approaches, it is found that similar times can be achieved for the integration approach and the run with 10 moment constraints. Specifically, the integration approach takes an average of $1.16 \cdot 10^4$ seconds over ten independent computations, while the moment constraint approach takes $1.1 \cdot 10^4$ seconds. This discrepancy to the results of Sec. 6.2.1 can be attributed mostly to the use of an advanced Monte Carlo technique.

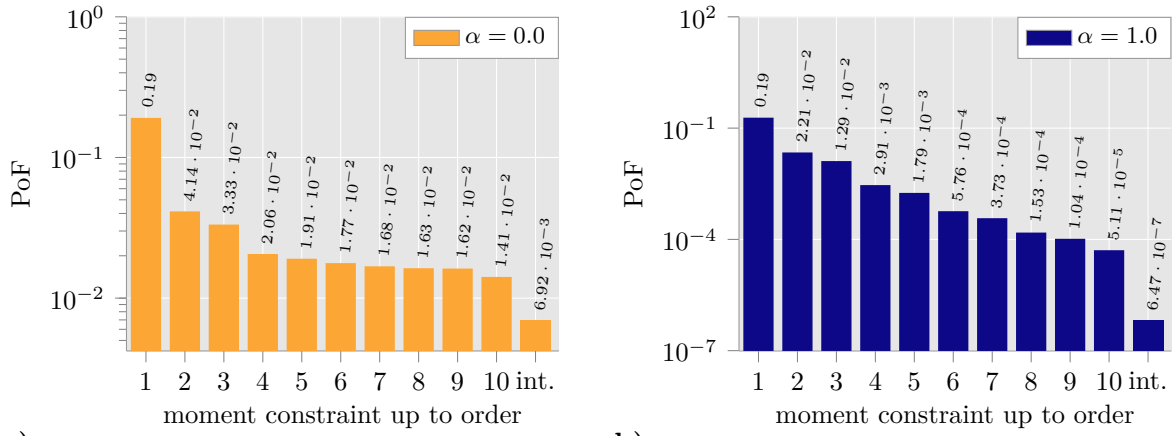

Figure 6.15: Convergence of the upper bound on the PoF for an increasing amount of moment constraints for **a)** the $\alpha = 0.0$ and **b)** the $\alpha = 1.0$ level of the fuzzy friction parameter. In both cases, the bar labelled "int." denotes the resulting bound from the integration approach, cf. also Eq. (6.10). Taken from Miska et al. [100].

Similar findings can be observed in the analysis at level $\alpha = 1.0$, where a consistent decrease in the upper bound of the PoF can also be observed. However, because the friction parameter has a tighter range, the calculated bounds on the PoF are smaller compared to the initial α-level that was investigated. Curiously, the upper bound for a single moment limitation on the strength coefficient remains unchanged. In this situation, the upper bound obtained via the integration method is significantly reduced, emphasizing the benefits of this strategy in including aleatory uncertainty. Furthermore, the derived bound is significantly smaller than the upper bound at level $\alpha = 0.0$, indicating that the forming process is much more feasible for the narrower friction range. This result is of major importance for the design of such a process. The identification of the most advantageous design can be achieved by incorporating various intervals on the parameter using fuzzy numbers. In this scenario, the manufacturer must guarantee that the friction parameter remains within the correct range by, for example, applying suitable lubrication.

Case 2: Analysis of Randomly Distributed Material Parameters Unlike the preceding scenario, in the second variant, the material parameters are assumed to vary in space and are therefore represented by random fields. Given the absence of spatial correlation data for parameter k, the example focuses on the most extreme scenario, where there is no autocorrelation among the elements of the finite element simulation. This implies that the correlation length of $l_c \to 0$, whilst in the previous variant, where the parameters were constant, an infinitely large correlation length $l_c \to \infty$ was present. Undoubtedly, neither of these examples accurately represents reality, but studying extreme cases enhances the understanding of the difference in results. The strength coefficient is distributed according to a beta distribution, whereas the hardening exponent is determined by the polynomial correlation fit.

The two alternatives proposed in Sec. 6.1.4 are applied and compared for the inclusion of the random field of material parameter k. The first variant involves doing a regression analysis on the statistical data obtained from a Monte Carlo simulation of the problem, which includes many realizations of a random field. The second variant involves applying the nested Optimal Uncertainty Quantification (OUQ) approach. Both approaches require the execution of Monte Carlo simulations on the problem, which includes random fields. Thus, a limited collection of friction coefficient points f_c is chosen, for each of which, 200 random fields of

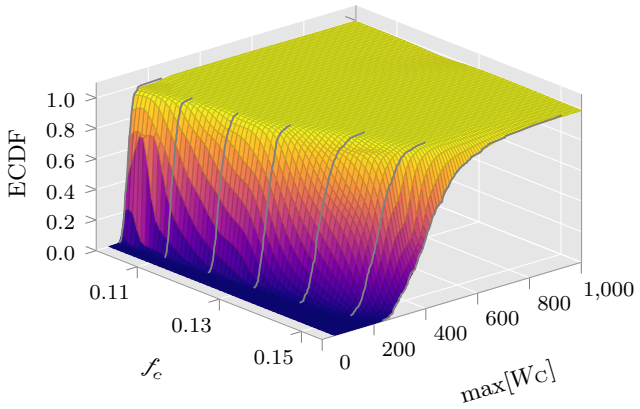

Figure 6.16: Illustration of the data obtained from the random field simulations, reordered as ECDF, and indicated by the thin grey lines. Additionally, the surface plot of the constructed ANN for the entire parameter space is shown. Adapted from Miska et al. [100].

the material parameter k are created and subsequently computed. The chosen points are $f_c \in \{0.10, 0.11, 0.12, 0.13, 0.14, 0.15, 0.155\}$. From each finite element solution, the maximum Cockroft-Latham value, denoted as $\max[W_c(k, f_c)]$, is derived and reordered in a manner that allows for the creation of estimated cumulative probability distribution functions (ECDF). These functions are represented by thin grey lines in Fig. 6.16. The generated data acts as the initial reference for the two examined variants that are subsequently described.

Construction of the ANN-surrogate An artificial neural network is constructed to predict the cumulative probability (ECDF) for a given friction coefficient f_c and the maximum Cockroft-Latham value $\max[W_c(k, f_c)]$ of a random field simulation. The ANN uses two hidden layers and eight hidden neurons in each layer, with a logistic activation function in each hidden neuron and the output neuron. The ANN is trained on 1400 FE simulations resulting from the 200 random field simulations for each of the values chosen for f_c. The ANN's predictions are compared with the results from the FE simulation results, showing good generalization and prediction performance.

Given that the material parameters are included in the random field simulation, the uncertainty quantification using the extended OUQ method is reduced to only the friction coefficient and the ultimate Cockroft-Latham value. The developed ANN is utilized to assess the probability of failure occurring for a specific combination of the two aforementioned variables. The optimization problems are solved using the LSHADE44-optimizer [119] implemented in the mystic optimization package [88, 87] with a population size of 100. The lower bound on the PoF is calculated as 0.0 for both investigated α-levels of the friction coefficient. The upper bound on the PoF is calculated to be 0.002 for level $\alpha = 0.0$ and to 0.0 for level $\alpha = 1.0$. This information can also be seen in the comparison of the findings shown in Fig. 6.17. Due to the fact that the OUQ problem involves just two quantities with at most a mean constraint, the optimizations within the OUQ are rather simple to solve. Specifically, with the given settings, it took $9.33 \cdot 10^1$ seconds and $8.86 \cdot 10^4$ seconds to solve the problem at the two levels, respectively. Nevertheless, since substantial preliminary work is necessary for the OUQ calculations, as it involves conducting Monte Carlo simulations on the finite element model and training and validating the artificial neural network, the overall time required for this method is higher.

Nested OUQ analysis As alternative to the regression of the ECDFs obtained from the random field simulations by an ANN, in this second variant only bounds on $\max[W_c(f_c)]$ and bounds on the moments therefrom should be considered. The maximum value obtained from the simulations, $\max[W_c(f_c)]$, depends not only on the realization of the random fields for the strength coefficient, but also on the constant uncertain friction coefficient. Therefore, the nested OUQ method, as proposed in Sec. 6.1.4 is applied. For this purpose, the standard deviation of the mean and the standard deviation of the variance resulting from the small sample size of the Monte Carlo simulations are computed and used as bounding values for the two moments, cf. the obtained values in Tab. 6.2. Therefore, the outer OUQ problem is comprised of the friction coefficient and the ultimate Cockroft-Latham value, taking into account their respective constraints and α-levels, similar to the previous variations. The inner problem consists of the maximum Cockroft-Latham value with the mentioned two moment constraints. The population size for the outer problem is defined to 50, whereas the inner problem utilizes a smaller population size of 30. Due to the substantial computing effort caused by the nested approach, which requires solving a large number of optimization problems, parallelizing the outer problem became necessary. In this case, a total of 10 individual threads are employed to address 10 inner optimization problems concurrently. When only the mean constraint is taken into account, the PoF has lower and upper bounds of 0.4098 and 0.356 respectively, at the specified α-levels. By imposing the additional constraint on the variance, the upper and lower bounds are decreased to 0.049 and 0.008 correspondingly. This reduction is a result of the inclusion of additional information. The computation times are $5.85 \cdot 10^3$ seconds and $5.45 \cdot 10^3$ seconds for the mean constraint only, and $1.17 \cdot 10^4$ seconds and $7.19 \cdot 10^4$ seconds for both the mean and variance constraints. These values are considerably larger than those of the previous method, as anticipated. For neural networks, the optimizer can evaluate the entire population in one iteration by leveraging the vectorizing capabilities of current CPUs. On the other hand, in the nested OUQ approach, a separate optimization problem must be formulated and solved for each individual in the population. This is considerably more costly in terms of computer resources.

The upper bounds on the PoF resulting from the various proposed approaches are depicted in Fig. 6.17 for the two examined levels, $\alpha = 0.0$ and $\alpha = 1.0$. The bounds obtained from the nested OUQ approach, specifically when using only a mean constraint (NOm) or both a mean and variance constraint (NOv), are considerably larger than the bounds derived from the OUQ computations, in which the ANN was employed to regress the ECDF, referred to as ANN_{RF}. This can be attributed to the data obtained from the random field, which was incorporated for the individual calculations. In the ANN_{RF} approach, the complete distribution of the target quantity is represented by the empirical cumulative distribution function, but in the nested OUQ approaches, only a limited amount of moment information on that target quantity is considered. As a result, the inner OUQ problems were able to generate more unrestricted

Table 6.2: Resulting upper bounds on $\max[W_c(f_c)]$ from the random field.

f_c	mean in MPa	variance in MPa^2
0.10	121.5 ± 4.7	319.5 ± 87.7
0.11	136.8 ± 4.6	306.4 ± 40.6
0.12	160.7 ± 6.1	526.2 ± 53.5
0.13	185.5 ± 6.8	671.6 ± 69.3
0.14	236.4 ± 11.8	1980.8 ± 249.4
0.15	299.4 ± 14.5	3006.2 ± 317.1

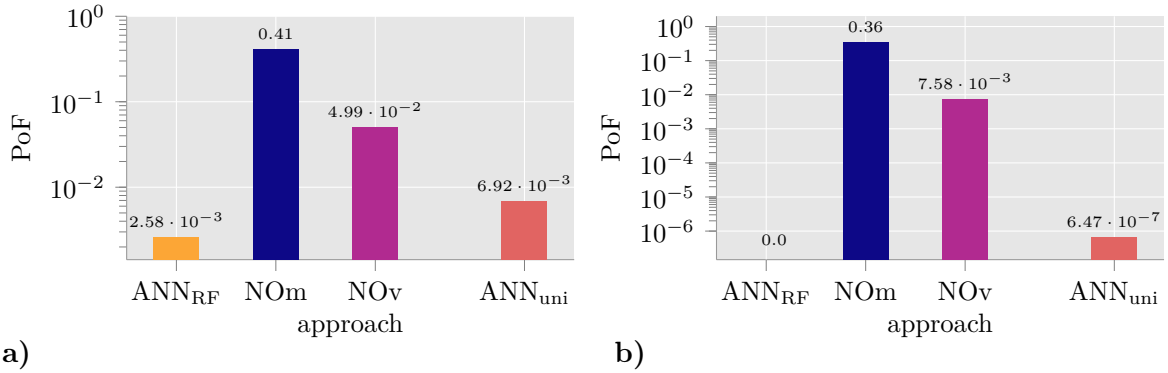

Figure 6.17: Comparison of the resulting upper bounds on the PoF for **a)** the $\alpha = 0.0$ and **b)** the $\alpha = 1.0$ level of the fuzzy friction parameter. Bounds resulting from the approach assuming uniform material parameters are labelled "ANN_{uni}", bounds resulting from random fields with the utilization of an ANN for the regression of the ECDF are labelled "ANN_{RF}". If only limited data from the random field is incorporated following the proposed nested OUQ approach, the bounds labelled "NOm" (only mean constraint) and "NOv" (mean and variance constraint) were obtained. Taken from Miska et al. [100].

probability measures, thus resulting in wider limits on the PoF. Again, the results emphasize the significance of the decision regarding the quantity of information that can be inferred from random field simulations. Nevertheless, none of the suggested methodologies can be universally favored over the other, and the selection of the technique must be based on the data that is accessible. Furthermore, the findings obtained from the calculations assuming uniform material parameters are displayed in Fig. 6.17, and are labeled as ANN_{uni}. As anticipated, the various assumptions on the distribution of material parameters result in distinct limits on the PoF. The bounds obtained using the uniform material distribution method (taking into account the complete distribution function) are larger compared to those obtained from the random field simulation, which also considers the complete ECDF information.

7 Reliability-Based Design Optimization Incorporating the Extended OUQ

With the availability of a framework for the computation of the mathematically sharpest bounds possible on a probabilistic event of interest in form of the extended Optimal Uncertainty Quantification from the preceding Chapter 6, the remaining challenge of a design optimization with reliability constraints is accounted for in this chapter. Then, the overall objective of this thesis, the design optimization of a car front bumper can be examined in the numerical example section of this chapter. The methods and examples shown in this chapter are already published as a preprint in Miska and Balzani [98] and are submitted to an international journal for publication. Additionally, parts of this chapter have been published in a conference proceeding Miska and Balzani [97].

7.1 Reliability-Based Design Optimization

Methods from the field of reliability-based design optimization (RBDO) aim to find the most optimum solution for a specific problem while ensuring that it meets at least one reliability constraint. In this regards, the reliability of said problem is often assessed in terms of the by now well-known probability of failure (PoF). However, as the problem can be influenced not only by aleatory uncertainties, which can be accurately described using probability density functions, but also by epistemic uncertainties, which involve intervals or fuzzy numbers, the PoF cannot be calculated to be a precise scalar value but rather to lie within a certain interval, as already discussed previously. Therefore, it is essential to utilize a sophisticated framework such as the extended OUQ for the polymorphic uncertainty quantification, which is necessary within the RBDO. Therein, the polymorphic uncertainties do not only have an influence on the PoF and by that, on the reliability constraint, but also on the evaluation of the cost function itself. Based on these premises, the challenge of a reliability-based design optimization can be formally expressed by

$$\min_{\boldsymbol{\theta}} K(\boldsymbol{\theta}, \boldsymbol{Z}) \quad \text{s.t. } C_j(\boldsymbol{\theta}, \boldsymbol{Z}) \leq 0, \tag{7.1}$$

wherein K represents the cost function, $\boldsymbol{\theta}$ is the vector of optimization parameters, i.e. the degrees of freedom of the optimization problem, and $\boldsymbol{Z} := [\boldsymbol{Y}, \widehat{\boldsymbol{Y}}]$ denotes the vector of epistemic $\boldsymbol{Y}$ and aleatory $\widehat{\boldsymbol{Y}}$ uncertain quantities influencing the physical problem M. Since the cost K is influenced by aleatory and epistemic uncertainties, by the same reasoning as used for the PoF, a probabilistic quantity can only computed to be within an certain interval. Therefore, in addition to the design optimization, inner optimizations are required to identify the optimal bounds, leading to the definition of the cost function as

$$K(\boldsymbol{\theta}, \boldsymbol{Z}) := \max_{\boldsymbol{Y}} \left[\mathbb{E}_{\widehat{\boldsymbol{Y}}}(M(\boldsymbol{\theta}, \boldsymbol{Z})) \right]. \tag{7.2}$$

Here, the expectation $\mathbb{E}$ is chosen to quantify the impact of aleatory uncertainties on the physical model M. This is however neither necessary nor an unique choice, exemplary alternatives are quantiles. Then, an optimization as known from the extended OUQ is performed to identify the bound of interest.

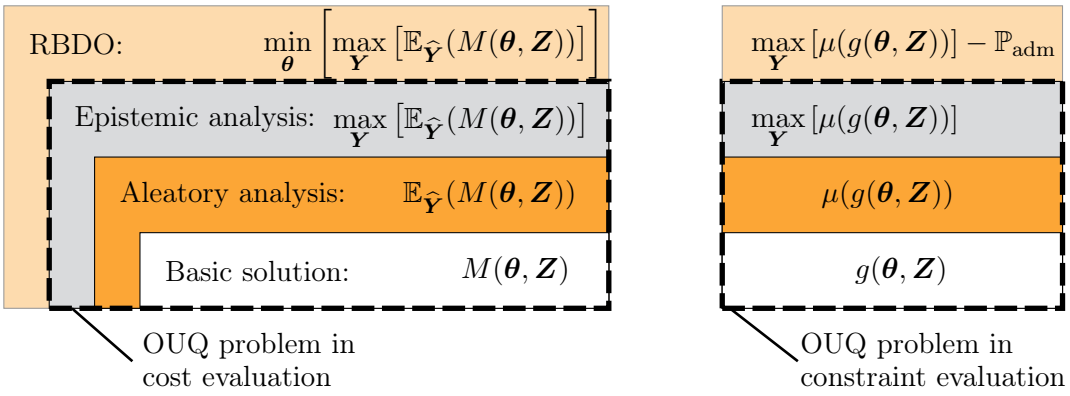

Figure 7.1: Integration of the extended OUQ framework within a RBDO context with the necessary steps for the evaluation of the cost function on the left and for the reliability constraint on the right. Adapted from Miska and Balzani [98] and Miska and Balzani [97], respectively.

In addition to the cost function, at least one constraint is present for the RBDO, the reliability constraint. The reliability constraint ensures, that any design $\boldsymbol{\theta}$, which leads to a PoF larger than an admissible threshold defined before, is discarded as infeasible design. By that, only safe designs are considered for the optimization and the required safety of the product is ensured. Formally, the reliability constraint reads

$$C_1(\boldsymbol{\theta}, \boldsymbol{Z}) := \max_{\boldsymbol{Y}} [\mu(g(\boldsymbol{\theta}, \boldsymbol{Z}))] - \mathbb{P}_{\text{adm}}, \tag{7.3}$$

wherein $\mathbb{P}_{\text{adm}}$ denotes the maximum admissible value for the PoF and $\max_{\boldsymbol{z}} [\mu(g(\boldsymbol{\theta}, \boldsymbol{Z}))]$ poses a second inner optimization problem in order to identify the largest bound on the PoF of the problem due to the presence of uncertainties. Whilst the notation used here assumes the PoF as suitable quantification of the safety or reliability of a problem, different measures may be used as well, if the problem mandates.

Based on the definitions of the cost function in Eq. (7.2) and the reliability constraint in Eq. (7.3), two optimal bounds on probabilistic quantities need to be computed for the evaluation of a single design $\boldsymbol{\theta}$. Hence, employing the extended Optimal Uncertainty Quantification as introduced in Chapter 6 is a sensible decision. Using this approach, all explained features such as the computation of the mathematically sharpest bounds without the necessity for an uncertified specification of a PDF on epistemic quantities can be used. Thereby, different uncertainty models ranging from simple intervals, fuzzy numbers over bounds on moments to imprecise or precise probability distribution functions can be utilized for the polymorphic uncertainty quantification. The incorporation of the extended Optimal Uncertainty Quantification into a reliability-based Design Optimization framework results in a nested optimization or a double-loop approach, as illustrated by Fig. 7.1 and Alg. 9.. The outer optimization focuses on optimizing the design for which the design parameters $\boldsymbol{\theta}$ represent the degrees of freedom. The inner optimizations specifically target the quantification of uncertainty utilizing the extended Optimal Uncertainty Quantification approach. Hence, the efficiency of the extended OUQ is a crucial factor, since the solution of two independent OUQ problems for each design candidate $\boldsymbol{\theta}$ leads easily to a large number of necessary OUQ solutions for the entire design optimization, in which a significant number of designs has to be evaluated.

The description of the RBDO until now suggested a distinction between design parameters $\boldsymbol{\theta}$ and uncertain quantities $\boldsymbol{Z}$. Yet, the double-loop approach enables the combination of both, i.e. a dependency of an uncertainty quantity from a design parameter such as $Y^{(m)}(\theta^{(j)})$ can

Algorithm 9: Cost function for RBDO

Data: Design candidate $\boldsymbol{\theta}_m$, max. bound on PoF $\mathbb{P}_{\text{adm}}$, uncertainties $\boldsymbol{Z}$
Result: cost value K

update $\boldsymbol{Z}(\boldsymbol{\theta})$ if dependency exist
compute value for cost $K = \max_{\boldsymbol{Y}} \left[\mathbb{E}_{\widehat{\boldsymbol{Y}}}(M(\boldsymbol{\theta}, \boldsymbol{Z}))\right]$
compute PoF $\mu = \max_{\boldsymbol{Y}} \left[\mu(g(\boldsymbol{\theta}, \boldsymbol{Z}))\right]$

if $\mu > \mathbb{P}_{adm}$**:**
  discard candidate $\boldsymbol{\theta}_m$

if $K < K_{best}$**:**
  $K_{\text{best}} = K$
  $\boldsymbol{\theta}_{\text{best}} = \boldsymbol{\theta}_m$

return K

be considered. Such a scenario can be interesting to determine the allowable uncertainty in a specific quantity, whilst a desired target in terms of the cost function are met. Due to the formulation of the dependency, the uncertainty model resulting from $Y^{(m)}(\theta^{(j)})$ is a fixated model for a specific design candidate and the uncertainty analysis can be performed as done before. For a changing design however, the model of the uncertainty may change in dependence of the actual implemented dependency, such that the uncertainties can evolve during the design optimization. In practice, a rather easy example is an interval of fixed size w, for which the midpoint can be considered as design variable, leading to $Y^{(m)} \in \left[\theta^{(j)} - w/2, \theta^{(j)} + w/2\right]$. Due to the unique features of the extended OUQ, not only the range of uncertain quantities can be modified, but also the bounds on moments or imprecise probability functions. Generally, it is even possible to change the type of a PDF in dependence of a design parameter $\theta^{(j)}$. For the scope of this work, however, only the optimization of an interval midpoint is considered in example pertaining the optimization of the car front bumper.

7.2 Numerical Examples

After the theoretical introduction of the integration of the extended OUQ within a reliability-based design optimization context, in this section the performance of the resulting framework is studied by means of two examples. The first example is the continuation of the benchmark problem of Papaioannou et al. [116], from which the first challenge was solved in Sec. 6.2.2. The straightforward nature of the underlying analytic problem enables the comparison of various frameworks for uncertainty quantification, as it eliminates the need for costly numerical simulations such as finite elements. The second scenario involves the investigation of a more intricate problem, which aims to determine the best arrangement of locally laser-hardened zones on a exemplary car front bumper. This example involves the numerical simulation of three sequential processes and therefore depends on the creation of surrogate models to ensure that the computational costs for the Reliability-Based Design Optimization (RBDO) remains within a manageable range.

Both examples utilize the programming language Julia, cf. Bezanson et al. [12], to accomplish the design optimization and uncertainty quantification. Again, the LSHADE44 algorithm, cf. Polakova [119] as an extension to the Differential Evolution method [144] is used for all examples to solve all optimization frameworks, which are in general global and non-convex.

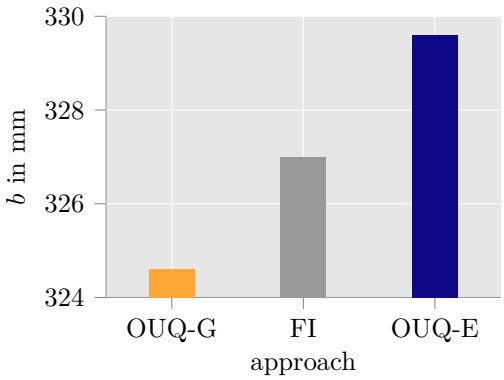

Figure 7.2: Comparison of the computed necessary width b for the column, which ensures that the admissible PoF is not exceeded. Therein, OUQ-G represents the approach utilizing the Gumbel distribution function and OUQ-E characterizes the incorporation of the environmental load as epistemic uncertainty. FI denotes the fuzzy-interval approach from [116]. Taken from Miska and Balzani [98].

The computations are performed on nodes equipped with an Intel Xeon Phi 7210 processor, which has 64 cores running at a maximum frequency of 1.50 GHz, and 92 GB of RAM.

7.2.1 Benchmark of DFG Priority Program 1886

The second challenge of the benchmark [116] consists of a simple reliability-based optimization problem. The first challenge was already assessed in Sec. 6.2.2. The problem of interest is a column with an H-shaped cross-section, which is loaded by a compression force P and will fail due to buckling, see also the illustration in Fig. 6.11. The benchmark's challenge is optimizing the cross-section to minimize the area and, consequently, the amount of material required, while ensuring that the probability of failure does not exceed $\mathbb{P}_{\text{adm}} = 1.3 \cdot 10^{-6}$. While the cross-section has several defining dimensions, just the width b and height h need to be optimized. Furthermore, the ratio between these two dimensions is constant at $b/h = 1$, meaning that there is only one design parameter, $\boldsymbol{\theta} = [b]$, left for optimization. Using this information, the geometric properties of the cross-section are calculated by

$$A = 2bt_b + ht_h, \; W = \frac{ht_h^3}{6b} + \frac{b^2 t_b}{3}, \; I = \frac{ht_h^3}{12} + \frac{b^3 t_b}{6}, \tag{7.4}$$

with $t_h = 10$ mm and $t_b = 15$ mm. Since the area of the cross-section $A = A(\boldsymbol{\theta})$ is a deterministic value, an uncertainty quantification is only required for the reliability constraint. Uncertainties influencing the problem are listed in Sec. 6.2.2, as well as the limit-state function g for the identification of failure.

Since the design optimization problem is linear in its parameters, the outer optimization is solved by a gradient descent approach. The inner optimization problem remains non-linear, for which the mentioned LSHADE44 optimizer is used along with Combination Line Sampling for the Monte Carlo integrations, cf. Papaioannou and Straub [114]. Due to the comparable number of degrees of freedom required by both investigated variants for the environmental load P_{e}, a population size of $n_{\text{pop}} = 50$ and a convergence criterion of 100 iterations without change in the objective are used in both cases. Additionally, 50 sampling lines are employed for the integration. It is important to mention that the subsequent calculations were iterated 8 times to verify the presence of global optimizers. Indeed, the same results up to the precision given in the provided values were obtained for all 8 calculations.

Gumbel distribution with imprecise parameters (OUQ-G) A Gumbel distribution is used to model the environmental load in the first variant. The specific parameters for the imprecise representation of that probability distribution can be found in Sec. 6.2.2. With that, the design optimization yields $b = h = 324.6\text{mm}$ with an associated area $A = 12984\text{mm}^2$ as result. The average computational duration of the 8 computations is roughly 33 hours. When comparing the resulting width to the outcome of the fuzzy-interval approach described in [116], a lesser value is obtained, as shown in Fig. 7.2. The only difference among all the uncertainties taken into account is the environmental load. Therefore, the mean constraint on the parameters of the Gumbel distribution, is also here the decisive factor. The mean constraint limits the range of variation in the environmental load to a small extent, whereas the fuzzy-interval technique considers the worst-case scenarios by using parameter intervals, which in turn necessitates a wider cross-section to ensure safety.

Moment Constraints up to order 3 (OUQ-E) In the second example, only moment information derived from the histogram is included for the environmental load, refer to Sec. 6.2.2 for the specific values. This data provides less accurate information on the environmental load compared to using a probability density function with imprecise parameters. Consequently, the solution of this scenario results in a larger cross-section than for the fuzzy-interval approach. Specifically, $b = h = 329.6\text{mm}$ with $A = 13184\text{mm}^2$ are obtained. These calculations were performed with an average computation time of about 29 hours. This result not only aligns with the varying levels of knowledge for this specific uncertain quantity, but it also aligns with the discoveries from the first challenge of this benchmark in Sec. 6.2.2. In this second scenario, with fixated geometric parameters, a greater Probability of Failure (PoF) was seen compared to the previous scenario, which resulted in a lower PoF than the fuzzy-interval strategy.

7.2.2 Optimal Positions of Locally Laser-Hardened Traces in a Car Front Bumper

The second examined example involves optimizing the design of a car front bumper, with the objective of determining the ideal positioning of locally laser-hardened traces. The primary goal is to optimize the amount of energy absorbed by the front bumper during a crash in order to provide the highest level of protection to the passenger compartment. Finite element computations are used to simulate three distinct steps. Initially, the deep drawing process of a sheet metal is simulated to transform it into the desired shape of the front bumper, as depicted in Fig. 7.3a). Following that, the second phase involves removing surplus material and doing a spring-back analysis, as shown in Fig. 7.3b). Subsequently, in the third step, a basic frontal crash scenario is calculated, as depicted in Fig. 7.3c).

Local laser-hardening is a method that selectively enhances the characteristics of a material by inducing a phase transformation in the sheet metal through controlled melting and subsequent

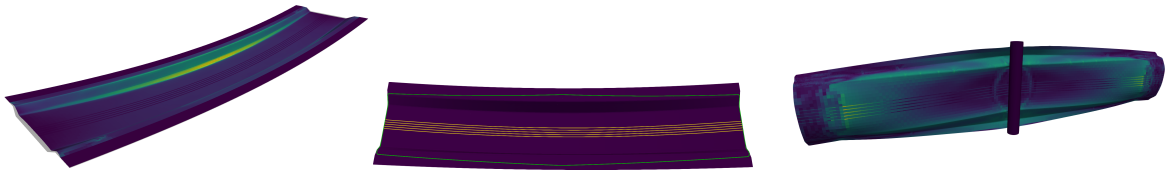

a) **b)** **c)**

Figure 7.3: The three investigated steps, **a)** deep-drawing of the sheet metal, **b)** trimming and spring back and **c)** simple frontal crash. The images are taken from Miska and Balzani [98].

controlled cooling of the steel, cf. e.g. Wagner et al. [159]. For instance, the yield strength of a steel base material can be enhanced by a multiplier of up to 3. Through this method, the sheet metal can be strengthened at specified areas, resulting in a greater likelihood of success in a forming process compared to unaltered sheet metal. Nevertheless, this procedure has certain constraints, as the traces cannot be positioned in close proximity to one another, meaning that the entire sheet cannot be fully covered by laser-hardened traces. This is a result of the process of melting and cooling. If a second line is placed too close to the first line, it will inevitably cause changes in the properties of the first line once again. In addition, laser-hardening requires a specific processing time, which might become too lengthy when dealing with an excessive number of traces and parts. In such instances, opting for a base sheet composed of a superior grade of steel may be advantageous. Moreover, the width of the hardened traces is restricted due to the diameters of the focusing lenses and the necessary laser energy. In this particular scenario, the maximum allowable width for the trace is restricted to 1.5mm, and the thickness of the sheet must not exceed 1.5mm. The separation between two traces must exceed 1.5 times the width of the traces.

The finite element simulations are conducted using LS-Dyna R8.1.0 [82]. These simulations are also run on the previously mentioned Xeon Phi nodes. However, even a single evaluation of the function χ, which is utilized in the extended OUQ to compute the probability of interest for a deterministic combination of points, necessitates a minimum of three numerical simulations. Consequently, performing uncertainty quantification or design optimization based on actual finite element simulations becomes excessively expensive in numerical terms. Thus, surrogate models are utilized, which produce results that are almost identical to those of the finite element simulations, but are far less expensive to analyze. This study utilizes feed-forward artificial neural networks, which are trained on a predetermined set of samples. Given the inherent difficulty in choosing the most suitable topology, the number of layers, number of neurons per layer, and activation functions within these neurons have been fine-tuned using the hyperband tuner from Tensorflow-Keras-Software.

The objective of the design optimization is to optimize the dissipated energy D during an accident in order to achieve the highest level of protection for the car's passenger cell. Three distinct failure modes are taken into account, with each mode being linked to one of the three simulation stages. The failure of sheet metal forming is primarily assessed using the Cockroft-Latham criterion $W_{\mathrm{C}} = \int_0^{\overline{\varepsilon}} \max(\sigma_1, 0) \mathrm{d}\overline{\varepsilon} \geq W_{\mathrm{C}}^{\mathrm{ult}}$ with $\overline{\varepsilon}$ being the equivalent plastic strain, σ_1 the first principial stress and $W_{\mathrm{C}}^{\mathrm{ult}}$ the ultimate admissible value, cf. e.g., Björklund et al. [17] or Tarigopula et al. [152]. This failure criterion has already been used in the numerical example of Sec. 6.2.3. Secondly, during the spring-back, a predetermined maximum limit for the displacement of the nodes is defined, which is used to evaluate the stability of the shape. Finally, the displacement of the car's front bumper is restricted in order to accurately simulate the presence of the engine and cooler located behind the bumper in an actual vehicle.

The degrees of freedom refer to the specific locations of the laser-hardened traces. To achieve this objective, the metal sheet is allocated 38 distinct positions where the traces can be placed, as seen in Fig. 7.4a). These locations take into account the specified geometric limitations, such as the width and minimum distance between the traces. In this case, the traces can only be positioned horizontally on the sheet to reduce the computing effort required for the finite element simulations needed to generate the surrogate models. In addition, there are exactly five traces placed, cf. e.g., Fig. 7.4b) for five traces centered in the middle of the sheet, while Fig. 7.4c) denotes a more distributed positioning of the traces. The chosen parameterization for the design optimization, denoted as $\boldsymbol{\theta} = [l_1, l_2, l_3, l_4, l_5]$ with l_i representing the trace index, results in an integer optimization. Due to the nature of the design optimization problem being a global, non-convex optimization problem, the LSHADE44 optimizer, as previously

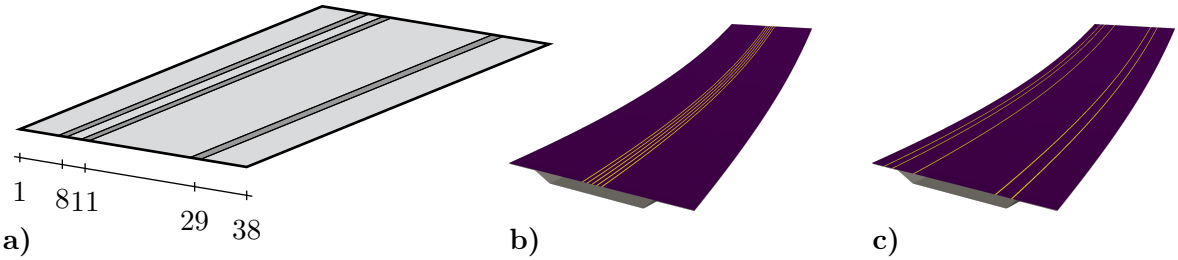

Figure 7.4: a) Schematic illustration of three (instead of the five used in the example) laser-hardened traces on the sheet metal with its positions in terms of the range 1 to 38. **b)** and **c)** are two different, possible laser trace positions. The images are taken from Miska and Balzani [98].

described, is utilized. Therein, the parameters are rounded to the nearest whole number, which could hinder the optimization's performance. Additionally, it is imperative to ensure that the locations are unique during the optimization process. This means that a duplication of a trace index is not acceptable for physical reasons.

Problem Setting, Uncertain Quantities and Surrogate Models As previously stated, the objective in this example is to optimize the dissipated energy during a basic crash scenario. Therefore, the maximization and minimization operation as described in equation (7.1) are swapped:

$$\max_{\boldsymbol{\theta}} \min_{\boldsymbol{y}} \left[\mathbb{E}_{\widehat{\boldsymbol{y}}}(D(\boldsymbol{\theta}, \boldsymbol{z})) \right], \tag{7.5}$$

in order to maximize the worst-case scenario, specifically the minimal expected dissipated energy D. In this example, the quantities that are being considered as uncertain are:

- **Material parameters k and N:** Since the same material as in the sheet metal forming example in Sec. 6.2.3 is used, the same uncertainties in these material parameters are assumed. Since both parameters are strongly correlated, only the strength coefficient k is an actual uncertain quantity, whilst N is computed by Eq. (6.18).
- **Material parameter k_{trace}:** Due to the phase transition, the hardening behavior of the steel changes. In this context, the parameter k_{trace} is regarded as an interval with values $k_{\mathrm{trace}} \in [1200.0, 1800.0]\,\mathrm{MPa}$.
- **Friction coefficient f_{c}:** In accordance to Figueiredo et al. [42], the friction coefficient is an uncertain quantity, however, only little data is available based on experiments. Therefore, the friction coefficient is here modeled as interval quantity with $f_{\mathrm{c}} \in [0.1, 0.15]$ and an additional mean constraint $\mathbb{E}[f_{\mathrm{c}}] \in [0.105, 0.115]$.
- **ultimate value $W_{\mathrm{C}}^{\mathrm{ult}}$:** Similar to the friction coefficient, only a few experiments are performed for the identification of the ultimate values for the Cockroft-Latham values, cf. e.g. [152] or Björklund et al. [17]. In [152], values for a DP-800 steel are given, which are here slightly reduced for the DP-600 steel. Thus, the ultimate value is modeled as interval quantity: $W_{\mathrm{C}}^{\mathrm{ult}} \in [450.0, 550.0]\,\mathrm{MPa}$.

Two variants are being studied for the inclusion of the material parameter k. Firstly, the inclusion as a random field, cf. Vořechovský [158], Ghanem and Spanos [50] and also Miska, Freitag, and Balzani [100] as seen in Sec. 6.2.3. Due to the absence of spatial correlation information, each finite element is allocated a random value of k realized from its beta distribution. This process ensures that a histogram following the distribution is created for the entire sheet. In the second variant, the strength coefficient k is assumed to be uniformly distributed across the entire sheet, as the variation in the material characteristic may occur at a smaller scale

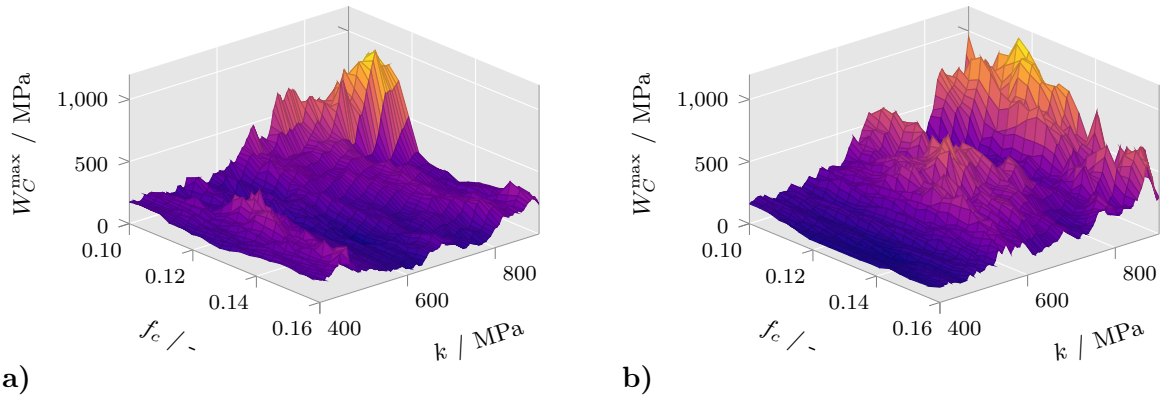

Figure 7.5: Response surfaces from the constructed ANNs for the resulting maximum Cockroft-Latham value $W_C^{\max}$ for a selected subspace of the considered parameters and uniform material parameters. In **a)**, a line combination of $\boldsymbol{\theta} = [4, 16, 34, 36, 37]$ and in **b)** the later identified best solution $\boldsymbol{\theta}_{\text{best}}$ are used. Adapted from Miska and Balzani [97].

than the size of the elements being analyzed. Thus, in this particular case, k represents a range of values, denoted as interval $k \in [617.35, 734.0]$ MPa. This interval corresponds to the standard deviation around the mean of the fitted beta distribution. Whilst the failure due to the simulation is estimated on the basis of an uncertain quantity, the ultimate values for failure due to spring-back and deformation during the crash are purely deterministic, since these are design specifications. In this case, a limit of 30mm is imposed on the nodal displacement following spring-back and a maximum deflection of 125mm is allowed after the crash. The acceptable maximum limit for the probability of failure is defined as $\mathbb{P}_{\text{adm}} = 0.1\%$.

Based on the described problem setting, finite element simulations are carried out in order to construct neural networks as surrogate models, cf. also Haddenhorst [59]. For this purpose, the input parameters are separated into equal segments, resulting in the creation of a training dataset that covers the complete range of inputs. A total of six artificial neural networks are created to evaluate the two options for the inclusion of the strength coefficient k, with three finite element simulations computed for each variant.

In the case of the random field, the inputs for the artificial neural networks consist of the line positions $\boldsymbol{\theta}$, the friction coefficient f_{c}, and the strength coefficient k_{trace} of the laser-hardened traces. For each possible combination of these input parameters, 30 instances of the random field representing the strength coefficient k are generated and calculated. From these instances, statistical information about the quantities of interest is derived. A total of 5400 unique configurations are tested, with each configuration undergoing 3 finite element simulations. The 30 highest values obtained for the Cockroft-Latham criterion, denoted as $\max W_{\text{C}}$, are subsequently compared to $W_{\text{C}}^{\text{ult}}$. Additionally, the maximum displacements of the nodes after the spring-back, resulting from 30 random field computations with a fixed input parameter combination, are arranged in ascending order and assigned a normalized frequency of occurrence. Consequently, an estimated cumulative distribution function is generated, as described previously in Sec. 6.2.3, which serves as an approximation for the proportion of random fields that yield critical values for both the maximum Cockroft-Latham value and the maximum node displacement. Thus, an additional parameter for the neural nets is $W_{\text{C}}^{\text{ult}}$ or the maximum admissible value for the node displacement, respectively, and the return value is the evaluated value of the constructed ECDF. The output of the artifical neural network is the calculated value of the created ECDF. The architecture of the neural network used to calculate the maximum dissipated energy is somewhat modified. The output is the average dissipated energy across all 30 randomly generated fields, denoted as $\mathbb{E}_{\widehat{\boldsymbol{y}}}(D(\boldsymbol{\theta}, \boldsymbol{z}))$.

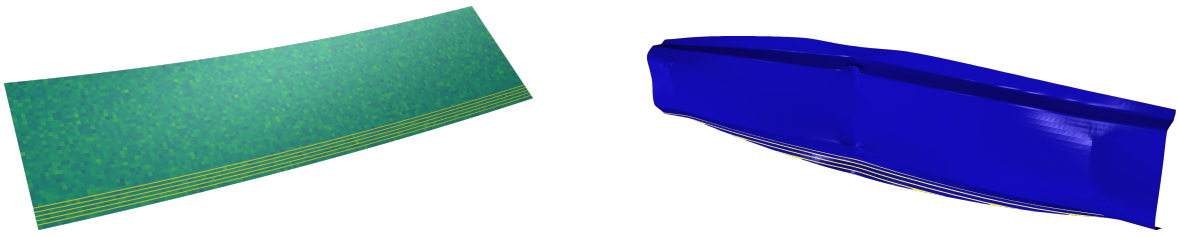

a) **b)**

Figure 7.6: Optimization result for the random-field case with laser-hardened traces mostly at the bottom of the sheet in **a)**, the deformation of the same sheet after the crash simulation in **b)**. Taken from Miska and Balzani [98].

In the case of the uniform scenario, 5400 individual configurations were simulated. However, in this variant, there was no need to create and simulate random fields. Therefore, the neural networks can be seen as regression models that directly use the line positions $\boldsymbol{\theta}$, the friction coefficient f_c, and the strength coefficient k_{trace} in the laser-hardened traces as inputs. The networks yield different return values according on the calculation of interest, which might be either the maximum value reached for the Cockroft-Latham criterion ($\max W_C$), the maximum deformation of the nodes, or the dissipated energy (D) during the crash. In Fig. 7.5, two exemplary surface plots from the ANN for $\max W_C$ are shown. It can be seen, that the approximated variable is not smooth, which can indicate underlying numerical problems with the identification of this parameter in the first place. For this example, however, the constructed ANNs are used as is, accepting potential drawbacks during the optimization due to the chaotic, non-smooth parameters.

Currently, the design parameters and uncertain values are clearly distinguished and there is no interdependence. Hence, an extra scenario is examined: does additional knowledge for the strength coefficient k_{trace} within the traces lead to an improvement in the dissipated energy? The increased knowledge can for example be interpreted as an improved production process, in which the process of the laser-hardening is better monitored to achieve more consistent results. Here, a mean constraint on k_{trace} is introduced to replicate this improved knowledge, additionally, the midpoint of the mean in bounds should be optimized for an improved design. By doing this, a range of 200 MPa is permitted for the interval width, namely, $\mathbb{E}[k_{\text{trace}}] \in [\theta_k - 100\text{MPa}, \theta_k + 100\text{MPa}]$, where θ_k represents the middle of the interval. The vector of design parameters is represented by $\boldsymbol{\theta} = [l_1, l_2, l_3, l_4, l_5, \theta_k]$. The surrogate models that have been built do not require any adjustments, as the interaction is not applied to a random field parameter, and can be utilized in the same manner as previously.

Optimization 1: Material Parameter as Random Field With the described problem settings, the design optimization can be performed. Due to the non-convex nature of both design optimization and uncertainty quantification, the LSHADE44 optimizer is used in both circumstances. The inner uncertainty quantifications employ a population size of 250 and a convergence requirement of 250 iterations. On the other hand, the design optimization utilizes a population of 128 and requires 50 iterations for convergence. Given its nested characteristic, several design candidates can be assessed in parallel in regards to the uncertainty quantification within a single iteration of the outer design optimization In this case, a total of 64 design parameters were simultaneously examined on the 64 cores of the utilized node.

The best trace combination for the initial scenario, where there is no interaction between design and uncertainties, is

$$\boldsymbol{\theta}_{\text{opt}} = [26, 29, 30, 31, 32], \tag{7.6}$$

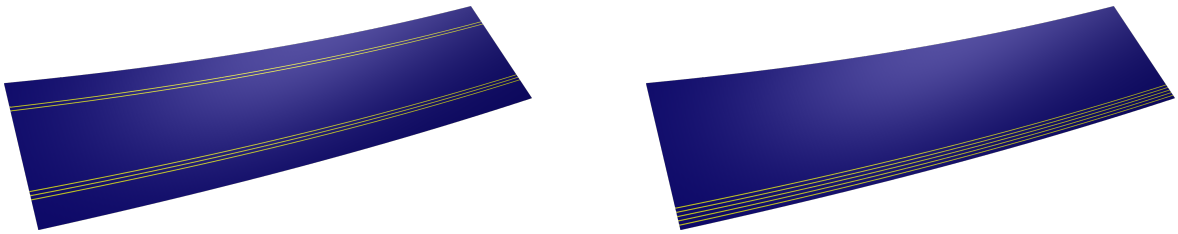

a) **b)**

Figure 7.7: Illustration of the traces for the uniform case in **a)**, in contrast to the trace locations of the random field case in **b)**, depicted without the random field. Taken from Miska and Balzani [98].

resulting in a maximized lower bound on the dissipated energy of $D = 490,864$ Joule. Fig. 7.6 displays a training sample of a random field, which exhibits a similar line arrangement as the found optimal solution. The high indices indicate the placements of all traces towards the bottom of the sheet metal. By incorporating the mean constraint $\mathbb{E}[k_{\text{trace}}]$, the optimizer settings remain unaltered, resulting in the optimal parameter vector

$$\boldsymbol{\theta}_{\text{opt}} = [26, 30, 31, 32, 33, 1700.0], \tag{7.7}$$

with dissipated energy equal to at least $D = 491,863$ Joule. When comparing the result with the constraint to the result without it, only a marginal improvement of 0.2% in the dissipated energy can be claimed. It is unlikely that this slight increase in benefit can justify the necessary effort and supervision in production. Furthermore, the analysis reveals that the maximum midpoint for the interval of the mean restriction was selected, i.e. $1,700$MPa.

Optimization 2: Uniform Material Parameter in Bounds As previously stated, the variability of the material characteristic being included may occur on a smaller scale than the element size being evaluated. Therefore, it would be more accurate to focus just on the average value of the beta distribution. In this case, a range of one standard deviation around the mean is employed, specifically $k \in [617.35, 734.0]$ MPa. Given that all other parameters of the problem stay the same, the optimizer settings used previously are employed. The best positions are determined to be

$$\boldsymbol{\theta}_{\text{opt}} = [2, 3, 23, 24, 28], \tag{7.8}$$

resulting in a maximized lower bound on the dissipated energy of $D = 485,035$ Joule. Unlike the previous scenario, where all traces were located at the bottom, the current solution leads to the formation of two distinct groups. There is one group located at the top of the sheet, and another group positioned closer to the middle of the sheet, cf. also Fig. 7.7a) for a similar training candidate. Nevertheless, the total dissipated energy is lower compared to the random field scenario. In addition, also the mean constraint $\mathbb{E}[k_{\text{trace}}]$ is examined, which leads to a different position vector of

$$\boldsymbol{\theta}_{\text{opt}} = [2, 3, 23, 24, 28, 1700.0], \tag{7.9}$$

with a maximized lower bound on the dissipated energy of $D = 487,536$ Joule. Similarly to previous observations, there is only a marginal enhancement of 0.5% in the dissipated energy. Furthermore, the midpoint once again represented the maximum attainable value that could be utilized.

The examined relationship between an optimization parameter and an uncertain quantity did not lead to an enhanced design for the given situations. However, it is demonstrated that the suggested framework for Reliability-Based Design Optimization using the extended Optimal Uncertainty Quantification can effectively capture dependencies like these.

8 Conclusion

The aim of this thesis is the development and application of a framework for the reliability-based design optimization under polymorphic uncertainties. This intention is divided in a few intermediate steps, which will be discussed individually.

The first chapters lay the foundations for uncertainty quantification by introducing important notations for the uncertainty quantification itself with its mathematical models. This is followed by a chapter for the fundamentals of continuum mechanics, finite elements and numerical homogenization. The numerical homogenization is used as virtual lab, since it allows the computation of effective material properties based on a virtual representation of the microstructure.

Afterwards, the optimal decomposition for subcells in the context of the finite cell method is discussed and analyzed. The finite cell method is motivated due to the ability of automated mesh generations for the numerical homogenization. Since in a later chapter, a large set of artificial microstructures is investigated in a virtual lab, manual mesh creation is not feasible. However, the conventional approach for the construction of subcells, the Octree, leads to an unnecessary high number of subcells, which impedes the numerical efficiency of the method. Additionally, the material bounds given by the geometry representation in terms of pixel/voxel may not exactly be represented by the created subcells. Therefore, the optimal decomposition exploits the perpendicular nature of voxel and aggregates voxels to larger cuboids. By that, not only the material interfaces are preserved, but also less subcells are created than for the Octree approach. Numerical examples prove, that the optimal decomposition performs well for numerical homogenization problems. It can be shown, that the solution of Octree decomposition converges against the Optimal decomposition results with finer Octrees, which leads to a better approximation of the material boundaries. Also, modifications of the Octree decomposition are investigated, which can perform better than the classical Octree approach, but not better than the proposed optimal decomposition.

In the next chapter, a method to quantify uncertain effective material parameters caused by a variation of the microstructure's morphology is presented. The method enables a general description of the variation of microstructure morphologies by the utilization of higher order statistical measures without being restricted to specific, potentially unique, parameterization of the microstructure morphology. The higher order statistical measures are evaluated in a distance functional, which quantifies the deviation of a selected subset of the microstructure from the representative volume element. The latter is usually considered to represent the average of the microstructure morphology, and thus the quantified deviation can be considered as deviation of the mean in a statistical sense. An evaluation of the distance functional for many different subsets of the materials microstructure allows the quantification of the inner variability of the materials microstructure. Subsequently, a set of artificial microstructures, the so called Statistically Similar Volume Elements (SSVEs), can be constructed, which exhibit the same inner variability. This set of SSVEs is used in the aforementioned virtual lab to compute the macroscopic material properties for each of the SSVEs. The efficiency of the virtual lab is further improved by the application of a multilevel Monte Carlo method. The method is applied to a dual-phase steel microstructure, for which a large two-dimensional microstructure scan is available. A set of SSVEs matching the same variation is constructed

and tested, both in a conventional and the multilevel Monte Carlo approach, which proves the efficiency gain of the latter. In this example, the effective yield stress and hardening modulus are deduced from the computed stress-strain-curves. The method itself is not limited to these exact parameters, in principle, any parameter may be derived from the available stress-strain-curves. Finally, the derived material parameters are compiled in histograms reflecting the variation of said parameters. These histograms prove to be comparatively smooth, so that the discrete distributions of the parameters can be approximated by using a continuous beta distribution function.

Next, the Optimal Uncertainty Quantification (OUQ) is introduced and extended to the ability of polymorphic uncertainty quantification. Since in its original form, all uncertainties are considered as epistemic uncertainties, a method for the inclusion of aleatory uncertainties was added. For this purpose, the probability density function of aleatory uncertainties is integrated over the failure region. This integral depends on the values of the remaining epistemic uncertainties and hence, the integral has to be performed for every possible combination of epistemic support points. Furthermore, the extended OUQ framework is combined with fuzzy numbers in their discretized form using α-levels. This allows a structured analysis of different combinations of intervals. The computational efficiency of this method is ensured by the transformation of the objective function to the space of canonical moments. The extended OUQ framework is then tested by means of two examples. The first example is meant to prove the convergence behavior of the resulting bounds due to the incorporation of an aleatory uncertainty. Furthermore, the incorporation of canonical moments leads to a higher efficiency, or, in some cases, enable a computation at all. In the second example, a benchmark problem for polymorphic uncertainty quantification from the DFG Priority Program 1886 is computed. Therein, two different ways to incorporate an epistemic uncertain parameter are investigated. The influence of assumptions on the available data is emphasized, as the two investigated possibilities lead to a large difference in the calculated upper bound for the probability of failure (PoF). Both examples prove, that the extended OUQ framework is a reliable and versatile tool for the polymorphic uncertainty quantification. In contrast to existing methods, the assumption regarding the type of distribution function can be avoided for uncertainties for which the choice of an appropriate distribution function is difficult.

Subsequently, the extended OUQ framework is further developed by the integration of spatially varying parameters in form of random fields. The idea is to perform computations involving the random field before the uncertainty analysis. The resulting data is then used to construct a surrogate model, here in form of artificial neural networks (ANNs). The surrogate models are used to predict the statistical response of the system due to the random field. In the computational example, a sheet metal forming process is investigated. Since the process is solved numerically in terms of finite elements, the surrogate model serves a second purpose and avoids the costly computations during the uncertainty quantification. In this example, the ANN is trained to determine the estimated probability for failure of the sheet metal for a given input combination of further uncertain parameters and the random field of material parameters related to the hardening behavior. These material parameters are identified based on the set of SSVEs as described before.

Finally, the extended Optimal Uncertainty Quantification framework is integrated in a Reliability-Based Design Optimization (RBDO) context. This integration leads to a nested optimization, sometime also referred to as double-loop optimization. The resulting RBDO-framework allows the incorporation of both aleatory and epistemic uncertainties, whilst the mathematically sharpest bounds on the objective function as well as on the reliability constraint can be computed. Further unique capabilities of the extended OUQ are preserved, i.e., it is possible to include moment information on epistemic uncertainties without specifying an

underlying probability density function. The developed framework is tested by two numerical examples. The initial example serves as a benchmark for polymorphic uncertainty quantification. The results obtained from this example are compared with alternative approaches relying on fuzzy numbers or intervals for handling epistemic uncertainties. The investigation involves two scenarios with varying levels of data on epistemic uncertainties, and the results prove to be meaningful. The second, more complex example comprised a multi-step simulation of the production process and crash behavior of a simplified car front bumper. In this case, the optimization focused on positioning locally laser-hardened traces within the sheet metal to maximize energy dissipation during a crash. The increasing computational demands poses a challenge, which is mitigated by leveraging neural networks as surrogate models for regressing the model responses. In addition to the first example, a dependency between an optimization variable and an uncertain quantity is inspected, for which the midpoint of an interval is optimized. While these cases do not end in improvements in the objective, the technical integration works as anticipated, demonstrating that such dependencies can be seamlessly incorporated within a design optimization. However, the overall objective of this thesis was reached, since the successful integration of the extended OUQ within the RBDO context represent the sought framework and a simplified car front bumper was optimized.

Although the presented extension of the Optimal Uncertainty Quantification as well as the method for the quantification of uncertain macroscopic material properties offer many advantages as extensively discussed in this thesis, they are hardly an universal tool like a swiss army knife. Uncertainty quantification in itself is a very subjective topic and thus, someone may want to consider effects or models, which cant be dealt with the presented approaches. And certainly, there will be a method out there, which may be employed for that specific application. Therefore, the presented method can hardly close any research topic, since all questions asked are answered completely, but they do enrich the zoo of available methods for uncertainty quantification. In doing so, hopefully at some point in the future, the proposed methods fill the gap for some engineer, such that some structures can be made safer.

While the investigated topics and developed methods of this thesis are able to answer specific posed research questions, they are certainly not concluding and additional research can improve the presented approaches even further, offering starting points for future research. Quite obviously, in order to quantify the variation of a macroscopic material response, not only the variation of the microstructure morphology, but also the variation of material properties of individual phases on the microscale should be considered. With the rise of artificial neural networks and other surrogate models, the efficiency of the method may be improved, if the costly homogenization in terms of finite elements can be substituted by an appropriate ANN. A faster homogenization would allow for the consideration of more different microstructures and thus, the method would yield more reliable statistics. Also, it may be meaningful to use the set of SSVEs directly in a fully-coupled micro-macro simulation, in which the microstructure vary in each macroscopic quadrature point. By that, the full information on the macroscopic behavior of the microstructures could be utilized, omitting the choice and quantification for only a few, selected macroscopic material properties. In addition to that, alternative approaches for the subcell decomposition may be worth to be researched, since the Optimal Decomposition approach turned out to be not applicable to crack propagation problems, cf. Wingender and Balzani [161].

Similarly, also the extended OUQ may be further enhanced and studied. For now, all uncertain quantities are assumed to be stochastically independent, which is hardly true for all realistic scenarios. Thus, by further research the important reduction theorem may be applied to correlated stochastic quantities. Also, the efficiency is still a major concern, especially for the design optimization with a double-loop optimization. Therein, two optimizations are nested,

which requires substantial numerical effort. In addition, a nested application of the OUQ was proposed to incorporate limited statistical data from random fields, such that a combination of that with an design optimization would require a three times nested optimization. Thus, additional research for example towards multi-level surrogate models can be very beneficial, cf. the works of Freitag et al. [45]. In the end, more realistic examples will help to evaluate the performance and applicability of the developed methods even further.

List of Figures

List of Tables

Bibliography

[1] C. C. Aggarwal. *Neural Networks and Deep Learning: A Textbook*. Springer International Publishing, Cham, 2018. ISBN 978-3-319-94462-3 978-3-319-94463-0. doi: 10.1007/978-3-319-94463-0.

[2] S.-K. Au and J. L. Beck. Estimation of small failure probabilities in high dimensions by subset simulation. *Probabilistic Engineering Mechanics*, 16(4):263–277, 2001. ISSN 02668920. doi: 10.1016/S0266-8920(01)00019-4.

[3] D. Balzani, D. Brands, and J. Schröder. Construction of statistically similar representative volume elements. In *Plasticity and beyond: Microstructures, Crystal-Plasticity and Phase Transitions*, chapter Construction of statistically similar representative volume elements. CISM Lecture Notes No. 550, 2013.

[4] D. Balzani, L. Scheunemann, D. Brands, and J. Schröder. Construction of two- and three-dimensional statistically similar RVEs for coupled micro-macro simulations. *Computational Mechanics*, 54(5):1269–1284, 2014. ISSN 0178-7675, 1432-0924. doi: 10.1007/s00466-014-1057-6.

[5] D. Balzani, N. Miska, and S. Prüger. Construction of Statistically Similar RVEs for the Quantification of Uncertainty Associated with the Material's Microstructure Morphology. In *Proceedings of the 2nd International Conference on Uncertainty Quantification in Computational Sciences and Engineering*, Rhodes Island, 2017.

[6] D. Balzani, T. Schmidt, and M. Ortiz. Method for the quantification of rupture probability in soft collagenous tissues: QUANTIFICATION OF RUPTURE PROBABILITY IN SOFT COLLAGENOUS TISSUES. *International Journal for Numerical Methods in Biomedical Engineering*, 33(1):e02781, 2017. ISSN 20407939. doi: 10.1002/cnm.2781.

[7] D. Balzani, M. Köhler, T. Neumeier, M. A. Peter, and D. Peterseim. Multidimensional rank-one convexification of incremental damage models at finite strains. *Computational Mechanics*, 2023. ISSN 1432-0924. doi: 10.1007/s00466-023-02354-3.

[8] K.-J. Bathe and P. Zimmermann. *Finite-Elemente-Methoden*. Springer, Berlin Heidelberg, 2., vollst. neu bearb. und erw. aufl edition, 2002. ISBN 978-3-540-66806-0.

[9] P. Beaurepaire, H. Jensen, G. Schuëller, and M. Valdebenito. Reliability-based optimization using bridge importance sampling. *Probabilistic Engineering Mechanics*, 34: 48–57, 2013. ISSN 02668920. doi: 10.1016/j.probengmech.2013.04.001.

[10] M. Beer, S. Ferson, and V. Kreinovich. Imprecise probabilities in engineering analyses. *Mechanical Systems and Signal Processing*, 37(1-2):4–29, 2013. ISSN 08883270. doi: 10.1016/j.ymssp.2013.01.024.

[11] T. Belytschko, W. K. Liu, B. Moran, and K. I. Elkhodary. *Nonlinear Finite Elements for Continua and Structures*. Wiley, Chichester, West Sussex, United Kingdom, second edition edition, 2014. ISBN 978-1-118-63270-3.

[12] J. Bezanson, S. Karpinski, V. B. Shah, and A. Edelman. Julia: A Fast Dynamic Language for Technical Computing, 2012.

[13] J. Biehler, M. W. Gee, and W. A. Wall. Towards efficient uncertainty quantification in complex and large-scale biomechanical problems based on a Bayesian multi-fidelity scheme. *Biomechanics and Modeling in Mechanobiology*, 14(3):489–513, 2015. ISSN 1617-7959, 1617-7940. doi: 10.1007/s10237-014-0618-0.

[14] P. Billingsley. *Probability and Measure*. John Wiley & Sons, Inc., 1995 (3rd Ed.). ISBN 0-471-00710-2.

[15] C. M. Bishop. *Pattern Recognition and Machine Learning*. Information Science and Statistics. Springer, New York, 2006. ISBN 978-0-387-31073-2.

[16] J. Bishop. Rapid stress analysis of geometrically complex domains using implicit meshing. *Computational Mechanics*, 30(5-6):460–478, 2003. ISSN 0178-7675, 1432-0924. doi: 10.1007/s00466-003-0424-5.

[17] O. Björklund, R. Larsson, and L. Nilsson. Failure of high strength steel sheets: Experiments and modelling. *Journal of Materials Processing Technology*, 213(7):1103–1117, 2013. ISSN 09240136. doi: 10.1016/j.jmatprotec.2013.01.027.

[18] A. A. Borovkov. *Probability Theory*. Universitext. Springer London, London, 2013. ISBN 978-1-4471-5200-2 978-1-4471-5201-9. doi: 10.1007/978-1-4471-5201-9.

[19] D. Brands, D. Balzani, L. Scheunemann, J. Schröder, H. Richter, and D. Raabe. Computational modeling of dual-phase steels based on representative three-dimensional microstructures obtained from EBSD data. *Archive of Applied Mechanics*, 86(3):575–598, 2016. ISSN 0939-1533, 1432-0681. doi: 10.1007/s00419-015-1044-1.

[20] B. T. Cao, M. Obel, S. Freitag, L. Heußner, G. Meschke, and P. Mark. Real-time risk assessment of tunneling-induced building damage considering polymorphic uncertainty. *ASCE-ASME Journal of Risk and Uncertainty in Engineering Systems, Part A: Civil Engineering*, 8(1):04021069, 2022. doi: 10.1061/AJRUA6.0001192.

[21] B. D. Coleman and W. Noll. *The Thermodynamics of Elastic Materials with Heat Conduction and Viscosity*, pages 145–156. Springer Berlin Heidelberg, Berlin, Heidelberg, 1974. ISBN 978-3-642-65819-8 978-3-642-65817-4. doi: 10.1007/978-3-642-65817-4_9.

[22] M. de Angelis, E. Patelli, and M. Beer. Advanced Line Sampling for efficient robust reliability analysis. *Structural Safety*, 52:170–182, 2015. ISSN 01674730. doi: 10.1016/j.strusafe.2014.10.002.

[23] H. Deng, Y. Liu, D. Gai, D. Dikin, K. W. Putz, W. Chen, L. C. Brinson, C. Burkhart, M. Poldneff, B. Jiang, and G. J. Papakonstantopoulos. Utilizing real and statistically reconstructed microstructures for the viscoelastic modeling of polymer nanocomposites. *Composites Science and Technology*, 72:1725–1732, 2012.

[24] H. Dette and W. J. Studden. *The Theory of Canonical Moments with Applications in Statistics, Probability, and Analysis*. Wiley Series in Probability and Statistics Applied Probability and Statistics. Wiley, New York, NY, 1997. ISBN 978-0-471-10991-4.

[25] Deutsches Institut für Normung. DIN EN 10034:1994-03, I- und H-Profile aus Baustahl; Grenzabmaße und Formtoleranzen; Deutsche Fassung EN_10034:1993. Technical report, Beuth Verlag GmbH, 1994.

[26] Deutsches Institut für Normung. DIN EN 1993-3-1:2010-12, Eurocode_3: Bemessung und Konstruktion von Stahlbauten_- Teil_3-1: Türme, Maste und Schornsteine_- Türme und Maste; Deutsche Fassung EN_1993-3-1:2006_+ AC:2009. Technical report, Beuth Verlag GmbH, 2010.

[27] M. Drieschner, Y. Petryna, R. Gruhlke, M. Eigel, and D. Hömberg. Comparison of various uncertainty models with experimental investigations regarding the failure of plates with holes. *Reliability Engineering & System Safety*, 203:107106, 2020. ISSN 09518320. doi: 10.1016/j.ress.2020.107106.

[28] M. Drieschner, Y. Petryna, S. Freitag, P. Edler, A. Schmidt, and T. Lahmer. Decision making and design in structural engineering problems under polymorphic uncertainty. *Engineering Structures*, 231:111649, 2021. ISSN 01410296. doi: 10.1016/j.engstruct.2020.111649.

[29] W. J. Drugan and J. R. Willis. A micromechanics-based nonlocal constitutive equation and estimates of representative volume element size for elastic composites. *Journal of the Mechanics and Physics of Solids*, 44(4):497–524, 1996. ISSN 0022-5096. doi: 10.1016/0022-5096(96)00007-5.

[30] A. Düster, J. Parvizian, Z. Yang, and E. Rank. The finite cell method for three-dimensional problems of solid mechanics. *Computer Methods in Applied Mechanics and Engineering*, 197(45-48):3768–3782, 2008. ISSN 00457825. doi: 10.1016/j.cma.2008.02.036.

[31] M. Ebden. Gaussian Processes: A Quick Introduction, 2015.

[32] P. Edler, S. Freitag, K. Kremer, and G. Meschke. Optimization approaches for the numerical design of structures under consideration of polymorphic uncertain data. *ASCE-ASME Journal of Risk and Uncertainty in Engineering Systems Part B: Mechanical Engineering*, 5(4):041013 (12 pages), 2019. doi: 10.1115/1.4044153.

[33] I. Enevoldsen and J. Sørensen. Reliability-based optimization in structural engineering. *Structural Safety*, 15(3):169–196, 1994. ISSN 01674730. doi: 10.1016/0167-4730(94)90039-6.

[34] M. Faes, B. Von Doninck, M. Imholz, and D. Moens. Product reliability optimization under plate sheet forming process variability. In *8th International Workshop on Reliable Engineering Computing, "Computing with Confidence"*, 2018.

[35] Y. F. Fangye, N. Miska, and D. Balzani. Simulation of Dual-Phase Steel Using the Finite Cell Method and Voxel-Based Microstructure Data. *Proceedings in Applied Mathematics and Mechanics*, 19(1), 2019. ISSN 1617-7061, 1617-7061. doi: 10.1002/pamm.201900316.

[36] Y. F. Fangye, N. Miska, and D. Balzani. Simulation of Dual-Phase steel microstructures using optimized arrangements of Finite cells. In *Proceedings of 8th GACM Colloquium on Computational Mechanics*, 2019. doi: 10.19211/KUP9783737650939.

[37] Y. F. Fangye, N. Miska, and D. Balzani. Automated simulation of voxel-based microstructures based on enhanced finite cell approach. *Archive of Applied Mechanics*, 90 (10):2255–2273, 2020. ISSN 0939-1533, 1432-0681. doi: 10.1007/s00419-020-01719-x.

[38] J. Ferreita Duarte and A. Barata da Rocha. A brief description of an S-rail benchmark. In J. K. Lee, G. L. Kinzel, and R. H. Wagoner, editors, *Numerical Simulation of 3-D Sheet Metal Forming Processes - Verification of Simulations with Experiments*, 1996.

[39] T. Fetz and M. Oberguggenberger. Propagation of uncertainty through multivariate functions in the framework of sets of probability measures. *Reliability Engineering & System Safety*, 85(1-3):73–87, 2004. ISSN 09518320. doi: 10.1016/j.ress.2004.03.004.

[40] F. Feyel. Multiscale FE2 elastoviscoplastic analysis of composite structures. *Computational Materials Science*, 16(1-4):344–354, 1999. ISSN 09270256. doi: 10.1016/S0927-0256(99)00077-4.

[41] F. Feyel and J.-L. Chaboche. FE2 multiscale approach for modelling the elastoviscoplastic behaviour of long fibre SiC/Ti composite materials. *Computer Methods in Applied Mechanics and Engineering*, 183(3-4):309–330, 2000. ISSN 00457825. doi: 10.1016/S0045-7825(99)00224-8.

[42] L. Figueiredo, A. Ramalho, M. Oliveira, and L. Menezes. Experimental study of friction in sheet metal forming. *Wear*, 271(9-10):1651–1657, 2011. ISSN 00431648. doi: 10.1016/j.wear.2011.02.020.

[43] D. M. Frangopol and K. Maute. Life-cycle reliability-based optimization of civil and aerospace structures. *Computers & Structures*, 81(7):397–410, 2003. ISSN 00457949. doi: 10.1016/S0045-7949(03)00020-8.

[44] S. Freitag. Artificial neural networks in structural mechanics. In Y. Tsompanakis, J. Kruis, and B. Topping, editors, *Computational Technology Reviews*, volume 12, pages 1–26. Saxe-Coburg Publications, Stirlingshire, 2015. doi: 10.4203/ctr.12.1.

[45] S. Freitag, P. Edler, K. Kremer, and G. Meschke. Multilevel surrogate modeling approach for optimization problems with polymorphic uncertain parameters. *International Journal of Approximate Reasoning*, 119:81–91, 2020. ISSN 0888613X. doi: 10.1016/j.ijar.2019.12.015.

[46] M. Geers, V. G. Kouznetsova, and W. A. M. Brekelmans. MultiScale First-Order and Second-Order Computational Homogenization of Microstructures towards Continua. *International Journal for Multiscale Computational Engineering*, 1(4):371–386, 2003. ISSN 1543-1649. doi: 10.1615/IntJMultCompEng.v1.i4.40.

[47] M. Geers, E. Coenen, and V. Kouznetsova. Multi-scale computational homogenization of structured thin sheets. *Modelling and Simulation in Materials Science and Engineering*, 15(4):S393–S404, 2007. ISSN 0965-0393, 1361-651X. doi: 10.1088/0965-0393/15/4/S06.

[48] M. Geers, V. Kouznetsova, and W. Brekelmans. Multi-scale computational homogenization: Trends and challenges. *Journal of Computational and Applied Mathematics*, 234(7):2175–2182, 2010. ISSN 03770427. doi: 10.1016/j.cam.2009.08.077.

[49] M. Geers, V. Kouznetsova, K. Matouš, and J. Yvonnet. Homogenization Methods and Multiscale Modeling: Nonlinear Problems. In E. Stein, R. de Borst, and T. J. R. Hughes, editors, *Encyclopedia of Computational Mechanics Second Edition*, pages 1–34. John Wiley & Sons, Ltd, Chichester, UK, 2017. ISBN 978-1-119-00379-3 978-1-119-17681-7. doi: 10.1002/9781119176817.ecm2107.

[50] R. G. Ghanem and P. D. Spanos. *Stochastic Finite Elements: A Spectral Approach*. Springer New York, New York, NY, 1991. ISBN 978-1-4612-7795-8 978-1-4612-3094-6. doi: 10.1007/978-1-4612-3094-6.

[51] M. B. Giles. Multilevel Monte Carlo Path Simulation. *Operations Research*, 56(3):607–617, 2008. ISSN 0030-364X, 1526-5463. doi: 10.1287/opre.1070.0496.

[52] I. Gitman, H. Askes, and LJ. Sluys. Representative volume: Existence and size determination. *Engineering Fracture Mechanics*, 74(16):2518–2534, 2007. ISSN 0013-7944.

[53] R. Glowinski and Yu. Kuznetsov. Distributed Lagrange multipliers based on fictitious domain method for second order elliptic problems. *Computer Methods in Applied Mechanics and Engineering*, 196(8):1498–1506, 2007. ISSN 00457825. doi: 10.1016/j.cma.2006.05.013.

[54] R. Glüge, M. Weber, and A. Bertram. Comparison of spherical and cubical statistical volume elements with respect to convergence, anisotropy, and localization behavior. *Computational Materials Science*, 63:91–104, 2012. ISSN 0927-0256. doi: 10.1016/j.commatsci.2012.05.063.

[55] I. Goodfellow, Y. Bengio, and A. Courville. *Deep Learning*. Adaptive Computation and Machine Learning. The MIT Press, Cambridge, Massachusetts London, England, 2016. ISBN 978-0-262-03561-3.

[56] M. Götz. *Numerische Entwurfsmethoden unter Berücksichtigung polymorpher Unschärfe: Aspekte zeitlicher und räumlicher Abhängigkeiten*. PhD thesis, Technische Universität Dresden, Dresden, 2017.

[57] M. Götz, W. Graf, and M. Kaliske. Numerical concepts for structural design with polymorphic uncertainty modelling. *International Journal of Reliability and Safety*, 9 (2):112–131, 2015. doi: http://dx.doi.org/10.1504/IJRS.2015.072715.

[58] R. Hable. *Einführung in die Stochastik*. Springer-Lehrbuch. Springer Berlin Heidelberg, Berlin, Heidelberg, 2015. ISBN 978-3-662-43497-0 978-3-662-43498-7. doi: 10.1007/978-3-662-43498-7.

[59] H. H. Haddenhorst. Maximierung der dissipierten Energie einer lokal laserverfestigten Crashstruktur mit Hilfe künstlicher neuronaler Netzwerke, 2022.

[60] Z. Hashin. Analysis of Composite Materials—A Survey. *Journal of Applied Mechanics*, 50(3):481–505, 1983. ISSN 0021-8936, 1528-9036. doi: 10.1115/1.3167081.

[61] S. S. Haykin. *Neural Networks: A Comprehensive Foundation*. Prentice Hall, Upper Saddle River, NJ, 2. ed., [nachdr.] edition, 1999. ISBN 978-0-13-273350-2.

[62] S. Heinrich. Multilevel Monte Carlo Methods. In *Large-Scale Scientific Computing*, pages 58–67, 2001.

[63] C. Henning, S. Herbrandt, K. Ickstadt, and T. Ricken. Combining Finite Elements and Random Fields to Quantify Uncertainty in a Multi-phase Structural Analysis. *PAMM*, 18(1), 2018. ISSN 1617-7061, 1617-7061. doi: 10.1002/pamm.201800333.

[64] R. Hill. Elastic properties of reinforced solids: Some theoretical principles. *Journal of the Mechanics and Physics of Solids*, 11(5):357–372, 1963. ISSN 00225096. doi: 10.1016/0022-5096(63)90036-X.

[65] R. Hill. On constitutive macro-variables for heterogeneous solids at finite strain. *Proceedings of the Royal Society of London. A. Mathematical and Physical Sciences*, 326 (1565):131–147, 1972. ISSN 2053-9169. doi: 10.1098/rspa.1972.0001.

[66] B. Hiriyur, H. Waisman, and G. Deodatis. Uncertainty quantification in homogenization of heterogeneous microstructures modeled by XFEM: UNCERTAINTY QUANTIFICATION IN XFEM HOMOGENIZATION. *International Journal for Numerical Methods in Engineering*, 88(3):257–278, 2011. ISSN 00295981. doi: 10.1002/nme.3174.

[67] G. A. Holzapfel. *Nonlinear Solid Mechanics: A Continuum Approach for Engineering*. Wiley, Chichester Weinheim, repr edition, 2010. ISBN 978-0-471-82304-9 978-0-471-82319-3.

[68] D. Hose and M. Hanss. Possibilistic calculus as a conservative counterpart to probabilistic calculus. *Mechanical Systems and Signal Processing*, 133:106290, 2019. ISSN 08883270. doi: 10.1016/j.ymssp.2019.106290.

[69] S. Hubrich, P. Di Stolfo, L. Kudela, S. Kollmannsberger, E. Rank, A. Schröder, and A. Düster. Numerical integration of discontinuous functions: Moment fitting and smart octree. *Computational Mechanics*, 60(5):863–881, 2017. ISSN 0178-7675, 1432-0924. doi: 10.1007/s00466-017-1441-0.

[70] J. Hurtado. Analysis of one-dimensional stochastic finite elements using neural networks. *Probablistic Engineering Mechanics*, 17:35–44, 2002.

[71] M. Joulaian, S. Hubrich, and A. Düster. Numerical integration of discontinuities on arbitrary domains based on moment fitting. *Computational Mechanics*, 57(6):979–999, 2016. ISSN 0178-7675, 1432-0924. doi: 10.1007/s00466-016-1273-3.

[72] S. Kastian, D. Moser, L. Grasedyck, and S. Reese. A two-stage surrogate model for Neo-Hookean problems based on adaptive proper orthogonal decomposition and hierarchical tensor approximation. *Computer Methods in Applied Mechanics and Engineering*, 372: 113368, 2020. ISSN 00457825. doi: 10.1016/j.cma.2020.113368.

[73] A. D. Kiureghian and O. Ditlevsen. Aleatory or epistemic? Does it matter? *Structural Safety*, 31(2):105–112, 2009. ISSN 01674730. doi: 10.1016/j.strusafe.2008.06.020.

[74] S. Klinkel. *Theorie und Numerik eines Volumen-Schalen-Elementes bei finiten elastischen und plastischen Verzerrungen*. PhD thesis, Inst. für Baustatik, Karlsruhe, 2000.

[75] B. Kouchmeshky and N. Zabaras. Microstructure model reduction and uncertainty quantification in multiscale deformation processes. *Systematic Organisation of Information in Fuzzy Systems*, 48:213–227, 2010.

[76] K. Kremer, P. Edler, N. Miska, F. Leichsenring, D. Balzani, S. Freitag, W. Graf, M. Kaliske, and G. Meschke. Modeling of structures with polymorphic uncertainties at different length scales. *GAMM-Mitteilungen*, 42(1):e201900006, 2019. ISSN 0936-7195, 1522-2608. doi: 10.1002/gamm.201900006.

[77] L. Kudela, N. Zander, S. Kollmannsberger, and E. Rank. Smart octrees: Accurately integrating discontinuous functions in 3D. *Computer Methods in Applied Mechanics and Engineering*, 306:406–426, 2016. ISSN 00457825. doi: 10.1016/j.cma.2016.04.006.

[78] J. Lampinen. A constraint handling approach for the differential evolution algorithm. In *Proceedings of the 2002 Congress on Evolutionary Computation. CEC'02 (Cat. No.02TH8600)*, volume 2, pages 1468–1473, Honolulu, HI, USA, 2002. IEEE. ISBN 978-0-7803-7282-5. doi: 10.1109/CEC.2002.1004459.

[79] B. G. Lindsay. Moment Matrices: Applications in Mixtures. *The Annals of Statistics*, 17(2):722–740, 1989. ISSN 0090-5364. doi: 10.1214/aos/1176347138.

[80] Y. Liu, M. S. Greene, W. Chen, D. Dikin, and W. K. Liu. Computational microstructure characterization and reconstruction for stochastic multiscale material design. *Comput. Aided Design*, 45:65–76, 2013.

[81] LSTC Inc. and DYNAmore GmbH. *LS-Dyna R8.1.0*, 2015.

[82] LSTC Inc. and DYNAmore GmbH. *LS-Opt 5.2*, 2015.

[83] H. Ma, W. Xu, and Y. Li. Random aggregate model for mesoscopic structures and mechanical analysis of fully-graded concrete. *Computers & Structures*, 177:103–113, 2016. ISSN 00457949. doi: 10.1016/j.compstruc.2016.09.005.

[84] M. Mäck, I. Caylak, P. Edler, S. Freitag, M. Hanss, R. Mahnken, G. Meschke, and E. Penner. Optimization with constraints considering polymorphic uncertainties. *GAMM-Mitteilungen*, 42(1):e201900005, 2019. ISSN 09367195. doi: 10.1002/gamm.201900005.

[85] J. Mandel. *Plasticite classique et viscoplasticite*. Springer, 1972. ISBN 978-3-211-81197-9.

[86] J. E. Marsden and T. J. R. Hughes. *Mathematical Foundations of Elasticity*. Dover, New York, NY, unabr., corr. repub. of the ed. publ by. prentice-hall, englewood cliffs, 1983 edition, 1994. ISBN 978-0-486-67865-8.

[87] M. McKerns, H. Owhadi, C. Scovel, T. J. Sullivan, and M. Ortiz. The Optimal Uncertainty Algorithm in the Mystic Framework. *arXiv:1202.1055 [cs]*, 2012.

[88] M. McKerns, L. Strand, T. Sullivan, A. Fang, and M. A. G. Aivazis. Building a Framework for Predictive Science. *arXiv:1202.1056 [cs]*, 2012.

[89] C. Miehe, J. Schotte, and J. Schröder. Computational micro–macro transitions and overall moduli in the analysis of polycrystals at large strains. *Computational Materials Science*, 16(1-4):372–382, 1999. ISSN 09270256. doi: 10.1016/S0927-0256(99)00080-4.

[90] C. Miehe, J. Schröder, and J. Schotte. Computational homogenization analysis in finite plasticity Simulation of texture development in polycrystalline materials. *Computer Methods in Applied Mechanics and Engineering*, 171(3-4):387–418, 1999. ISSN 00457825. doi: 10.1016/S0045-7825(98)00218-7.

[91] N. Miska and D. Balzani. A Method to Quantify Material Parameter Uncertainties Resulting from Microstructure Variation based on Artificial Microstructures. *Proceedings in Applied Mathematics and Mechanics*, 18(1):e201800394, 2018. ISSN 1617-7061. doi: 10.1002/pamm.201800394.

[92] N. Miska and D. Balzani. Optimal Bounds for the Probability of Failure of Sheet Metal Forming Processes of DP Steel. *Proceedings in Applied Mathematics and Mechanics*, 19 (1), 2019. ISSN 1617-7061, 1617-7061. doi: 10.1002/pamm.201900215.

[93] N. Miska and D. Balzani. Quantification of uncertain macroscopic material properties resulting from variations of microstructure morphology based on statistically similar volume elements: Application to dual-phase steel microstructures. *Computational Mechanics*, 64(6):1621–1637, 2019. ISSN 0178-7675, 1432-0924. doi: 10.1007/s00466-019-01738-8.

[94] N. Miska and D. Balzani. Computation of the Sharpest Bounds on Probabilities under the Influence of Polymorphic Uncertainties. *Proceedings in Applied Mathematics and Mechanics*, 20(1), 2021. ISSN 1617-7061, 1617-7061. doi: 10.1002/pamm.202000046.

[95] N. Miska and D. Balzani. Efficient Computation of the Sharpest Bounds on the Probability of Failure of a Sheet Metal Forming Process. *PAMM*, 21(1):e202100070, 2021. ISSN 1617-7061. doi: 10.1002/pamm.202100070.

[96] N. Miska and D. Balzani. Method for the Analysis of Epistemic and Aleatory Uncertainties for a Reliable Evaluation of Failure of Engineering Structures. *International Journal for Uncertainty Quantification*, 12(6):23–45, 2022. ISSN 2152-5080. doi: 10.1615/Int.J.UncertaintyQuantification.2022042145.

[97] N. Miska and D. Balzani. Reliability-Based Design Optimization of Laser-Hardened Traces in a Car Front Bumper Under the Influence of Polymorphic Uncertainties. *PAMM*, 22(1), 2023. ISSN 1617-7061, 1617-7061. doi: 10.1002/pamm.202200038.

[98] N. Miska and D. Balzani. Reliability-Based Design Optimization Incorporating Extended Optimal Uncertainty Quantification, 2024.

[99] N. Miska, S. Prüger, and D. Balzani. Basic Ideas for the Quantification of Uncertainty Associated with the Material's Microstructure Morphology using Statistically Similar RVEs. *Proceedings in Applied Mathematics and Mechanics*, 17(1):431–432, 2017. ISSN 1617-7061. doi: 10.1002/pamm.201710185.

[100] N. Miska, S. Freitag, and D. Balzani. Nested Optimal Uncertainty Quantification for an efficient incorporation of random fields - Application to sheet metal forming. *International Journal for Uncertainty Quantification*, 14(1):89–106, 2024. ISSN 2152-5080. doi: 10.1615/Int.J.UncertaintyQuantification.2023047256.

[101] B. Möller, W. Graf, and M. Beer. Fuzzy structural analysis using α-level optimization. *Computational Mechanics*, 26(6):547–565, 2000. ISSN 0178-7675, 1432-0924. doi: 10.1007/s004660000204.

[102] B. Möller, W. Graf, and M. Beer. Safety assessment of structures in view of fuzzy randomness. *Computers & Structures*, 81(15):1567–1582, 2003. ISSN 00457949. doi: 10.1016/S0045-7949(03)00147-0.

[103] T. Most and C. Bucher. Probabilistic analysis of concrete cracking using neural networks and random fields. *Probabilistic Engineering Mechanics*, 22(2):219–229, 2007. ISSN 02668920. doi: 10.1016/j.probengmech.2006.11.001.

[104] G. E. Neu, P. Edler, S. Freitag, V. Gudžulić, and G. Meschke. Reliability based optimization of steel-fibre segmental tunnel linings subjected to thrust jack loadings. *Engineering Structures*, 254:113752, 2022. ISSN 01410296. doi: 10.1016/j.engstruct.2021.113752.

[105] T. Neumeier, M. A. Peter, D. Peterseim, and D. Wiedemann. Computational polyconvexification of isotropic functions, 2023.

[106] M. Oberguggenberger. Analyzing uncertainty in civil engineering. In *7th International Workshop on Reliable Engineering Computing, "Computing with Confidence"*, volume 1 of *Proceedings of REC 2016*, pages 41–64, 2016.

[107] W. L. Oberkampf, S. M. DeLand, B. M. Rutherford, K. V. Diegert, and K. F. Alvin. Error and uncertainty in modeling and simulation. *Reliability Engineering & System Safety*, 75(3):333–357, 2002. ISSN 0951-8320. doi: 10.1016/S0951-8320(01)00120-X.

[108] R. W. Ogden. *Non-Linear Elastic Deformations*. Ellis Horwood Series in Mathematics and Its Applications. Horwood [usw.], Chichester, 1984. ISBN 978-0-85312-273-9 978-0-470-27508-5.

[109] M. Ostoja-Starzewski. The use, misuse, and abuse of stochastic random media. In *Proceedings of European Conference on Computational Mechanics*, volume 148, 2001.

[110] H. Owhadi, C. Scovel, T. J. Sullivan, M. McKerns, and M. Ortiz. Optimal Uncertainty Quantification. *SIAM Review*, 55(2):271–345, 2013. ISSN 0036-1445, 1095-7200. doi: 10.1137/10080782X.

[111] D. Padmanabhan, H. Agarwal, J. E. Renaud, and S. M. Batill. A study using Monte Carlo Simulation for failure probability calculation in Reliability-Based Optimization. *Optimization and Engineering*, 7(3):297–316, 2006. ISSN 1389-4420, 1573-2924. doi: 10.1007/s11081-006-9973-8.

[112] M. Papadrakakis and N. D. Lagaros. Reliability-based structural optimization using neural networks and Monte Carlo simulation. *Computer Methods in Applied Mechanics and Engineering*, 191(32):3491–3507, 2002. ISSN 00457825. doi: 10.1016/S0045-7825(02)00287-6.

[113] M. Papadrakakis, V. Papadopoulos, and N. D. Lagaros. Structural reliability analysis of elastic-plastic structures using neural networks and monte carlo simulation. *Computer Methods in Applied Mechanics and Engineering*, 136:145–163, 1996.

[114] I. Papaioannou and D. Straub. Combination line sampling for structural reliability analysis. *Structural Safety*, 88:102025, 2021. ISSN 01674730. doi: 10.1016/j.strusafe.2020.102025.

[115] I. Papaioannou, C. Papadimitriou, and D. Straub. Sequential importance sampling for structural reliability analysis. *Structural Safety*, 62:66–75, 2016. ISSN 01674730. doi: 10.1016/j.strusafe.2016.06.002.

[116] I. Papaioannou, M. Daub, M. Drieschner, F. Duddeck, M. Ehre, L. Eichner, M. Eigel, M. Götz, W. Graf, L. Grasedyck, R. Gruhlke, D. Hömberg, M. Kaliske, D. Moser, Y. Petryna, and D. Straub. Assessment and design of an engineering structure with polymorphic uncertainty quantification. *GAMM-Mitteilungen*, 42(2):e201900009, 2019. ISSN 0936-7195, 1522-2608. doi: 10.1002/gamm.201900009.

[117] J. Parvizian, A. Düster, and E. Rank. Finite cell method: h- and p-extension for embedded domain problems in solid mechanics. *Computational Mechanics*, 41(1):121–133, 2007. ISSN 0178-7675, 1432-0924. doi: 10.1007/s00466-007-0173-y.

[118] D. Pivovarov, R. Zabihyan, J. Mergheim, K. Willner, and P. Steinmann. On periodic boundary conditions and ergodicity in computational homogenization of heterogeneous materials with random microstructure. *Computer Methods in Applied Mechanics and Engineering*, 357:112563, 2019. ISSN 00457825. doi: 10.1016/j.cma.2019.07.032.

[119] R. Polakova. L-SHADE with competing strategies applied to constrained optimization. In *2017 IEEE Congress on Evolutionary Computation (CEC)*, pages 1683–1689, Donostia, San Sebastián, Spain, 2017. IEEE. ISBN 978-1-5090-4601-0. doi: 10.1109/CEC.2017.7969504.

[120] R. Rackwitz. Reviewing probabilistic soils modelling. *Computers and Geotechnics*, 26 (3-4):199–223, 2000. ISSN 0266352X. doi: 10.1016/S0266-352X(99)00039-7.

[121] I. Ramière, P. Angot, and M. Belliard. A fictitious domain approach with spread interface for elliptic problems with general boundary conditions. *Computer Methods in Applied Mechanics and Engineering*, 196(4-6):766–781, 2007. ISSN 00457825. doi: 10.1016/j.cma.2006.05.012.

[122] R. Rojas. *Neural Networks - a Systematic Introduction*. Springer Berlin Heidelberg, 1996. ISBN 978-3-540-60505-8.

[123] S. Sankararaman and S. Mahadevan. Distribution type uncertainty due to sparse and imprecise data. *Mechanical Systems and Signal Processing*, 37(1-2):182–198, 2013. ISSN 08883270. doi: 10.1016/j.ymssp.2012.07.008.

[124] T. Sasagawa, M. Tanaka, R. Omote, and D. Balzani. Construction of statistically similar representative volume elements for discontinuous fiber composites. *Composite Structures*, 203:193–203, 2018. ISSN 0263-8223. doi: 10.1016/j.compstruct.2018.06.014.

[125] D. Savvas, G. Stefanou, M. Papadrakakis, and G. Deodatis. Homogenization of random heterogeneous media with inclusions of arbitrary shape modeled by XFEM. *Computational Mechanics*, 54(5):1221–1235, 2014. ISSN 0178-7675, 1432-0924. doi: 10.1007/s00466-014-1053-x.

[126] L. Scheunemann, D. Balzani, D. Brands, and J. Schröder. Construction of statistically similar RVEs. In S. Conti and K. Hackl, editors, *Analysis and Computation of Microstructure in Finite Plasticity (Lecture Notes in Applied and Computational Mechanics 78)*. Springer, 2015.

[127] L. Scheunemann, D. Balzani, D. Brands, and J. Schröder. Design of 3D statistically similar Representative Volume Elements based on Minkowski functionals. *Mechanics of Materials*, 90:185–201, 2015. ISSN 01676636. doi: 10.1016/j.mechmat.2015.03.005.

[128] F. N. Schietzold, A. Schmidt, M. M. Dannert, A. Fau, R. M. N. Fleury, W. Graf, M. Kaliske, C. Könke, T. Lahmer, and U. Nackenhorst. Development of fuzzy probability based random fields for the numerical structural design. *GAMM-Mitteilungen*, 42 (1):e201900004, 2019. ISSN 0936-7195, 1522-2608. doi: 10.1002/gamm.201900004.

[129] F. N. Schietzold, W. Graf, and M. Kaliske. Multi-Objective Optimization of Tree Trunk Axes in Glulam Beam Design Considering Fuzzy Probability-Based Random Fields. *ASCE-ASME J Risk and Uncert in Engrg Sys Part B Mech Engrg*, 7(2):020913, 2021. ISSN 2332-9017, 2332-9025. doi: 10.1115/1.4050370.

[130] F. N. Schietzold, F. Leichsenring, M. Götz, W. Graf, and M. Kaliske. Robustness versus Performance – Nested Inherence of Objectives in Optimization with Polymorphic Uncertain Parameters. *Advances in Engineering Software*, 156:102932, 2021. ISSN 09659978. doi: 10.1016/j.advengsoft.2020.102932.

[131] D. Schillinger and M. Ruess. The Finite Cell Method: A Review in the Context of Higher-Order Structural Analysis of CAD and Image-Based Geometric Models. *Archives of Computational Methods in Engineering*, 22(3):391–455, 2015. ISSN 1134-3060, 1886-1784. doi: 10.1007/s11831-014-9115-y.

[132] A. Schmidt and T. Lahmer. Efficient domain decomposition based reliability analysis for polymorphic uncertain material parameters. *PAMM*, 21(1), 2021. ISSN 1617-7061, 1617-7061. doi: 10.1002/pamm.202100014.

[133] A. Schmidt, C. Henning, S. Herbrandt, C. Könke, K. Ickstadt, T. Ricken, and T. Lahmer. Numerical studies of earth structure assessment via the theory of porous media using fuzzy probability based random field material descriptions. *GAMM-Mitteilungen*, 42(1):e201900007, 2019. ISSN 0936-7195, 1522-2608. doi: 10.1002/gamm.201900007.

[134] K. Schneider, B. Klusemann, and S. Bargmann. Automatic three-dimensional geometry and mesh generation of periodic representative volume elements for matrix-inclusion composites. *Advances in Engineering Software*, 99:177–188, 2016. ISSN 09659978. doi: 10.1016/j.advengsoft.2016.06.001.

[135] J. Schröder. *Homogenisierungsmethoden Der Nichtlinearen Kontinuumsmechanik Unter Beachtung von Instabilitäten*. Institut für Mechanik (Bauwesen), Lehrstuhl I, Universität Stuttgart, Stuttgart, 2000.

[136] J. Schröder. A numerical two-scale homogenization scheme: The FE2-method. In J. Schröder and K. Hackl, editors, *Plasticity and Beyond*, volume 550, pages 1–64. Springer Vienna, Vienna, 2014. ISBN 978-3-7091-1624-1 978-3-7091-1625-8.

[137] G. Schuëller and H. Jensen. Computational methods in optimization considering uncertainties – An overview. *Computer Methods in Applied Mechanics and Engineering*, 198 (1):2–13, 2008. ISSN 00457825. doi: 10.1016/j.cma.2008.05.004.

[138] C. Schwab and R. A. Todor. Karhunen–Loève approximation of random fields by generalized fast multipole methods. *Journal of Computational Physics*, 217(1):100–122, 2006. ISSN 00219991. doi: 10.1016/j.jcp.2006.01.048.

[139] J. Simo. Algorithms for static and dynamic multiplicative plasticity that preserve the classical return mapping schemes of the infinitesimal theory. *Computer Methods in Applied Mechanics and Engineering*, 99(1):61–112, 1992. ISSN 00457825. doi: 10.1016/0045-7825(92)90123-2.

[140] R. Smit, W. Brekelmans, and H. Meijer. Prediction of the mechanical behavior of nonlinear heterogeneous systems by multi-level finite element modeling. *Computer Methods in Applied Mechanics and Engineering*, 155(1-2):181–192, 1998. ISSN 00457825. doi: 10.1016/S0045-7825(97)00139-4.

[141] G. Stefanou. The stochastic finite element method: Past, present and future. *Computer Methods in Applied Mechanics and Engineering*, 198(9-12):1031–1051, 2009. ISSN 00457825. doi: 10.1016/j.cma.2008.11.007.

[142] G. Stefanou, D. Savvas, and P. Metsis. Random Material Property Fields of 3D Concrete Microstructures Based on CT Image Reconstruction. *Materials*, 14(6):1423, 2021. ISSN 1996-1944. doi: 10.3390/ma14061423.

[143] J. Stenger, F. Gamboa, M. Keller, and B. Iooss. Optimal Uncertainty Quantification of a risk measurement from a thermal-hydraulic code using Canonical Moments. *International Journal for Uncertainty Quantification*, 10(1):35–53, 2020. ISSN 2152-5080. doi: 10.1615/Int.J.UncertaintyQuantification.2020030800.

[144] R. Storn and K. Price. Differential Evolution – A Simple and Efficient Heuristic for Global Optimization over Continuous Spaces. *Journal of Global Optimization*, 11(4): 341–359, 1997. ISSN 09255001. doi: 10.1023/A:1008202821328.

[145] B. Sudret. Stochastic Finite Element Methods and Reliability A State-of-the-Art Report. Technical report, ETH Zürich, 2000.

[146] B. Sudret, S. Marelli, and J. Wiart. Surrogate models for uncertainty quantification: An overview. In *2017 11th European Conference on Antennas and Propagation (EUCAP)*, pages 793–797, Paris, France, 2017. IEEE. ISBN 978-88-907018-7-0. doi: 10.23919/EuCAP.2017.7928679.

[147] T. Sullivan. *Introduction to Uncertainty Quantification*, volume 63 of *Texts in Applied Mathematics*. Springer International Publishing, Cham, 2015. ISBN 978-3-319-23394-9 978-3-319-23395-6. doi: 10.1007/978-3-319-23395-6.

[148] H. Swift. Plastic instability under plane stress. *Journal of the Mechanics and Physics of Solids*, 1(1):1–18, 1952. ISSN 00225096. doi: 10.1016/0022-5096(52)90002-1.

[149] D. Tal and J. Fish. Stochastic multiscale modeling and simulation framework for concrete. *Cement and Concrete Composites*, 90:61–81, 2018. ISSN 09589465. doi: 10.1016/j.cemconcomp.2018.03.016.

[150] E. Tamsen. *A Fully Coupled Dynamic Framework for Two-Scale Simulations of SHCC*. PhD thesis, Ruhr-Universität Bochum, Bochum, 2021.

[151] E. Tamsen and D. Balzani. A general, implicit, finite-strain FE2 framework for the simulation of dynamic problems on two scales. *Computational Mechanics*, 67(5):1375–1394, 2021. ISSN 0178-7675, 1432-0924. doi: 10.1007/s00466-021-01993-8.

[152] V. Tarigopula, O. S. Hopperstad, M. Langseth, A. H. Clausen, F. Hild, O.-G. Lademo, and M. Eriksson. A study of large plastic deformations in dual phase steel using digital image correlation and FE analysis. *Experimental Mechanics*, 48:181–196, 2008.

[153] S. Torquato. *Random Heterogeneous Materials*, volume 16 of *Interdisciplinary Applied Mathematics*. Springer New York, New York, NY, 2002. ISBN 978-1-4757-6357-7 978-1-4757-6355-3. doi: 10.1007/978-1-4757-6355-3.

[154] M. A. Valdebenito and G. I. Schuëller. A survey on approaches for reliability-based optimization. *Structural and Multidisciplinary Optimization*, 42(5):645–663, 2010. ISSN 1615-147X, 1615-1488. doi: 10.1007/s00158-010-0518-6.

[155] E. Vanmarcke. *Random Fields: Analysis and Synthesis (Revised and Expanded New Edition)*. WORLD SCIENTIFIC, 2010. ISBN 978-981-256-297-5 978-981-4307-59-8. doi: 10.1142/5807.

[156] S. S. Vel and A. J. Goupee. Multiscale thermoelastic analysis of random heterogeneous materials Part I: Microstructure characterization and homogenization of material properties. *Computational Materials Science*, 48:22–38, 2010.

[157] P. Virtanen, R. Gommers, T. E. Oliphant, M. Haberland, T. Reddy, D. Cournapeau, E. Burovski, P. Peterson, W. Weckesser, J. Bright, S. J. van der Walt, M. Brett, J. Wilson, K. J. Millman, N. Mayorov, A. R. J. Nelson, E. Jones, R. Kern, E. Larson, C. J. Carey, İ. Polat, Y. Feng, E. W. Moore, J. VanderPlas, D. Laxalde, J. Perktold, R. Cimrman, I. Henriksen, E. A. Quintero, C. R. Harris, A. M. Archibald, A. H. Ribeiro, F. Pedregosa, P. van Mulbregt, SciPy 1.0 Contributors, A. Vijaykumar, A. P. Bardelli, A. Rothberg, A. Hilboll, A. Kloeckner, A. Scopatz, A. Lee, A. Rokem, C. N. Woods, C. Fulton, C. Masson, C. Häggström, C. Fitzgerald, D. A. Nicholson, D. R. Hagen, D. V. Pasechnik, E. Olivetti, E. Martin, E. Wieser, F. Silva, F. Lenders, F. Wilhelm, G. Young, G. A. Price, G.-L. Ingold, G. E. Allen, G. R. Lee, H. Audren, I. Probst, J. P. Dietrich, J. Silterra, J. T. Webber, J. Slavič, J. Nothman, J. Buchner, J. Kulick, J. L. Schönberger, J. V. de Miranda Cardoso, J. Reimer, J. Harrington, J. L. C. Rodríguez, J. Nunez-Iglesias, J. Kuczynski, K. Tritz, M. Thoma, M. Newville, M. Kümmerer, M. Bolingbroke, M. Tartre, M. Pak, N. J. Smith, N. Nowaczyk, N. Shebanov, O. Pavlyk, P. A. Brodtkorb, P. Lee, R. T. McGibbon, R. Feldbauer, S. Lewis, S. Tygier, S. Sievert, S. Vigna, S. Peterson, S. More, T. Pudlik, T. Oshima, T. J. Pingel, T. P. Robitaille, T. Spura, T. R. Jones, T. Cera, T. Leslie, T. Zito, T. Krauss, U. Upadhyay, Y. O. Halchenko, and Y. Vázquez-Baeza. SciPy 1.0: Fundamental algorithms for scientific computing in Python. *Nature Methods*, 17(3):261–272, 2020. ISSN 1548-7091, 1548-7105. doi: 10.1038/s41592-019-0686-2.

[158] M. Vořechovský. Simulation of simply cross correlated random fields by series expansion methods. *Structural Safety*, 30(4):337–363, 2008. ISSN 01674730. doi: 10.1016/j.strusafe.2007.05.002.

[159] M. Wagner, A. Jahn, E. Beyer, and D. Balzani. Design and Optimization of Steel Car Body Structures via Local Laser-Strengthening. *Engineering*, 08(05):276–286, 2016. ISSN 1947-3931, 1947-394X. doi: 10.4236/eng.2016.85024.

[160] P. Wen, N. Takano, and D. Kurita. Probabilistic multiscale analysis of three-phase composite material considering uncertainties in both physical and geometrical parameters at microscale. *Acta mechanica*, 227:2735–2747, 2016.

[161] D. Wingender and D. Balzani. Simulation of crack propagation through voxel-based, heterogeneous structures based on eigenerosion and finite cells. *Computational Mechanics*, 70(2):385–406, 2022. ISSN 1432-0924. doi: 10.1007/s00466-022-02172-z.

[162] G. Winkler. Extreme Points of Moment Sets. *Mathematics of Operations Research*, 13 (4):581–587, 1988. ISSN 0364-765X, 1526-5471. doi: 10.1287/moor.13.4.581.

[163] P. Wriggers. *Nonlinear Finite Element Methods*. Springer, Berlin, 2008. ISBN 978-3-540-71000-4 978-3-540-71001-1.

[164] Yong Wang, Zixing Cai, Yuren Zhou, and Wei Zeng. An Adaptive Tradeoff Model for Constrained Evolutionary Optimization. *IEEE Transactions on Evolutionary Computation*, 12(1):80–92, 2008. ISSN 1941-0026, 1089-778X. doi: 10.1109/TEVC.2007.902851.

[165] L. A. Zadeh. Fuzzy sets. *Information and Control*, 8(3):338–353, 1965. ISSN 0019-9958. doi: 10.1016/S0019-9958(65)90241-X.

[166] L. A. Zadeh. Probability measures of Fuzzy events. *Journal of Mathematical Analysis and Applications*, 23(2):421–427, 1968. ISSN 0022247X. doi: 10.1016/0022-247X(68)90078-4.

[167] J. Zhang. Modern Monte Carlo methods for efficient uncertainty quantification and propagation: A survey. *WIREs Computational Statistics*, 13(5), 2021. ISSN 1939-5108, 1939-0068. doi: 10.1002/wics.1539.

[168] J. Zhang and M. D. Shields. The effect of prior probabilities on quantification and propagation of imprecise probabilities resulting from small datasets. *Computer Methods in Applied Mechanics and Engineering*, 334:483–506, 2018. ISSN 00457825. doi: 10.1016/j.cma.2018.01.045.

[169] J. Zhang and M. D. Shields. On the quantification and efficient propagation of imprecise probabilities resulting from small datasets. *Mechanical Systems and Signal Processing*, 98:465–483, 2018. ISSN 08883270. doi: 10.1016/j.ymssp.2017.04.042.

[170] S. Zschocke, W. Graf, and M. Kaliske. Polymorphic Uncertain Structural Analysis: Challenges in Data-Driven Inelasticity. *PAMM*, 22(1):e202200023, 2023. ISSN 1617-7061, 1617-7061. doi: 10.1002/pamm.202200023.

Educational Background

10/2017 – present	Research associate at the Chair of Continuum Mechanics, Department of Civil and Environmental Engineering, Ruhr-Universität Bochum
11/2016 – 09/2017	Research associate at the Institute of Mechanics and Shell Structures, Department of Civil Engineering, Technische Universität Dresden
10/2011 – 10/2016	Civil Engineering studies at Technische Universität Dresden Graduated with title Dipl.-Ing.
06/2011	General qualification for university entrance (Abitur)

Mitteilungen aus dem Institut für Mechanik
RUHR-UNIVERSITÄT BOCHUM
Nr. 191

ISBN 978-3-935892-69-8